Tribologie du Ti-6AI-4V et d'un revêtement DLC en fretting : applications au contact tige/col dans les prothèses de hanches modulaires

Haohao Ding

N°d'ordre NNT : 2018LYSEC029

THESE de DOCTORAT DE L'UNIVERSITE DE LYON
opérée au sein de l'Ecole centrale de Lyon

Ecole Doctorale N° 34
Ecole Doctorale des Matériaux de Lyon

Spécialité de doctorat :
Matériaux

Soutenue le 24 octobre 2018, par :
Haohao DING

TRIBOLOGY OF Ti–6Al–4V AND DLC COATING IN FRETTING:
APPLICATIONS TO STEM / NECK CONTACT OF MODULAR HIP IMPLANT

TRIBOLOGIE DU Ti–6Al–4V ET D'UN REVETEMENT DLC EN FRETTING :
APPLICATIONS AU CONTACT TIGE / COL DANS LES PROTHESES DE HANCHES MODULAIRES

Devant le jury composé de :

Donnet, Christophe	Professeur, Université Jean Monnet	Président de jury
Langlade, Cécile	Professeur, UTBM	Rapporteure
Denape, Jean	Professeur, ENI Tarbes	Rapporteur
Carpentier, Luc	Maître de conférences, UBFC	Examinateur
Sfarghiu, Ana-Maria	Chargée de recherche CNRS, INSA de Lyon	Examinatrice
Kapsa, Philippe	Directeur de recherche émérite au CNRS, ECL	Directeur de thèse
Fridrici, Vincent	Maître de conférences, ECL	Co-directeur de thèse
Fontaine, Julien	Chargé de recherche CNRS, ECL	Membre invité
Géringer, Jean	Maître-Assistant, Mines St-Etienne	Membre invité

ACKNOWLEDGEMENTS

I express my sincere gratitude to Prof. Philippe KAPSA, my supervisor of the thesis, for giving me basics of research and supporting me during the whole thesis work.

I address my special appreciation to Dr. Vincent FRIDRICI, my co-supervisor of the thesis. During my three years of thesis, he gave me uncountable suggestions and professional guidance to my work. He also patiently and critically proofread the manuscript.

I would like to express my thanks to all the colleagues in the laboratory for their generous help. In particular, I would like to thank Dr. Marième FALL for her great help on my study and life in France. I would also like to present my thanks to Gaëtan BOUVARD and Thomas MALHOMME for training in testing and analytical machines and to Dr. Gaylord GUILLONNEAU and Dr. Julien FONTAINE for their valuable suggestions on my work.

I would like to acknowledge the support from LabEx MANUTECH-SISE and IREIS. I would also express my thanks to Dr. Jean GÉRINGER and Dr. Sergio SAO-JOAO from Ecole des Mines de Saint-Etienne for valuable suggestions on my work.

I am so grateful to Prof. Wenjian WANG and Prof. Qiyue LIU, for being my supervisors of master's thesis at Southwest Jiaotong University in China. They brought me into the tribology world. I would also like to thank Prof. Minhao ZHU and Prof. Zhongrong ZHOU for recommending me to study in LTDS.

I would like to thank China Scholarship Council for its financial support.

At the end, I must appreciate my parents and sisters for their supporting on my overseas study.

Abstract

The use of modular neck adapter when placing a total hip prosthesis introduces a new interface, between the femoral stem and the neck adapter, which is propitious to fretting damage during walking. Ti–6Al–4V alloy has been widely used in neck adapters and femoral stems. However, the Ti–6Al–4V / Ti–6Al–4V contacts present high friction and severe adhesive wear under fretting conditions. Diamond-like carbon (DLC) coatings have been widely used as protective coatings for metallic parts. Thus, they can be introduced into Ti–6Al–4V neck adapter / Ti–6Al–4V femoral stem contacts.

The objective of this thesis is to investigate the tribological behaviors of DLC coating and Ti–6Al–4V alloy under fretting conditions for application to neck adapter / femoral stem contact. Fretting tests are conducted with a cylinder / flat contact under different values of displacement amplitude (±20 µm, ±40 µm, and ±70 µm) and normal force (between 200 N and 1 200 N). Furthermore, the effects of different DLC coatings (DLC A and DLC B), different surface roughness (smooth and rough), different coating positions (coating on the flat, on the cylinder, and on both surfaces), different environments (laboratory air and calf serum) are analyzed. Besides, the origin of low friction of Ti–6Al–4V / DLC coating contact is explored. The mechanical properties of tribofilm formed on the rubbed Ti–6Al–4V surface is studied.

For fretting tests without coating (Ti–6Al–4V / Ti–6Al–4V contact) under laboratory air condition, the friction coefficient is high, between 0.8 and 1.2. The wear volume increases with the displacement amplitude. For fretting tests with coating, Ti–6Al–4V can be well protected under relatively low load conditions. The friction coefficient is low (around 0.2) and the wear volume is small. Under high load conditions, the coating is almost totally removed. The friction and wear volume are similar to tests without coating. The harder coating (DLC A) has better tribological property than DLC B. The coating on the smooth surface exhibits better fretting performance than on the rough surface. Coating on a cylindrical surface shows better tribological performance than on a flat surface. The DLC coating is damaged more severely when it slides against a DLC coating than against the uncoated Ti–6Al–4V alloy. The coating performs better under the serum condition than under the laboratory air condition. A tribofilm is formed on the rubbed Ti–6Al–4V surface when sliding against a DLC coating under low load conditions. The tribofilm shows higher hardness, higher Young's modulus, higher compression modulus, higher yield strength than the Ti–6Al–4V alloy. A tribological model is proposed for tribofilm formation and explanation of origin of low friction, by in-depth analysis of contact surfaces, on mechanical and chemical points of view.

Keywords: Fretting, friction, wear, Ti–6Al–4V, diamond-like carbon coating, surface roughness, coating position, serum, tribofilm.

Résumé

L'utilisation d'un col modulaire lors de la pose d'une prothèse totale de hanche introduit une nouvelle interface, entre la tige et le col, qui est susceptible de s'endommager par fretting lors de la marche. L'alliage Ti–6Al–4V est très largement utilisé pour les tiges et les cols. Cependant, les contacts Ti–6Al–4V / Ti–6Al–4V présentent un frottement élevé et une forte usure adhésive dans les conditions de fretting. Les revêtements DLC (diamond-like carbon) ont été largement utilisés comme revêtements protecteurs pour les pièces métalliques. Ainsi, ils peuvent être introduits dans les contacts entre la tige en Ti–6Al–4V et le col en Ti–6Al–4V.

L'objectif de cette thèse est d'étudier les comportements tribologiques du revêtement DLC et de l'alliage Ti–6Al–4V dans les conditions de fretting pour application au contact entre la tige et le col. Les essais de fretting sont menés avec un contact cylindre sur plan sous différentes valeurs d'amplitude de déplacement (± 20 µm, ± 40 µm, et ± 70 µm) et de force normale (entre 200 N et 1 200 N). En outre, les effets de différents revêtements (DLC A et DLC B), différentes rugosités de surface (lisse et rugueuse), différentes positions de revêtement (revêtement sur le plan, sur le cylindre et sur les deux surfaces), différents environnements (dans l'air et dans le sérum de veau) sont analysés. Par ailleurs, l'origine du faible frottement du contact entre Ti–6Al–4V et revêtement DLC est explorée. Les propriétés mécaniques du tribofilm formé sur la surface de Ti–6Al–4V frottée sont également étudiées.

Pour les tests de fretting sans revêtement (contact Ti–6Al–4V / Ti–6Al–4V) dans l'air, le coefficient de frottement est élevé, entre 0.8 et 1.2. Le volume d'usure croît avec l'amplitude de déplacement. Pour les tests avec revêtement, le Ti–6Al–4V peut être bien protégé, sous des charges relativement faibles. Le coefficient de frottement (d'environ 0,2) et le volume usé sont faibles. Sous fortes charges, le revêtement est presque totalement éliminé. Le frottement et le volume d'usure sont similaires à ceux des essais sans revêtement. Le revêtement plus dur (DLC A) a de meilleures propriétés tribologiques que le DLC B. Le revêtement sur la surface lisse présente une meilleure performance en fretting que sur la surface rugueuse. Le revêtement sur une surface cylindrique présente une meilleure performance tribologique que sur une surface plane. Le revêtement DLC est plus endommagé lorsqu'il glisse contre un revêtement DLC que contre du Ti–6Al–4V non revêtu. Le revêtement fonctionne mieux en présence de sérum que dans l'air. Un tribofilm est formé sur la surface de Ti–6Al–4V frottée lorsqu'il glisse contre un revêtement DLC sous de faibles charges. Le tribofilm présente une dureté plus élevée, un module de Young plus élevé, un module de compression plus élevé, une limite d'élasticité plus élevé que l'alliage Ti–6Al–4V. Un modèle tribologique est proposé pour la formation du tribofilm et l'explication de l'origine du faible frottement, par une analyse approfondie des surfaces de contact, sur les points de vue mécaniques et chimiques.

Mot-clés : Fretting, frottement, usure, Ti–6Al–4V, revêtement diamond-like carbon, rugosité de surface, position de revêtement, sérum, tribofilm.

CONTENTS

INTRODUCTION

In this thesis, DLC coatings are studied in order to analyze their possible application at the neck adapter / femoral stem (Ti–6Al–4V / Ti–6Al–4V) contact to improve its tribological performance in fretting. The influences of surface roughness, coating position, and environment on the performance of DLC coatings and Ti–6Al–4V alloy are investigated. At last, the origin of low friction of DLC coating is discussed.

Background

Modular neck adapter has been introduced into total hip arthroplasty (THA) to facilitate the replacement surgery. However, it introduces a new interface, neck adapter / femoral stem (as shown in Figure Intro.1), which is under fretting condition during people walking. Furthermore, Ti–6Al–4V alloy has been widely used in neck adapters and femoral stems due to its high specific strength, corrosion resistance and biocompatibility. However, the Ti–6Al–4V / Ti–6Al–4V contacts present high friction and severe adhesive wear under fretting conditions. Therefore, the anti-fretting properties of Ti–6Al–4V neck adapter / Ti–6Al–4V femoral stem contacts should be improved.

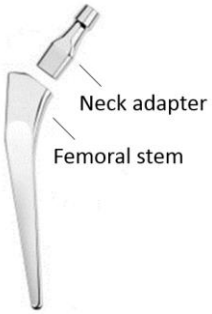

Figure Intro.1. Bi-modular femoral stem.

Diamond-like carbon (DLC) coatings can be used as protective coatings for metallic parts. They exhibit excellent tribological performance due to their low friction and high hardness, in many environments. Furthermore, DLC coatings show high biocompatibility, which makes them proper for implant applications.

In this thesis, tribological performance of DLC coatings in fretting is studied in order to analyze the possible application of DLC at the neck adapter / femoral stem (Ti–6Al–4V / Ti–6Al–4V) contact.

Objectives and research approaches

The objectives of this thesis are to investigate the fretting behavior of DLC coatings and Ti–6Al–4V alloy for neck adapter and femoral stem applications.

In order to reach these objectives, the following research approaches will be realized. At first, literature study will be carried out to investigate the development of THA, coatings for tribological applications, and the development of DLC coatings. Based on the literature study, DLC coatings are determined for neck adapter / femoral stem (Ti–6Al–4V / Ti–6Al–4V) applications. Then, fretting experiments will be performed to investigate the fretting behavior of DLC coating and Ti–6Al–4V alloy. Furthermore, the influence of different parameters, including surface roughness, coating position and serum environment, on the fretting behavior of DLC coatings and Ti–6Al–4V will be explored. Finally, the origin of low friction of DLC coating will be discussed.

Organization of the manuscript

The manuscript is organized as presented in Figure Intro.2.

In Chapter I, literature study will be summarized, including the development of modular hip implant, the coating types and deposition methods, the DLC coatings and their tribological response, and the influences of different parameters on tribological behavior of contacts.

Chapter II will introduce the materials under investigation, including the Ti–6Al–4V substrate and DLC coatings, the experimental and analytical methods, and the test conditions.

In Chapter III, the fretting behavior of Ti–6Al–4V / Ti–6Al–4V contact will be investigated under laboratory air condition. The effect of surface roughness will be explored. The results will serve as baselines for the study of the effect of DLC coating in next chapters.

Chapter IV will investigate the fretting behavior of DLC coatings under laboratory air condition. The influence of different parameters will be explored, including different DLC coatings, different surface roughness, and different coating positions.

In Chapter V, the influence of serum on the fretting behavior of Ti–6Al–4V will be investigated with a Ti–6Al–4V / Ti–6Al–4V contact. The influence of serum on the tribological performance of a DLC coating will be investigated with a coating / Ti–6Al–4V contact.

Chapter VI investigates the origin of low friction for the DLC coating / Ti–6Al–4V contact under low load conditions. At last, a tribological model for the evolution of DLC coating / Ti–6Al–4V contact under low load condition will be proposed.

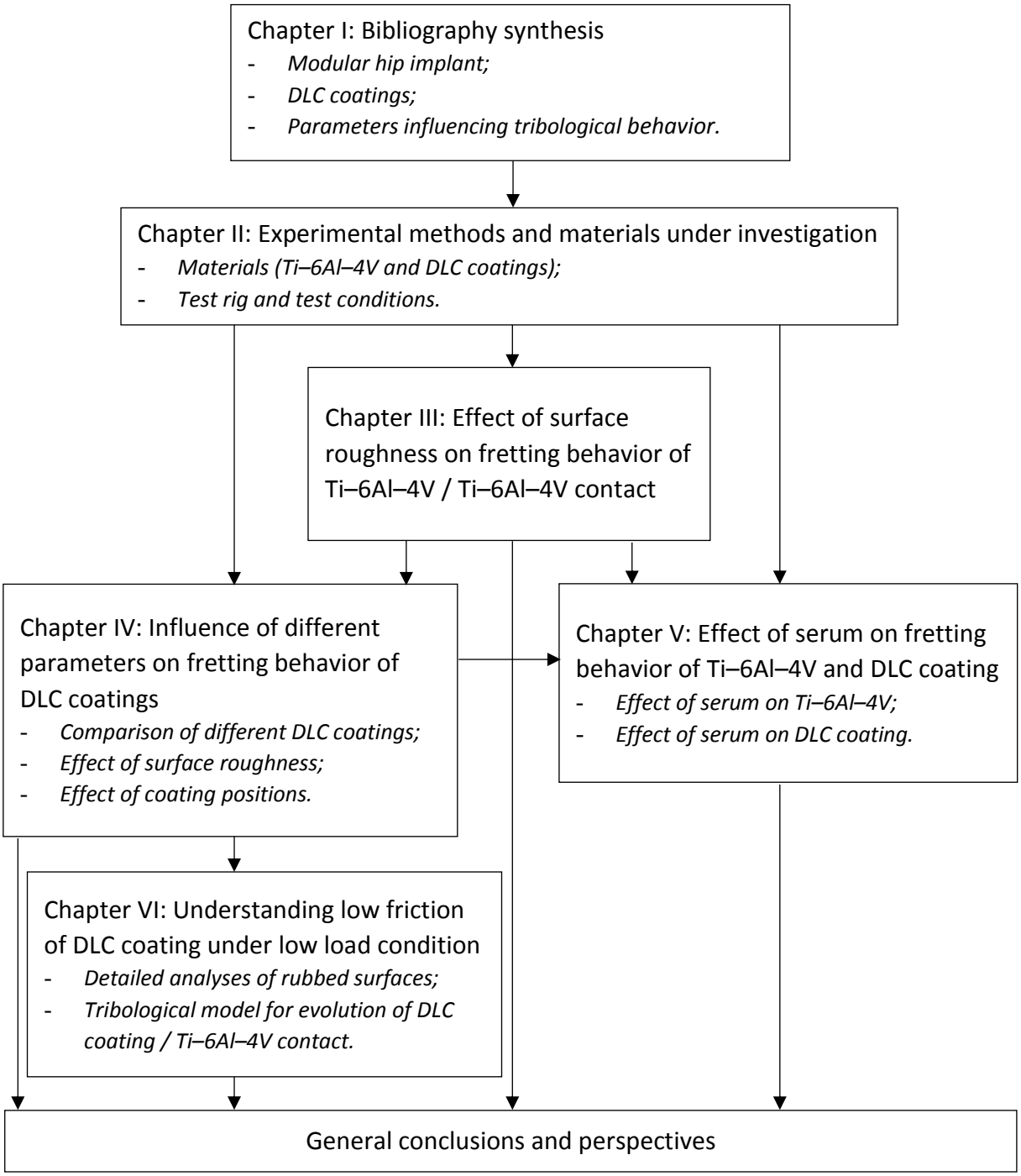

Figure Intro.2. Organization of the manuscript.

CHAPTER I

BIBLIOGRAPHY SYNTHESIS

CHAPTER I : BIBLIOGRAPHY SYNTHESIS

CHAPTER I: BIBLIOGRAPHY SYNTHESIS

In this chapter, literature study is summarized to understand the research context, including the modular hip implant, coating types, coating deposition methods, diamond-like carbon coatings and their mechanical and tribological properties, and some parameters influencing tribological behavior of contacts.

1. Introduction

In the year of 1962, Doctor John Charnley developed low-friction arthroplasty of the hip at Wrightington Hospital. Since then, total hip replacement (THR) has become a popular surgery to restore the hip function [1]. More than 500 000 THRs are done every year in the UK and USA, with excellent clinical outcomes showing greater than 95% survivorship at 10-year follow-up, and greater than 80% implant survivorship at 25-year follow-up [2].

Since 1990s, modular neck adapters have been introduced into THRs to fit different individuals by using different neck adapters with different shapes (i.e. neck adapter length, neck–stem angles, etc.) and thus to facilitate the replacement surgery [3]. However, the use of neck adapters introduces a new interface, neck adapter–femoral stem interface, which is under fretting conditions, i.e. cyclic loading and relative micromotions, during walking [4].

Ti–6Al–4V has been widely used in hip implants owing to its high specific strength, corrosion resistance and biocompatibility. However, Ti–6Al–4V / Ti–6Al–4V contacts present poor tribological performance including high friction coefficients and severe adhesive wear under fretting conditions [5].

Diamond-like carbon (DLC) coatings, which offer the combination of high hardness and low friction in many environments, can improve the tribological performance of the metallic substrates [6]. DLC coatings are used in many applications including bearings, gears, cams, valves, forming tools, computer hard discs, etc. Furthermore, DLC coatings have excellent corrosion resistance and biocompatibility, which enable them to be used in hip prosthesis applications [6].

The objective of this thesis is to study the influence of DLC coatings on the fretting behaviors of Ti–6Al–4V alloy for neck adapter–femoral stem contact in modular hip implant applications.

In this Chapter, literature study will be summarized, including the development of modular hip implant, the coating types and deposition methods, the DLC coatings and their tribological response, and the influences of different parameters on tribological behavior of contacts.

2. Modular hip implant

2.1. Total hip replacement (THR)

THR is amongst the most common and successful surgical procedures performed today, and aims to restore function and relieve pain by replacing the articulating surfaces of the joints and can result in significant improvements in patient's quality of life [7–9]. THR has become popular since John Charnley developed the low friction arthroplasty over 50 years ago using a metal ball articulating with a Teflon® cup and subsequently (with significantly greater success) a polyethylene cup [10, 11]. In England and Wales, almost 65 000 and over 71 000 THRs were performed during 2008 and 2011, respectively, and 93% of them were performed for osteoarthritis [7–9].

The components in a total hip replacement consist of an acetabular cup, a femoral head, and a femoral stem. The femoral head articulates with the acetabular cup or a liner placed within the cup. The head may be made from stainless steel, cobalt-chromium or ceramic. The acetabular component may be made of polyethylene or metal, or be metal backed using a polyethylene or ceramic liner. The metal-on-polyethylene bearing is the most frequently used [7], as shown in Figure I.1.

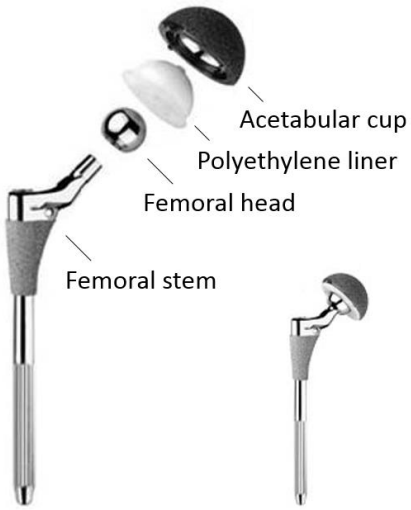

Figure I.1. Total hip replacement with a metal-on-polyethylene contact [12].

Fixation of THRs to patients may be cemented, uncemented, or hybrid (e.g., the stem is cemented and the cup is uncemented) [7, 9, 13]. Cemented implants are placed into a bed of polymethyl methacrylate (PMMA) bone cement which ensures the components into the prepared acetabulum and femoral canal. Uncemented implants have either a porous coating into which bone can grow or a roughened surface, produced by blasting the surface of the

implant with microscopic particles, to increase surface area for bone to grow onto [7]. Long-term outcomes for cemented and uncemented techniques demonstrate no clear difference [9]. There is an increasing tendency to use uncemented implants in younger patients because of the potential for a permanent bone-implant interface [7].

2.2. Modular design of femoral stem

A conventional monoblock femoral stem is made of a single piece, as shown in Figure I.1. Studies have demonstrated that a monoblock stem has a limited capacity to accurately restore the hip center of rotation and femoral offset in a significant proportion of patients [14]. Femoral offset is the distance from the center of rotation of the femoral head to a line dissecting the long axis of the femur. In case of THR, the offset is considered as the distance from the center of rotation of the femoral head to a line dissecting the long axis of the stem.

Since 1990s, modular neck adapters have been introduced, thus the bi-modular femoral stem prostheses are made of two modules: a femoral stem and a neck adapter [3], as shown in Figure Intro.1. The femoral head is fixed on the neck adapter. The introduction of modular neck adapters can improve the capacity to accurately restore the hip joints as the femoral stem and neck adapter can be made in different sizes with different neck angle versions to tailor the implant to an individual [14, 15]. Gofton *et al.* reported modular titanium alloy neck adapters which could provide various types of modular necks: neutral (135°), varus (127°), valgus (143°), anteverted / retroverted (8° / 15°), or a combination or varus / valgus + anteverted / retroverted, and two neck lengths (short or long), as shown in Figure I.2 [14].

Figure I.2. Types of modular femoral necks (Wright Medical Technology; Arlington TN). Neck types are neutral (135°), varus (127°), valgus (143°), anteverted / retroverted (8° / 15°), or a combination or varus / valgus + anteverted / retroverted [14].

2.3. Materials for femoral stem

At present, the most widely used materials for femoral stems are stainless steels, cobalt–chromium alloys, and titanium alloys [5, 16]. For the bi-modular femoral stem systems, same material couples (such as titanium alloy stem / titanium alloy neck adapter) and different material couples (such as titanium alloy stem / cobalt–chromium alloy neck adapter) are used [4].

2.3.1. Stainless steels

Stainless steels are used in hip implant applications owing to their availability, low cost, excellent fabrication properties, accepted biocompatibility and toughness [16]. 316L stainless steel was developed in the 1950s and has been widely used in implants [17]. The chemical compositions and mechanical properties of 316L stainless steel are shown in Table I.1 and Table I.2, respectively. 316L stainless steel contains high amounts of chromium and nickel [5, 18]. Chromium is important for formation of the surface oxide layer which improves the corrosion resistance. However, nickel is toxic and harmful to the surrounding organisms [5]. Furthermore, 316L stainless steel implants are often damaged due to pitting, crevices, corrosion fatigue, fretting corrosion, stress corrosion cracking and galvanic corrosion in the body [16, 17]. Today, 316L stainless steels are widely used in a variety of surgical instruments and short-term implant devices such as the fracture fixation [16]. Furthermore, high-nitrogen, nickel-free stainless steels have been developed as stem materials in permanent hip prostheses [16].

Table I.1. Chemical compositions of 316L steel, CoCrMo based alloys, and Ti–6Al–4V alloy [19, 20].

Elements in weight (%)	316L steel	CoCrMo	CoNiCrMo	Ti–6Al–4V
Fe	Bal	≤1.0	≤1.0	0.03
Cr	16.0–19.0	26.5–30.0	19.0–21.0	–
Ni	10.0–16.0	≤2.5	33.0–37.0	–
Mo	2.0–3.5	4.5–7.0	9.0–10.5	–
Co	–	Bal	Bal	–
C	≤0.03	≤0.35	≤0.025	0.08
Mn	≤2.0	≤1.0	≤0.15	–
Ti	–	–	≤1.0	Bal
Al	–	–	–	5.5–6.75
V	–	–	–	3.5–4.5
Other	≤0.9	≤1.0	≤0.2	≈0.7

Table I.2. Mechanical properties of 316L steel, CoCrMo based alloys, and Ti–6Al–4V alloy [5, 21, 22].

Alloy	Processing	Young's modulus (GPa)	Yield strength (MPa)	Ultimate strength (MPa)	Fatigue strength (MPa)
316L steel	Annealing	200	314[21]	588	200–350[22]
CoCrMo	Hot forging	210	1000	1500	750
CoNiCrMo	Hot forging	230	980	1210	500
	Cold deformation	230	1500	1800	740
Ti–6Al–4V	Cast	117	850	1137	360
	Annealing	–	680	780	400
	Hot forging	110	900	1000	600

2.3.2. Cobalt–chromium alloys

Cobalt–chromium based alloys are in general superior to stainless steels in terms of mechanical properties and corrosion resistance [5, 16]. The two predominant cobalt–chromium alloys used for orthopedic implants are CoCrMo and CoNiCrMo [5, 23]. Their chemical compositions and mechanical properties are shown in Table I.1 and Table I.2, respectively. CoCrMo and CoNiCrMo alloys contain high amounts of cobalt, chromium, molybdenum, and nickel [24]. Their superior mechanical properties over stainless steels are due to the crystallographic nature of the base element cobalt [5]. Their superior corrosion resistance over stainless steels is related to their chemical compositions. Chromium, molybdenum and nickel are responsible for improvement in corrosion resistance [16]. One of the disadvantages of CoCrMo based alloys is their toxicity to human bodies. Metal ion toxicity to human bodies has been studied [25], classified in decreasing order of toxicity as follows: cobalt > vanadium > nickel > chromium > titanium > iron. Cobalt toxicity has been reported to contribute to the pathology of systemic and neurological symptoms in some patients with metal-on-metal hip prostheses after 4–5 years of implantation [26]. Another disadvantage of CoCrMo based alloys is their high price, which has limited their percentage of the medical market, compared with stainless steels [16]. Although imperfect, approximately 20% of THR is made from CoCrMo based alloy [5].

2.3.3. Titanium alloys

Titanium alloys have begun to be widely used for implants due to their excellent mechanical properties approaching the properties of human bones (high strength, low density, relative low elastic modulus) and high specific strength, corrosion resistance and biocompatibility [27–30].

Pure titanium undergoes an allotropic transformation at approximately 885°C, changing from a low temperature hexagonal close packed (HCP) crystal structure (α phase) to a high temperature face-centered cubic (FCC) crystal structure (β phase). Based on their microstructure after processing, titanium alloys are categorized into four classes: α alloys, near α alloys, α–β alloys, and β alloys [5, 16]. Nowadays, the most commonly used titanium-based biomaterial for hip implants is the α–β alloy Ti–6Al–4V, accounting for approximately 45% of total titanium production [5]. The microstructure of a forged Ti–6Al–4V alloy is shown in Figure I.3. The chemical compositions and mechanical properties are shown in Table I.1 and Table I.2, respectively.

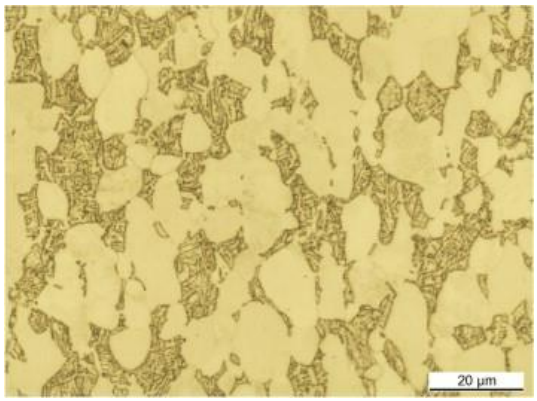

Figure I.3. Microstructure of a forged Ti–6Al–4V alloy depicting α (lighter areas) and α + β (darker lamellar areas) phases [31] (optical microscopy after chemical etching).

The strength of Ti–6Al–4V alloy is higher than 316L stainless steel, but slightly lower than the cobalt–chromium alloys. The density of titanium is about 60% of the density of iron and half of the density of cobalt. Therefore, Ti–6Al–4V alloy has excellent specific strength (strength / density), which is superior to those of the stainless steels and the cobalt–chromium alloys [16].

The Young's modulus of Ti–6Al–4V alloy is around half of the stainless steels and the cobalt–chromium alloys. The human bones have relatively low elastic modulus (range from few GPa to 20 GPa). Thus, the Ti–6Al–4V alloy is superior in elastic modulus to the stainless steels and the cobalt–chromium alloys [16].

The titanium alloys are superior in corrosion resistance to the stainless steels and cobalt–chromium alloys, because the matrix element of titanium has an excellent corrosion resistance by itself. The purpose of alloying is to enhance the mechanical properties for titanium alloys. For stainless steels and cobalt–chromium alloys, the main purpose of alloying is to improve their corrosion resistance [16].

Compared to stainless steels and cobalt alloys, titanium alloys are superior in terms of biocompatibility [32]. Titanium is not found in human body, and does not play any known biological role, and is non-toxic even in large doses [16]. When the quantity of titanium is too high, most titanium is found to be excreted without being digested or absorbed [16]. Vanadium can have both negative and positive cellular responses, with toxicity mainly from its compounds such as oxides [16, 33]. Aluminum is a naturally element in human body. It has toxicity only in very high doses. The increased amount of dietary aluminum may contribute to the reduced skeletal mineralization observed in infants and to neurological problems [34]. Fortunately, the contents of vanadium and aluminum are low in the Ti–6Al–4V alloy. Ti–6Al–4V has no significant mutagenicity to human cells, indicating that titanium alloys are relatively safe for humans, compared to other implant alloys.

The biggest disadvantage of Ti–6Al–4V alloy is its poor tribological properties, compared to cobalt alloys. The wear resistance of titanium alloys could be improved by the incorporation

of hard metal elements (e.g. W and Nb) and by surface modification (e.g. ion implantation) [16].

2.4. Tribological response of total hip implants

2.4.1. Load conditions at femoral stem / neck adapter contact interface

Forces and moments are transferred from the upper body to the leg across the hip joint. Bergmann *et al.* measured the hip contact forces in 4 patients during different activities and on activity records from 31 patients. They found that walking caused the average peak forces of 1 800 N and the high peak forces of 3 900 N; going up stairs caused the average peak forces of 1 900 N and the high peak forces of 4 200 N; and stumbling caused the high peak forces of 11 000 N [35].

In bi-modular stem systems, forces are transferred across the femoral stem / neck adapter interface [4]. The forces are complex at the femoral stem / neck adapter interface, and the study on the normal forces (and consequently contact pressures) and tangential forces on the femoral stem / neck adapter contact surfaces is insufficient at present. Baxmann *et al.* [36] conducted a non-linear finite element analysis according to ISO 7206-6 to determine the contact loads at the interface. Afterwards, they applied the maximum contact pressures (according to Hertz contact theory) with the values in the range of 398–857 MPa on the contact surfaces for the following-up experimental investigation.

Relative movements occur between the neck adapter and femoral stem components [4]. The observed displacement is caused by elastic deformation of contact surfaces and the micromotions between the femoral stem and neck adapter during walking [3, 4]. According to finite element analysis and experimental studies, the relative movements are influenced by the applied load, the femoral stem / neck adapter material coupling, the clean or contaminated conditions, etc. [3, 37]. Titanium alloy neck adapters show significantly larger displacements than cobalt–chromium alloy neck adapters [3, 37]. Contaminated interfaces also exhibit significantly larger displacements than cleaned interfaces [3, 37]. Over all simulation and experimental studies, the relative movements range between 3 μm and 41 μm [4].

With the contact pressures (398–857 MPa) and the small displacements (3–41 μm), the femoral stem / neck adapter interface is under the fretting situations [4, 36]. Furthermore, synovial fluid is present in the hip joint. Therefore, there is a possibility that the body fluid enters the interface. In this case, the fretting can be accompanied by corrosive effects (fretting corrosion) [38]. Consequently, the femoral stem / neck adapter contact surfaces are mainly suffering from fretting, friction, wear, corrosion, and fractures [4].

2.4.2. Fretting

The ASM Handbook on Fatigue and Fracture defines fretting as: "A special wear process that occurs at the contact area between two materials under load and subject to minute relative motion by vibration or some other force" [39]. Fretting is mainly controlled by the material properties such as the elastic modulus, surface properties such as the roughness, and the load conditions such as the normal contact force (or contact pressure) and displacement [40, 41].

During a fretting test, it is important to record the tangential force (Q) and the instantaneous displacement (δ) for every cycle, which enable us to plot the Q–δ loop, as shown in Figure I.4, and the fretting log (3 D representation of Q–δ–number of cycles), as shown in Figure I.5 [41, 42].

- **Sliding conditions**

Under relatively small displacement and high normal force conditions (Figure I.4a), the sliding condition is partial slip. The ball-on-flat contact area is composed of a stick centered and circular zone surrounded by a sliding annulus. The Q–δ loop is then elliptic. The higher the relative displacement amplitude or the lower the normal force, the smaller the inner stick zone. Under relatively high displacement amplitude and low normal force conditions (Figure I.4b), the sliding condition is gross slip. Sliding occurs all over the contact area. The Q–δ loop is then trapezoidal [42].

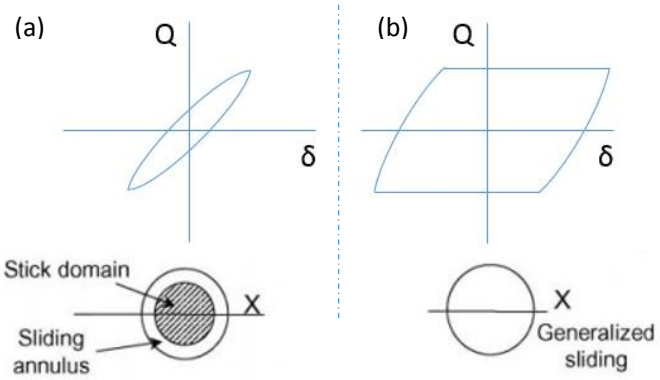

Figure I.4. Sliding conditions for a ball-on-flat contact:
(a) partial slip condition; (b) gross slip condition [42].

- **Fretting regimes**

Under different normal force and displacement amplitude conditions, three fretting regimes could be developed: the partial slip regime (PSR), the gross slip regime (GSR), and the mixed slip regime (MSR), as shown in Figure I.5. The PSR is defined if the partial slip condition prevails during the entire test. The GSR is defined in cases where the gross slip condition remains during the entire test. The sliding condition can evolve from one to another sliding condition: this is the MSR. In most situations, the MSR corresponds to an initial gross slip

condition followed by a stabilized partial slip situation, due to evolution of the contact interface [42].

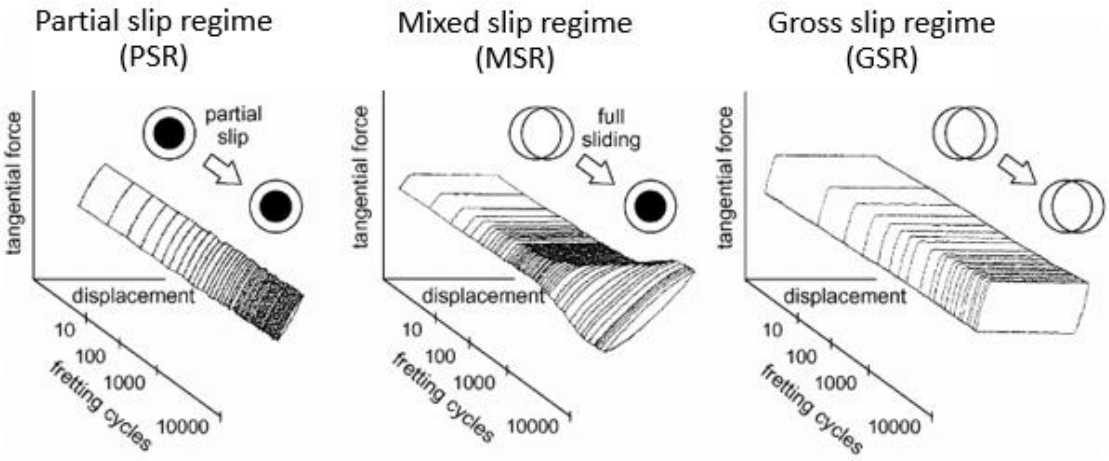

Figure I.5. Fretting regimes: PSR, MSR, and GSR [42].

- **Fretting maps**

The concept of fretting map was initially proposed by Vingsbo *et al.* in 1988 [43]. In 1992, Zhou and Vincent [40] proposed two kinds of fretting maps: running condition fretting map (RCFM) and material response fretting map (MRFM), as shown in Figure I.6. The RCFM includes the PSR, MSR and GSR depending upon the fretting log and shows the boundary between these regimes in (normal force / displacement amplitude) axes. With the increase in displacement amplitude or the decrease in normal force, the fretting regime changes from the PSR to MSR and then to GSR. Through post-test examinations, the MRFM is divided into three domains: slight degradation, cracking and wear domains (Figure I.6). Concerning correspondence to the RCFM, slight degradation domain is mainly located in the PSR with very low displacement, while wear with severe particle detachment occurs in the GSR. Cracking lies within the PSR and the MSR [40, 44].

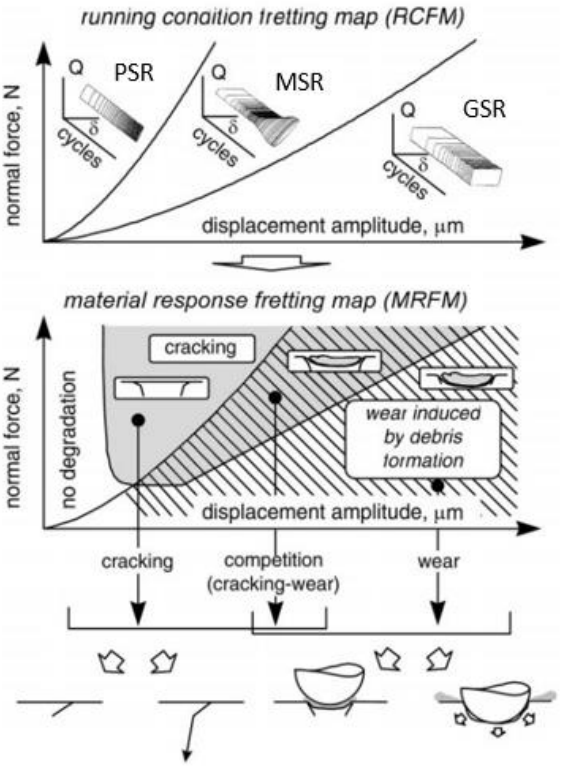

Figure I.6. Fretting maps: RCFM and MRFM [44].

2.4.3. Friction of metallic materials for implants

For femoral stems and neck adapters, they are normally made of metals (stainless steels, CoCr alloys, and Ti–6Al–4V alloys). For femoral heads, they are generally made of metals or ceramic. According to *in vitro* experiments, the friction coefficients of 316L, CoCr alloys, and Ti–6Al–4V alloys are relatively high (generally above 0.5) when they are sliding against another metal or against a ceramic.

Krishna *et al.* conducted sliding tests between an alumina ball and a 316L disc at room temperature and ambient conditions and the friction coefficients were in the range of 0.6–0.9 [45, 46]. Duisabeau *et al.* reported friction coefficients between 0.7 and 0.8 for a 316L cylinder sliding against a Ti–6Al–4V flat in air [47].

Chiba *et al.* conducted tests with a CoCr alloy pin sliding on a CoCr alloy disc and the friction coefficients were in the range of 0.5–0.7 [48]. Celik *et al.* reported the friction coefficient between 0.6 and 0.7 for a WC-Co pin sliding against a CoCr alloy disc at room temperature (around 18°C) and a relative humidity of about 50% [49].

Fridrici *et al.* reported high friction coefficients between 0.8–1.1 for a Ti–6Al–4V cylinder sliding against a Ti–6Al–4V flat under the GSR conditions [50, 51]. Itoh *et al.* studied the friction response of a steel ball sliding against a Ti–6Al–4V flat immersed in lubricant oil. The friction coefficient was relatively lower in the range of 0.5–0.6 [52].

2.4.4. Wear of metallic materials for implants

Stainless steel generally presents poor tribological properties and consequently high wear rates due to the low hardness [53, 54] and weak passivation layer [5]. Nickel-free steels have higher wear resistance compared to 316L [55]. Thomann *et al.* compared the wear resistance of the 316L steel (with the hardness of 155 ± 3 HV_{30}) and of the nickel–free steel (with the hardness of 367 ± 4 HV_{30}) though pin-on-disk sliding wear tests [55]. The wear volumes of nickel-free steel were approximately 70%–80% of the wear volumes of 316L.

Cobalt–chromium based alloys have high wear and scratch resistance due to their higher hardness (300–400 HV_{10}) among any biomedical alloys. Compared to 316L stainless steel, CoCrMo alloy has a 10 times lower wear rate [5]. The microstructure and the manufacturing process influence the wear resistance of cobalt–chromium based alloys [56]. The wrought components exhibit better wear resistance than cast components and lower carbon cobalt–chromium alloys have lower wear rates [5, 57].

Titanium alloys generally have relatively low wear resistance primarily due to the instability of their surface layer, low resistance to plastic shear, high adhesiveness and low work hardening ability [5]. Therefore, they are generally not used for sliding conditions against each other. Wear resistance for titanium alloys can be enhanced by using modern manufacturing technologies (such as powder metallurgy) and surface modifications. The surface thermal oxidation treatment improves the wear resistance of Ti–6Al–4V in corrosive environments [58, 59].

2.4.5. Corrosion of metallic materials for implants

The body fluid is present in the hip joints [60–62]. The local solution chemistry could accelerate the corrosion process of the metal-on-metal contacts [63]. Stainless steels containing at least 11 wt.% of chromium have generally good corrosion resistance, which even improves with the increase in the chromium content due to the formation of a protective chromic oxide (Cr_2O_3) layer [5, 16]. The corrosion resistance of CoCr-based alloys is far greater than the stainless steels owing to their high chromium content and the formation of the protective oxide layer [16]. The titanium alloys are superior in corrosion resistance to the stainless steels and CoCr alloys. Their excellent corrosion resistance is provided primarily by the protective TiO_2 surface layer [5].

Once the corrosion process is coupled with fretting at the contact surfaces, known as the fretting-corrosion, it produces very large scale destructive damage mode at the interface. The mechanical processes lead to the removal of the protective oxide layer while the electrochemical processes cause the repassivation of the oxide layer [61].

2.4.6. Fracture failure of modular hip implant components

Implant fracture at the neck adapter / femoral stem contact has been increasingly reported [64]. Grupp *et al.* investigated 5 000 titanium neck adapters which were implanted between August 2004 and November 2006 [3]. Until the end of 2008, 1.4% (n=68) of the implanted neck adapters failed with an average time of 2.0 years (0.7 to 4.0 years) postoperatively. Figure I.7a shows a typical X-ray of a failed titanium neck adapter. After market launch in the year 2004, an increasing number of neck fractures of the Metha Short Hip System (Aesculap AG, Tuttlingen, Germany [3, 65]) occurred. Neck fractures were almost only observed for the titanium neck adapter and titanium stem combination. In 2006, Metha Short Hip System was taken off the market and re-introduced with cobalt–chromium neck adapters in 2007. However, the H-Max M design (Limacorporate, Villanova di san Daniele (UD), Italy [66]) just has sporadic neck failures and is still using the titanium neck adapter and titanium stem combination [4]. It is still unclear why the titanium neck adapters tends to fail in one system while functions well in another system. Wodecki *et al.* reported a fracture of the femoral stem (as shown in Figure I.7b and Figure I.7c) [67]. The fracture of the femoral stem has not yet been often described in the literature.

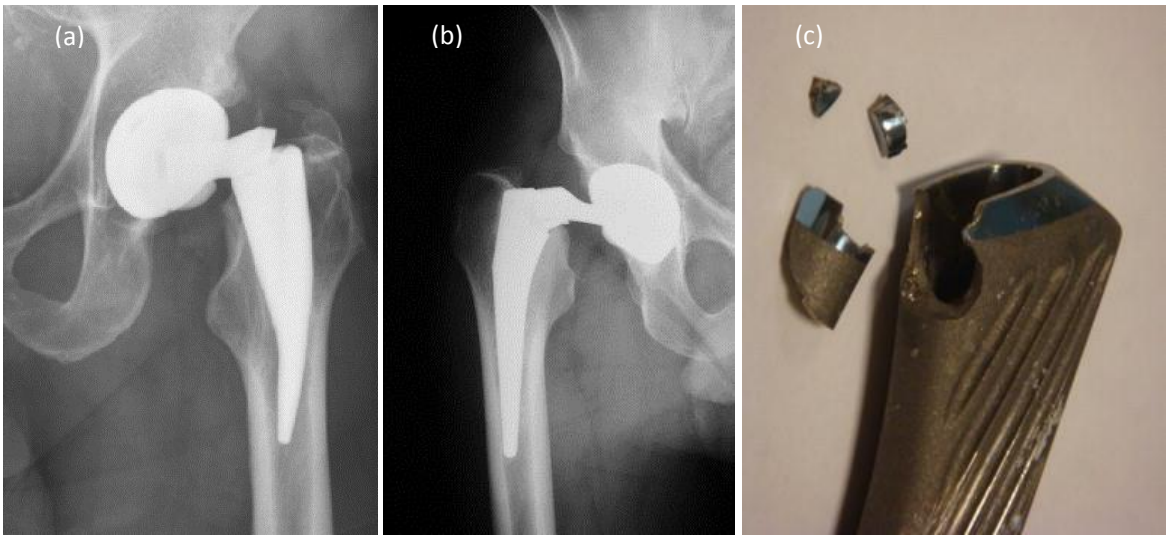

Figure I.7. (a) X-ray of a failed neck adapter [3], (b) x-ray and (c) photo of a failed stem [67].

It seems that fractures often occur slightly below the proximal end of the stem in a mechanically stressed region with high bending loads [4]. Except sudden high forces during patient's activities, the micromotions on the neck adapter / femoral stem interface might lead to fretting-induced fatigue and might be responsible for initiating the failure mechanism [4].

It can be concluded from Section 2 that, stainless steels, CoCr alloys, Ti–6Al–4V alloys are widely used materials for the neck adapter and femoral stem components. The neck adapter / femoral stem is under fretting condition during walking. However, the metals (stainless steels, CoCr alloys, Ti–6Al–4V alloys) present poor tribological properties, including high friction coefficients (generally above 0.5) and poor wear resistance. Furthermore, the fretting-

induced fatigue on the neck adapter and femoral stem surfaces might lead to fracture failures. In order to improve the durability of neck adapter and femoral stem components, their tribological properties should be improved.

Coatings have been widely used to protect metallic substrates in many applications [68–72]. Various types of coatings have been produced. And particular coatings might be suitable to the neck adapter / femoral stem contact to reduce the friction and wear. The coating types and deposition techniques will be discussed in the following sections.

3. Coatings for tribological applications

Coatings are widely used to control friction and wear in many kinds of sliding contacts [68–72]. In the last decades, many new deposition techniques were developed and an increasing number of coatings are available [73].

3.1. Type of coatings

For convenience, coatings could be divided into two broad categories according to their hardness: soft coatings (coating hardness less than 10 GPa) and hard coatings (coating hardness higher than 10 GPa) [74, 75], as shown in Figure I.8.

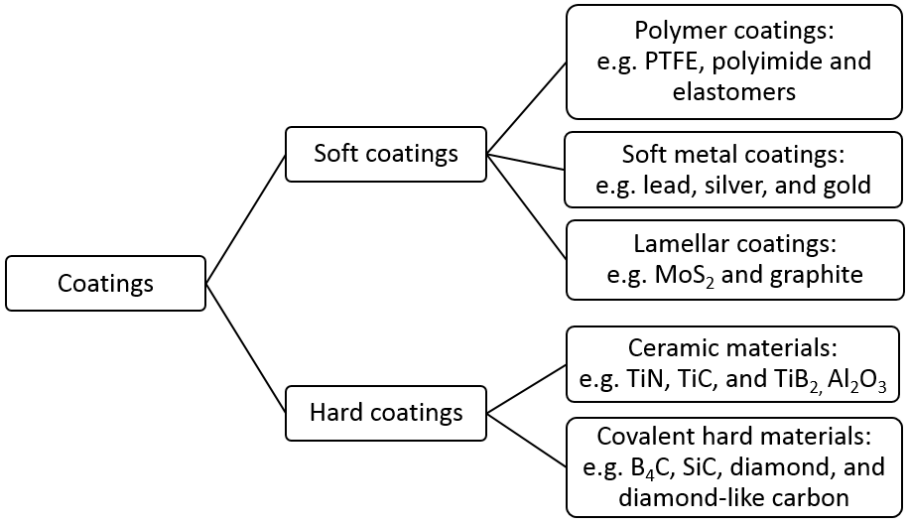

Figure I.8. Categories of coatings [75].

3.1.1. Soft coatings

The advantage of using a soft coating to a hard substrate is the reduced friction [72]. The reduction of friction can be explained according to the macromechanical friction mechanism proposed by Holmberg [72]. When a ball is sliding on a flat, the frictional force is ideally the product of the shear strength and the contact area. A harder flat can result in a decreased contact area but an increased shear strength. A softer flat can cause a decreased shear strength but an increased contact area. The combination of a soft coating and a hard substrate could reduce both the shear strength and the contact area, thus the friction force. Soft coatings include polymer coatings (such as, polytetrafluorethylene (PTFE), polyimides,

elastomers) [75, 76], soft metal coatings (such as, lead, silver, gold) [77, 78], lamellar coatings (such as, molybdenum disulfide (MoS_2), graphite) [79, 80], etc.

3.1.2. Hard coatings

A hard coating on a soft substrate can reduce the wear of the substrate [72, 83]. Low friction can be achieved if a tribofilm with low shear strength is formed on the top of the coating, or/and on the countersurface. Thus, the low shear strength takes place within the tribofilm and the load is supported by the hard coating. Hard coatings include ceramic materials (such as, TiN [75, 85–88], Al_2O_3 [75, 89–91]), and covalent hard materials [92–95] (such as, B_4C, SiC, diamond [94–96], diamond-like carbon), etc. The properties of widely used hard materials for coatings are shown in Table I.3.

Table I.3. Properties of some hard materials [75, 84].

Material	Formula	Density (g/cm^3)	Melting point (°C)	Hardness (HV)	Young's modulus (GPa)	Thermal expansion coefficient (α) ($10^{-6}K^{-1}$)
Titanium nitride	TiN	5.40	2950	2100	590	9.4
Titanium carbide	TiC	4.93	3067	2800	470	8.3
Titanium diboride	TiB_2	4.50	3225	3000	560	7.8
Corundum	Al_2O_3	3.98	2047	2100	400	8.4
Boron carbide	B_4C	2.52	2450	4000	441	4.5
Silicon carbide	SiC	3.22	2760	2600	480	5.3
Diamond	C	3.52	3800	8000	910	1

TiN is one of the widely used hard coatings in tool industries [86]. It is able to form a coherent or semi-coherent interface with metallic substrates [75]. Furthermore, it presents high chemical inertness, high temperature stability, and abrasive wear resistance [86].

Al_2O_3 coatings have been applied in industries because of their high temperature stability, high melting point, good wear resistance, excellent corrosion resistance, and high insulation [89, 90].

Covalent hard materials (such as, B_4C, SiC, diamond) have been used in many applications because of their high hardness, high elastic modulus and high chemical stability [92]. The main disadvantage of such coatings is the poor cohesion to the metallic substrates, which may lead to early delamination of coatings [93]. Diamond-like carbon (DLC) coatings can overcome this problem in some extent because they have relatively lower hardness and lower elastic modulus, thus greater cohesion, depending on the deposition process, composition and structures of coatings [97]. DLC coatings also exhibit excellent tribological properties such as low friction and wear resistance. Furthermore, DLC coating has been used in orthopedic applications due to its biocompatibility [6]. The structure, deposition mechanism, mechanical and tribological properties, and biocompatibility of DLC coatings will be discussed in detail in Section 4.

3.2. Coating deposition methods

The progress of coating deposition techniques promotes the improvement of existing coatings and causes new generations and new types of coatings. A given deposition method can produce various types of coatings, and a given coating can be produced through various deposition methods. The most common deposition methods for tribological coatings include bonding, ion beam deposition (IBD), physical vapor deposition (PVD), CVD, etc. [68].

3.2.1. Bonding

A bonding process has been widely used to produce solid lubricant coatings which possess low friction coefficients and mitigate wear, adhesion and scuffing of mechanical parts [98]. Solid lubricant particles, such as MoS_2, graphite and PTFE, are mixed into a resin system, which contains binder, solvent, and modifier, etc. [99]. After that, the liquid mixture is applied on the substrate surface through immersion, brushing, or spraying, etc. [68]. And then the coating should be dried and hardened at a suitable temperature for an appropriate time period [68]. Similar to most deposition techniques, the substrate surface should be pretreated before the deposition process to improve the bonding strength of coatings on the substrates, such as degreasing via ultrasonic cleaning and roughing via sand blasting [68]. The biggest advantages of bonded coatings are the cheap technical process and large thickness they can achieve [100].

3.2.2. IBD

The IBD technique has been used to grow thin films at low temperatures and to synthesize a variety of materials such as oxides, nitrides, and silicides at surfaces [101]. The principle process of IBD is shown in Figure I.9. It mainly consists of an ion source, the ion extraction system and the substrate [102]. In the ion source, source materials in the form of a gas, an evaporated solid, or a solution (liquid) are ionized. After that, ions are accelerated, focused or deflected using high voltages or magnetic fields. Then the selected ions can reach the substrate. Thus, IBD has the ability to select a single or a range of ion species for deposition, in order to avoid contamination.

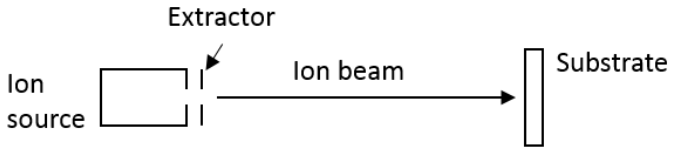

Figure I.9. Schematic illustration of IBD process [103].

3.2.3. PVD

PVD refers to the deposition processes in which material is vaporized from a solid or liquid source in the form of atoms or molecules and transported in the form of a vapor through a vacuum or low pressure gaseous (or plasma) environment to the substrate, where it

condenses [104, 105]. PVD processes can be used to deposit coatings of elements (such as DLC), alloys, and compounds (such as TiN and TiC). Typically, the thickness of PVD coatings is in the range of a few nanometers to several micrometers [104]. The main categories of PVD processing are vacuum deposition (sometimes called vacuum evaporation), sputter deposition, ion plating, etc. as shown in Figure I.10.

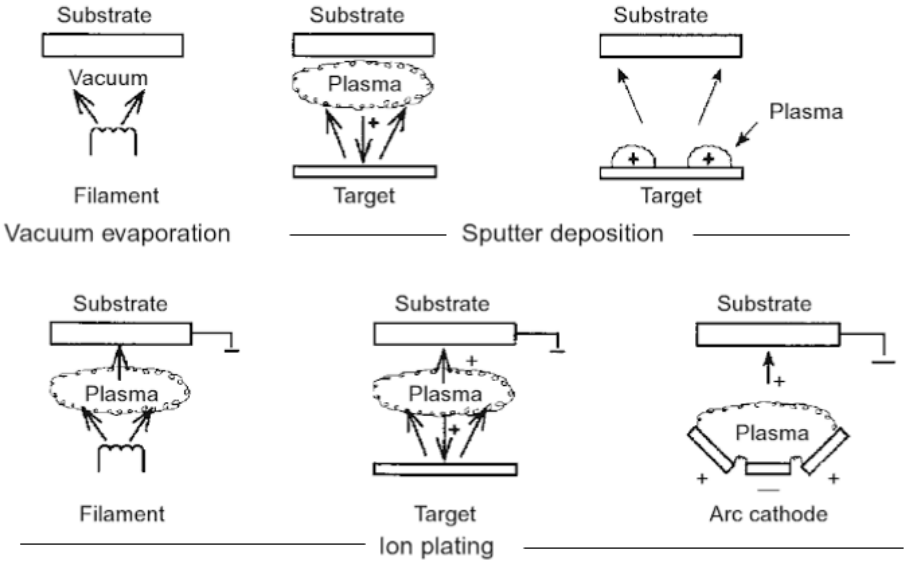

Figure I.10. PVD processing techniques [104].

- **Vacuum evaporation**

In the vacuum evaporation process, the coating materials are heated to vaporize using tungsten wire coils or high energy electron beam, then transported through a vacuum environment to the substrates surface where solid coatings condense. The trajectory of the vaporized material is “line-of-sight”.

- **Sputter deposition**

In the sputter deposition (sometimes called sputtering) process, particles are vaporized from a target surface through bombardment by atomic-sized energetic particles, which are usually gaseous ions, accelerated from plasma. The sputter deposition can be performed in vacuum using an ion gun or low pressure plasma (<5 mTorr), or in higher plasma pressure (5–30 mTorr).

- **Ion plating**

In the ion plating processes, the depositing material may be vaporized either by evaporation, sputtering, or decomposition of a chemical vapor precursor. The characteristic process of ion plating is that the depositing coating is bombarded concurrently or periodically by atomic-sized energetic particles to modify and control the properties of the coating. The energetic particles used for bombarding the coating are usually ions of an inert or reactive gas, or, in some cases, ions of the condensing coating materials. The ion plating may be performed in a plasma environment where the bombarding ions are extracted from the plasma or

performed in a vacuum environment where the bombarding ions are formed in a separate ion gun. The latter ion plating process is often called ion beam-assisted deposition (IBAD).

PVD process has a number of advantages. The main advantage is the low temperature of the substrate during deposition. The limit of DLC process is its low achievable thickness, because of the high internal stresses.

3.2.4. CVD

CVD refers to a family of processes that a solid material is deposited from a vapor by a chemical reaction occurring on or in the vicinity of a normally heated substrate surface [106–108]. It is a widely used method to produce coatings of metals, nonmetallic elements (such as silicon and DLC), compounds (such as carbides, nitrides, and oxides), as well as other materials [68]. There exists a multitude of CVD processes, as shown in Table I.4.

Table I.4. Summary of CVD process family [108, 109].

Type	Description
Atmospheric pressure CVD (APCVD)	Processes at atmospheric pressure
Low-pressure CVD (LPCVD)	Processes at subatmospheric pressures
Ultrahigh vacuum CVD (UHVCVD)	Processes at a very low pressure
Aerosol-assisted CVD (AACVD)	Precursors are transported to the substrate by means of a liquid or gas aerosol, which can be generated ultrasonically
Direct liquid injection CVD (DLICVD)	Precursors are in liquid form (liquid or solid dissolved in a convenient solvent). Liquid solutions are injected in a vaporization chamber towards injectors (typically car injectors). Then the precursor's vapors are transported to the substrate as in classical CVD process
Plasma-assisted CVD (PACVD) Plasma-enhanced CVD (PECVD)	Utilizes a plasma to enhance chemical reaction rates of the precursors, and allows deposition at lower temperatures
Atomic layer CVD (ALCVD or ALD)	Deposits successive layers of different substances to produce layered, crystalline films
Hot wire CVD (HWCVD)	Also known as catalytic CVD (Cat-CVD) or hot filament CVD (HFCVD). Uses a hot filament to chemically decompose the source gases
Metal-organic chemical vapor deposition (MOCVD)	Based on metal-organic precursors
Hybrid physical–chemical vapor deposition (HPCVD)	Vapor deposition processes that involve both chemical decomposition of precursor gas and vaporization of a solid source
Rapid thermal CVD (RTCVD)	Uses heating lamps or other methods to rapidly heat the wafer substrate
Vapor-phase epitaxy (VPE)	Gases are decomposed and then meet and react on the substrate, generating an epitaxial film on the surface [109]

The principle in every CVD process is as shown in Figure I.11. Gaseous reactants are admitted into a reactor. Near or on a heated substrate surface, a chemical reaction occurs, generating a solid coating and gaseous byproducts. The CVD system generally includes three parts: gas dispensing system, reactor, and exhaust system [108].

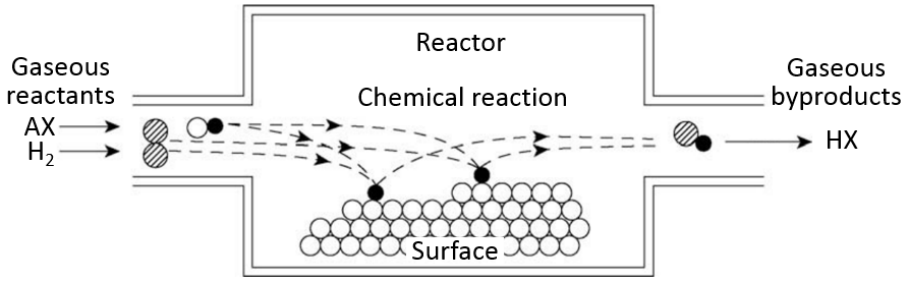

Figure I.11. The principle of CVD [108].

- **Gas dispending system**

In the gas dispensing system, reactants, which are gases at room temperature, are stored in gas bottles, and are flowed into the reactor under controlled pressure and flow rate. Reactants, which are liquid or solid at room temperature, are heated above the boiling or sublimation point using an evaporator or sublimator. The material is transferred to the vapor by evaporating or sublimation (solid gas) and then transported to the reactor by carrier gas.

- **Reactor**

There are two main reactor types: hot wall reactor and cold wall reactor. In a hot wall reactor, the reactor is surrounded by a furnace. The substrates and walls of the reactor all have the same temperature. The coating grows not only on the substrate but also on the wall. There is a risk that particles will break loose and fall down on the surface of the growing coating, thus introducing pinholes. In a cold wall reactor, the substrates are heated; however the walls of reactor are unheated and, as a result, no deposition occurs on the walls. Various techniques exist for heating the substrates. Conductive substrates can be heated resistively or by radiofrequency induction. Non-conductive substrates are normally heated by optical techniques (tungsten filament lamps, lasers), thermal radiation techniques, or by susceptors and radiofrequency induction.

- **Exhaust system**

The exhaust system contains a vacuum pump, total pressure control, scrubbers, and a recycling system (if needed). Processes working at atmospheric pressure do not require vacuum pumps and total pressure control.

CVD process has a number of advantages. One of the primary advantages is that CVD coatings are generally quite conformal, which means that the CVD coatings can be applied on complex-shaped substrates [106]. In contrast, PVD techniques, such as sputtering or evaporation, require a line-of-sight between the substrate surface and the source. CVD also has disadvantages. One primary disadvantage is the high substrate temperature, which may

induce the distortion of the substrates. Fortunately, PECVD utilizes a plasma to enhance chemical reaction rates of the precursors, and allows deposition at lower temperatures [108].

4. DLC coatings

DLC is a metastable form of amorphous carbon with significant sp^3 bonding [97]. DLC coatings offer outstanding properties such as low friction coefficients, high hardness, wear resistance, chemical inertness, optical transparency in the infrared radiation spectral range and low electrical conductivities [110]. Thus, they have been widely used as protective coatings in areas like magnetic storage disks and read/write heads [111, 112], car and engine parts [113, 114], biomedical implants [115–118] and cutting and forming tools [119, 120].

4.1. Structure of DLC

A carbon atom has four valence electrons. They can exist in three hybridizations: sp^3, sp^2 and sp^1, as shown in Figure I.12 [97, 121, 122]. In the sp^3 configuration, all the four valence electrons enter tetrahedrally directed sp^3 orbitals. Each sp^3 orbital makes a strong σ bond to an adjacent atom. In the sp^2 configuration, three valence electrons enter trigonally directed sp^2 orbitals, which form σ bonds in a plane. The forth valence electron enters a π orbital with a normal direction to the σ bonding plane. This π orbital forms a weaker π bond with one or more neighboring atoms. In the sp^1 configuration, two of the four valence electrons enter σ orbitals, which form σ bonds in the directed of ±x-axis, and the other two valence electrons enter π orbitals in the y and z directions.

The strong σ bonding results in many extreme physical properties [97, 123]. Like diamond, it has a wide 5.5 eV band gap, the smallest thermal expansion coefficient and the highest hardness of any solid material on Earth. DLC consists of a significant fraction of sp^3 hybridized carbon [124]. The remaining is sp^2 and occasionally sp^1, generally containing various quantities of hydrogen [125]. DLC has some extreme properties similar to diamond, such as the hardness, elastic modulus and chemical inertness, due to its high fraction of σ bonds.

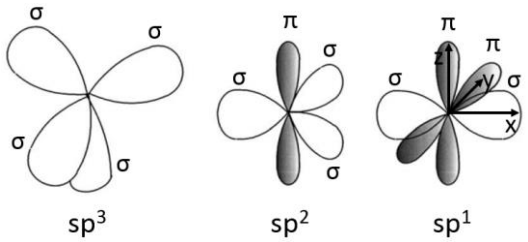

Figure I.12. The sp^3, sp^2, and sp^1 hybridized bonding [97].

Structural models of DLC have been produced since the 1980s [110, 126–129]. Representatively, Robertson and O'Reilly proposed a cluster model [6, 7]. According to the cluster model, DLC contains both sp^3 and sp^2. The sp^3 forms four σ bonds while the sp^2 forms three σ bonds and one weaker π bond. The π bonds are stabilized by forming parallel oriented pairs. After that, they are stabilized by forming planar 6-fold aromatic rings. Then, the rings

fuse together into graphitic clusters. Thus, the cluster model proposed that sp^2 ring clusters were embedded in a sp^3 bonded matrix, as shown in Figure I.13. The sp^3 matrix controls the mechanical properties while the sp^2 cluster size controls the optical gap. The problem is that the cluster model is valid for the case of low disorder [126], such as a plasma deposited DLC which contains similar concentrations of sp^3 and sp^2. However, the DLC is often produced with high disorder. In this case, the appropriate structural description is that the DLCs contain both ring and chain forms of sp^2 hybridized carbons [126].

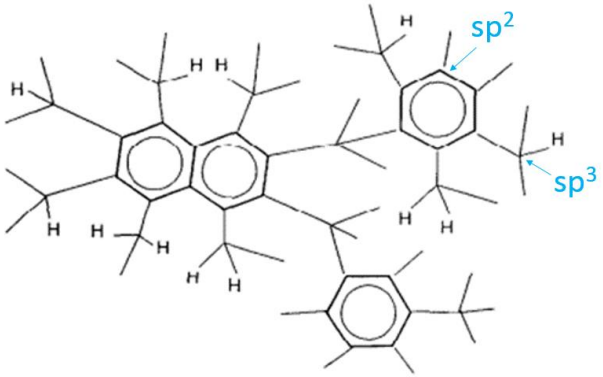

Figure I.13. Schematic diagram for cluster model of plasma deposited DLC [126].

4.2. Types of DLC coatings

The term DLC describes a broad range of amorphous carbon coatings, with different ratios of sp^2 and sp^3 bonded carbons and different levels of hydrogen [115]. Sometimes, metal or non-metal elements are doped into coatings to optimize their properties [110]. In order to distinguish different types of DLC coatings, names of branches are as follow [110]:

(1) a–C, hydrogen free amorphous carbon coatings;

(2) ta–C, hydrogen free tetrahedral amorphous carbon coatings with a high fraction of tetrahedral coordinated sp^3 bonded carbon atoms;

(3) a–C:Me, metal containing hydrogen free amorphous carbon coatings, where the metal often is a carbide forming metal like titanium or tungsten;

(4) a–C:H, hydrogenated amorphous carbon coatings;

(5) ta–C:H, hydrogenated tetrahedral amorphous carbon coatings;

(6) a–C:H:Me, metal containing hydrogenated amorphous carbon coatings;

(7) a–C:H:X, modified hydrogenated amorphous carbon coating, where X is related to a non-metallic element such as silicon, oxygen, nitrogen, fluorine, and boron.

The ternary phase diagram is a convenient method to describe the structure and composition of different DLC coatings, as shown in Figure I.14. It was firstly used by Jacob and Moller in 1993 [130]. After that, it has been widely used by later researchers [115, 131, 132]. This diagram has three phases: sp^3, sp^2 and hydrogen. The extreme top and left-bottom corner of the triangle represent 100% sp^3 like diamond and 100% sp^2 like graphite, respectively. There are graphitic carbons, such as soot, chars and glassy carbon, lying in the left-bottom corner

(graphitic C area). In the right-bottom corner, the carbons cannot exist as C–C networks, only as molecules (no films area). With higher content of carbon, hydrocarbon polymers form (HC polymers area). The a–C:H coatings have the hydrogen content of around 20–40 at.%. The ta–C:H coatings have the same level of hydrogen content (around 25–30 at.%) but higher sp^3 content (even above 70 %). The a–C(:H) coatings have low H content (less than 20 at.%) and high sp^2 content. The ta–C coatings have almost no hydrogen and high content of sp^3.

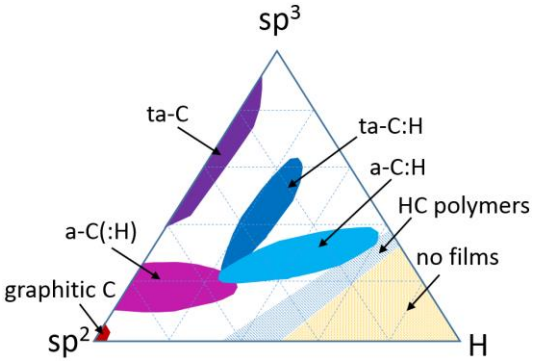

Figure I.14. Ternary phase diagram of DLCs [132].

4.3. Growth mechanism of DLC coatings

DLC coatings can be produced by various methods, such as IBD, sputtering, and PECVD [97, 110].

Several theoretical studies on growth mechanisms of DLC coatings were reported in the past 30 years [133–139]. Among these studies, the subplantation model was well developed. This model was proposed by Y. Lifshitz *et al.* in 1989 and 1990 when they used Auger analysis of the depth profile of the C ions incident on the Ni substrate and found that the growth was subsurface [133, 134]. After that, it was improved by J. Robertson and other researchers [135, 136].

The growth of DLC films derives from the incidence of carbonous particles (such as C^+ ions, C atoms, and C-based molecules) [97]. For the IBD, the carbon source is a graphite target. The incident particles are mainly composed of C^+ ions. For the plasma deposition, the carbon sources are gases like CH_4, C_2H_2 and C_6H_6. They are dissociated, ionized and dehydrogenated before incidence. The incident particles consist of atomic ions, molecular ions, unionized atoms and molecules, and significant amounts of atomic hydrogen.

The key aims of deposition process are to increase the film thickness and to promote the sp^3 bonding in the film. To clarify the subplantation model, the ion beam deposited ta–C will be firstly explained in details. After that, the plasma deposited a–C:H will be discussed.

4.3.1. Ion beam deposited ta–C

J. Robertson proposed that the subplantation caused an increase in density, i.e., local stress [135, 136]. He assumed that the atomic hybridization can be changed to sp^2 if the local density is low and to sp^3 if the local density is high [97].

From the atomic scale, in the energy range of 10–1 000 eV, the carbon ions have the sizes of a range of a few nanometers, and the atomic radius decreases at a higher ion energy. The target surface can be regarded as a wall with interstices. For a C^+ ion with low energy (large size), it cannot pass though the interstice, so it just sticks to the surface and remains in its lowest energy state of sp^2, resulting in the increase in the coating thickness. For a C^+ ion with high energy, it has a probability to penetrate the surface and enter a subsurface interstitial site, leading to an increase in the local density and the local stress, thus changing the sp^2 to sp^3 [135, 136].

Penetration can be realized in two ways, directly or indirectly by knock-on, as shown in Figure I.15. About the direct penetration, as mentioned in the above paragraph, the C^+ ions pass though the surface, generating the sp^3 hybridized carbons from the incident ions or from both the incident ions and the surrounding sp^2 carbon atoms if the local density is high enough. About the indirect penetration (knock-on), the incident ion cannot pass through the surface. It impacts the surface and displaces the surface atom into the subsurface, thus leading to a high local density and transfer sp^2 to sp^3. The incident atom bounces off the surface, resulting in a vacancy, or sticks to the surface and occupies the vacancy. For the case of ion assisted deposition, the assisted ion, Ar^+, has a larger size, so that it cannot pass though the surface, that only knock-on penetration occurs [97].

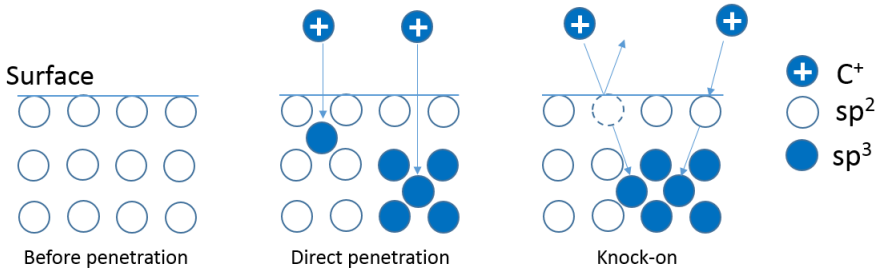

Figure I.15. Schematic of direct penetration and indirect penetration by knock-on [136].

At higher ion energy, ions can penetrate deeper into the subsurface, where the penetrating ions lead to high local density. After that, some of the ions relax to the surface and the excess density decreases to zero. The relaxation process causes a decrease in the sp^3 bonding [140]. Figure I.16 shows the numerically calculated result [97] and experimental data [140] of the relationship between the sp^3 fraction and the ion energy. The sp^3 fraction increases firstly and then decreases with the ion energy. The increasing sp^3 is due to the higher penetration probability of the incident ion with high energy. The decrease in the sp^3 fraction is caused by the relaxation [97].

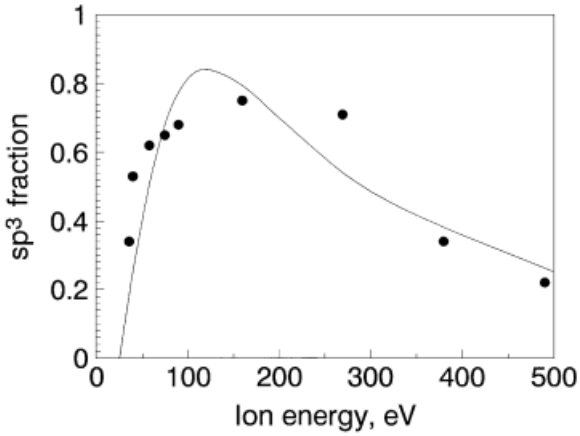

Figure I.16. Relationship between sp^3 fraction of DLC coating and ion energy in term of numerically calculated and experimental data [97].

The growth mechanism of the ion beam deposited ta–C film is established according to the subplantation model, as shown in Figure I.17. The ion beam incidents the original surface. The ions with low energy stick to the surface, leading to outward growth of sp^2 layer. The ions with higher energy penetrate directly or indirectly into the subsurface, increasing the local density and promoting the sp^3 bonding. Some penetrating ions relax to the surface leading to a slight decrease of sp^3 bonding.

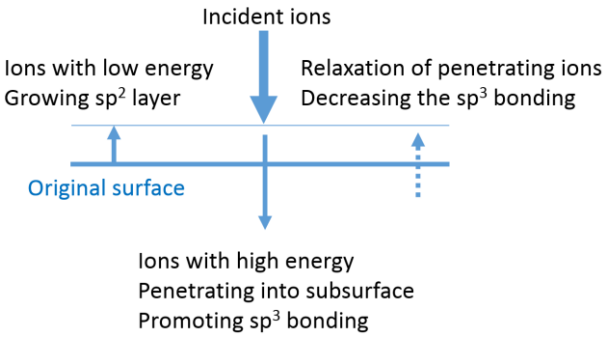

Figure I.17. Schematic diagram of subplantation model of deposition mechanism of ion beam deposited ta–C film.

4.3.2. Plasma deposited a–C:H

The incident plasma includes atomic carbon ions, molecular hydrocarbon ions, hydrocarbon neutrals and hydrogen atoms and ions [97]. An energetic modular ion will break up into atomic ions. The action of incident atomic ions is still via subplantation as discussed in Section 4.3.1. Besides, the neutral hydrocarbons cannot penetrate the surface. They just stay at the surface, contributing to the coating growth. Hydrogen atoms and ions can penetrate about 2 nm into the subsurface because of the small size [141]. The incident hydrocarbon particles and the atomic hydrogen improve the hydrogen quantity in the a–C:H.

4.4. Mechanical properties of DLC coating

DLC coatings are characterized by high hardness and high elastic modulus, but also high internal stresses [131]. These properties are directly correlated to their composition and structure, i.e. the sp^3/sp^2 ratio and the hydrogen content, which depend on the deposition process [118].

4.4.1. Hardness and elasticity

The sp^3/sp^2 ratio in DLC coatings is influenced by the incident ion energy during deposition [97]. The variations of sp^3 and sp^2 fractions with ion energy are shown in Figure I.16 and Figure I.18, respectively. The maximum sp^3 fraction occurs at the ion energy in the range of around 100 eV. More sp^2 hybridized carbons are generated at low and high ion energies.

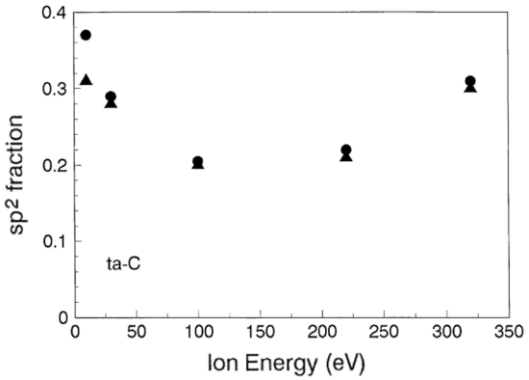

Figure I.18. Relationship between sp^2 fraction of DLC coating and incident ion energy [142].

The sp^3/sp^2 ratio in DLC coatings is also strongly dependent on the deposition temperature [143]. Figure I.19 shows the variation of the sp^3 fraction as a function of the substrate temperature at the incident ion energy of 90 eV. It falls sharply at a transition temperature of around 150–200°C, suggesting that DLC coatings appear to undergo a transition from sp^3 bonded ta–C to sp^2 bonded a–C above the transition temperature. The decline of sp^3 is attributed to the relaxation, i.e. the subplanted atoms are diffused to the surface via activated thermal diffusion [143].

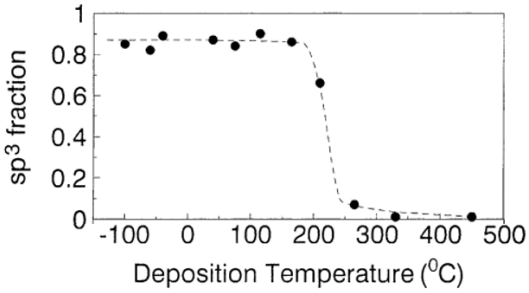

Figure I.19. Relationship between sp^3 fraction of DLC coating and deposition temperature [143].

The hardness and elasticity of DLC films have a positive relationship with the sp^3 fraction [144, 145], because a sp^3 carbon forms 4 strong σ bonds with neighboring atoms, while a sp^2

carbon forms 3 σ bonds and a weak π bond. A high sp^3 fraction means more σ bonds in the coating, leading to high hardness and high elasticity.

Therefore, the hardness and elasticity of the DLC coatings are strongly determined by incident ion energy and deposition temperature [146, 147], as shown in Figure I.20. The highest hardness and Young's modulus occur at the ion energy of around 100 eV. The hardness and Young's modulus decline sharply at a transition of substrate temperature, i.e. high hardness and high elasticity are generated when the substrate is below the transition temperature.

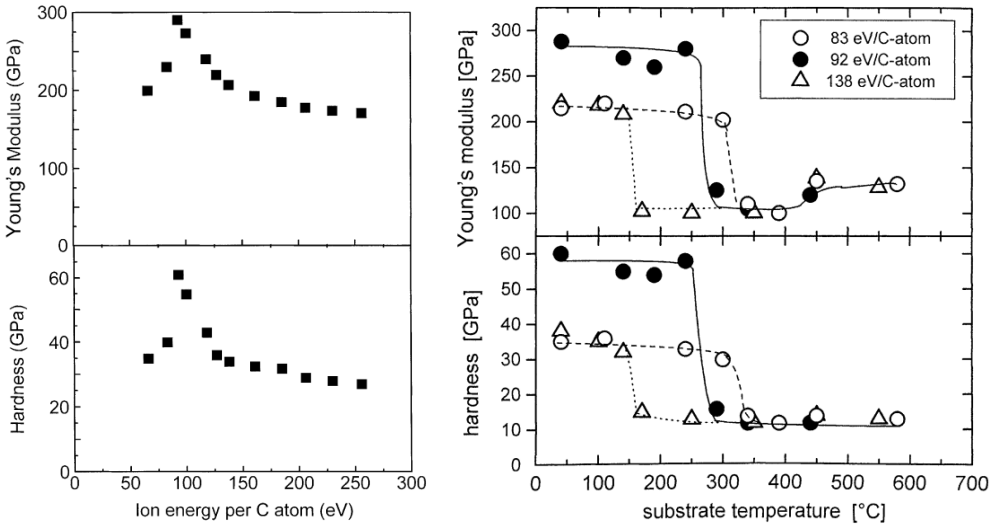

Figure I.20. Influence of ion energy [146] and substrate temperature [147] on hardness and Young's modulus of DLC coatings.

For hydrogenated DLC coatings, besides the sp^3/sp^2 ratio, the hydrogen content is another important parameter influencing their mechanical properties. During deposition, a hydrocarbon, such as CH_4, C_2H_2 or C_6H_6, is used as the precursor material. The source gas with shorter hydrocarbon chains produces higher hydrogen content [115]. Therefore, the hydrogen content of DLC coatings prepared from CH_4 is larger than that prepared from other precursors [97]. In addition, the hydrogen content is also influenced by the ion energy or bias voltage used in deposition [146, 148–150], as shown in Figure I.21. They have a negative influence on the hydrogen content.

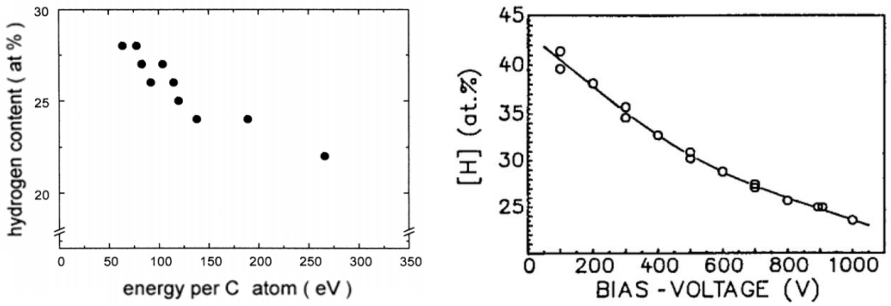

Figure I.21. Influence of ion energy [146] and bias voltage [148] on the hydrogen content in the DLC coatings.

The hydrogen, as a bond terminating atom in the DLC coating, has direct influence on the degree of cross-linking in the amorphous network. The hardness appears to be correlated with the degree of the three dimensional cross-linking of the film network [148]. In general, higher hardness are measured on DLC coatings with lower hydrogen content [97, 110, 115, 148].

4.4.2. Compressive stresses

The DLC coatings are also characterized by the high internal compressive stresses. The high stress limits the maximum deposition thickness [131, 151].

As mentioned in Section 4.3, during the ion subplantation, the high local stress (i.e. high local density) is produced in order to generate sp^3 carbons. Therefore, the compressive stress, in general, has a positive relationship with the sp^3 fraction in DLC coatings [140, 143, 146, 151].

Fortunately, the stress can be released by some methods, such as incorporation of metal or non-metal elements, building multilayer structures or annealing [131, 151]. The incorporation of elements and multilayer structures will be discussed in Section 5.6. In this section, the annealing method will be discussed.

According to Ferrari [151, 152], the stress is necessary to form sp^3 carbons during deposition, but after the sp^3 phase is formed, the stress is no longer needed for stabilization. So that the stress can be released without appreciable structural change. Annealing a ta–C coating up to 600–700°C allows a relaxation of the compressive stress almost to 0, as shown in Figure I.22.

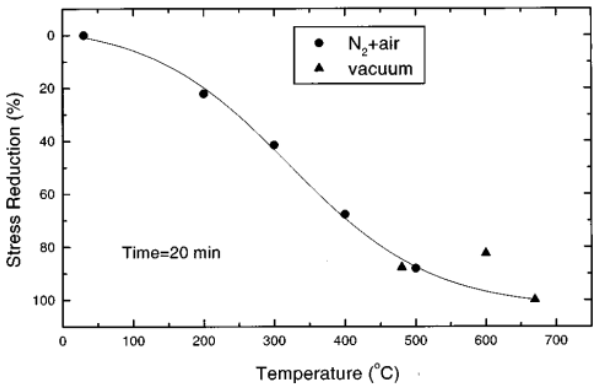

Figure I.22. Steady state stress reduction as a function of annealing temperature, for samples annealed both in flowing nitrogen and in vacuum [152].

This stress release is attributed to the rearrangement within the sp^2 phase [151]. The sp^2 bond (C=C) is shorter than the sp^3 bond (C–C). At the annealing temperature, the π orbitals are oriented perpendicularly to the substrate surface. Their σ bonds form a plane of compression and relieve a bi-axial compressive stress. Furthermore, a slight amount of sp^3 carbons convert to sp^2, which also attributes to the stress release. Fortunately, only 2% of sp^3 convert to sp^2 for stress release; so, the coating hardness shows no obvious change [152].

4.4.3. Summary of mechanical properties of DLC coatings

Table I.5 exhibits an overview of mechanical properties of diamond, ta–C, a–C:H and graphite according to [110, 123, 131, 145]. The ta–C coatings have high sp^3 fractions up to about 90% with very low hydrogen [131]. They have high hardness (in the range of 40–80 GPa) and high Young's modulus (even reaching 900 GPa) [145]. On the other hand, the internal compressive stress can reach a high value of 13 GPa [131]. The a–C:H coatings have lower sp^3 fractions (in the range of 20%–60%) with more hydrogen (in the range of 10%–50%). Their hardness is lower in the range of 10–45 GPa, and the Young's modulus is lower than 300 GPa. The internal compressive stress is in the range of 0.5–7 GPa.

Table I.5. Mechanical properties of diamond, ta–C, a–C:H and graphite [110, 131].

	Diamond	ta–C	a–C:H	Graphite
sp^3 content / %	100	50-90	20-60	0
Hydrogen content / at.%	0	~1	10-50	0
Hardness / GPa	100	40-80	10-45	<5
Young's modulus / GPa	-	~900	60-300	-
Internal compressive stress / GPa	-	~13	0.5-7	-

4.5. Cohesion between DLC coatings and substrate

The high compressive stress and the difference of mechanical properties between DLC coatings and the substrates result in poor cohesion on the interface [153]. Thus, DLC coatings are easily failed by delamination from the relatively soft substrates such as steels and titanium alloys [154]. To improve the cohesion between the coating and the substrate, various strategies are used.

One method is to clean the surface by argon ion bombardment before deposition [97].

Another method is to produce an ion beam mixed interface between coating and substrate, using a high ion energy for the first stage of deposition [153].

Besides, the adhesion can be improved by decreasing the compressive stress, such as annealing (as discussed in section 4.4.2 [152]), incorporation of elements and multilayer structures. The incorporation of elements and multilayer structures will be discussed in Section 5.6.

4.6. Biocompatibility of DLC coatings

4.6.1. *In vitro* and *in vivo* experiments

From *in vitro* and *in vivo* animal experiments which have been conducted so far, DLC coatings show good biocompatibility [6, 116, 155].

Early in 1991, Thomson *et al.* conducted *in vitro* tests to assess the biocompatibility of DLC [156]. Two types of mouse cells (mouse peritoneal macrophages and mouse fibroblasts)

were grown on the DLC coated tissue culture plates. The DLC, in the form of an undamaged coating, showed no toxic or inflammatory response on mouse cells.

In 2001, Matthew Allen *et al.* carried out both *in vitro* and *in vivo* tests [157]. For the *in vitro* tests, two osteoblast-like cell lines were cultured on uncoated and DLC coated tissue culture plates for periods of up to 72 h. There was no evidence that the presence of the DLC coating had any adverse effect on any of the parameters measured in this study (production of three osteoblast-specific marker proteins: alkaline phosphatase, osteocalcin, and type I collagen). For the *in vivo* tests, DLC coated cobalt–chromium cylinders were implanted in intramuscular locations in rats and in transcortical sites in sheep. Histologic analysis of specimens retrieved 90 days after surgery showed that the DLC coated specimens were well tolerated in both sites. These data indicate that DLC, in the form of coating, is biocompatible in *in vitro* and *in vivo* tests.

From the results of *in vitro* and *in vivo* animal experiments, DLC, in the form of coating, exhibits good biocompatibility. Furthermore, the biocompatibility of DLC in the form of particles, such as wear debris, is very important for their further application as implants. But it seems there are very limited studies conducted to investigate this so far.

4.6.2. Clinical application

For the studies on DLC coated implants in patients, Taeger *et al.* compared the performance of a DLC coated Ti–6Al–4V femoral head with a ceramic (Al_2O_3) head, both in contact with an ultrahigh molecular weight polyethylene (UHMWPE) cup [158]. From April 1993 to January 1995, 202 surgeries were carried out. 101 patients with a DLC coated head and the other 101 with a ceramic head. After an average of 9 years (8.5–10.1 years), 178 of the samples were retrieved. During these 9 years, 67 patients had required revisions, the reasons for which are detailed in Table I.6.

Table I.6. Reasons for implant revisions [158].

Reason for revision	DLC coated Ti-6Al-4V	Ceramic heads
Total (of total 178 follow-ups)	46 (25.8 %)	21 (11.8 %)
Aseptic loosening	41	10
Ossification	1	6
Dislocations	0	3
Pain	2	2
Infection	1	0
Implant failure	1	0

More heads with DLC coating required revisions (46) than ceramic heads (21). In the 46 failures of DLC coated heads, 41 were induced by aseptic loosening, while 10 failures of ceramic heads were caused by aseptic loosening. The average time before revision was very similar: 3.9 years (ranging between 0.2 and 9.2 years) for DLC coated heads and 4.1 years (0.4–

8.7 years) for ceramic heads. However, the DLC coated heads had no aseptic failures in the first year and half, unlike the ceramic heads, which first showed aseptic failure after 9 months.

The retrieved DLC samples all showed delamination of the DLC coating, as shown in Figure I.23. Taeger *et al.* thought that the delamination was the major cause of failure through aseptic loosening of the implants, as the loose DLC material triggered an adverse reaction.

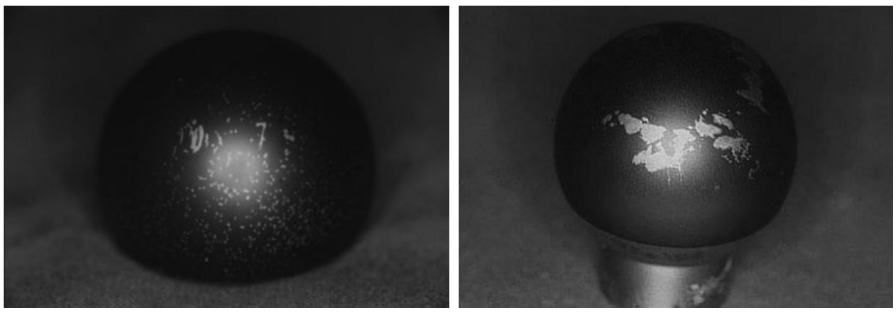

Figure I.23. Delamination of DLC coating on femoral head [158].

The performance of the DLC coated implant in human bodies is not as good as that from *in vitro* and *in vivo* animal testing. The reasons for the difference is still unclear. But the tests results are still important for further application and optimization of the DLC coatings.

In this section (Section 4), the structure of DLC coatings, different types of DLC coatings, and the growth mechanism of DLCs were explained. The mechanical properties (such as the hardness and elastic modulus) and the biocompatibility were discussed. The tribological properties of DLC coatings and methods to improve the cohesion between coating and substrate will be discussed in detail in the next section (Section 5).

5. Tribological response of DLC coatings

DLC coatings are known to have excellent tribological properties, including low friction and high wear resistance. The low friction of DLC coatings will be discussed firstly. After that, the reasons for the low friction will be explained, including the passivation of the DLC surface, the rehybridization of sp^3 to sp^2, and the transfer from DLC surface to the countersurface. After that, the wear resistance of DLC coatings will be explained. At last, methods to enhance the cohesion between the coating and the substrate, and consequently to improve the tribological performance of DLC coating will be discussed.

5.1. Low friction

DLC coatings are notable for their low friction coefficients [97]. The friction properties of DLCs have been reviewed by Grill [131, 159, 160], Hauert [118, 161], Robertson [97], etc. The friction properties of the DLC coatings are dependent on both the nature of the coating (such as the hydrogen content inside the coating [125]) and the environment conditions (such as the relative humidity (RH) [162], the hydrogen and oxygen gas pressure [163]).

The hydrogen content inside the DLC coating has a great effect on the friction properties. Donnet and Grill [164] reported the friction coefficients of a variety of hydrogenated DLC

coatings with different hydrogen contents deposited on a steel surface via d.c. PACVD, sliding against a steel pin under the ambient air and the UHV conditions. Whatever the hydrogen content of the DLC coatings, the friction coefficients were in the range of 0.12–0.18 in ambient air. In UHV, friction coefficients were higher than 0.58 for the DLC coatings with lower hydrogen contents (equal to or lower than 34 at.%), while it was near 0.02 for the DLC coating with a higher hydrogen content (42 at.%).

Enke *et al.* reported the effect of RH on the friction coefficient of hydrogenated DLC (a–C:H) coatings deposited on silicon via rf plasma deposition using acetylene as working gas, sliding against a steel ball [97, 159, 162]. In the nitrogen at a RH of less than 1%, the friction coefficients were in the range of 0.01–0.02. It increased with the increase in the RH, attaining values of 0.05 at a RH of 10% and up to 0.19 at the RH of approximately 100%. Moreover, the presence of water vapor increased the friction of hydrogenated DLC films, whereas it decreased the friction of hydrogen-free DLC films [125].

Fontaine *et al.* reported the effect of hydrogen and oxygen gas pressures on the friction properties of a silicon oxide-doped hydrogenated amorphous carbon (a–C:H:Si:O) deposited on a silicon wafer via PECVD, sliding against steel ball [163]. Low friction coefficients below 0.1 were obtained under higher gas pressures (10 mbar < oxygen pressure; 50 mbar < hydrogen pressure).

In addition, low friction is not universal for all the DLC films. The achievement of low friction needs several requirements such as proper material mating, proper tribological conditions and proper environment. As reported in [163], high friction coefficients (even approaching 1.2 ± 0.2) were obtained between the DLC coating and a steel ball under lower gas pressures (oxygen pressure < 10 mbar; hydrogen pressure < 50 mbar).

The low friction coefficients of DLC coatings can be explained by the contact surface changes, such as the coating surface passivation and rehybridization, and the material transfer from DLC to the countersurface, which will be discussed in the following sections (Section 5.2 and Section 5.3, respectively).

5.2. Structural and chemical changes of DLC surface during sliding

Structural and chemical changes of DLC surface are observed when sliding, such as passivation [165] and rehybridization [166].

5.2.1 Passivation

The passivation of diamond surface will be first discussed to serve as a reference to better understand the passivation of the DLC surface.

The diamond surface is inert because the surface is normally terminated by an adsorbed layer and its dangling carbon bonds are generally passivated by C–H bonds. Two diamond surfaces will contact through van der Waals forces. When the diamond / diamond contact

slides in air, it will break the weaker van der Waals bonds (Figure I.24a), not the bulk C–C bonds (Figure I.24b), so the friction has an adhesive / deformation nature rather than abrasive [97] and the friction coefficient is low [159]. When the diamond / diamond contact slides in a high vacuum, the adsorbed layer is removed. Strong C–C bonds then occurs across the interface, leading to high values of friction coefficient [159]. It can be decreased again by bleeding in hydrogen into the diamond / diamond interface [94].

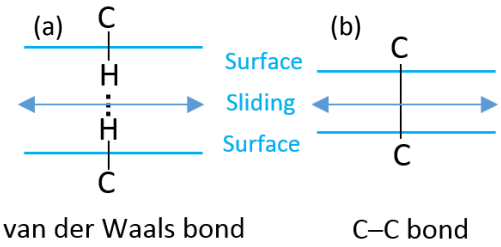

Figure I.24. Schematic representation of atomic interaction during sliding: (a) passivated surfaces; (b) un-passivated surfaces [165].

For the hydrogenated DLC coating, in addition to the hydrogen in the sliding environment, the hydrogen trapped in the film during deposition can serve as a source for passivation [165]. In UHV, a low friction is observed for hydrogenated DLC films during a short running-in period, which is probably due to the diffusion of hydrogen species (especially the hydrogen unbonded to carbon) from the bulk of the coating towards the sliding surface. After that, for the DLC coating with a high hydrogen content (40 at%), the friction remains low in UHV because this coating can provide enough hydrogen for passivation. For the coating with a low hydrogen content, the friction coefficient rises after the running-in period because the film is running out of the supply of hydrogen. If a certain amount of hydrogen (above 10 mbar) is introduced into the UHV chamber, a low friction occurs for the low hydrogenated DLC film, similarly to the low friction observed with the high hydrogenated DLC coating [165].

Various gaseous species, such as H_2 and water vapor, can serve as sources for passivation. Konicek *et al.* [167] reported that the dangling carbon bonds were either –OH or –H terminated in the water vapor environment.

5.2.2 Rehybridization

Many studies reported that a sp^2-bonded carbon rich surface layer formed on the DLC coating surface after sliding, which reveals a transformation of sp^3- to sp^2-bonded carbon [163, 166]. This rehybridization phenomenon is supported by experimental analysis [163] and atomistic simulations [166]. Figure I.25 shows a schematic representation of atomistic simulation of rehybridization occurring at the DLC coating / DLC coating sliding interface [166].

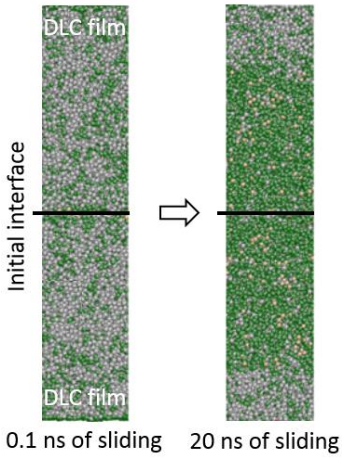

Figure I.25. Schematic representation of atomistic simulation of DLC coating / DLC coating. Grey: 4-fold (sp^3); green: 3-fold (sp^2); yellow: 2-fold (sp^1) [166].

A temperature-induced rehybridization hypothesis has been proposed to explain the transformation process from sp^3 to sp^2 bonding [168]. According to the temperature-induced rehybridization hypothesis, the repeated friction is expected to raise the temperature, probably up to the point where some sp^3 carbon atoms transform to sp^2 carbon atoms. Meanwhile, at a high temperature (about 450°C), the hydrogen is released from the hydrogenated DLC coating. The hydrogen atoms are thought to promote the sp^3 bonding. The hydrogen release from the DLC coating is expected to destabilize the tetrahedral bonding and to promote its transformation to sp^2 carbon.

A mechanically-induced rehybridization hypothesis has also been proposed [166]. According to the mechanically-induced rehybridization hypothesis, any event that promotes the transformation of an sp^3 carbon atom into an sp^2 state requires the breaking of a bond. With the shear stress at the siding surface, the sp^3–sp^3 bonds are easier to be elongated and thus weakened, while the sp^2–sp^2 bonds could stay relatively intact during this procedure. The tribomechanical process progresses through plastic events that transform the surrounding material to a weaker state. The shear-induced force will break the weak bonds, thus the sp^3–sp^3 bonds will be broken first. Therefore, the tribomechanical process will promote the transformation from sp^3 to sp^2 bonding.

It should be noted that there is no evidence so far of long range order with sp^2 hybridized carbon, such as graphite sheets or graphene. Only an increase of the fraction of sp^2 hybridized carbon in the rubbed surface was verified [163]. At present, the hybridization process is not completely understood.

5.3. Transfer from DLC surface to the countersurface

In the cases of low friction for tribology tests of a DLC coating sliding against an uncoated surface, transfer films formed on the countersurface have been widely observed [163, 169].

Ronkainen *et al.* [118, 170–172] described the formation process of a transfer layer formed on a steel ball against a DLC coating. At the beginning of the test, the small contact area of the ball / flat configuration generates an extremely high contact pressure. Material was worn off from the ball and adhered on the coating. After that, the contact area grows and the contact pressure drops. Wear products may be deposited on the ball, resulting in the buildup of the transfer layer. The adhesion of the transfer layer to the steel ball is governed by the chemical activity of the ball surface towards the wear products, and is also influenced by the tribological conditions and the environment conditions. As soon as the transfer layer is present, low friction (down to 0.02) and little further wear is observed, because the DLC is sliding against its transfer layer. In addition, the formation of transfer layer is not universal. It depends on several requirements, such as proper material mating, proper contact pressure and proper sliding velocity [118, 170].

The transfer layer is composed of the wear products from the DLC coating and from the countersurface. The sp^2-bonded carbon rich surface layer generated through rehybridization of the DLC coating can act as a lubricant, which could be adhered to the countersurface. Therefore, the analysis of the transfer layer by Fourier transform infrared spectroscopy (FTIR) or Raman spectroscopy reveals that the transfer layer has a graphite-like and/or disordered graphitic structure [118]. If the countersurface is metallic, the wear products from the metal may be oxidized. So, a certain amount of oxygen is detected by energy dispersive X-ray spectroscopy (EDX) on the transfer layer [163].

5.4. Wear resistance

DLC coatings are notable for their high wear resistance [97, 159]. According to Archard wear theory [97], the wear coefficient is proportional to the hardness of the surface, and in general, DLC coatings have high hardness.

Voevodin *et al.* [173] proposed that the wear mechanism of the hydrogen-free DLC coatings was adhesive wear, via transfer layer. Surface enhanced micro-Raman studies of the wear tracks, wear debris and the transfer film demonstrated that an sp^3 to sp^2 phase transition occurred in the wear tracks on the DLC coating surface. The transformed phase on the coating surface was then transferred to the countersurface via adhesive wear.

Marchon *et al.* proposed a tribochemical mechanism to explain the carbon depletion at the ceramic / DLC coating interface in the presence of gaseous oxygen [174, 175]. It included two steps: oxygen chemisorption, and –CO and CO_2 desorption. The former occurred naturally on the surface dangling bonds and the latter was activated by the sliding motion of the interface.

Namura *et al.* [159] investigated the failure mechanisms of sputtered carbon coating by contact start–stop (CSS) tests against Al_2O_3–TiC sliders. The wear of the carbon layer was found to be minimal under the investigated conditions. Coating failure was found to occur

abruptly. Fatigue cracks were observed to develop and to propagate to the surface of the substrate with repeated CSS cycles. When the cracks reached the substrate, flaking occurred abruptly.

The wear of DLC coatings is influenced by many parameters, such as the deposition processes and the contact force [159]. Agarwal *et al.* [159] described the wear of the sputtered carbon coatings. The wear was found to increase with the normal load and the number of revolutions but was independent of the linear speed.

5.5. Improvement of DLC coating properties

DLC coatings present excellent mechanical and tribological properties, such as high hardness, low friction coefficients, and high wear resistance [97]. However, they also have weaknesses such as the presence of high compressive stresses in the coating [131, 151] and a poor cohesion between the hard DLC coatings and the soft substrates [153]. Many methods have been explored to overcome the shortcomings mentioned above, such as element incorporation [176] and multilayer structures. These methods have improved the mechanical and tribological properties of DLC coatings and broadened the application of DLC as protective coatings.

5.5.1. Incorporation of elements

The nature and properties (internal stresses, hardness, electrical conductivity, surface energy, etc.) of the DLC can be modified by controlling the incorporation of dopants, such as silicon [177, 178], fluorine [179], nitrogen [180, 181], and various metals [176].

- **Silicon-containing DLC coatings**

Meneve *et al.* investigated the tribological behavior of silicon-doped DLC coatings (a–C_x:H:Si_{1-x}, with $0.7 < x < 0.9$) deposited via c.f. PACVD [176]. According to the authors, the addition of silicon to an a–C:H film reduces the hardness, elastic modulus and internal stresses. In ambient humid air, the friction of Si-doped DLC film appears to be significantly reduced (below 0.1) compared to conventional undoped DLC, with a comparable wear resistance. However, this tribological behavior seems to be observed under low contact pressure conditions (below 1 GPa). Under higher contact pressures, the lower wear resistance of Si-doped DLC becomes increasingly unacceptable. Ban *et al.* [178] investigated Si-containing DLC films deposited using CH_4 and SiH_4 by an electron beam excited plasma (EBEP) CVD system. As the Si content was varied from 0 to 32 at.%, the internal compressive stresses linearly decreased from 2.5 to 1.0 GPa while the hardness remained nearly constant. From the correlations between the internal stresses and the structural properties, the authors suggested that the formation of Si–H bonds caused the relaxation of a three-dimensional rigid network of DLC film, resulting in the reduction in the compressive stresses. It was also implied

that a transformation of the unbonded hydrogen into the bonded hydrogen in Si–H bonds was correlated with the compressive stresses reduction.

- **Fluorine-containing DLC coatings**

Like silicon, fluorine incorporation in the DLC structure induces a significant reduction of the surface energy and reduction in the internal stresses compared to conventional DLC coatings [176, 179]. The reduction in surface energy is higher with fluorine than with silicon. However, the fluorinated DLC coatings appear to be soft and show worse wear resistance, especially with a high fluorine content.

- **Nitrogen-containing DLC coatings**

According to [164], nitrogen incorporation in DLC coatings exhibits good wear resistance, low friction coefficients, and reduced internal stresses [160, 176]. Up to 34 at.% nitrogen can be incorporated into the DLC coating structure, generally reducing the stresses but preserving hardness and resistance. It has been found that nitrogen incorporation in the DLC structure decreases the fraction of sp^3 carbon hybridization [176], while the sp^3 phase is generally accepted as being responsible for the excellent mechanical properties of pure DLC films [180]. Dekempeneer *et al.* [179] investigated amorphous hydrogenated carbon nitride ($a–C_x:H:N_{1-x}$) coatings with the nitrogen contents varying between 0 and 13 at.% and reported that nitrogenation of hard DLC coatings resulted in the formation of softer, less stressed and less wear resistant materials. In summary, the results on the mechanical and tribological properties of the nitrogen-containing DLC coatings do not agree from one investigation to another [176, 180, 181]. Less work has been performed on the tribological investigation of the nitrogen-containing DLC films [176].

- **Metal-containing DLC coatings**

Metallic elements, such as tantalum (Ta), niobium (Nb), titanium (Ti), tungsten (W), chromium (Cr), silver (Ag) etc., can be incorporated into DLC coatings to improve their adhesion and thus tribological properties [182–185]. A pure metallic or a metal carbide target is used to prepare a–C:H:Me coatings in an argon-hydrocarbon atmosphere.

Comparing to a–C:H coatings, a–C:H:Me coatings have lower compressive stresses, but also lower hardness and lower elasticity [110]. For example, Benndorf *et al.* [186] prepared Nb-containing DLC coatings, which have lower compressive stresses of around 0.1-0.3 GPa, as well as lower hardness of around 13 GPa and lower Young's modulus of around 100 GPa, with NbC contents of around 20–40% (vol. %). An explanation for the variation of mechanical properties is that, the matrix of metal free DLC coatings consists of highly cross-linked CH_x units [186], while the metal containing DLC coatings consist of nanocrystalline metal or carbide particles embedded in an amorphous matrix [182] and thus contains weaker cross-linkages [110, 187].

5.5.2. Multilayer structure

Due to the high compressive stresses of the DLC coatings and the difference of mechanical properties between DLCs and metals, the cohesion of DLC coatings to metallic substrates is often not sufficiently high; thus, the DLC coating tends to fracture and delaminate under high contact pressures [188]. Therefore, adhesive interlayers and multilayer constructions are applied to address this issue [189, 190].

- **Adhesive interlayer**

Adhesive interlayers mitigate the high compression by releasing stresses, reduce coating / substrate mismatching, and promote stronger chemical bonds at the interfaces [191, 192].

Silicon-containing interlayer is widely used as an adhesive interlayer, because silicon has chemical affinity with the metallic atoms present in the substrate alloy and with the carbon atoms constituting the DLC coating, enhancing the cohesion between the DLC coating and the substrate and improving the critical load values for delamination [191, 193]. Cemin *et al.* exhibited the cross section of a DLC coating with a silicon-containing interlayer deposited on a steel substrate, as shown in Figure I.26 [191]. From left to right, the outermost layer is a microstructured material containing a relatively high signal of carbon and hydrogen, which is the DLC coating (called the DLC film in this figure). Subsequently, a submicrometric layer is present, containing a relatively high signal of carbon, hydrogen and silicon, which is the adhesive silicon-containing interlayer (a–C:H:Si).

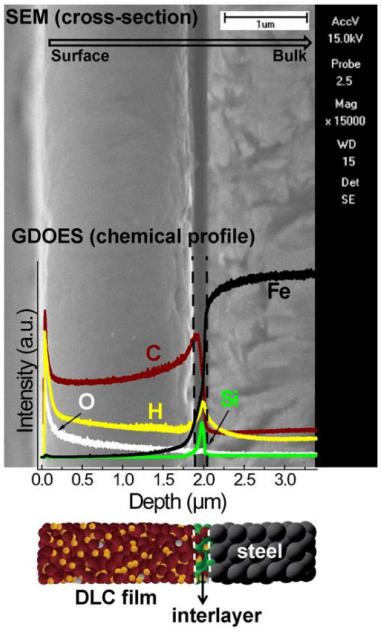

Figure I.26. Cross section of a DLC coating with a silicon-containing interlayer deposited on steel [191].

Metal-containing interlayers (titanium-, chromium-, and aluminum-containing interlayers) are also used. Wei *et al.* [189, 194, 195] have performed investigation on metal-containing interlayers deposited on different substrates (metallic substrate, like steel and non-metallic substrate, like silicon and glass). According to their results, the metal-containing

interlayers improve the cohesion for DLC on steel, but degrade the cohesion for DLC on silicon. The reason is the different thermal stresses induced by the mismatch of coefficient of thermal expansion. Specifically, for the silicon substrate, the deposition of interlayer increases the thermal stress and degrades the adhesion. For the steel substrate, the deposition of interlayer reduces the thermal stresses which are advantageous to cohesion [194]. The chromium-containing interlayer improves the cohesion strength between the DLC and the glass substrate when the coating is thin (200 nm). As the coating thickness increases, the peeling of the DLC coating deteriorates [189].

- **Multilayer construction**

DLC multilayer coatings have been designed and constructed to achieve better mechanical and tribological properties than the single DLC coatings [190, 196, 197].

Lin *et al.* investigated DLC multilayer coatings consisting of alternating layers of soft and hard carbon films deposited on a silicon substrate. The transmission electron microscopy (TEM) of the cross section is shown in Figure I.27 [190]. The carbon/carbon multilayer coatings can withstand the maximum contact stress of around 3.65 GPa, while the single layer hard DLC coating fails when the stress is higher than 2.30 GPa. The wear rate of the carbon/carbon multilayer is 10 times lower than that of the single layer DLC coating. Zhang *et al.* [196] proposed that the soft sub-layer relaxes the internal stresses and enhances the cohesion, and the hard sub-layer contributes to the improvement of the durability of the whole multilayer coating. Yang *et al.* [197] compared the carbon/chromium multilayer coating and the single layer carbon coating. The single layer coating has very good wear properties at low load whilst the coatings with the optimized chromium content have excellent tribological performance at high load.

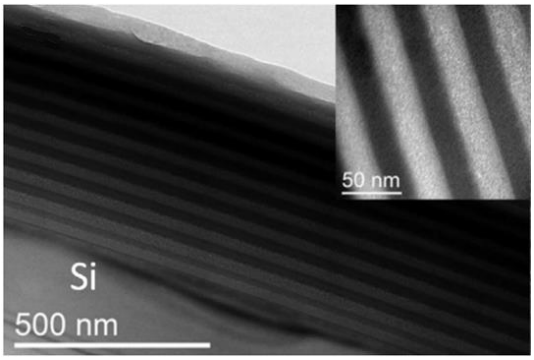

Figure I.27. TEM cross-sectional image of carbon/carbon multilayer construction of the DLC coating [190].

The need to apply supporting interlayers is obvious to prevent the top DLC coating cracking and delamination under load on a soft substrate [198]. The supporting interlayers need to satisfy the following properties: load support, stress equalization, crack braking, a diffusion barrier to carbon dissolving elements, and good cohesion to the substrate. If each of the properties is assigned to a single layer, then we obtain a complicated multilayer structure, as shown in Figure I.28a [198]. Voevodin *et al.* constructed a multilayer composite coating,

Ti/TiN/TiCN/TiC/Ti-DLC/TiC/Ti-DLC, which can provide all necessary properties, as shown in Figure I.28b [198]. The top titanium containing DLC coating layers are used for friction and wear reduction; the ceramic TiCN and TiN layers are used for a load support; thin layers of Ti and TiC are used to enhance coating cohesion and toughness.

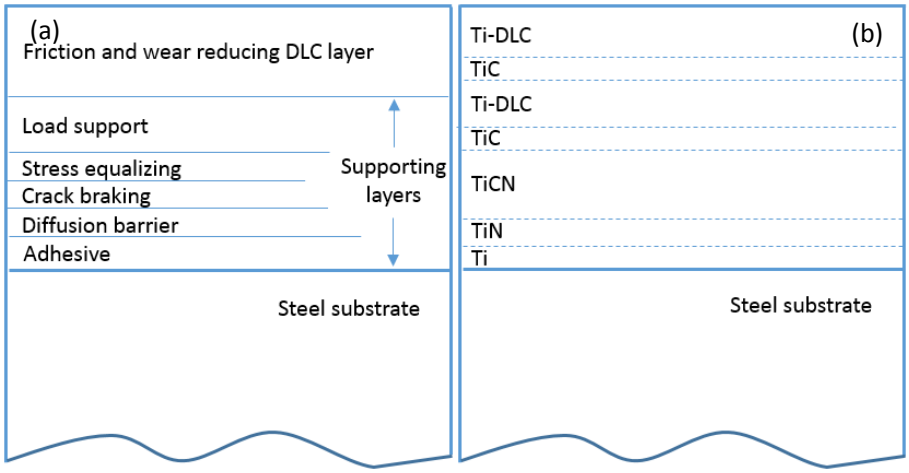

Figure I.28. Diagram representing schematically a complicated multilayer composite coating: (a) theoretical constitution; (b) coating developed by Voevodin *et al.* [198].

6. Influence of different parameters on tribological behavior of contacts

The tribological behaviors of contacts are influenced by a variety of parameters, including the surface roughness, the coating positions, and the environment.

6.1. Roughness

In many tribological applications, it is neither possible to control the surface degradation process nor to modify the contact loads. Therefore, the initial design of the friction pairs is the only manner in which the friction phenomenon and surface damage can be prevented or minimized. The initial roughness is an important parameter that could be optimized [199].

6.1.1. Metal / metal contact

For the metal-on-metal contacts, the initial surface roughness has an influence on friction and wear processes [200]. Kubiak *et al.* conducted fretting tests (under gross slip conditions) of a bearing steel (AISI 52100) ball sliding against low carbon alloy (AISI 1034) or Ti–6Al–4V flats with different values of roughness (R_a: 0.15–2.52 µm). The increase in the initial surface roughness caused a slight decrease in friction coefficient, as shown in Figure I.29. Elleuch *et al.* performed sliding tests between a steel (100Cr6, similar to AISI 52100) ball and elastomer flats with different values of surface roughness (R_a: 3.2–13.2 µm) [201]. The friction coefficient also decreased with the increase in the surface roughness. The authors explained that the increase in the roughness decreases the real contact area, thus the adhesion force and the friction coefficient.

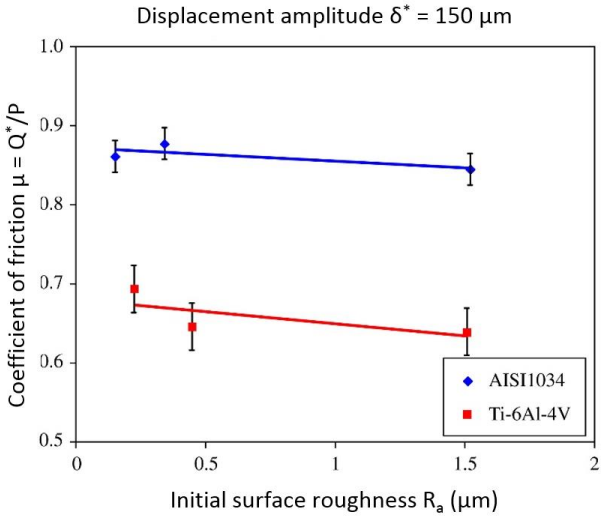

Figure I.29. Friction coefficient as a function of initial surface roughness [200].

However, many studies reported that the influence of initial surface roughness on the friction and wear processes of metal-on-metal contacts were negligible. For tests with a steel ball (AISI 52100) sliding on steel flats (AISI 1034) with various values of surface roughness (S_a: 90–4 150 nm), similar stable friction coefficients remained in the range of 0.5–0.8 [199].

6.1.2. Metal / coating contact

For the metal / coating contacts, the surface roughness has a great influence on the friction and damage processes of the contact surfaces. Furthermore, tribological processes are also controlled by the coating and substrate hardness and the coating thickness, as shown in Figure I.30 [72].

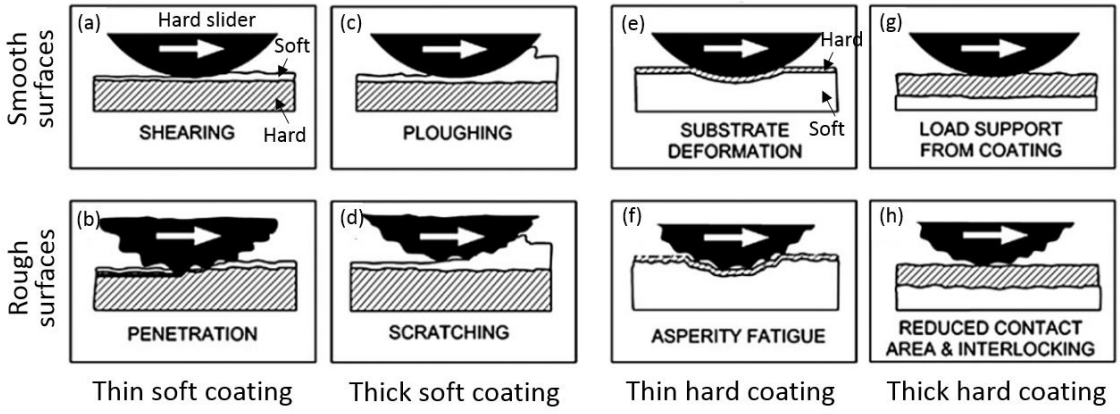

Figure I.30. Influence of surface roughness, hardness and coating thickness on tribological processes. Characteristic tribological contact phenomena are shown schematically in (a)–(h) [72].

- **Thin soft coating**

For a thin soft coating on a hard substrate, when the contact surfaces are smooth (Figure I.30a), the friction is determined by the shear strength of the coating and the contact area. The contact area is related to the deformation of the substrate. In the case of the combination of a coating which possesses the properties of low shear strength and the substrate with high

hardness or high elastic modulus, the friction coefficient is low. The most typical example is a steel ball sliding on a smooth steel flat on which a MoS_2 coating is deposited, resulting in friction coefficients as low as 0.02 [72].

When the contact surfaces are rough (Figure I.30b), the influence of the roughness is considerable. The penetration of asperities through the coating will cause increased shear resistance and ploughing of either the substrate or the countersurface, leading to an important increase in friction [72].

- **Thick soft coating**

For a thick soft coating on a hard substrate, when the contact surfaces are smooth (Figure I.30c), too large thickness of coating leads to an increase in friction. This can be explained by the increased contact area at the interface and the ploughing on the coating.

When the contact surfaces are rough (Figure I.30d), the influence of roughness can be neglected if the roughness is considerably smaller than the coating thickness and the coating is stiff enough to carry the load. If the roughness is larger enough, the frictional effect can be observed. Aubert measured the friction coefficient between a 100Cr6 steel ball and MoS_2 coated stainless steel flats and obtained a decrease in the friction coefficient with the increase in the flat roughness [202]. Holmberg attributed the decrease in friction coefficient to an improvement in the carrying capacity by the coated substrate asperities or decreased shear strength by increased pressure at coating between the asperities and the countersurface [72].

- **Thin hard coating**

For a thin hard coating on a soft substrate, when the contact surfaces are smooth (Figure I.30e), it is unable to support the load if the coating is very thin. The function of the coating is to separate the substrate from the countersurface and to prevent ploughing by hardening the top layer of the surface. The prevention of ploughing has a reducing effect on both the friction and the wear. However, the higher shear strength introduced at the contact interface by the hard coating has an increasing effect on friction. The increase in friction by increased shear strength generally seems to be more dominant than the reduction in friction by decreased ploughing. Therefore, high friction coefficients are often measured on hard coatings. But, if a tribofilm with low shear strength is formed on the contact surfaces, friction coefficients are low. Furthermore, when loaded, the coating will deflect in accordance with the substrate deformation. The repeated deflection of coating may cause fracture or fatigue cracks that destroy the coating [72].

When the contact surfaces are rough (Figure I.30f), the probability of fatigue failure of the hard coating is higher.

- **Thick hard coating**

For a thick hard coating on a soft substrate, when the contact surfaces are smooth (Figure I.30g), the coating can carry part of the load, and the deformation of the substrate will be

smaller. The frictional situation is more favorable compared with the thin hard coatings. However, too large thickness generally causes poor cohesion between the hard coating and the soft substrate because of the high internal stresses in coating.

When the contact surfaces are rough (Figure I.30h), the surface roughness may remain or be smoothened to some extent. The effective contact area has been reduced to the asperity contacts. If the shear strength at the asperity contacts is low, the friction coefficient will be extremely low. In addition, the friction may be increased by asperity interlocking and breaking mechanisms if both contact surfaces are rough.

6.2. Coating position

6.2.1. Influence of substrate curvature

In experimental studies, coatings are generally deposited on a flat surface and are sliding against an uncoated curved surface (a ball or a cylinder). The influence of curvature of the substrate on the tribological behaviors of the coating is ignored [70]. Recently, soft coatings on a curved substrate showed promising tribological performance [203, 204]. Yang *et al.* reported longer durability of a soft coating (MoS_2 dry lubricant) deposited on spherical and on cylindrical surfaces than on a flat surface [203]. The authors attributed the shorter lifetime of the coating on a flat surface to the higher sensitivity of the flat surface to plastic deformation, i.e., the flat surface was subjected to more serious plastic deformation so that the coating material was easier to be “pushed” to the end of the contact. Therefore, less coating material was left for forming the transfer film on the countersurface, leading to a shorter durability. At present, the study on the influence of the substrate curvature on tribological behaviors of hard coatings (such as the DLC coatings) is insufficient.

6.2.2. Coating on both contact surfaces

The tribological performance of coating on both contact surfaces was studied using a soft MoS_2 bonding coating [203]. The MoS_2 bonded coating on both surfaces has similar friction coefficient with the coating on one surface, because the coating material is transferred to the uncoated countersurface, leading to a similar coating-on-coating contact. For hard coatings (such as DLC coatings), the tribological behavior of coating-on-coating contacts has not yet been well studied.

6.3. Environment

Implants are exposed to human tissues and fluids. The presence of body fluids at the interfaces between implant components and between the implant and host influences the tribological behaviors of contacts [23]. For the tribological study on the hip implants, various solutions have been applied to simulate the body fluid environment, including distilled water,

saline solution, synovial fluid, Hank's solution [205], bovine serum, calf serum, etc. Among these solutions, the serum has been the most widely used, especially in the last 30 years [206].

Metallic materials are suffering corrosive processes under the solutions conditions. Furthermore, the relative sliding at the interface accelerates the corrosion process due to the removal of protective oxide layer by sliding. As discussed in Section 2.4.5, Ti alloys and CoCr alloys have greater corrosion resistance than stainless steels.

Different coatings have different corrosion resistance to body fluids, depending on the coating compositions, structures and manufacture processes, etc. DLC coatings generally have high corrosion resistance [207–209]. Chandra *et al.* immersed the DLC-coated stainless steel and DLC-coated Ti–6Al–4V in different fluids, i.e. distilled water, saline solution, or bovine serum, for four weeks at 37°C. FTIR and Raman spectroscopic results reveal that there are no changes in the atomic structure of the DLC coating during exposure [210]. However, the exposure to body fluid may affect the cohesion between the DLC coating and the metallic substrate. Chandra *et al.* measured the cohesion of the coatings before and after the exposure to fluids [210, 211]. The results show that the saline solution causes localized debonding, whereas the distilled water and serum have no apparent effect [210]. The authors explained that the saline solution tended to penetrate the coating through pinholes and slowly corroded the interface, which may lead to coating delamination [211].

7. Conclusions

Neck adapters have been introduced into total hip implants to facilitate the replacement surgery. However, the neck adapter / femoral stem contacts, which are metal / metal contacts, undergo fretting damage during people walking. In this case, DLC coatings might be used at the neck adapter / femoral stem interface to protect the metallic parts. In order to understand this situation, in this chapter, bibliography synthesis was carried out from the following aspects:

- Modular hip implants,
- General coating types and deposition methods,
- DLC coatings and their mechanical and tribological properties,
- Important parameters influencing the tribological performance of contacts.

In modular hip implants, the most widely used materials for femoral stems are stainless steels, cobalt–chromium alloys, and titanium alloys. Among these alloys, Ti–6Al–4V has been becoming the most promising alloy owing to its high specific strength, corrosion resistance and biocompatibility. The neck adapter / femoral stem contacts are suffering the cyclic normal loads in the range of approximately 398–857 MPa and the relative movements in the range of approximately 3–41 μm during people walking. However, Ti–6Al–4V / Ti–6Al–4V contact has poor tribological performance including high friction coefficient and severe adhesive wear under fretting conditions.

At present, an increasing number of tribological coatings are available due to the development of many deposition techniques. Each of them is suitable for certain application fields depending on its properties and the requirements. DLC coatings have many promising properties including high hardness, low friction and excellent wear resistance in many environments, high corrosion resistance, and high biocompatibility. Thus, they can be used in implant applications. Furthermore, DLC coatings include a broad range of amorphous carbon coatings with different mechanical properties and tribological performance depending on their compositions and structures. The optimal DLC coating for neck adapter / femoral stem contacts should be explored.

The performance of coatings is influenced by many parameters including the initial surface roughness, the coating positions (coating on flat or on curved substrate, coating on one contact surface or on both contact surfaces), and the environment. About the roughness influence, a rougher surface causes a higher probability of fatigue failure of the hard coating. Fortunately, the surface roughness can be optimized during initial design. About the effect of coating positions, the soft coating (MoS_2 bonding coating) presents better tribological performance on a cylindrical surface than on a flat surface. However, the influence of the substrate curvature on tribological behaviors of hard DLC coatings has not yet been completely studied. Furthermore, the comparison of DLC coating on one contact surface and on both contact surfaces has not yet been well investigated.

Implants are exposed to body fluids. The presence of fluids at the interfaces between implant components influences the tribological behaviors of metallic substrates and the DLC coatings.

According to the literature study, the following five aspects are very important, and they will be discussed in the subsequent chapters:

- Fretting behavior of Ti–6Al–4V / Ti–6Al–4V contact,
- Fretting behavior of DLC coatings on Ti–6Al–4V substrate,
- Influences of coating hardness, substrate roughness, and coating positions (coating on flat or on cylindrical substrate, coating on one contact surface or on both contact surfaces), on the tribological performance of DLC coatings,
- Influence of serum on fretting behaviors of Ti–6Al–4V and DLC coating,
- Origin of the low friction property of the DLC coating.

CHAPTER II

EXPERIMENTAL METHODS AND MATERIALS UNDER INVESTIGATION

CHAPTER II: EXPERIMENTAL METHODS AND MATERIALS UNDER INVESTIGATION

CHAPTER II: EXPERIMENTAL METHODS AND MATERIALS UNDER INVESTIGATION

This chapter introduces the materials under investigation, including the Ti–6Al–4V substrate and DLC coatings, the experimental and analytical methods, and the test conditions.

1. Introduction

This chapter presents the materials under investigation, including the Ti–6Al–4V substrate and two types of DLC coatings. It also introduces the test rig for fretting testing. Furthermore, test parameters, including the normal force, displacement amplitude, number of cycles, surface roughness, coating position, and environment, are presented in detail. Moreover, the analytical methods are explained in this chapter, such as the 2D profilometer, interferometer, digital microscope, SEM, nano-indentation, and compression of micro-pillar.

2. Materials and surfaces

2.1. Ti–6Al–4V

2.1.1. Microstructure and chemical composition of Ti–6Al–4V

The substrate of samples was made of Ti–6Al–4V to simulate the real neck adapter and femoral stem components (XO Femoral Stems with modular neck adapter, as shown in Figure I.3, from the company *SEM Science et Médecine,* established in France [212]). Both the neck adapter and femoral stem are made of Ti–6Al–4V alloy. Figure II.1 shows the microstructure of Ti–6Al–4V alloy used in this thesis. It has the α–β structure. At the point labeled as α, it has a hexagonal close-packed (HCP) crystal structure (α phase). At the point labeled as α–β, it has a lamellar structure of α and β phases. The β phase has a face-centered cubic (FCC) crystal structure [30].

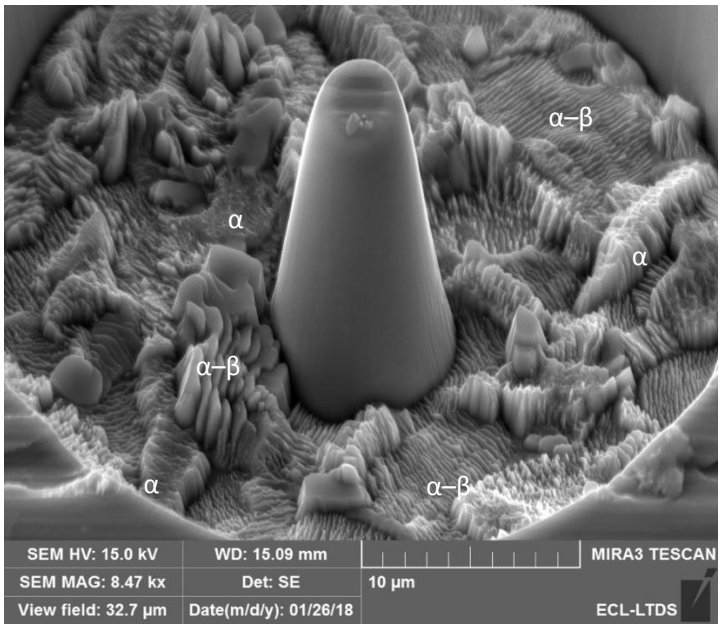

Figure II.1. FIB milled Ti–6Al–4V substrate. Around the central pillar, the structure is highlighted by the ionic etching in the MEB.

The chemical composition of Ti–6Al–4V alloy used in this thesis is shown in Table II.1. According to the EDX analysis, the Ti–6Al–4V alloy is mainly composed of 90% of Ti, 6% of Al, and 4% of V.

Table II.1. Chemical composition of Ti–6Al–4V from EDX analysis.

Wt%	Ti	Al	V
Ti–6Al–4V	90.06 ± 3.14	5.52 ± 1.11	3.96 ± 4.42

2.1.2. Surface roughness of Ti–6Al–4V samples

The real neck adapter surface and the femoral stem inner surface were observed through interferometry, as shown in Figure II.2. The roughness parameters, arithmetical mean height (S_a), skewness (S_{sk}), and kurtosis (S_{ku}), are shown in Table II.2. The S_a is also shown in Figure II.3. The S_a of neck adapter surface is around 340 nm, and the S_a of femoral stem inner surface is around 475 nm. The sliding direction on the contact surfaces during walking is shown in Figure II.2.

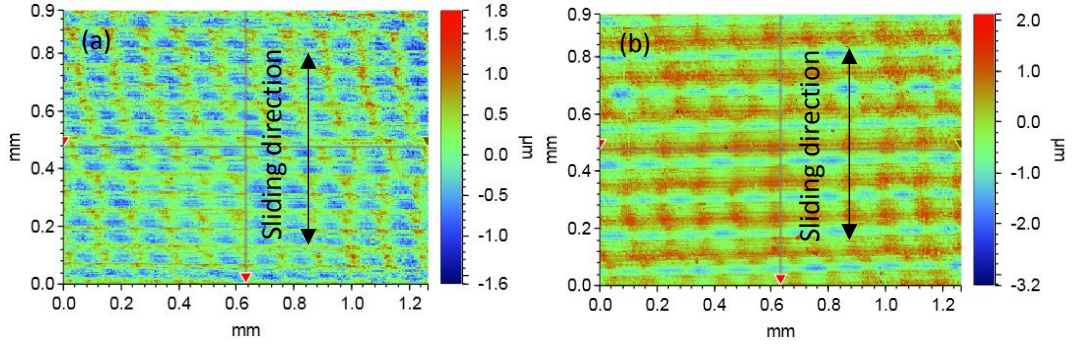

Figure II.2. 3D topography of (a) the neck adapter surface and (b) the femoral stem inner surface.

Table II.2. Surface roughness parameters of neck adapter, femoral stem, and uncoated flat and uncoated cylinder samples.

	Arithmetical mean height S_a (nm)	Skewness S_{sk}	Kurtosis S_{ku}
Neck adapter surface	340	0.085	2.67
Femoral stem inner surface	475	-0.22	2.58
Smooth flat without coating	27 ± 1	-	-
Rough flat without coating	394 ± 18	-0.10 ± 0.05	2.75 ± 0.13
Cylinder without coating	723 ± 11	0.23 ± 0.03	2.59 ± 0.04

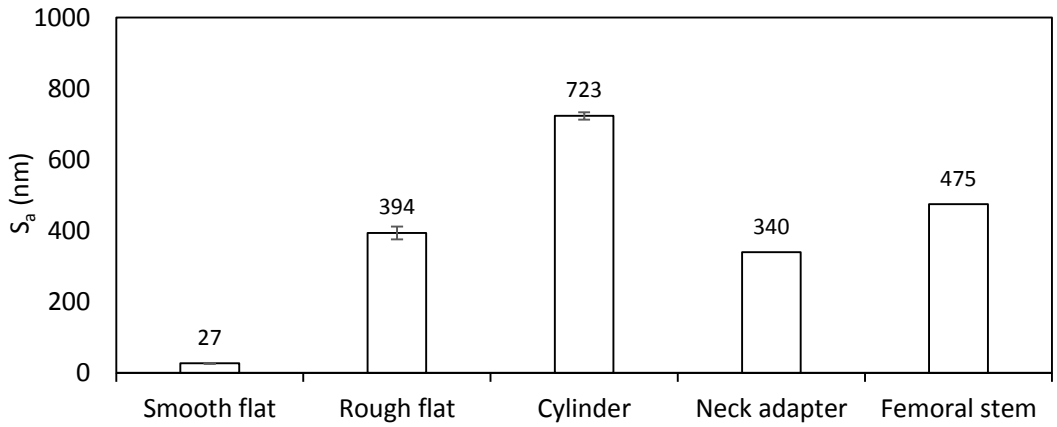

Figure II.3. Surface roughness of uncoated flat and uncoated cylinder samples, and neck adapter and femoral stem surfaces.

To investigate the influence of roughness, both smooth- and rough- surfaced flat samples were studied. All cylinder samples had a rough surface. The values of the roughness parameter for the rough flat and cylinder surfaces were close to those obtained from the real neck adapter and the femoral stem surfaces.

The flat and cylinder surfaces were observed via digital microscope, as shown in Figure II.4, and via interferometry, as shown in Figure II.5. The sliding direction for subsequent fretting testing is exhibited on images. The relation between the sliding direction and the roughness texture is the same in the flat–cylinder surface contact and in the real neck adapter–femoral stem contact.

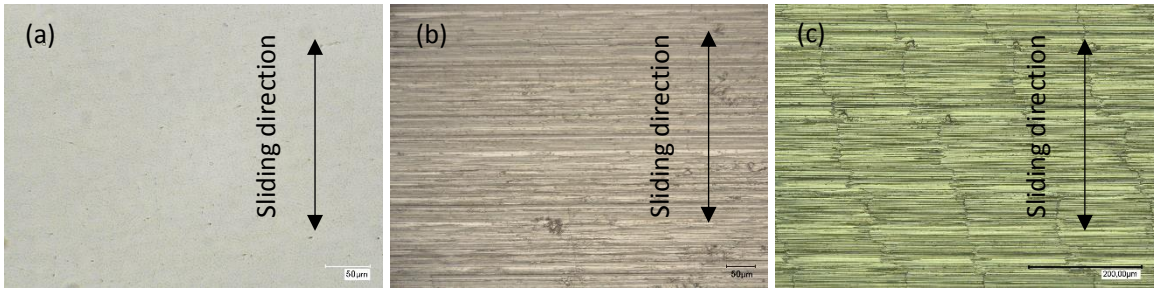

Figure II.4. Optical images of flat and cylinder samples without coating:
(a) smooth flat; (b) rough flat; (c) cylinder.

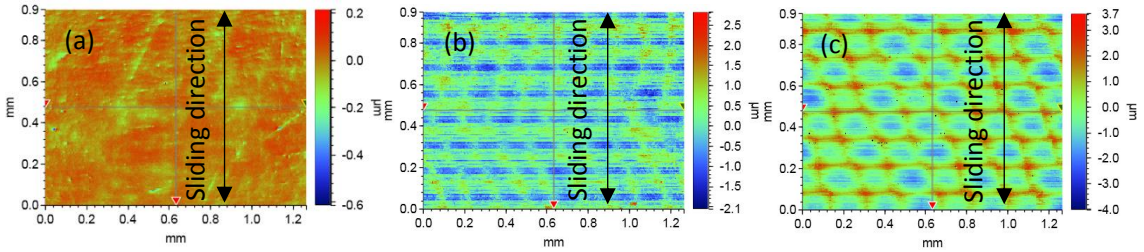

Figure II.5. 3D topography of flat and cylinder samples without coating:
(a) smooth flat; (b) rough flat; (c) cylinder (after removing the cylindrical shape).

The roughness parameters, arithmetical mean height (S_a), skewness (S_{sk}), and kurtosis (S_{ku}), are shown in Table II.2. The values of S_a are also shown in Figure II.3. Obviously, the smooth flat surface is significantly smoother than the rough flat and cylinder surfaces. The cylinder is rougher than the rough flat. More specifically, S_a of cylinder surface is higher than 700 nm. S_a of rough flat is around 400 nm. S_a of smooth flat is around 20 nm.

2.1.3. Mechanical properties of Ti–6Al–4V

Nano-indentation measurement using continuous stiffness measurement (CSM) method was conducted on a rough flat surface to measure the nano-hardness and the elastic modulus of Ti–6Al–4V substrate, as shown in Figure II.6. The nano-hardness is around 3.4 ± 0.5 GPa and the reduced elastic modulus is around 122 ± 14 GPa.

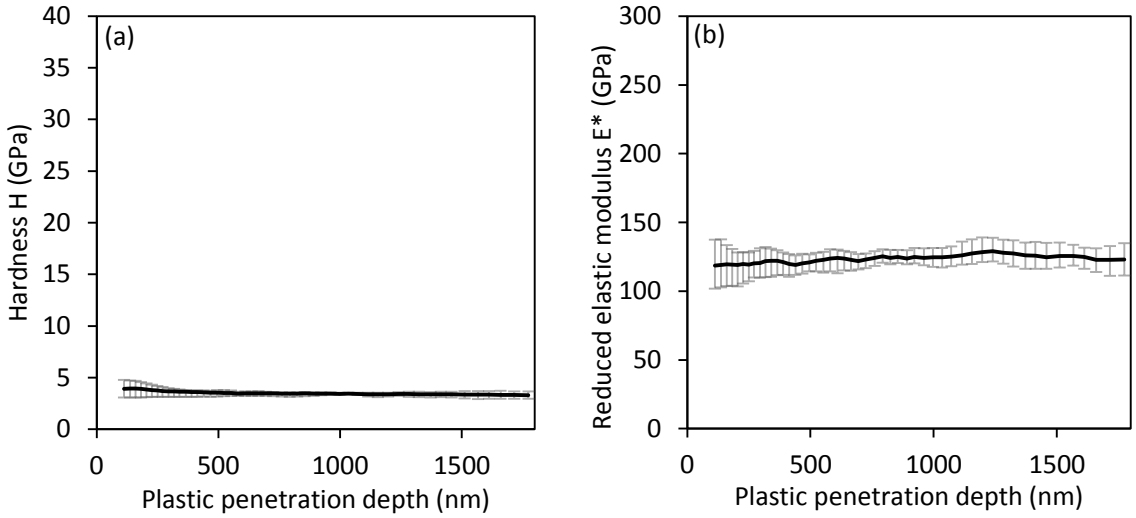

Figure II.6. (a) Nano-hardness and (b) elastic modulus of uncoated rough flat surface.

2.2. DLC coatings

2.2.1. Deposition process and chemical compositions

Some samples were coated with a DLC coating via the PACVD technique (with machine TSD 550, from HEF [213]). Two DLC coatings were studied: DLC A and DLC B. They were a–C:H (hydrogenated amorphous carbon) films. DLC B coating was designed with lower elastic modulus to avoid the elastic mismatch between the coating and the substrate. The elastic modulus of the two different coatings was controlled by changing the bias voltage during

deposition and the H content. DLC A contains 20% of hydrogen, while DLC B contains 40% of hydrogen.

2.2.2. Coating thickness and interlayer

The cross sections of rough and smooth coated flat samples were observed via the SEM and the EDX, as shown in Figure II.7. The DLC coatings are well continuous with a constant thickness of approximately 2.0 μm. A Si-rich interlayer is present as a bonding layer for gradual transition stress, thus enhancing the cohesion between the DLC coating and the Ti–6Al–4V substrate. The thickness of the Si-rich interlayer is around 0.5 μm. There is no obvious difference in the thickness between DLC A and DLC B.

From the EDX analysis, the DLC coating above the Si interlayer is mainly composed of C element. But it should be noted that H element cannot be detected via EDX. Therefore, the EDX analysis cannot distinguish the difference in the chemical compositions between DLC A and DLC B.

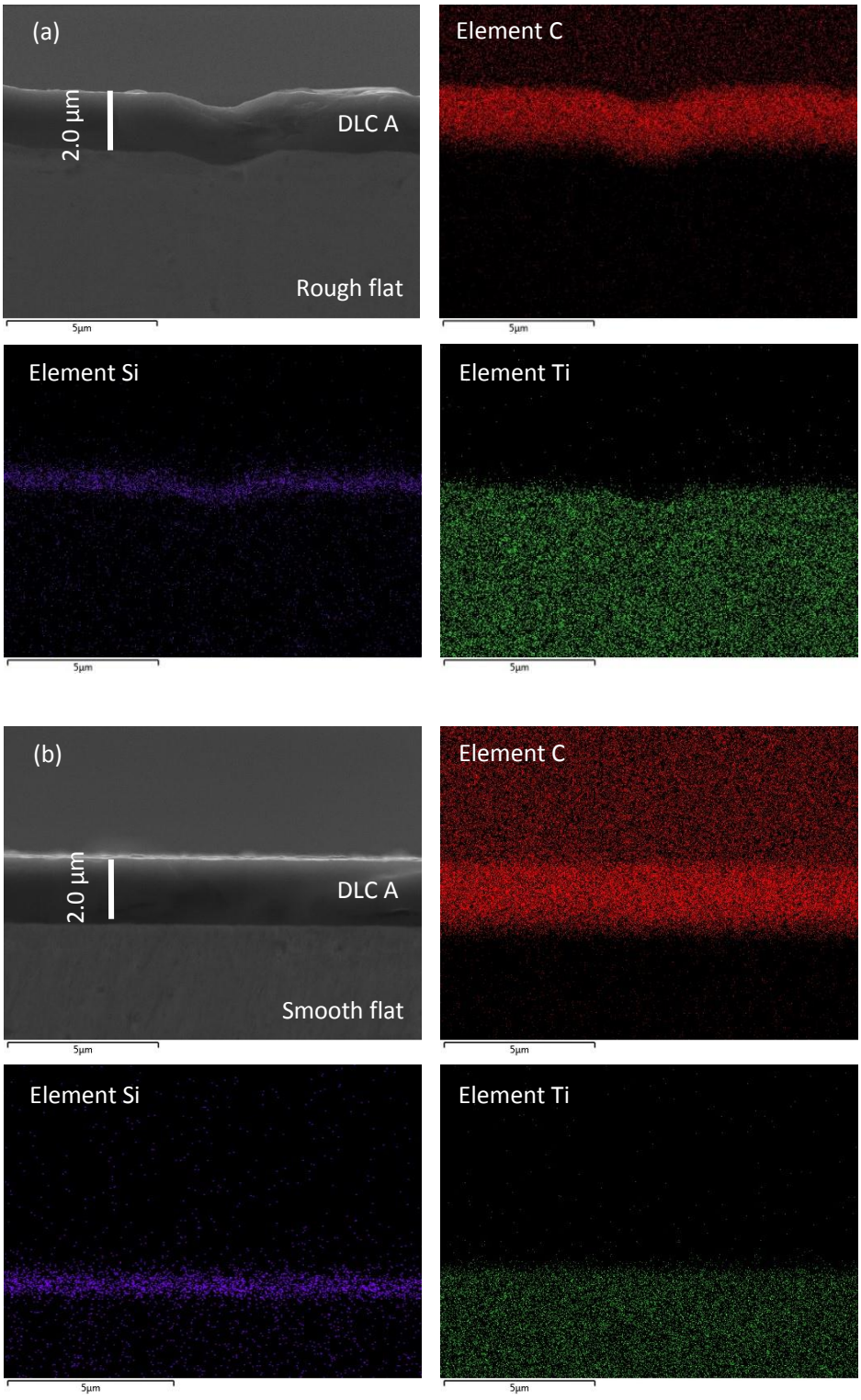
(a)
2.0 µm
DLC A
Rough flat
5µm
Element C
5µm
Element Si
5µm
Element Ti
5µm
(b)
2.0 µm
DLC A
Smooth flat
5µm
Element C
5µm
Element Si
5µm
Element Ti
5µm

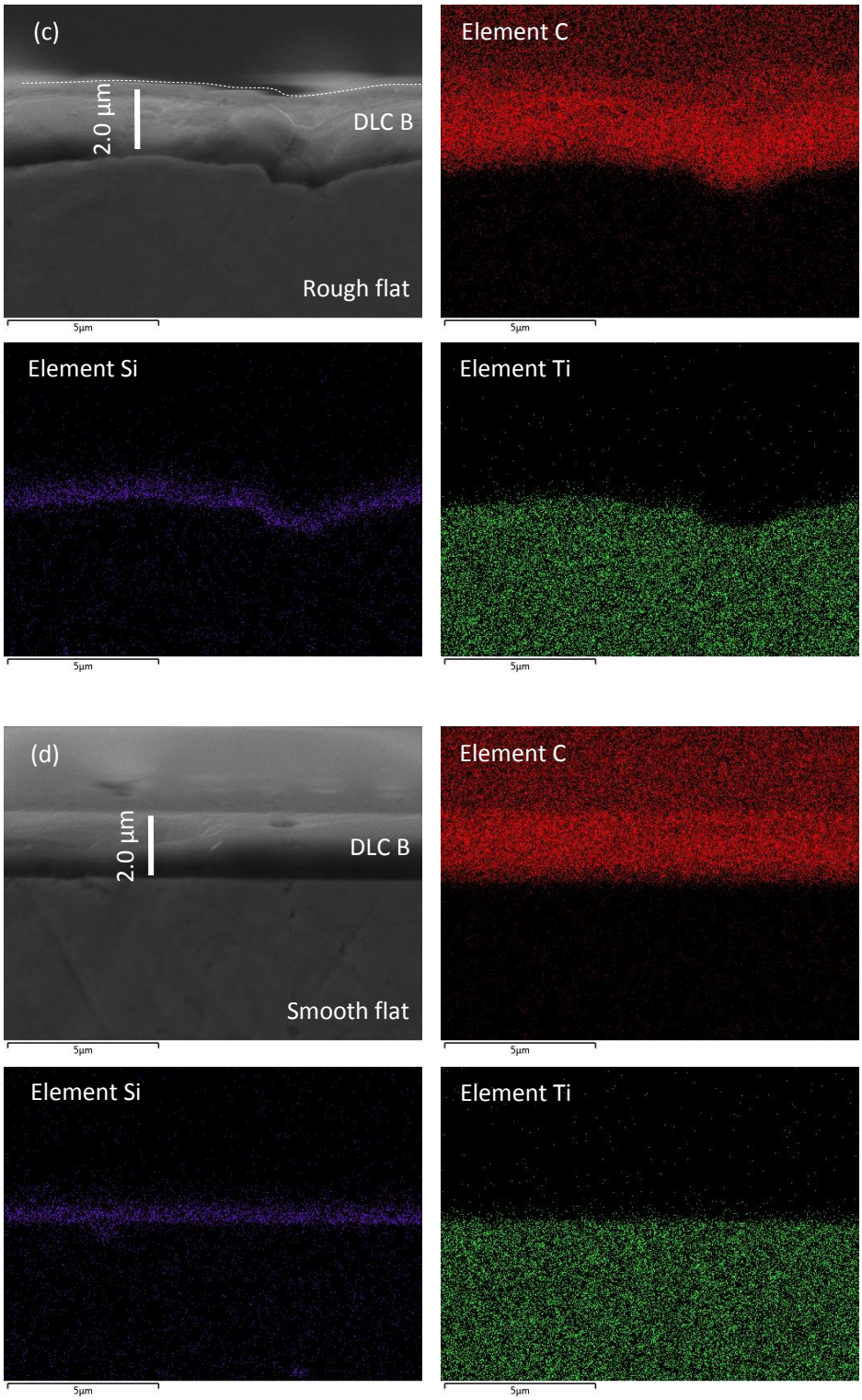

Figure II.7. SEM and EDX of cross sections of flat samples (a) rough flat with DLC A; (b) smooth flat with DLC A; (c) rough flat with DLC B; (d) smooth flat with DLC B.

2.2.3. Surface roughness of DLC coated samples

The DLC coated flat and coated cylinder surfaces were observed via digital microscope, as shown in Figure II.8, and via interferometry, as shown in Figure II.9. The sliding direction for subsequent fretting testing is exhibited on images. The relation between the sliding direction

and the roughness texture is the same in the flat–cylinder surface contact and in the real neck adapter–femoral stem contact.

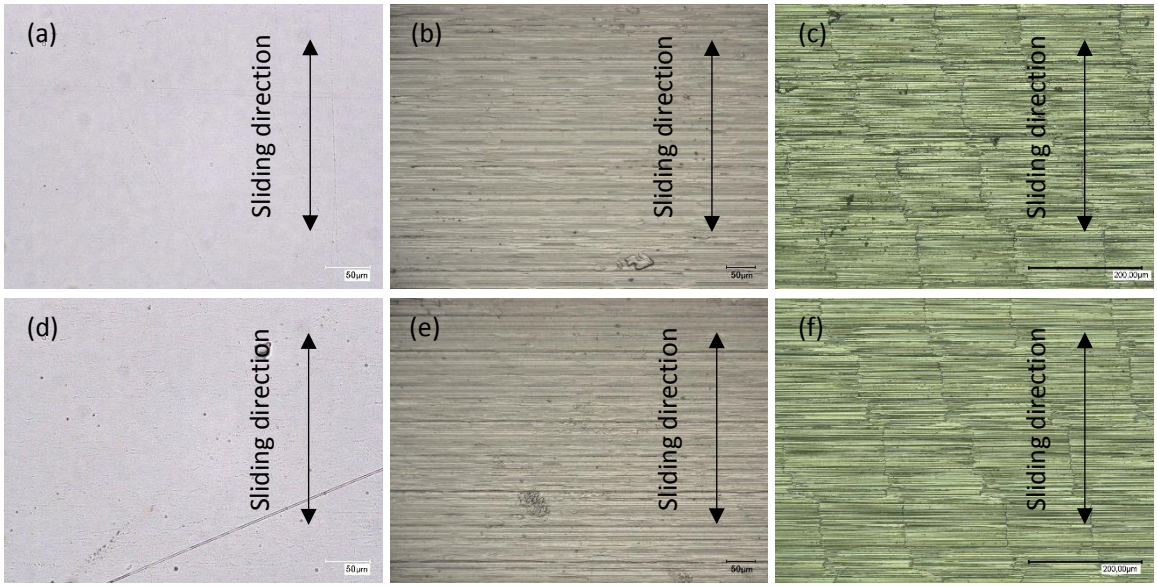

Figure II.8. Optical images of DLC coated flat and coated cylinder samples: (a) smooth flat with DLC A; (b) rough flat with DLC A; (c) cylinder with DLC A; (d) smooth flat with DLC B; (e) rough flat with DLC B; (f) cylinder with DLC B.

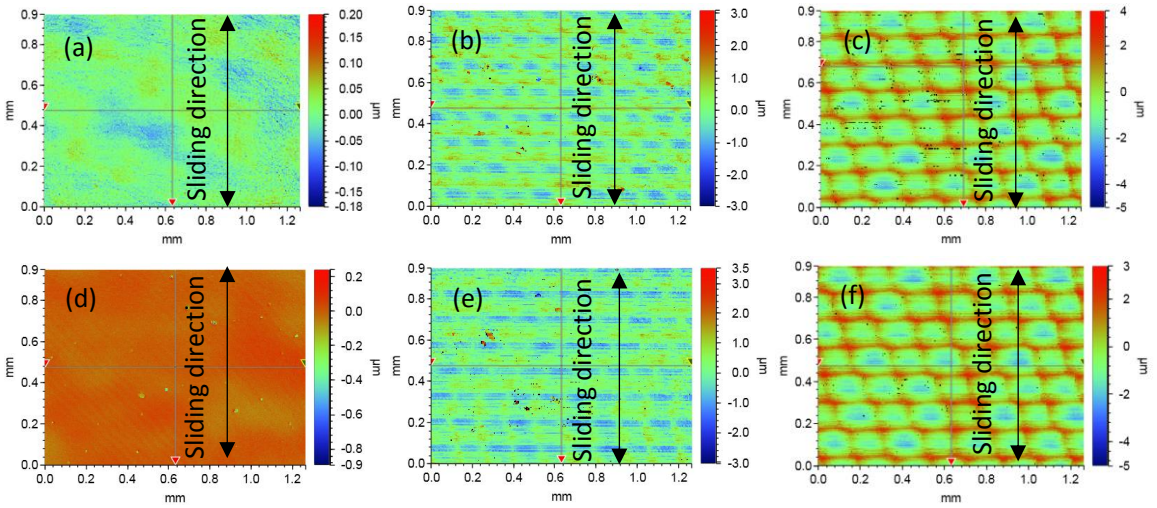

Figure II.9. 3D topography of DLC coated flat and coated cylinder samples: (a) smooth flat with DLC A; (b) rough flat with DLC A; (c) cylinder with DLC A (after removing the cylindrical shape); (d) smooth flat with DLC B; (e) rough flat with DLC B; (f) cylinder with DLC B (after removing the cylindrical shape).

The roughness parameters, arithmetical mean height (S_a), skewness (S_{sk}), and kurtosis (S_{ku}), are shown in Table II.3. The values of S_a are also shown in Figure II.10. Obviously, the deposition process has no significant influence on the surface roughness. More specifically, S_a of coated cylinder is higher than 700 nm. S_a of coated rough flat is around 400 nm. S_a of coated smooth flat is around 20 nm.

Table II.3. Surface roughness parameters of neck adapter, femoral stem, and flat and cylinder samples.

	Arithmetical mean height S_a (nm)	Skewness S_{sk}	Kurtosis S_{ku}
Neck adapter surface	340	0.085	2.67
Femoral stem inner surface	475	-0.22	2.58
Smooth flat without coating	27 ± 1	-	-
Smooth flat with DLC A	19 ± 5	-	-
Smooth flat with DLC B	18 ± 4	-	-
Rough flat without coating	394 ± 18	-0.10 ± 0.05	2.75 ± 0.13
Rough flat with DLC A	414 ± 16	-0.05 ± 0.05	3.35 ± 0.27
Rough flat with DLC B	403 ± 11	-0.11 ± 0.09	3.54 ± 0.65
Cylinder without coating	723 ± 11	0.23 ± 0.03	2.59 ± 0.04
Cylinder with DLC A	769 ± 18	0.17 ± 0.07	2.57 ± 0.01
Cylinder with DLC B	768 ± 9	0.16 ± 0.03	2.70 ± 0.19

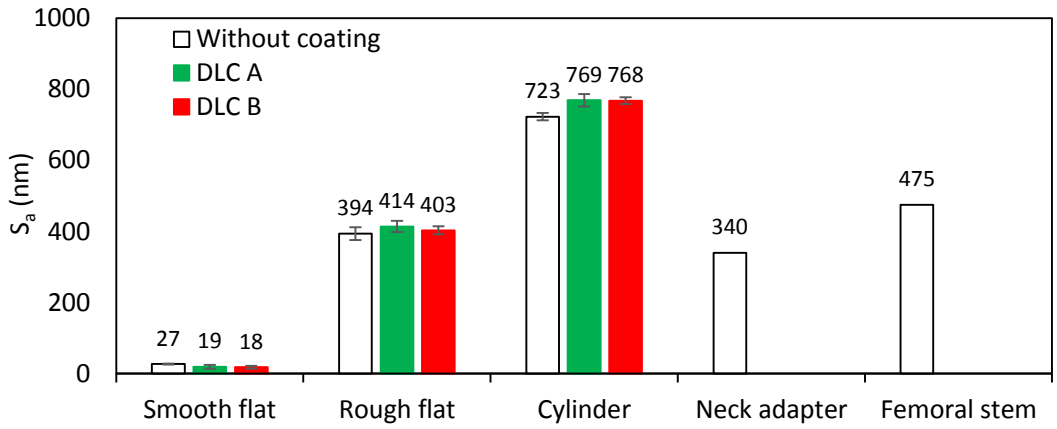

Figure II.10. Surface roughness of flat and cylinder samples, and neck adapter and femoral stem surfaces.

2.2.4. Mechanical properties of DLC coatings

Nano-indentation measurements using CSM method were conducted on DLC coatings (DLC A and DLC B) deposited on smooth flat surfaces. Results are shown in Figure II.11.

For the flat surface with DLC A coating, the hardness and the elastic modulus are higher than those of the substrate. Regarding the hardness as a function of the penetration depth, there is a short plateau between 50 and 200 nm, with an average hardness of 29.0 ± 4.5 GPa. After that, the hardness drastically drops because of the substrate effect. Regarding the elastic modulus, no plateau occurs because the substrate effect is stronger on elasticity than on hardness. The average value of the elastic modulus between 50 and 150 nm is 236 ± 24 GPa.

The DLC B coating was developed to avoid the elastic mismatch between the coating and the substrate, with the purpose of improving the cohesion at the substrate–coating interface. For the flat surface with the DLC B coating, the hardness and the elastic modulus are lower and closer to those of the substrate. The hardness between 100 and 250 nm has an average

value of 17.7 ± 1.9 GPa, and the average elastic modulus between 100 and 200 nm (with a small plateau) is 148 ± 8 GPa.

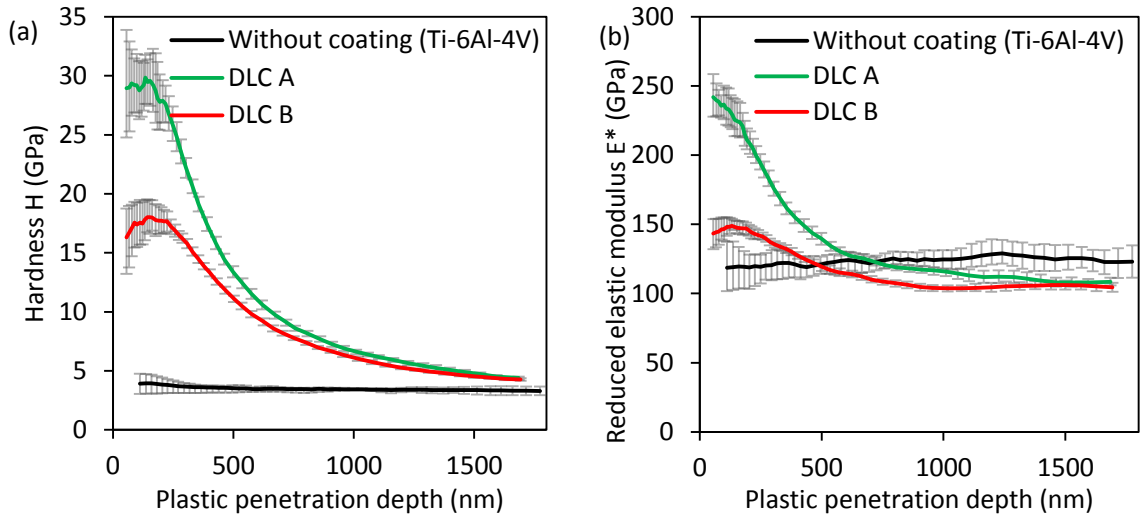

Figure II.11. (a) Nano-hardness and (b) elastic modulus of DLC coatings on smooth flats. Nano-hardness and elastic modulus of Ti–6Al–4V were measured on rough flat surface.

2.3. Summary

Flat and cylinder samples are used to simulate the real neck adapter and femoral stem component. The cylinder (S_a above 700 nm) is rougher than the rough flat (S_a around 400 nm). The rough flat is rougher than the smooth flat (S_a around 20 nm). The deposition process has no significant influence on the roughness. The thickness of DLC coatings is approximately 2 µm.

Mechanical properties of Ti–6Al–4V substrate and DLC coatings are shown in Table II.4. The hardness and elastic modulus of DLC coatings are higher than those of the Ti–6Al–4V substrate. DLC A is harder and stiffer than DLC B.

Table II.4. Mechanical properties of Ti–6Al–4V substrate and DLC coatings.

	Hardness	Elastic modulus
Uncoated	3.4 ± 0.5	122 ± 14
DLC A	29.0 ± 4.5	236 ± 24
DLC B	17.7 ± 1.9	148 ± 8

3. Fretting rig

Fretting tests were conducted using a tension-compression hydraulic machine (MTS Systems Corporation) with a cylinder-on-flat contact [51]. The schematic outline of the fretting-wear test rig is shown in Figure II.12. The flat moves up and down with a given amplitude, and rubs against the stationary cylinder under a given normal force P. The displacement of the flat increases within the first 10 cycles (which is called the ramping-in period); then, it reaches the given value and remains constant [51]. For the tests under serum

liquid conditions, a liquid system was fixed. The liquid is applied into the contact from above at a given rate, and it is collected and recycled via a pump throughout the entire test.

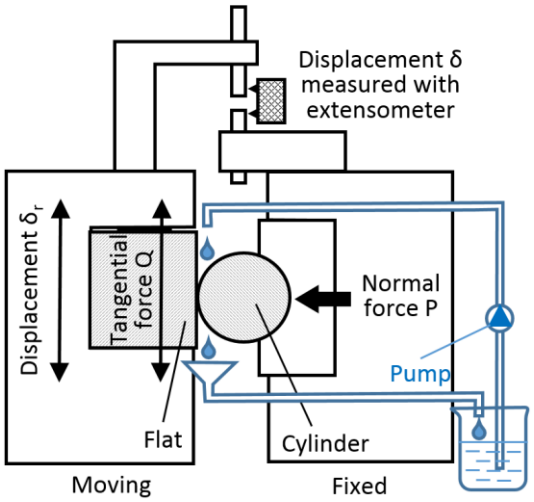

Figure II.12. Schematic outline of the fretting-wear test rig.

For pre-selected cycle numbers during a fretting test, the displacement δ, the normal force P, and the tangential force Q are measured and recorded, which enables us to plot the Q–δ fretting loop. A typical fretting loop is shown in Figure II.13. Because of the finite rigidity of the test device and the elastic deformation of samples, the real displacement in the contact, δ_0, is smaller than the imposed displacement, δ^* [51].

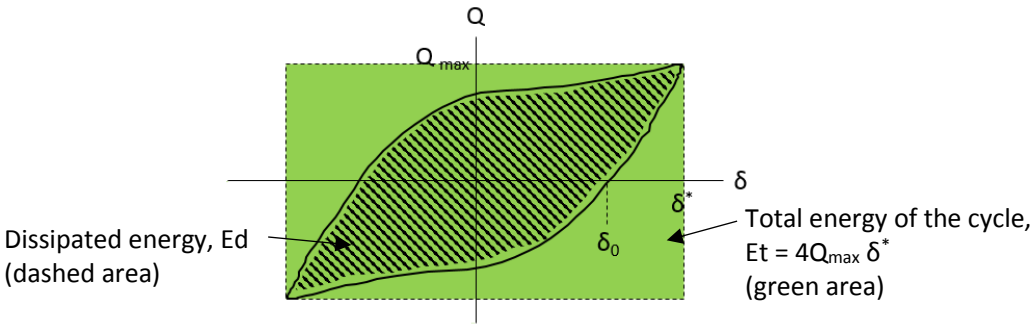

Figure II.13. Typical fretting loop.

4. Test conditions

- **Contact geometry**

The flat sample represents the neck adapter surface, and the cylinder sample represents the femoral stem inner surface. The contact geometry of the flat and cylinder samples is shown in Figure II.14. The diameter of the cylinder is 20 mm, and the contact width is 5 mm.

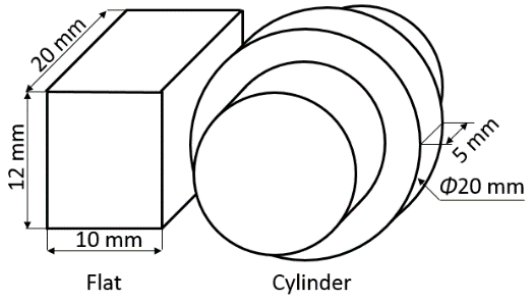

Figure II.14. Geometry of flat and the cylinder samples.

- **Normal force (contact pressure)**

According to the load situations at the neck adapter and femoral stem interface discussed in the bibliography, different values of initial maximum contact pressure (regardless of surface roughness) between 280 MPa and 690 MPa were adopted. Since the input value into the fretting rig is normal force, it was calculated using Hertz's theory. Normal forces between 200 N and 1 200 N were applied. The calculations can be found in Appendix A.

- **Displacement amplitude**

According to bibliography, the relative movements between the neck adapter and femoral stem are generally in the range between 3 µm and 41 µm [4]. In this study, three different displacement amplitudes between the flat and cylinder were adopted: ±20 µm, ±40 µm and ±70 µm.

- **Frequency**

Besides the fact that the average frequency of human walking is around 1 Hz, in this study, the frequency was fixed at 5 Hz, to achieve a large number of cycles in a relatively short test time period.

- **Number of cycles**

For most tests, the number of cycles was 100 000 cycles. In some particular cases, which are relative to the investigation on the origin of low friction of DLC coating, tests with smaller numbers of cycles were conducted: 0 cycle (contact with no sliding), 1 cycle, 20 cycles, 40 cycles, and 100 cycles.

Before testing, both the flat and the cylinder samples were ultrasonically cleaned in acetone, and the contact surfaces were cleaned with ethanol immediately before contact.

- **Surface roughness**

In this study, the influence of surface roughness on the fretting behaviors of Ti–6Al–4V and DLC coatings was investigated. Four configurations of tests were then conducted:

(1) Uncoated rough flat / uncoated rough cylinder contact;
(2) Uncoated smooth flat / uncoated rough cylinder contact;
(3) DLC coated rough flat / uncoated rough cylinder contact;
(4) DLC coated smooth flat / uncoated rough cylinder contact.

- **Coating position**

In this study, the influence of substrate curvature (flat substrate and cylindrical substrate) was investigated, and the tribological performance of DLC coating on one of the contact surfaces was compared with that of the coating on both the contact surfaces. Four configurations of fretting tests were then conducted:

(1) Uncoated rough flat / uncoated rough cylinder contact (i.e., without DLC coating);
(2) DLC coated rough flat / uncoated rough cylinder contact (i.e., DLC coating on the flat surface);
(3) Uncoated rough flat / DLC coated rough cylinder contact (i.e., DLC coating on the cylindrical surface);
(4) DLC coated rough flat / DLC coated rough cylinder contact (i.e., DLC coating on both the contact surfaces).

- **Environment**

The influence of serum on the fretting behaviors of Ti–6Al–4V and the DLC coating was investigated. Four configurations of fretting tests were then conducted:

(1) Uncoated rough flat / uncoated rough cylinder contact (i.e., Ti–6Al–4V / Ti–6Al–4V) under laboratory air condition;
(2) Uncoated rough flat / uncoated rough cylinder contact (i.e., Ti–6Al–4V / Ti–6Al–4V) under serum condition;
(3) DLC coated rough flat / uncoated rough cylinder contact (i.e., DLC coating / Ti–6Al–4V) under laboratory air condition;
(4) DLC coated rough flat / uncoated rough cylinder contact (i.e., DLC coating / Ti–6Al–4V) under serum condition.

Regarding the laboratory air condition, humidity and temperature cannot be controlled, but were recorded and ranged from 18°C to 23°C and 30 % to 50 %, respectively. Regarding the serum condition, the liquid was composed of half new born calf serum (Newborn calf serum N4637–Sigma-Aldrich) and half distilled water. The liquid was applied into the flat and cylinder contact at a rate of 2 drops per second.

5. Analysis methods

After testing, flat and cylinder surfaces were examined with various methods, including a 2D contact profilometer, an optical interferometer, a digital microscope, a SEM, a nano-indenter, a compression system of micro pillar, etc.

Then the flat samples were cut parallel to the sliding direction. The cross sections were grounded to 4000 grit and polished to 1-µm diamond, and then etched using the Keller's reagent (190 ml distilled water + 5 ml nitric acid + 3 ml hydrochloric acid + 2 ml hydrofluoric acid), for further observation.

Wear debris was collected for SEM observations.

5.1. 2D contact profilometer

A 2D contact profilometer (Surfascan, Somicronic^{TM}) was used to measure the wear profiles and then to calculate the wear volume. On each wear scar, 10 profiles were measured in the direction of sliding, and the interval between neighboring profiles was 0.5 mm. Then the wear volume was calculated according to the profiles and the flat / cylinder contact width. The details of calculation process can be found in Appendix B.

For some fretting tests, especially in the cases of Ti–6Al–4V / Ti–6Al–4V contact under the laboratory air condition, the material was easily transferred from one surface to the countersurface, which might lead to a negative value in the wear volume of one sample. Therefore, the total wear volume, i.e. the sum of the wear volumes of the flat and the cylinder, was used to evaluate the anti-wear properties of the contact.

5.2. Optical interferometer

An interferometer (Bruker, GT-K1) was used to obtain the 3D topography of samples, and to calculate the initial surface roughness parameters, including the roughness (S_a), the skewness (S_{sk}), and the kurtosis (S_{ku}). When measuring the surface roughness, at least three different locations were observed on each sample.

5.3. Digital microscope

A digital microscope (Keyence^{TM}, VHX-1000) was used to observe in large scale the wear scars and to measure the width and length of the wear scar. It was also used to observe the cross sections of the flat samples.

5.4. SEM

SEM (Tescan MIRA3 SEM) and EDX (OXFORD), were used to observe and analyze the wear scars, the wear debris, and the cross sections. On the cross sections (of flat samples), we could observe the cracks on the subsurface, the transformed structure of substrate, the coating thickness, and the thickness of the tribofilm formed on the Ti–6Al–4V surface. Generally, an angle of around 6° or 12° was adopted for the SEM observation on cross sections, as shown in Figure II.15.

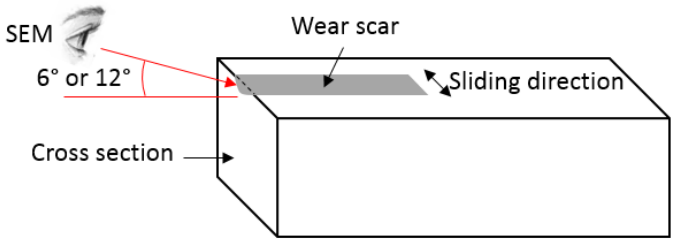

Figure II.15. Angles for SEM observation on cross section.

5.5. Nano-indenter

Nano-indentation tests were performed to measure the mechanical properties of surfaces, using the CSM method with a nano-indenter (Nano Indenter XP, MTS) equipped with a Berkovich diamond tip (a three-side pyramid tip with a half angle of 65.27°, measured from the axis to one of the pyramid flats). During CSM, a small displacement oscillation (1 nm) at a given frequency during the indentation test (32 Hz) was superimposed upon the indentation motion. This led to a succession of micro-loading-unloading segments, which allow the measurement of the stiffness of the contact (loading involves elastic and plastic deformation, while unloading involves only elastic deformation, and thus allows to compute stiffness). Therefore, the hardness, H, and the reduced elastic modulus, E^*, can be calculated. A continuous hardness and a continuous reduced elastic modulus are obtained along the penetration depth.

The indentation was repeated at least nine times at different positions on one sample. The load F was applied exponentially as a function of time, and the ratio F'/F was 0.03 s^{-1}. On the DLC coated samples, the maximal indentation load was 450 mN. On the Ti–6Al–4V substrate, two values of maximal indentation load were adopted: 100 mN and 450 mN. On the tribofilm formed on Ti–6Al–4V surface, the maximal indentation load was 100 mN.

5.6. Compression system of micro-pillar

The compression of micro-pillar in situ inside a SEM has been a favored technique. This is for two reasons: (1) the pillar shape yields a nearly uniaxial stress state for relatively straightforward stress-strain analysis; and (2) the compression allows to directly observe the deformation of pillar using the SEM for better understanding of the deformation mechanisms during the entire compression process [214, 215].

- **Preparation of micro-pillar**

Micro-pillars were prepared using a FIB on the tribofilm formed on the Ti–6A–4V rubbed surface, and also on the Ti–6Al–4V substrate surface. Pillars were machined using a gallium ion source in FEI Helios NanoLab™ DualBeam™ microscope. Several milling steps were conducted: from 21 nA to 80 pA at 30 kV to obtain clean and homogeneous pillar surfaces. Two pillar geometries were achieved: (1) smaller pillars: diameter ≈ 1.3 µm, height ≈ 2.0 µm, and tapering angle ≈ 4°; (2) larger pillars: diameter ≈ 4.0 µm, height ≈ 7.0 µm, and tapering angle ≈ 4°. Figure II.16 shows the geometry of the small micro-pillar milled on the tribofilm surface.

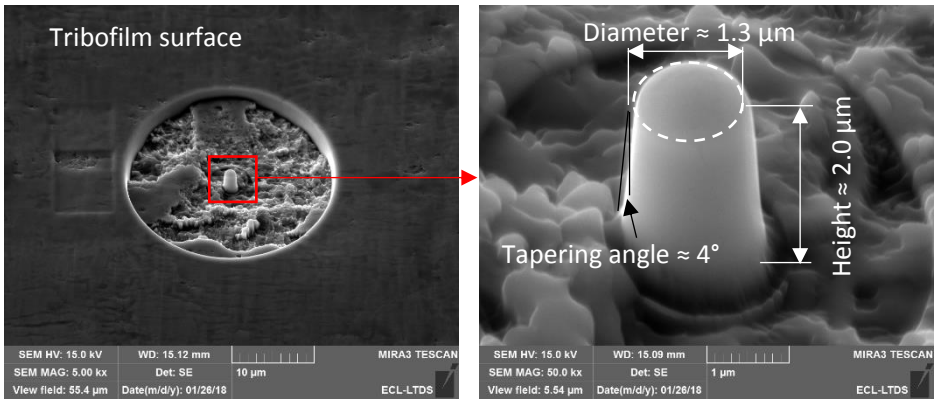

Figure II.16. Geometry of small micro-pillar on tribofilm surface.

- **Compression of micro-pillar**

Micro-pillars were compressed using a standard Alemnis SEM indenter [216, 217]. The micro-compression tests were in situ inside the SEM using a 10 µm flat punch made of diamond. The speed of the indenter was 0.014 µm/s. During compression, the compression force and the displacement were recorded. The displacement of the pillar was corrected from thermal drift and sample, tip, and frame compliance, the correction process is shown in Appendix C. Then the force–displacement curves were obtained.

The stress was calculated by dividing the load by the pillar upper surface area before compression. The strain was calculated by dividing the displacement by the tip height before compression [215]. Thus, the stress–strain curves were obtained.

6. Conclusions

In this chapter, experimental materials, test rig, test parameters, and analysis methods are presented.

To study the effects of surface roughness, coating positions and environment on the fretting behaviors of Ti–6Al–4V and the DLC coatings, 11 groups of fretting tests were conducted, as shown in Table II.5. For each group, three displacement amplitudes (±20, ±40, and ±70 µm) associated with different normal forces (between 200 and 1 200 N, leading to initial maximum contact pressures between 280 and 690 MPa), were applied. The displacement frequency was 5 Hz. The number of cycles for the tests was 100 000.

Table II.5. Tests parameters.

Group	Flat		Cylinder	Environment
	Roughness	Coating	Coating	
1	Rough	No	No	Dry
2	Smooth	No	No	Dry
3	Rough	DLC A	No	Dry
4	Rough	DLC B	No	Dry
5	Smooth	DLC A	No	Dry
6	Smooth	DLC B	No	Dry
7	Rough	No	DLC A	Dry
8	Rough	No	DLC B	Dry
9	Rough	DLC A	DLC A	Dry
10	Smooth	No	No	Serum
11	Smooth	DLC A	No	Serum

To investigate the origin of low friction of DLC coating, the evolution of contact surfaces was studied through observing the wear scars at different numbers of cycles. Therefore, tests with different cycle numbers were carried out, as shown in Table II.6.

Table II.6. Tests parameters with different numbers of cycles.

Group	Flat	Cylinder	Environment	Displacement	Normal force	Number of cycles
1	DLC coated rough flat	Uncoated cylinder	Dry	±20 µm	250 N	0, 1, 20, 40, 100, 100 000
2	DLC coated smooth flat	Uncoated cylinder	Dry	±20 µm	250 N	0, 1, 100, 100 000

CHAPTER III

EFFECT OF SURFACE ROUGHNESS ON FRETTING BEHAVIOR OF Ti–6Al–4V / Ti–6Al–4V CONTACT

CHAPTER III: EFFECT OF SURFACE ROUGHNESS ON FRETTING BEHAVIOR OF Ti–6Al–4V / Ti–6Al–4V CONTACT

CHAPTER III: EFFECT OF SURFACE ROUGHNESS ON FRETTING BEHAVIOR OF Ti–6Al–4V / Ti–6Al–4V CONTACT

This chapter investigates the effect of surface roughness on the fretting behavior of Ti–6Al–4V / Ti–6Al–4V contact under laboratory air condition. The results will serve as baselines for the study of the effect of DLC coating in next chapters.

1. Introduction

In this chapter, the fretting behavior of Ti–6Al–4V / Ti–6Al–4V contact under laboratory air condition is investigated. The results will serve as baselines for the study of the effect of DLC coating in next chapters. Furthermore, the initial surface roughness is an important parameter that might influence the tribological performance of surfaces in contact [199]. Therefore, the effect of initial surface roughness on the fretting behavior of Ti–6Al–4V / Ti–6Al–4V contact is investigated in this chapter.

To investigate the influence of roughness, both smooth and rough surfaced Ti–6Al–4V flat samples were used. Tests were conducted with the Ti–6Al–4V flat / Ti–6Al–4V cylinder contact under various values of displacement amplitude (±20, ±40, and ±70 µm) and normal force (250–1 000 N) condition. The number of cycles for each test was 100 000 cycles. Running condition fretting maps (RCFMs) were drawn according to analysis of fretting logs. Friction coefficient and wear volume were obtained. Wear scars, cross sections of flat samples, and wear debris were observed and analysed.

2. Tribological behaviors: presentation of results

2.1. RCFM

The fretting condition of a certain fretting cycle is determined by the shape of fretting loop, Q–δ loop or Q/P–δ loop. Energy ratio A is defined as the ratio between the dissipated energy (Ed) and the total energy of the cycle ($Et = 4Q_{max}\delta^*$), as shown in Figure II.12. When the fretting loop has a quadrangle shape, the energy ratio A has a high value, and the fretting cycle is under the gross slip condition. When the fretting loop has an elliptic shape, the energy ratio A has a low value, and the fretting cycle is under the partial slip condition.

The fretting regime of a test is determined by the fretting log (i.e., evolution of fretting loops with test time), which describes directly the evolution of the fretting condition during the whole test. The partial slip regime (PSR) is defined if the partial slip condition remains during the entire test. The gross slip regime (GSR) is defined in cases where the gross slip condition remains during the entire test. The mixed slip regime (MSR) is the state in which both the partial and the gross slip conditions exist in one test.

The displacement, normal force, and the surface roughness have influence on the fretting regime.

- **Rough flat surface**

For the fretting test on the rough flat under the largest displacement amplitude of ±70 µm and the lowest normal force of 250 N, the fretting log, the representative fretting loops, and the evolution of the energy ratio A are shown in Figure III.1. At the first 10 cycles, a ramping-in period occurs where the displacement of the test machine increases; after that, the displacement remains constant with the given value, which is ±70 µm in this case. The first cycle recorded after the ramping-in period is at 19 cycles. It is clear from Figure III.1a that at the beginning of the test (19 cycles), the fretting loop has a quadrangle shape. The corresponding energy ratio A is high (around 0.89, shown in Figure III.1c). With the test ongoing, the fretting loop at 199 cycles still has a quadrangle shape but with a tip (Figure III.1a), thus the energy ratio A has a slight decrease (around 0.61). After that, the energy ratio A shows a slight increase and then remains stable until the end of the test. At 9 999 cycles, the fretting loop has a quadrangle shape and the energy ratio A is around 0.70. According to the fretting log, the fretting test remains in the gross slip condition during the test; thus, the test is in the GSR.

This behavior is typical for Ti–6Al–4V / Ti–6Al–4V contacts in the GSR under fretting condition [50, 217].

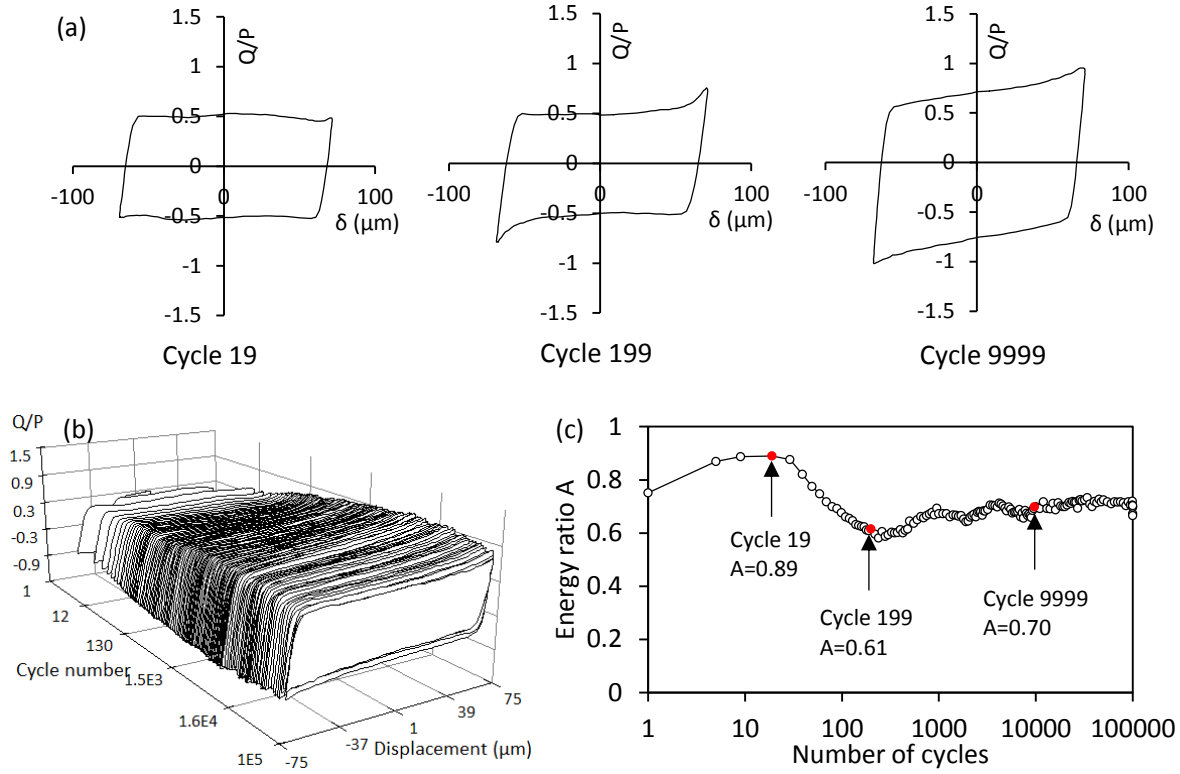

Figure III.1. Fretting test on rough flat under the large displacement amplitude of ±70 μm and the low normal force of 250 N: (a) representative fretting loops; (b) fretting log and (c) evolution of energy ratio A.

With the smallest displacement amplitude of ±20 μm and a higher normal force of 600 N, at the beginning of the test (19 cycles), the fretting loop has a quadrangle shape, as shown in Figure III.2a. The corresponding energy ratio A is high (around 0.61, as shown in Figure III.2c). The fretting cycle is under the gross slip condition. At 49 cycles, the fretting loop changes to an elliptic shape. The energy ratio A is low (around 0.23). The fretting cycle is under the partial slip condition. After that, the fretting loop changes to quadrangle with a high energy ratio A (around 0.71). This fretting cycle is under the gross slip condition. It is clear from Figure III.2 that, before around 4 000 cycles, both the partial and gross slip condition exist. After that, the fretting test remains stable under the partial slip condition. At 9 999 cycles (i.e. stable period), the fretting loop is elliptic, and the energy ratio A is around 0.30. According to the fretting log (Figure III.2b), the fretting test is under the MSR.

In addition, for the cycles under partial slip condition (such as cycle 49), the contact surfaces stick to each other. Because the frame and the samples were not absolutely rigid, the sudden release of the stuck surfaces might lead to a flowing fretting cycle with a larger displacement amplitude than the set value, such as the cycle 69 under the gross slip condition.

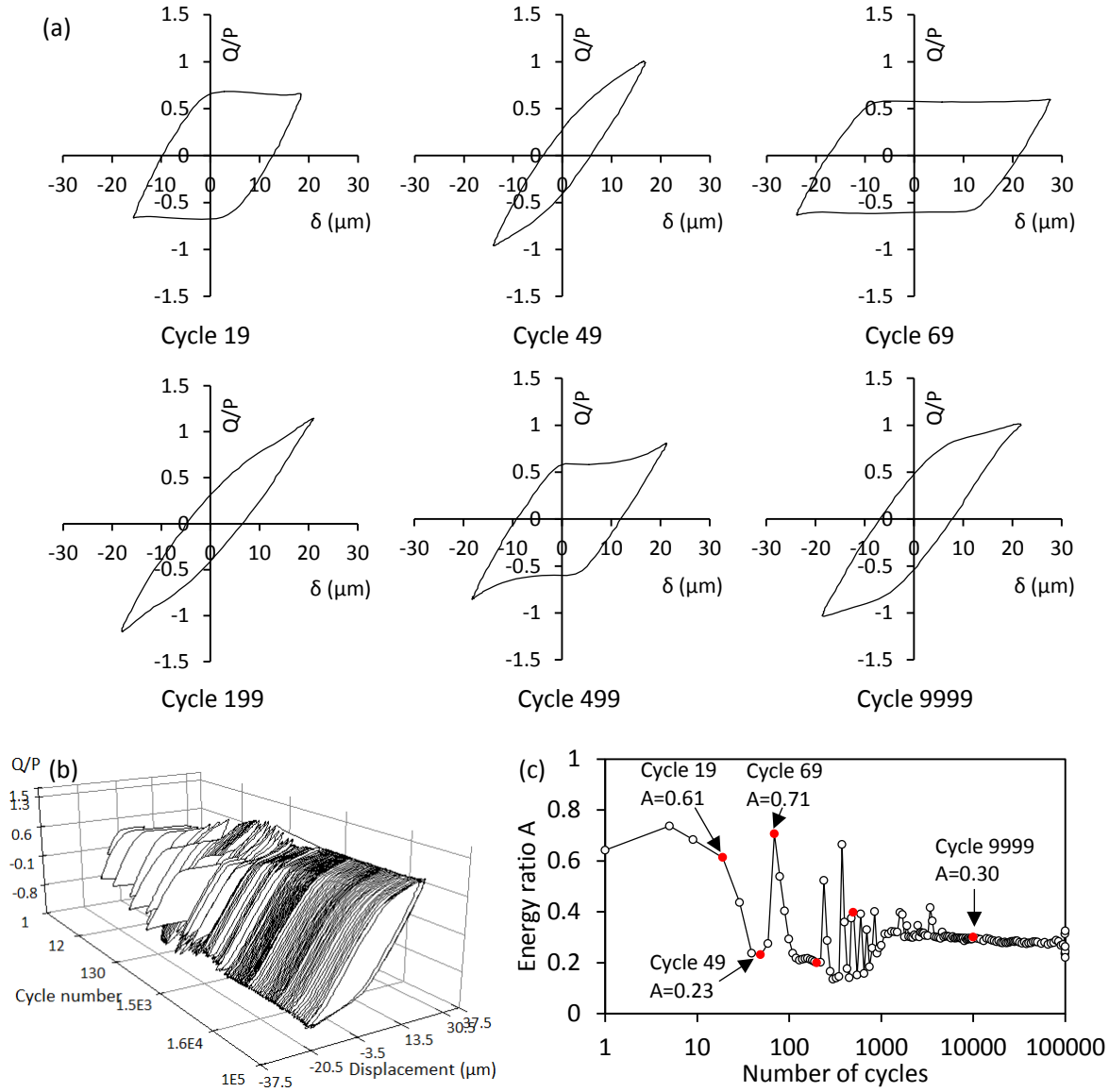

Figure III.2. Fretting test on rough flat under the small displacement amplitude of ±20 μm and the high normal force of 600 N: (a) representative fretting loops; (b) fretting log and (c) evolution of energy ratio A.

When the normal force keeps on increasing to the highest value of 1 000 N, the fretting loops are elliptic during the entire test. The energy ratio shows a slightly decrease from 0.20 at 19 cycles to 0.15 at 199 cycles and to 0.11 at 9 999 cycles. The test is in the PSR. The fretting log, representative fretting loops and the evolution of energy ratio A are shown in Figure III.3.

This behavior is typical for Ti–6Al–4V / Ti–6Al–4V contacts in the PSR under fretting condition [50, 218].

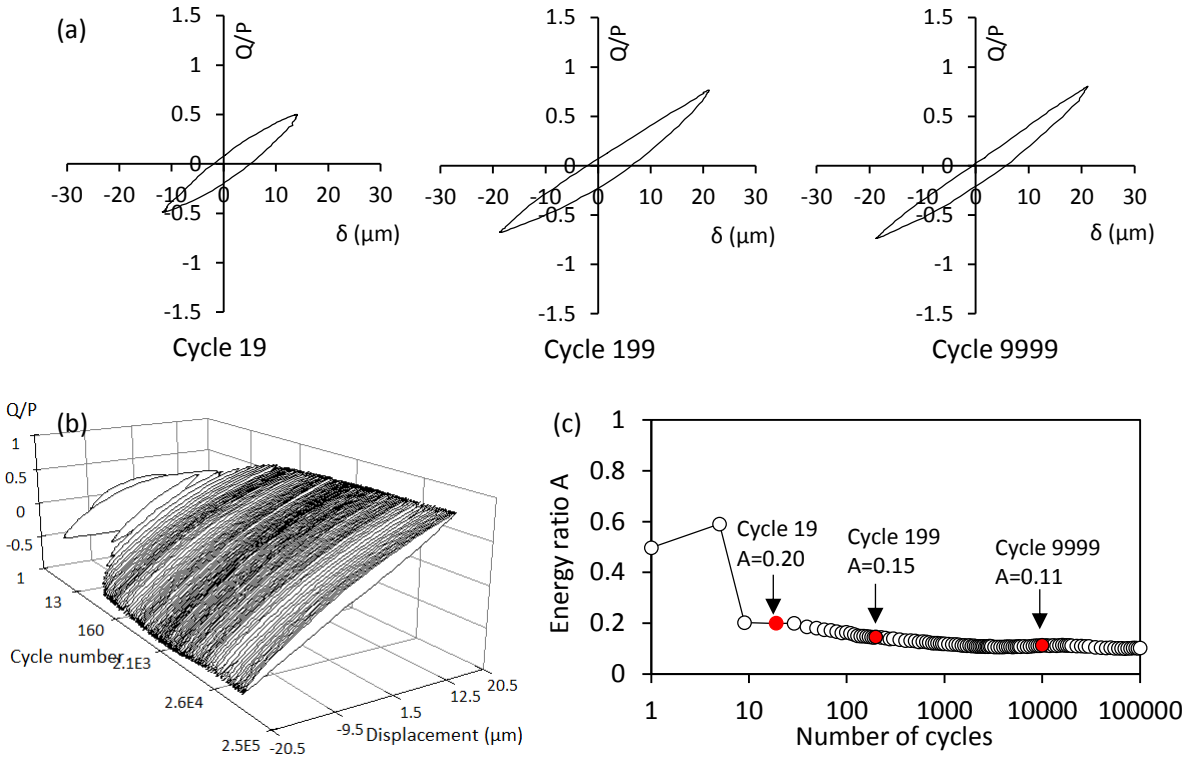

Figure III.3. Fretting test on rough flat under the smallest displacement amplitude of ±20 μm and the highest normal force of 1 000 N: (a) representative fretting loops; (b) fretting log and (c) evolution of energy ratio A.

RCFM was drawn according to fretting tests with different displacement amplitudes and normal forces. The RCFM for the tests on the rough flat is shown in Figure III.4. The values of A represent the average values of energy ratio during the entire test. As may be observed, the RCFM for tests on the rough flat samples is divided into GSR, MSR, and PSR. Furthermore, with the decrease in the displacement amplitude and the increase in the normal force, energy ratio A declines and the fretting regime changes from the GSR to the MSR and even to the PSR.

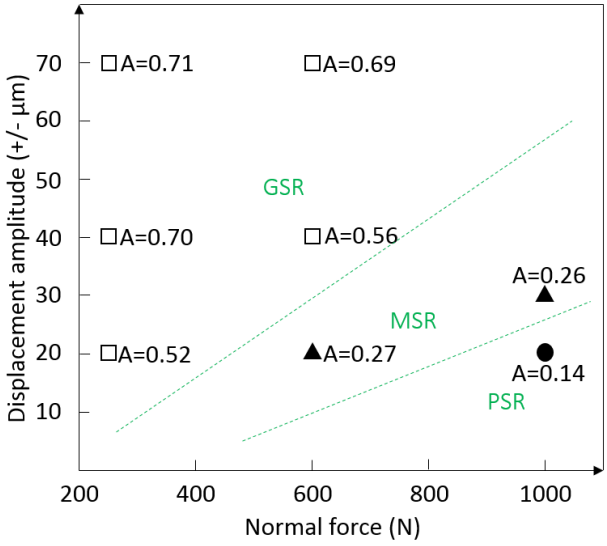

Figure III.4. RCFM on the rough flat sample. The A values represent the average values of energy ratio during the entire test.

- **Smooth flat surface**

The RCFM for the tests on the smooth flat surface is shown in Figure III.5. It is divided into GSR and MSR under the given test conditions (displacement amplitude between ±20 µm and ±70 µm, normal force between 250 N and 1 000 N, respectively).

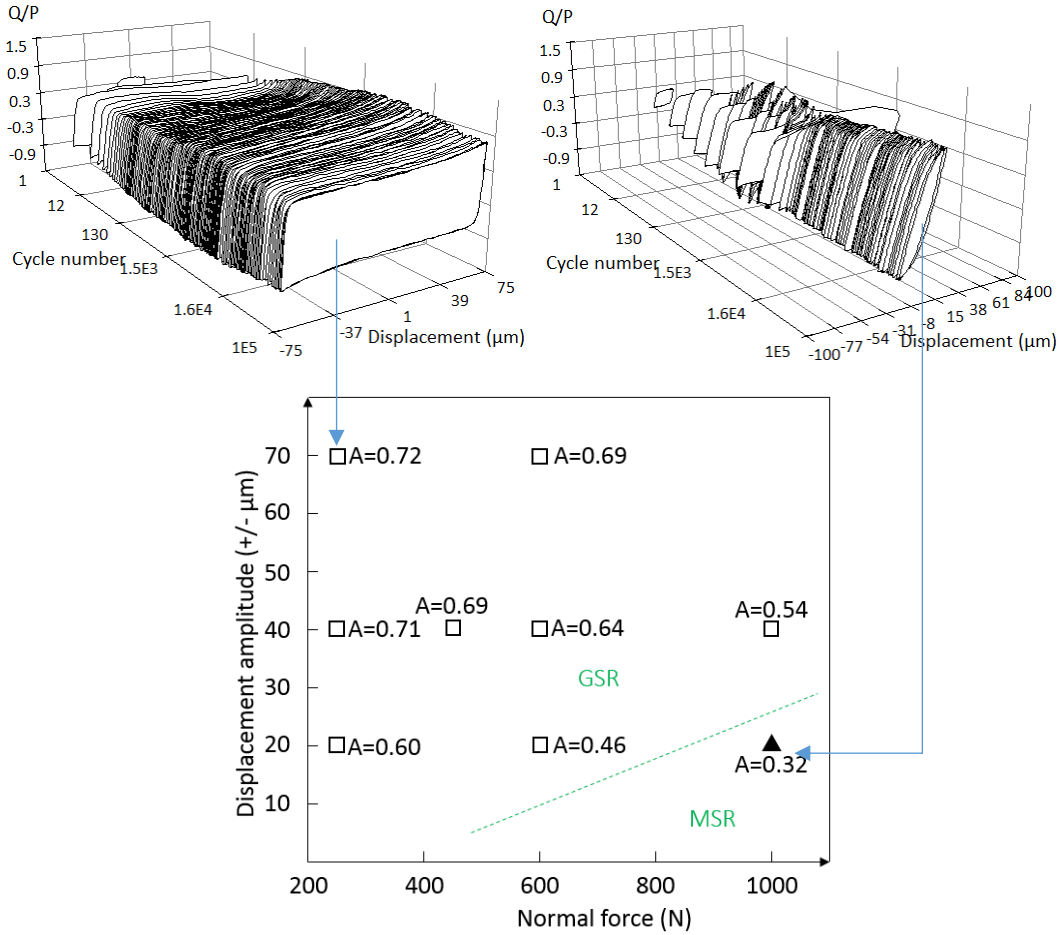

Figure III.5. RCFM on the smooth flat sample. The A values represent the average values of energy ratio during the entire test.

The roughness has an influence on the RCFM. Under the small displacement and high normal force conditions, where the values of energy ratio A were relatively low, the values of energy ratio A from tests on smooth flat samples were higher than those on rough flat samples. The difference was not obvious under large displacement and low normal force conditions, where the values of energy ratio A are relatively high. For example, under conditions of ±20 µm and 1 000 N, energy ratio A has a value of approximately 0.14 for the test on the rough flat sample (PSR), whereas it receives an obviously higher value, namely 0.32, for the test on the smooth flat sample (MSR). Under conditions of ±70 µm and 250 N, energy ratio A has a similar high value for both tests on rough (A = 0.71, GSR) and on smooth (A = 0.72, GSR) flat samples. As a result, for tests on smooth flat specimens, the GSR extends to the smaller displacement and higher normal force conditions; the PSR becomes eliminated under the given test conditions.

In addition, the fretting condition for a certain fretting cycle (gross slip condition or partial slip condition) is determined by the shape of the fretting loop. The fretting logs and the average values of energy ratio A are shown in Figure III.6.

It is clear that with the increase in the energy ratio A (average value during the stable period of the test), the slip regime changes from PSR to MSR, then to GSR. In the PSR, where the energy ratio A is lower than around 0.2, the fretting loop is stable and remains an elliptic shape during the entire test. In the GSR, where the energy ratio A is higher than around 0.4, the fretting loop is stable and remains a quadrangular shape during the entire test. In the MSR, where the energy ratio A is around 0.3, the fretting log is unstable at the beginning of the test and then reaches a stable state. In the unstable period, the fretting log consists of certain quadrangular loops among elliptic loops. In the stable period, the fretting loop remains an elliptic shape (with the energy ratio A near 0.3). Therefore, for the Ti–6Al–4V cylinder / Ti–6Al–4V flat contact in this thesis, the energy ratio of 0.3 can be regarded as the transition between the partial slip condition (i.e., elliptic loop) and the gross slip condition (i.e., quadrangular loop). This result is different with the previous work [41] stating that the energy ratio of 0.2 was regarded as the transition between the partial slip condition and the gross slip condition for the elastic ball-on-flat contact. The difference is probably because of the variation in the material properties (including plasticity) and in the contact configuration.

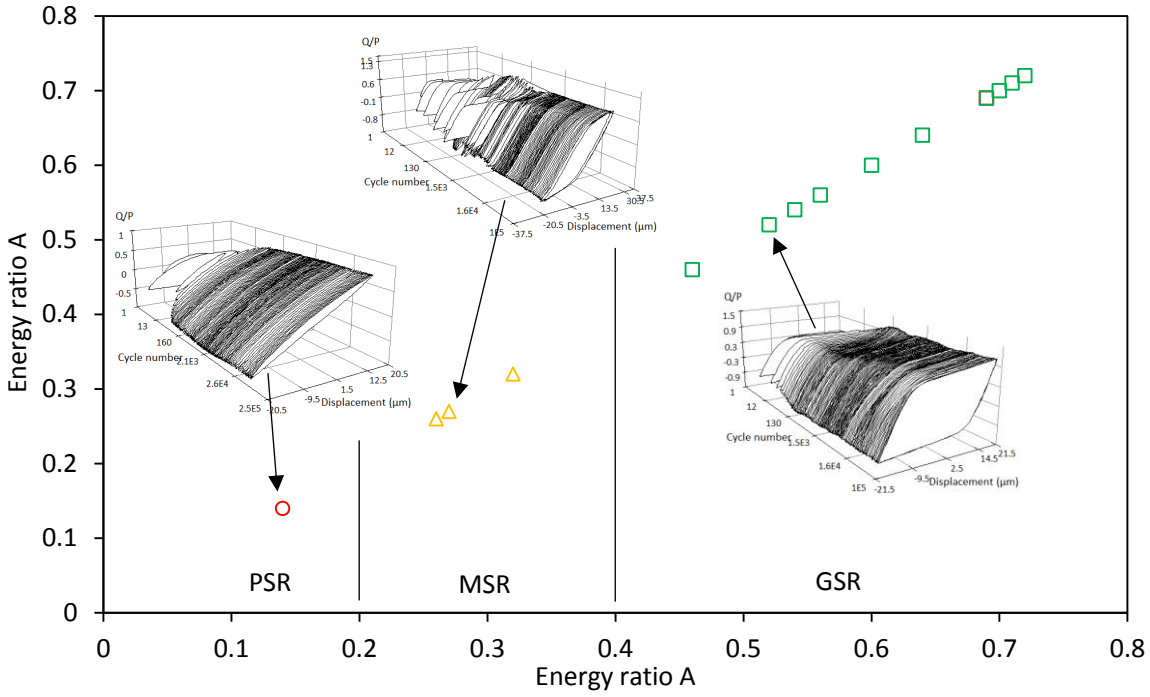

Figure III.6. Fretting logs and values of energy ratio A. The values of A are the average values during the stable period.

2.2. Friction coefficient

The Q_{max}/P ratio can be used to describe the friction response during the test. Q_{max} is the maximum tangential force during a given cycle (shown in Figure II.12) and P is the

corresponding normal force. The Q_{max}/P ratio is the classic coefficient of friction in the case of a gross slip condition; it can be regarded as a coefficient of tangential force in other cases [50]. Figure III.7 shows the evolution of Q_{max}/P for the rough flat surface under the displacement amplitude of ±20 µm with various normal forces. As may be observed, Q_{max}/P increases rapidly at the beginning of the test (for approximately 100 cycles), which is referred to as the running-in period, and then reaches a steady state until the end of the test. The ramping-in of the test rig (approximately 10 cycles) is within the running-in period. Furthermore, for the test in the MSR (displacement amplitude and normal force conditions of ±20 µm and 600 N, respectively), there is a fluctuation period prior to reaching a steady state.

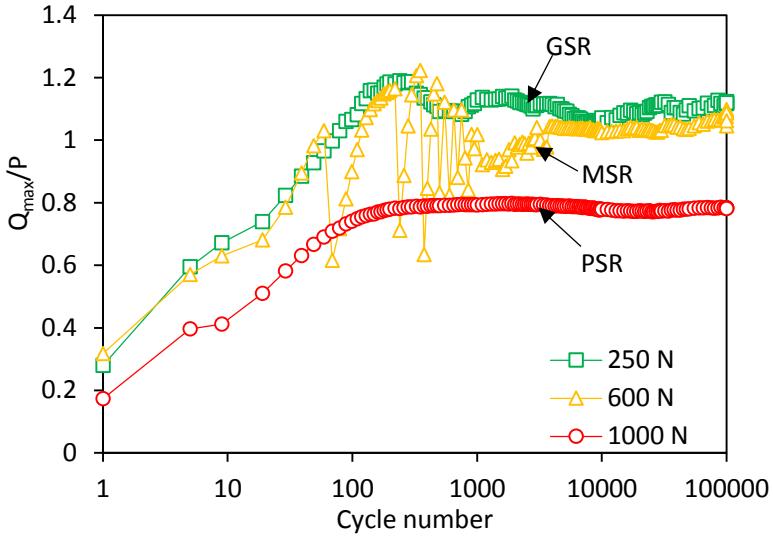

Figure III.7. The evolution of Q_{max}/P as a function of the number of cycles (logarithmic scale) for a rough flat sample, for a displacement amplitude of ±20 µm.

The average values of Q_{max}/P from 50 000 cycles until the end of the test (i.e., during stable friction) are shown in Figure III.8. It is clear that, in the GSR, the average values of Q_{max}/P are high and in the range between 0.8 and 1.2. This confirms previously obtained results [50, 51]. The roughness has no obvious influence on the values of the Q_{max}/P ratio.

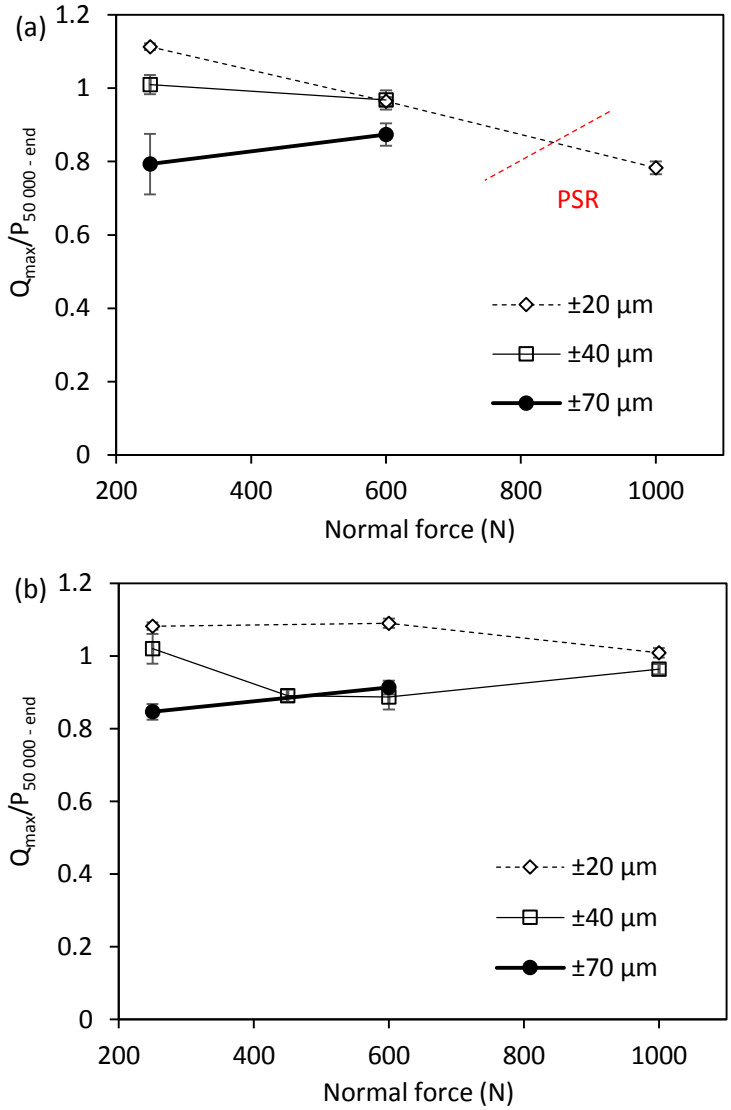

Figure III.8. Average values of Q_{max}/P from 50 000 cycles to the end of the test: (a) rough flat; (b) smooth flat.

2.3. Wear volume

Figure III.9 shows the total wear volumes (the sum of the wear volumes of the flat and the cylinder). In the PSR and the MSR, the wear volume is very low, approaching 0, i.e., the wear volume is not significantly measurable. In the GSR, the displacement has a great effect on the wear volume. With the increase in the displacement, the wear volume increases drastically. The normal force has a different effect on the wear volume, depending on the displacement conditions. With the increase in the normal force, the wear volume grows significantly under a large displacement amplitude of ±70 µm. Under the displacement amplitude of ±40 µm, no obvious change occurs because as the normal force increases under the displacement amplitude of ±40 µm, energy ratio A decreases, which may influence the wear volume. Under the small displacement amplitude of ±20 µm, the wear volumes always

remain very low, which are close to 0. Furthermore, the roughness presents no obvious influence on the wear volume.

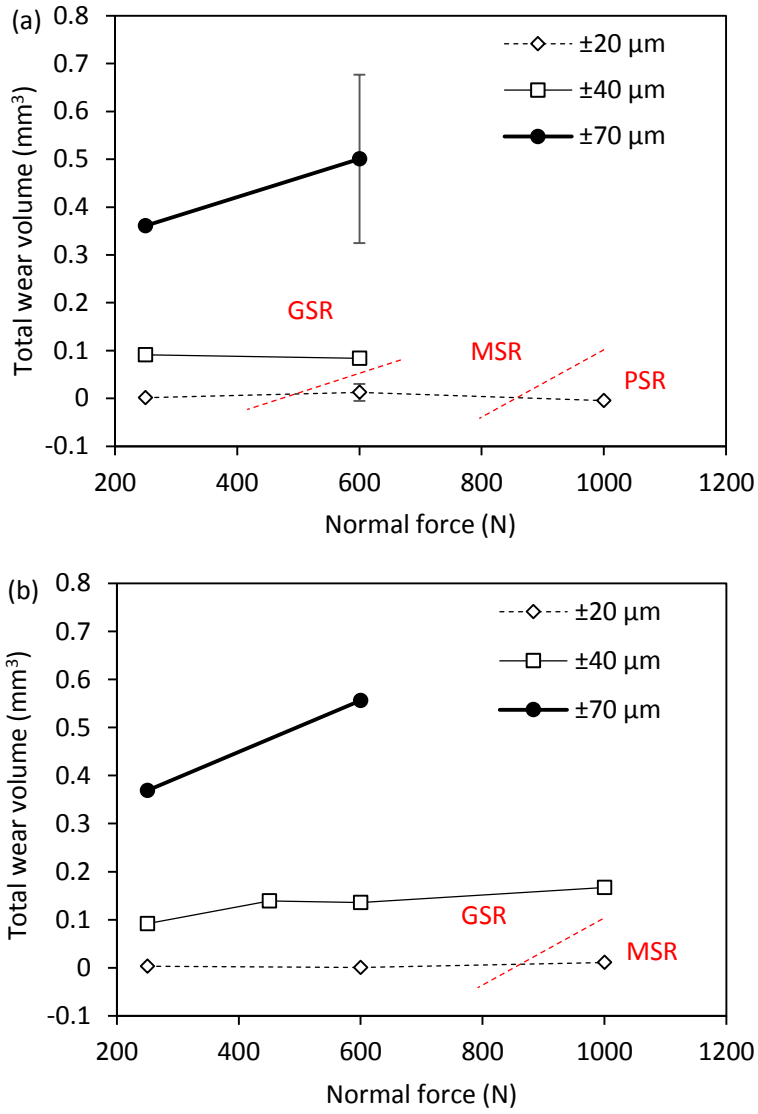

Figure III.9. Total wear volume: (a) test on rough flat; (b) test on smooth flat.

2.4. Wear scars

Wear scars were observed via SEM and EDX after testing. Figure III.10 shows a typical wear scar of the smooth flat surface after a test with a displacement amplitude of ±20 µm and a normal force of 250 N.

From the SEM images, some cracks are observed on the rubbed Ti–6Al–4V surface. Furthermore, titanium alloy is easily transferred from one body to the counterbody (sometimes leading to a negative value of wear volume for one sample, and a large wear volume of the counterbody), which suggests that adhesive wear occurs on the rubbed Ti–6Al–4V surface. This confirms previous findings that ductile materials like titanium alloys are very sensitive to adhesion phenomena [219].

EDX analysis indicates that the wear scar mainly consists of oxygen in addition to titanium, aluminum, and vanadium. Furthermore, six spots were detected via EDX on the rubbed surface (triangles Δ), and the content of oxygen reaches around 42 wt%. This means that the Ti–6Al–4V surfaces are oxidized during sliding in air. Oxidization occurs throughout the entire rubbed Ti–6Al–4V surface.

The displacement amplitude, the normal force, and the surface roughness have no obvious influence on wear scars.

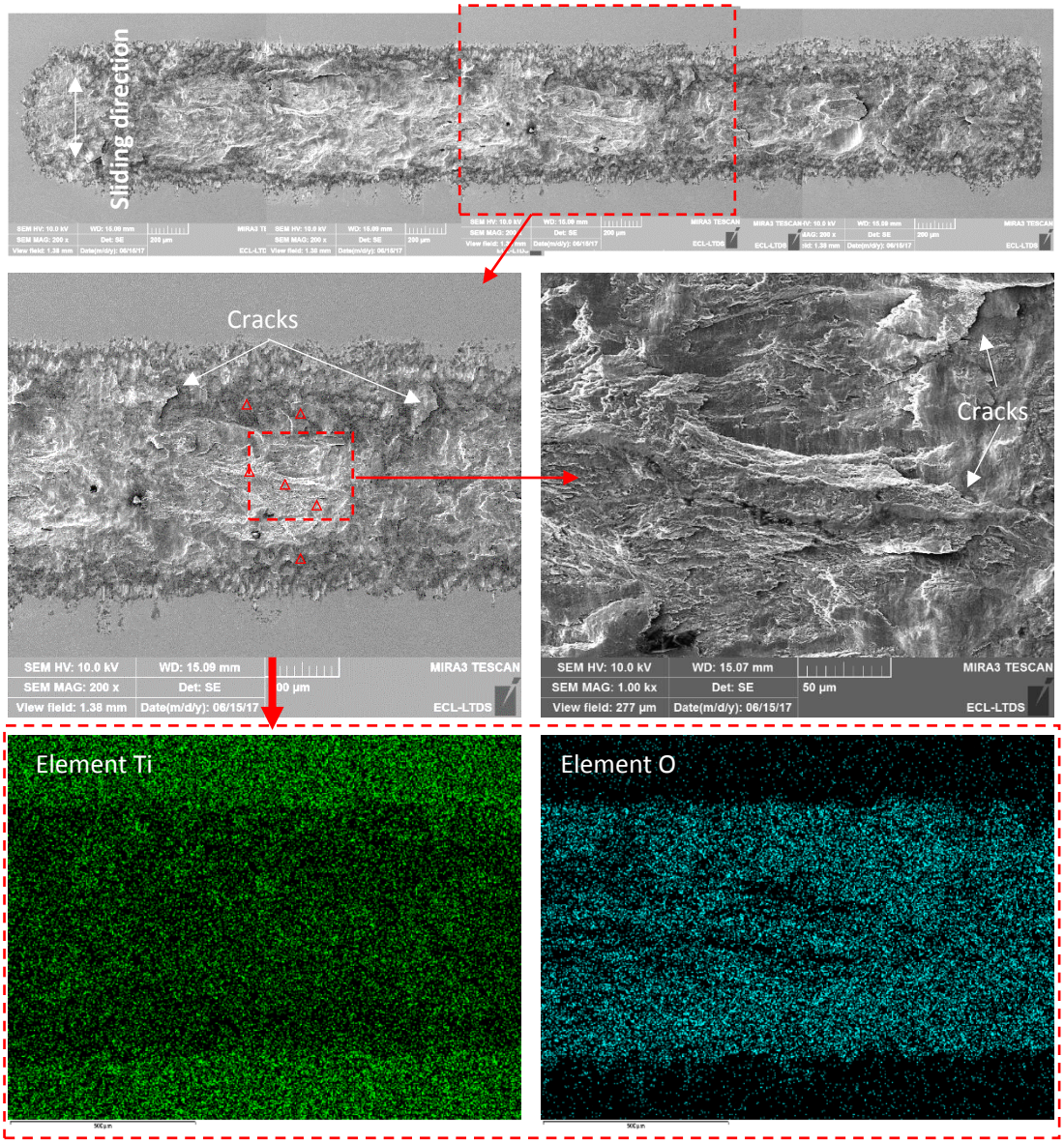

Figure III.10. SEM and EDX observations of the wear scar on the smooth flat surface after a test with a displacement amplitude of ±20 µm and a normal force of 250 N.

2.5. Tribologically transformed structure

Detachment of particles leading to material loss was one of the main degradation mechanism in fretting tests. Early in the degradation process, a superficial layer from which particles were detached was formed during the very first cycles [220–222]. After etching, this

layer looked different from the substrate. Differently from the microstructure of Ti–6Al–4V, this layer showed a very fine grained microstructure because of the presence of high plastic strain in the contact area [222]. This transformed structure is called the tribologically transformed structure (TTS).

In the present work, TTS was widely observed on the Ti–6Al–4V / Ti–6Al–4V contact areas. And the initial surface roughness has no obvious influence on the formation of TTS. Figure III.11 shows the observation of the TTS on the cross sections of flat samples. It may be observed that the TTS is transformed from the substrate by grains (Figure III.11b). Suggested by the reference [222], the TTS initiation involved recrystallization phenomena. In the sliding area, the contact pressure and shear stresses caused strong dislocation densities and plastic strain, which probably favored the nucleation. The nuclei then grew to form a new phase. Furthermore, it was verified that vanadium from Ti–6Al–4V was insoluble in the new phase of the TTS. It was segregated at grain boundaries. When a concentration threshold was reached, the growth of boundaries was stopped. As shown in Figure III.11c, the size of the grains in TTS reaches hundreds of nanometers, even approximately one micrometer. Moreover, grains on the top layer of the TTS are larger than the grains which are deep in the layer. This reveals that the new transformed grains (deep in the layer) grow until the growth of boundaries is stopped or the grains are detached.

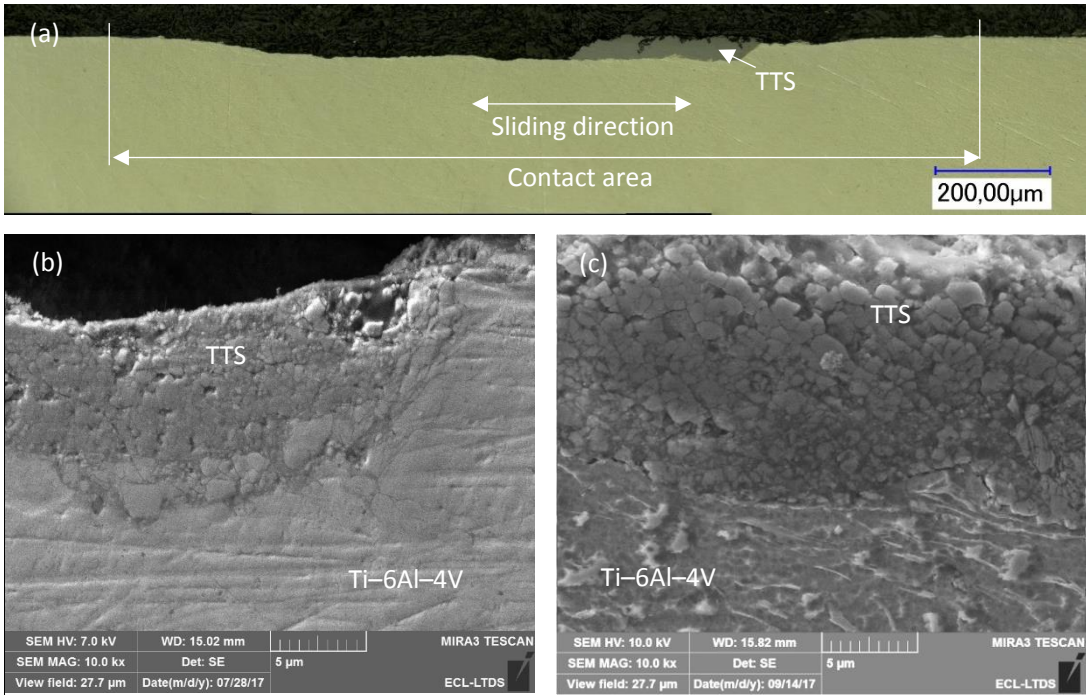

Figure III.11. TTSs on Ti–6Al–4V surfaces: (a) digital microscope of the flat cross section; (b) SEM of cross section; (b) SEM of etched cross section. Note that these three images were from different flats.

Because of the variation of mechanical properties between the TTS and the substrate, cracks were easily generated at the boundary area between them two (as shown in Figure III.12a). It is well known that the TTS is hard but brittle. Meanwhile, it had a loose structure i.e.

the bonding between grains was weak. Therefore, cracks could grow inside the TTS along the boundaries of grains (as shown in Figure III.12a).

From the results of reference [222], the TTS had a very small quantity of oxygen, in the same order of magnification as that observed in the bulk material. But in the present work, a large amount of oxygen was detected via EDX in TTS (as shown in Figure III.12c). This is probably because the oxygen element from the atmosphere permeated inside the TTS along its loose grain boundaries. As a result, the TTS was oxidized under the reciprocating sliding. Whether the presence of oxygen contributes to the formation of TTS is, nonetheless, still uncertain.

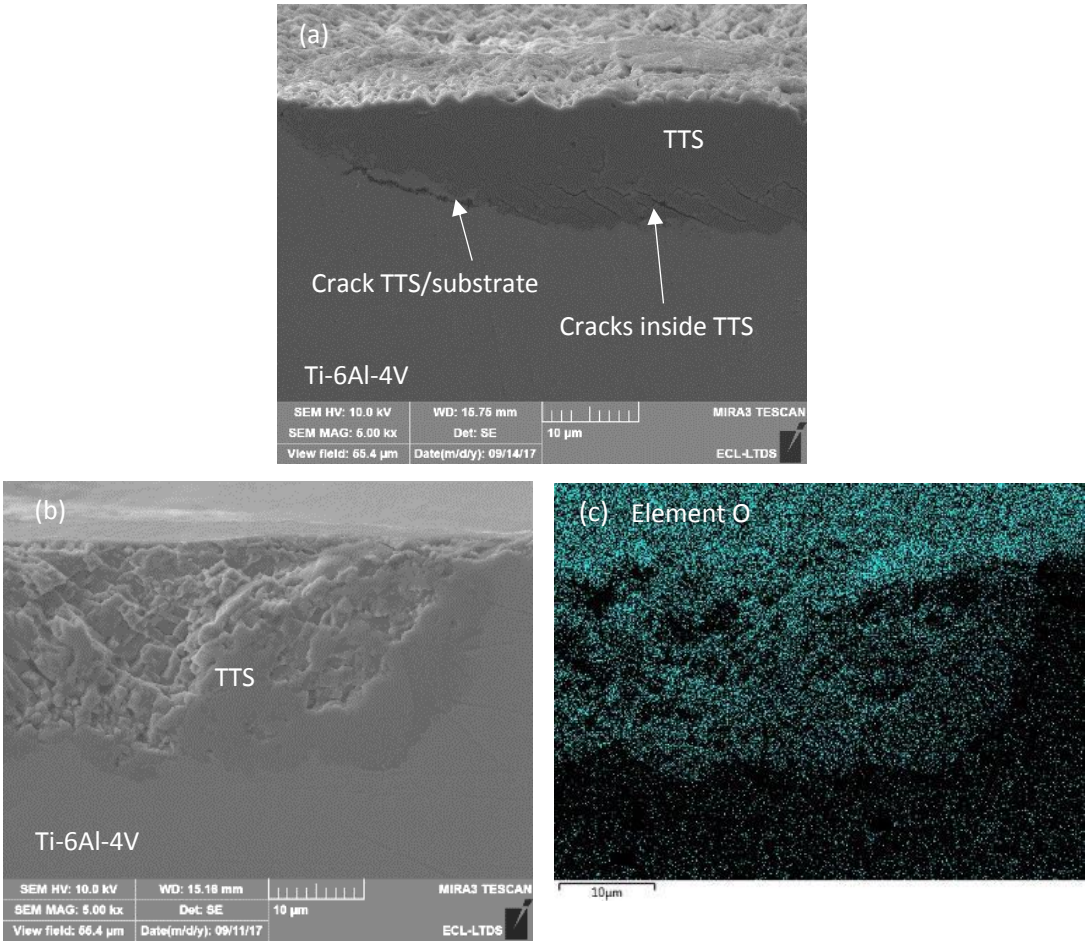

Figure III.12. SEM and EDX observations of cracks and oxidization of the TTS on Ti–6Al–4V cross sections: (a) cracks between TTS and substrate and cracks inside TTS; (b) TTS on the Ti–6Al–4V cross section; (c) EDX of figure (b).

2.6. Cracks on cross section

On the cross sections of flats, cracks were widely observed.

As mentioned in Section 2.5, cracks tended to be generated along the boundary between the TTS and the Ti–6Al–4V substrate because of the difference in their mechanical properties. Besides, TTS, sometimes, grew towards the subsurface (as shown in Figure III.13a). Thus, cracks are more likely to propagate following the TTS growth path.

Moreover, a plastic deformation layer was often observed, as shown in Figure III.13b. The different phases in Ti–6Al–4V were deformed into lamellar structure in this layer. Less energy was needed for cracks growth along the boundary between different phases than through the grain. Therefore, cracks tended to grow along the lamellar structure in the plastic deformation area.

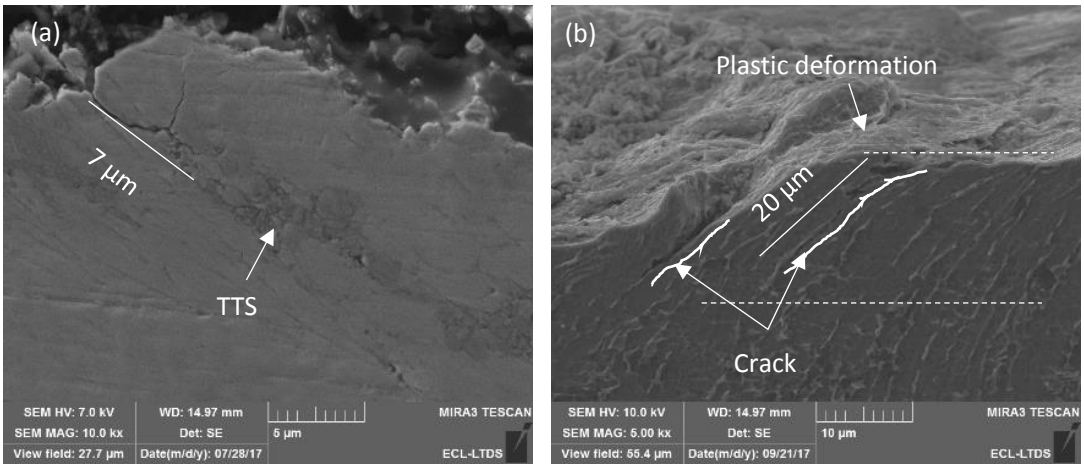

Figure III.13. SEM observation of cracks on Ti–6Al–4V cross sections: (a) crack along the TTS growth path; (b) cracks along the plastic deformation.

Figure III.14 shows the values of the maximal crack length measured on the cross section of flat samples. In the GSR, the main damage of material is wear [218, 223]. The maximal crack length is small due to the high loss of material. In the MSR and the PSR, the predominant damage is crack nucleation [218, 223]. The maximal crack length is large. In the MSR, it reaches the largest values.

It seems that the initial surface roughness has a slight influence on the crack length. In the MSR, the maximal crack length reaches 39 µm on the rough flat, while it reaches a slightly lower value of 23 µm on the smooth flat. But, it should be noted that the cross sections of rough flat samples were observed via digital microscope, while the cross sections of smooth flats were observed via SEM. Furthermore, for most of the tests, they were performed once under a certain displacement and normal force condition. And the cutting position of sections probably has influence on the results.

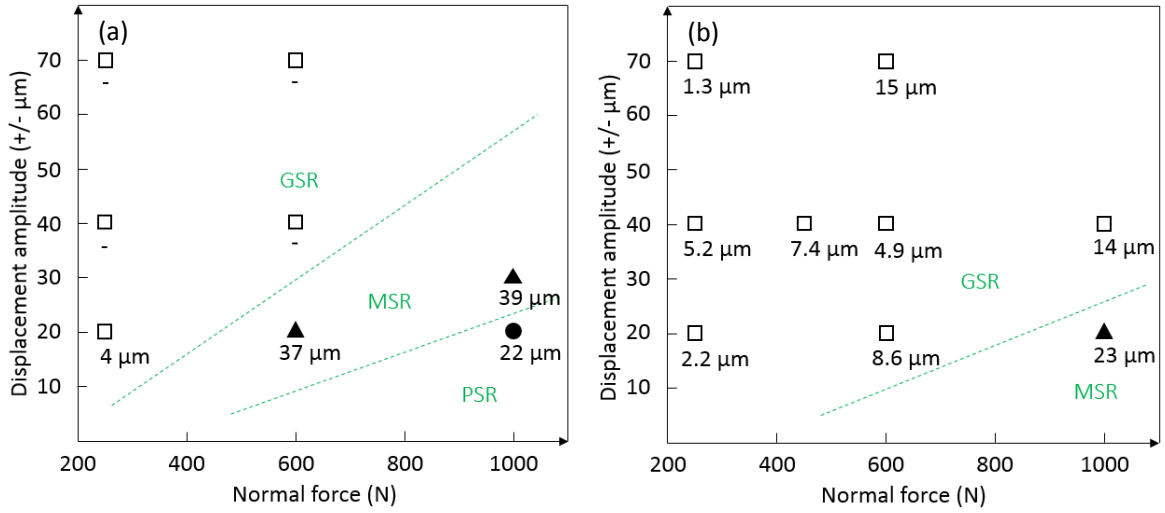

Figure III.14. Values of maximal crack length on cross sections of flat samples: (a) rough flat (observed via digital microscope); (b) smooth flat (observed via SEM). The hyphen - means that no obvious cracks were observed. The white square □ represents that the fretting test was under the GSR. The black triangle Δ represents that the fretting test was under the MSR.

2.7. Wear debris

For tests on smooth flat under large displacement condition, wear debris was collected for SEM and EDX observation, as shown in Figure III.15. It is clear that the wear debris is composed of flakes and powder. The size of large flakes reaches approximately 400 µm. Wrinkles (Figure III.15b) and cracks (Figure III.15c) can be observed on the flake surfaces. From the EDX analysis, the flake is mainly composed of titanium (wt% reaches 87%), aluminum, vanadium and a very small amount of oxygen, suggesting that the flake is mainly composed of Ti–6Al–4V, as a consequence of the fracture of cracks or of the abrasive wear from the substrate. The particles of powder have various sizes in a range between tens of nanometers and two micrometers (Figure III.15b). From the results of EDX, the powder is composed of titanium, aluminum, vanadium and a certain amount of oxygen, revealing that the powder is severely oxidized. The powder is probably a consequence of the adhesive wear of the oxidized contact surface, of the fragmentation of the TTS, and of the ejection of the third body particles those have undergone repeated sliding reaction during which the particles were oxidized.

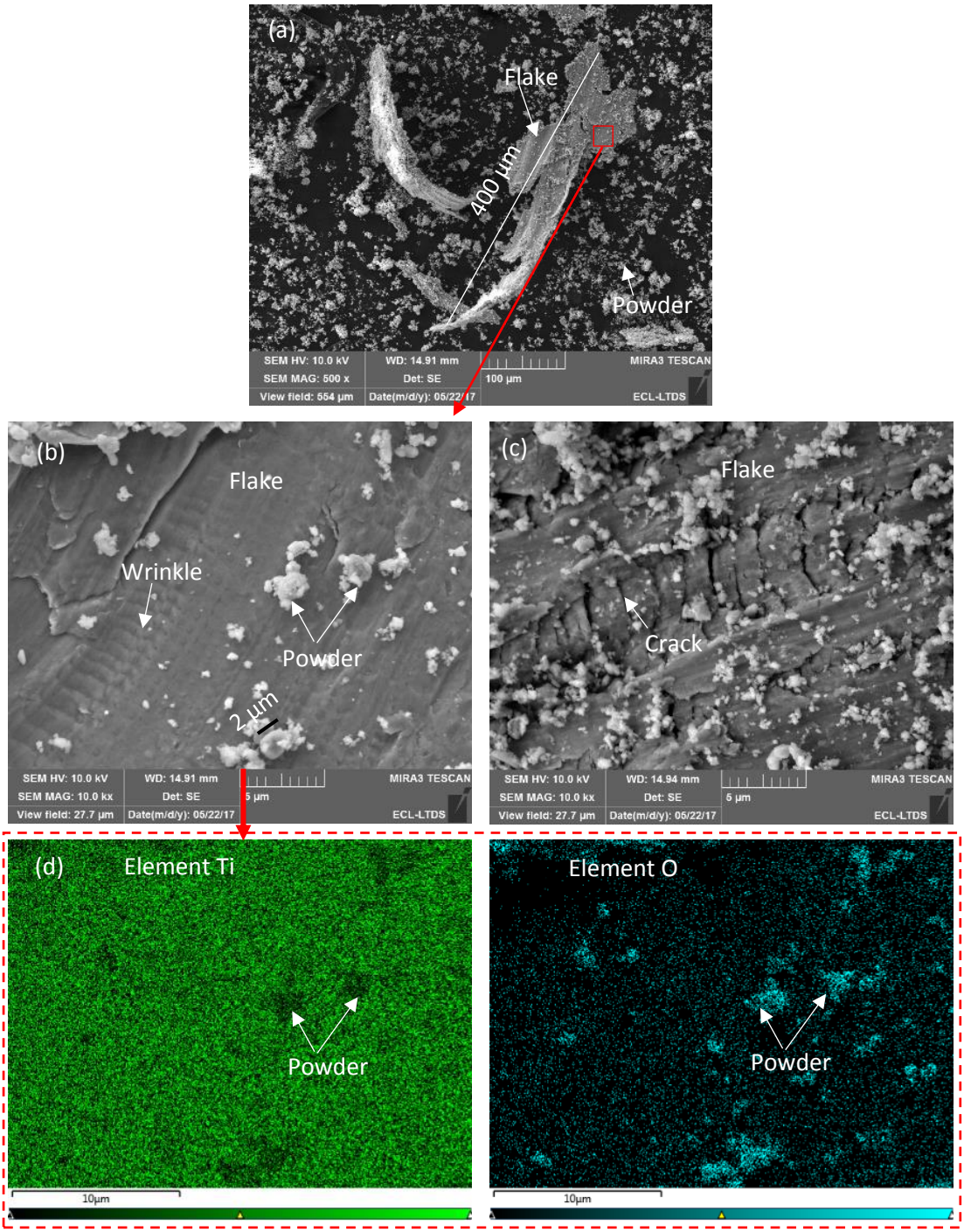

Figure III.15. SEM and EDX of wear debris for test under large displacement:
(a) large scale; (b) and (c) small scale; (d) EDX of (b).

3. Analysis of effect of surface roughness on fretting behaviors

The initial roughness had an influence on the fretting regime and then on the RCFM. The average values of energy ratio A for tests on smooth flats were higher than that on rough ones under the high normal force and low displacement conditions. But the difference was weak under the low normal force and high displacement conditions. The effect of roughness on the fretting regimes can be explained by the presence of asperities on rough surfaces, as shown in Figure III.16.

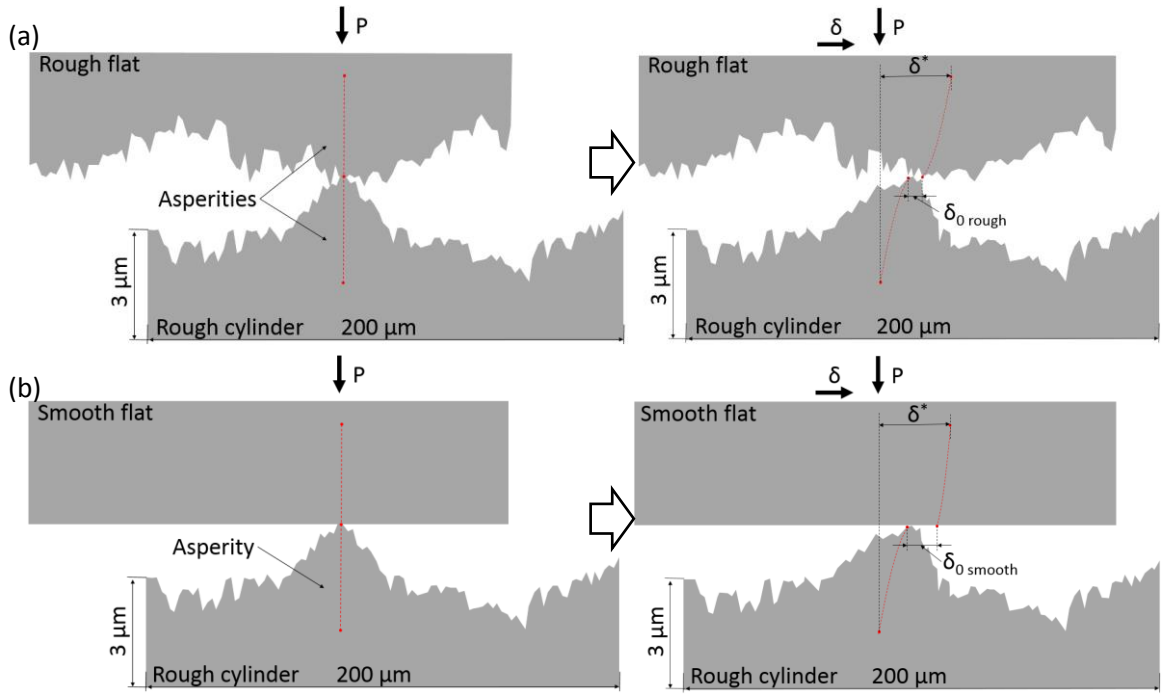

Figure III.16. Schematic illustration on the effect of roughness on fretting running conditions: (a) rough flat; (b) smooth flat.

From the elasticity point of view, comparing with the smooth flat (Figure III.16b), asperities on rough flat (Figure III.16a) give a higher elastic deformation in shearing to the surface, namely a lower tangential contact stiffness. Parameter δ_0 is the real displacement when the tangential force Q is 0, as shown in Figure II.12. The sliding displacement $\delta_{0\ rough}$ is smaller than $\delta_{0\ smooth}$ under the same normal force P and imposed displacement δ* condition (Figure III.16). A higher value of δ_0 corresponds to a higher value of energy ratio A, so the energy ratio A for the test on smooth flat is larger than that on rough one.

Under high force and small displacement conditions (1 000 N, ±20 µm), the rough flat surface leads to a narrower fretting loop than the smooth flat (Figure III.17a). Furthermore, the material loss is very low under these conditions. So, the effect of initial surface can last to the end of the test. Different fretting logs are obtained (Figure III.3b and Figure III.5). It is clear that the fretting is in the PSR on the rough flat (Figure III.4) and in the MSR on the smooth flat (Figure III.5).

Under low force and large displacement conditions (250 N, ±70 µm), the fretting is in the GSR. The wear loss is important. Both the rough and the smooth initial surfaces are worn off rapidly. Then, similar worn surface / worn surface contact is achieved. The effect of asperities eliminates. Therefore, similar fretting loops (Figure III.17b) and similar fretting logs (Figure III.1b and Figure III.5) are obtained. The average values of energy ratio A shows no important difference with different surface roughness under low force and high displacement conditions.

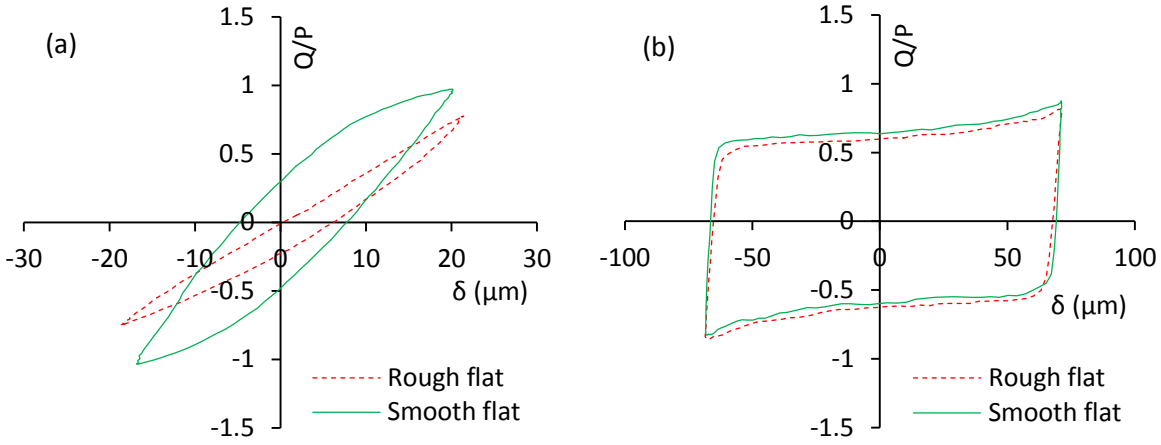

Figure III.17. Stabilized fretting loops: (a) ±20 µm, 1 000 N, 99 999 cycles; (b) ±70 µm, 250 N, 98 999 cycles.

4. Conclusions

In this chapter, the effect of surface roughness on fretting behavior of Ti–6Al–4V / Ti–6Al–4V contact was investigated under laboratory air condition.

The energy ratio A on a smooth flat was higher than that on a rough flat. And the increase was more significant under higher normal force and lower displacement conditions. The RCFM for tests on a rough flat was divided into the GSR, the MSR, and the PSR. On a smooth flat surface, the GSR and the MSR extended towards higher normal force and lower displacement, and the PSR vanished under the given displacement and normal force conditions.

The friction coefficient increased during the running-in period and then remained steady until the end of the test. The stable friction coefficients were in the range of 0.8–1.2.

The wear volumes were very low in the MSR and in the PSR. In the GSR, the wear volume increased significantly with the increase in the displacement. With the increase in the normal force, the wear volume showed an increase under the displacement amplitude of ±70 µm, and showed no obvious change under the displacement amplitude of ±40 µm.

On the wear scars, adhesive wear was dominant. And the wear scar was oxidized.

TTS was widely formed on the rubbed Ti–6Al–4V surfaces. And the TTS was oxidized.

Cracks were widely observed, and longer cracks were observed in the MSR and in the PSR.

The wear debris consisted of Ti–6Al–4V flaks and oxidized powder.

The initial surface roughness had no visible influence on the friction coefficient, the wear volume, the wear scars, and the TTS.

The results will serve as baselines for the study of the effect of DLC coating in next chapters.

CHAPTER IV

INFLUENCE OF DIFFERENT PARAMETERS ON FRETTING BEHAVIOR OF DLC COATINGS

CHAPTER IV: INFLUENCE OF DIFFERENT PARAMETERS ON FRETTING BEHAVIOR OF DLC COATINGS

CHAPTER IV: INFLUENCE OF DIFFERENT PARAMETERS ON FRETTING BEHAVIOR OF DLC COATINGS

This chapter investigates the influence of different parameters on the fretting behavior of DLC coatings under laboratory air condition. The parameters include different DLC coatings, different surface roughness, and different coating positions. At last, a coating failure process and a tribological model for coating response are proposed.

1. Introduction

DLC coatings were widely used in many applications to decrease friction and wear between two metallic parts in contact [114, 117]. Furthermore, DLC coatings showed high biocompatibility in previous works [156, 157]. In this study, DLC coatings are used as protective coatings into Ti–6Al–4V / Ti–6Al–4V interface for neck adapter / femoral stem contact.

In this chapter, the influence of different parameters on the fretting behavior of DLC coatings is investigated under laboratory air condition. The parameters include two DLC coatings (DLC A and DLC B), two types of surface roughness (smooth flat surface and rough flat surface), and three coating positions (coating deposited on the flat, on the cylinder, and on both the flat and the cylinder). Tests were conducted under various values of displacement amplitude (±20, ±40, and ±70 µm) and normal force (200–1 200 N). The number of cycles for each test was 100 000 cycles.

Firstly, the tribological behavior of DLC coatings is presented in this chapter, including friction coefficient, wear volume, and analysis of wear scars. After that, coating response wear maps are constructed according to the comprehensive analysis of friction and wear. Then, the running condition fretting map (RCFM) is drawn for tests with a rough flat coated with DLC A in contact with an uncoated cylinder.

Secondly, the effect of parameters on fretting behavior of DLC coating is discussed, including two different DLC coatings (DLC A and DLC B), two types of substrate roughness (rough surface and smooth surface), and three types of coating positions (coating on flat, on cylinder, on both).

At last, based on the observation of wear scars and analysis of friction and wear results, a hypothesis on the coating process is proposed. In addition, a tribological model is built to explain the friction and damage response of the DLC coating and the Ti–6Al–4V substrate.

2. Tribological behavior

In this section, the tribological behavior of DLC coatings is presented. Specifically, evolution of friction coefficient was recorded during the test. Wear volumes were measured on both flat and cylinder samples. Wear scars were observed after testing. After that, coating response wear maps are drawn according to the analysis of friction and wear. Running condition fretting map (RCFM) is drawn for tests with a rough flat coated with DLC A in contact with an uncoated cylinder. At last, cross sections of flat samples, and the wear debris were observed and analyzed via digital microscope, SEM and EDX.

2.1. Friction coefficient

- **Evolution of Q_{max}/P**

The evolution of Q_{max}/P is influenced by loading conditions (the displacement amplitude and the normal force) and the contact conditions (including the DLC coating types, the surface roughness, and the coating positions). We will take the fretting tests with a smooth flat coated with DLC B in contact with an uncoated cylinder as examples to discuss the effect of loading conditions on the evolutions of Q_{max}/P.

Figure IV.1 shows the evolutions of Q_{max}/P under the small displacement amplitude of ±20 μm with different values of normal force. Under low normal force (250 N and 450 N), the Q_{max}/P ratio decreases to a low value, reaching approximately 0.1, during the running-in period of approximately 100 cycles; then, it remains stable until the completion of the test. Under high normal force (800 N and 1 000 N), Q_{max}/P increases rapidly to a high value, around 0.8, which reveals the failure of the coating. After that, the Q_{max}/P remains high until the completion of the test. Under the intermediate normal force (500 N, 600 N, and 700 N), Q_{max}/P receives intermediate values, and it shows an increase trend with the increase in the normal force.

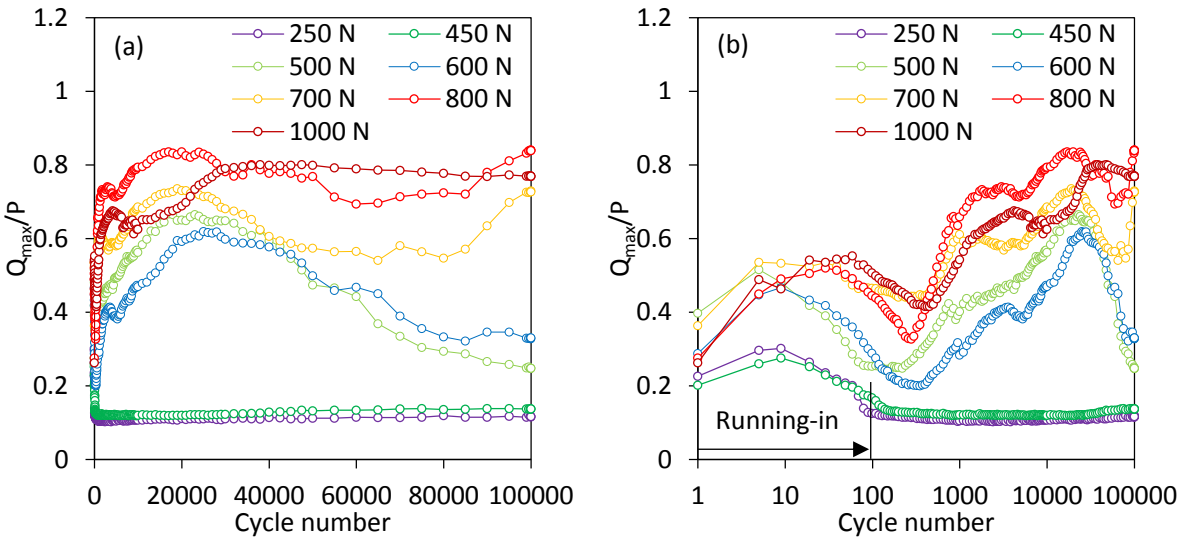

Figure IV.1. Evolution of Q_{max}/P as a function of the number of cycles for a smooth flat coated with DLC B in contact with an uncoated cylinder under the displacement amplitude of ±20 µm: (a) linear scale; (b) logarithmic scale.

Figure IV.2 shows the evolutions of Q_{max}/P under the displacement amplitude of ±40 µm with different values of normal force. Under low normal force (250 N and 550 N), the Q_{max}/P ratio remains low after the running-in period. Under high normal force (600 N and 1 000 N), the Q_{max}/P ratio remains high after the running-in period.

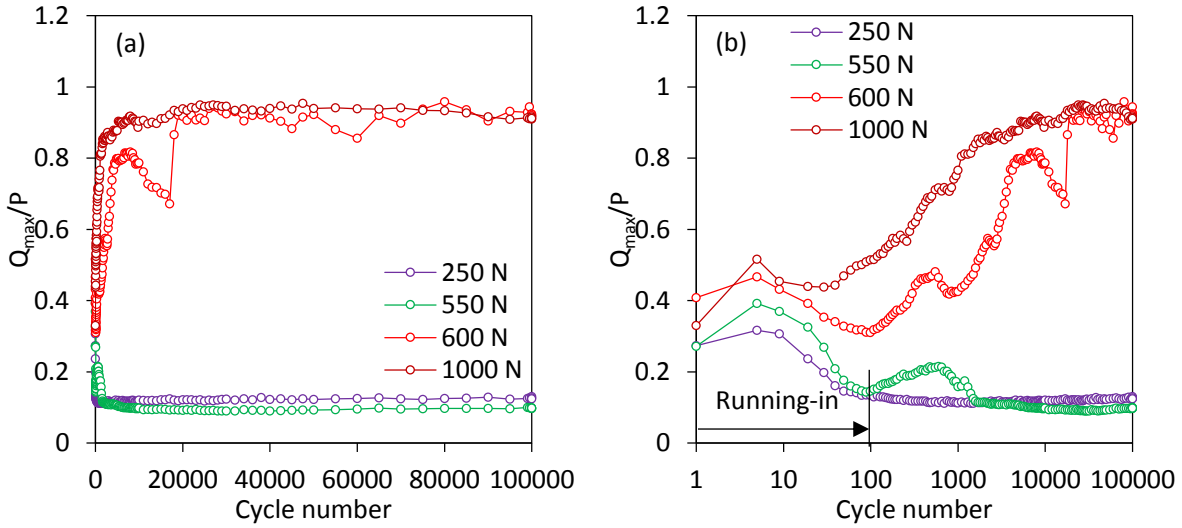

Figure IV.2. Evolution of Q_{max}/P as a function of the number of cycles for a smooth flat coated with DLC B in contact with an uncoated cylinder under the displacement amplitude of ±40 µm: (a) linear scale; (b) logarithmic scale.

Figure IV.3 shows the evolutions of Q_{max}/P under the large displacement amplitude of ±70 µm with different values of normal force. Under the low normal force (250 N), the Q_{max}/P ratio remains low after the running-in period. Under high normal force (350 N and 450 N), the Q_{max}/P ratio remains high after the running-in period. Under the intermediate normal force

(300 N), Q_{max}/P keeps low until around 40 000 cycles, then it increases sharply, and then remains high until the end of the test.

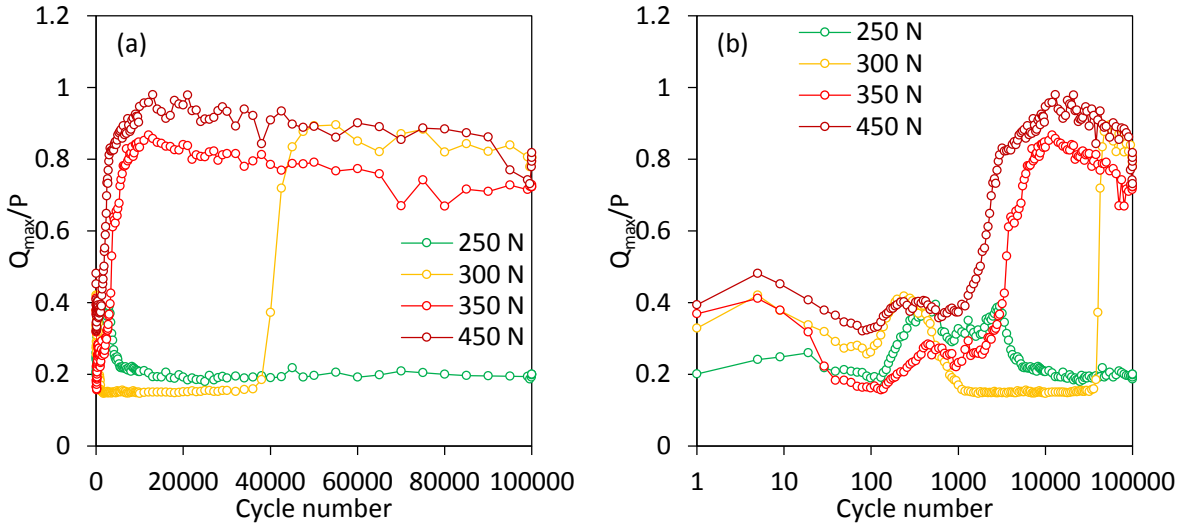

Figure IV.3. Evolution of Q_{max}/P as a function of the number of cycles for a smooth flat coated with DLC B in contact with an uncoated cylinder under the displacement amplitude of ±70 µm: (a) linear scale; (b) logarithmic scale.

- **Average values of Q_{max}/P**

Figure IV.4 shows the average values of Q_{max}/P during the stable period for tests with different DLC coatings, different surface roughness, and different coating positions, under various values of normal force and displacement. For tests under ±20 µm and ±40 µm conditions, Q_{max}/P is the average value from 50 000 cycles to the end of the test. For tests under ±70 µm, Q_{max}/P is the average value from 10 000 cycles to the end of the test.

It is clear that under the large displacement amplitudes of ±70 µm and ±40 µm, a threshold occurs in the normal force. Under the small displacement amplitude of ±20 µm, the normal force presents a transition area. For tests with the contact of smooth flat with DLC A/uncoated cylinder under the displacement amplitude of ±20 µm (Figure IV.4c), the transition area is not obvious. It can also be regarded that a threshold occurs between 600 N and 700 N.

When the applied normal force is lower than the threshold or the transition area, the value of Q_{max}/P is low, approximately equal to or lower than 0.2. When the applied normal force is higher than the threshold or the transition area, Q_{max}/P is high. In the transition area, Q_{max}/P has an intermediate value and presents an increasing trend as the normal force increases.

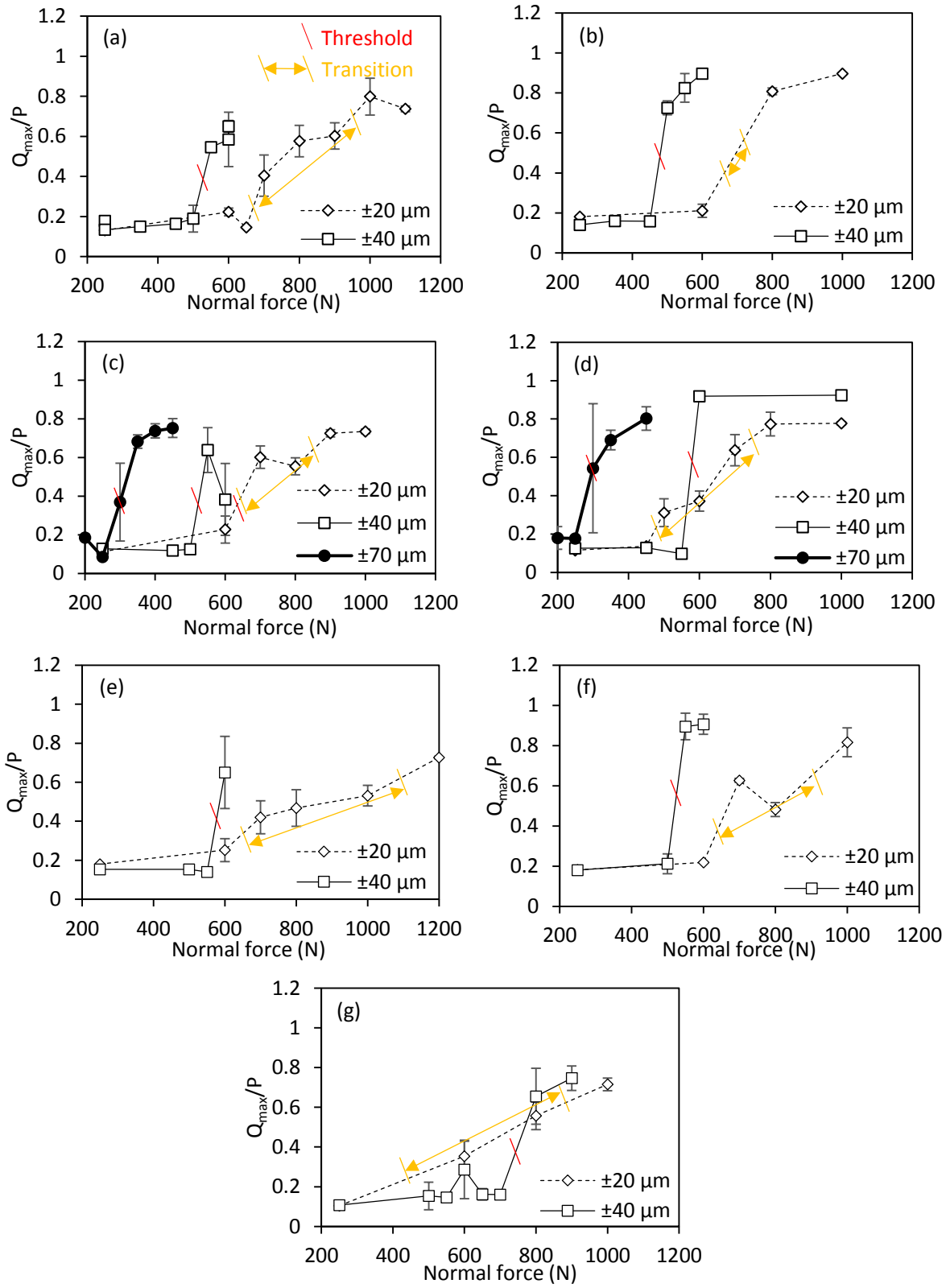

Figure IV.4. Average values of Q_{max}/P for tests with DLC coating: (a) rough flat with DLC A / uncoated cylinder; (b) rough flat with DLC B / uncoated cylinder; (c) smooth flat with DLC A / uncoated cylinder; (d) smooth flat with DLC B / uncoated cylinder; (e) uncoated rough flat / cylinder with DLC A; (f) uncoated rough flat / cylinder with DLC B; (g) rough flat with DLC A / cylinder with DLC A. Q_{max}/P is the average value from 50 000 cycles to the end of the test under ±20 µm and ±40 µm conditions. It is the average value from 10 000 cycles to the end of the test under ±70 µm condition.

Furthermore, the threshold position (i.e., the normal force where the threshold occurs) is influence by the displacement amplitude. Under larger displacement amplitude condition, the threshold lies at lower normal force. Concerning the smooth flat with DLC B / uncoated cylinder contact (Figure IV.4d), the threshold lies between 550 N and 600 N under the displacement amplitude of ±40 µm; it lies at around 300 N under the displacement amplitude of ±70 µm.

The positions of threshold and transition area are different depending on the coating types, the surface roughness, and the coating positions, which will be discussed in Section 3.

2.2. Wear volume

The total wear volume (sum of wear volumes of the flat and cylinder samples) is shown in Figure IV.5. The calculation process of wear volume is explained in Appendix B. When the applied normal force is lower than the threshold or the transition area, the wear volume is small. When the applied normal force is higher than the threshold or the transition area, the wear volume is similar to the results from the tests without the DLC coating. More specifically, the wear volume increases drastically with the increase in displacement. With the increase in the normal force, the wear volume increases under the displacement amplitude of ±70 µm; no obvious change can be observed in the wear volume under the displacement amplitude of ±40 µm; and it approaches 0 under the displacement amplitude of ±20 µm. In the transition area, the wear volume is near 0 because the transition area only occurs under the small displacement amplitude of ±20 µm, for which the wear volume for the test on samples without coating was near 0 as well.

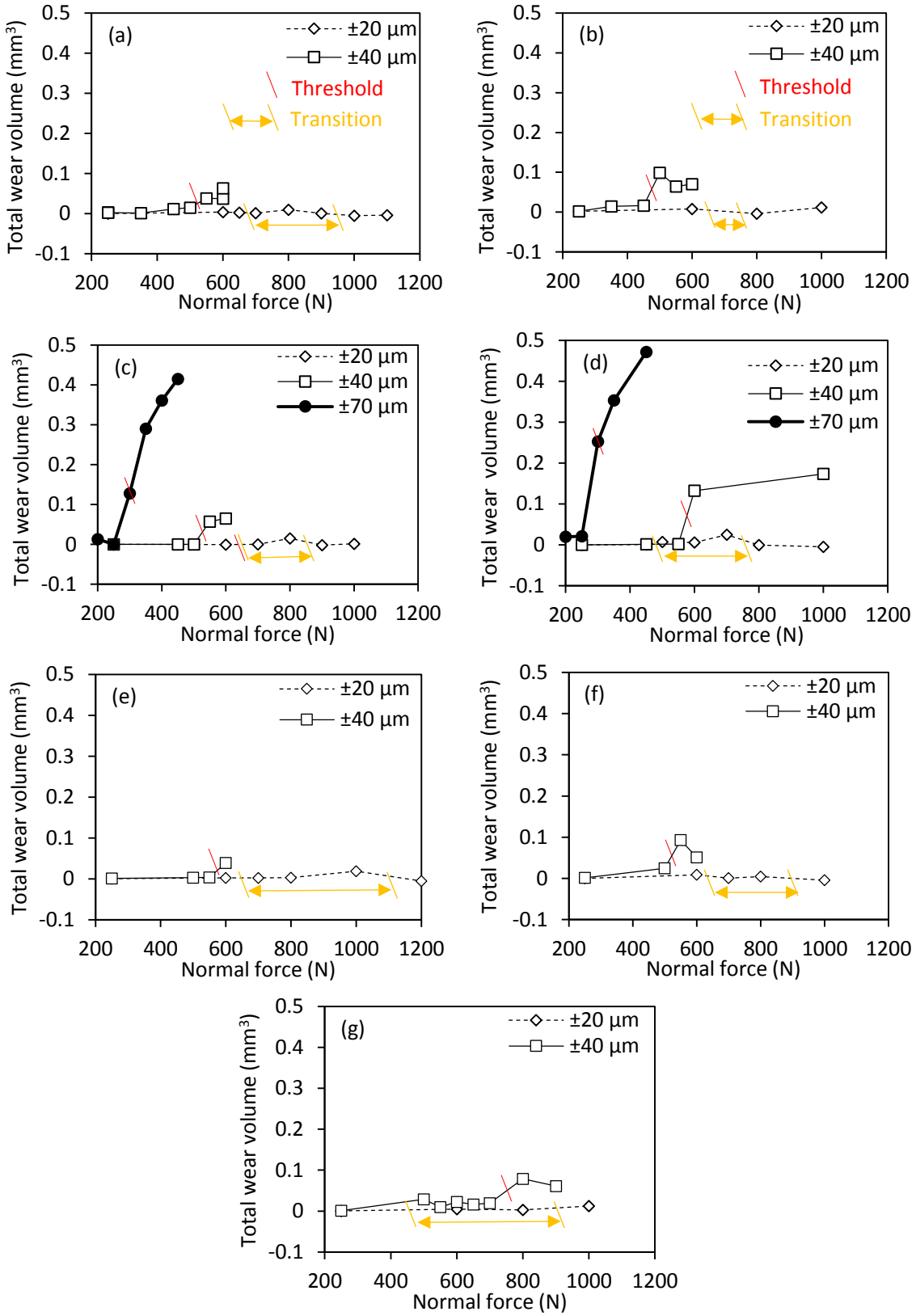

Figure IV.5. Total wear volume for tests with DLC coating: (a) rough flat with DLC A / uncoated cylinder; (b) rough flat with DLC B / uncoated cylinder; (c) smooth flat with DLC A / uncoated cylinder; (d) smooth flat with DLC B / uncoated cylinder; (e) uncoated rough flat / cylinder with DLC A; (f) uncoated rough flat / cylinder with DLC B; (g) rough flat with DLC A / cylinder with DLC A.

2.3. Wear scars

Figure IV.6 shows the wear scars of a contact pair, i.e., rough flat coated with DLC A / uncoated cylinder contact, under the displacement amplitude of ±20 µm and the normal force of 600 N. The wear scars are composed of mild wear areas and severe wear areas. Furthermore, the severe wear areas on the flat sample and on the cylinder sample lie in the same contact area, so do the mild wear areas.

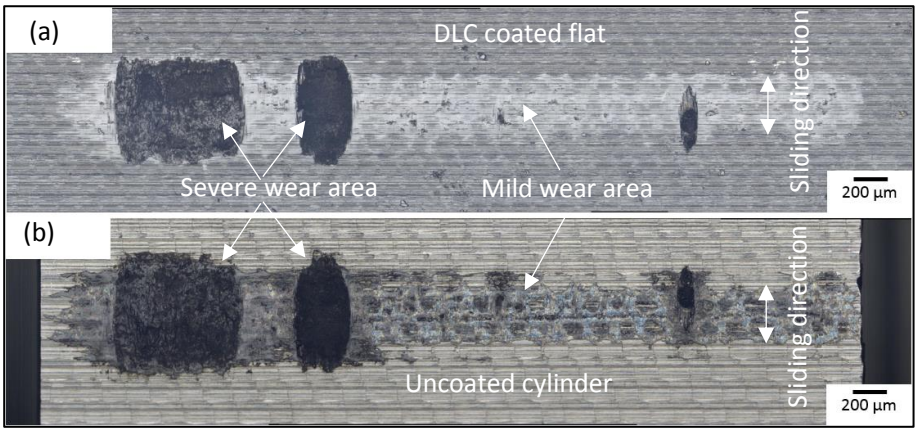

Figure IV.6. Optical observation of wear scars of a contact pair under the displacement amplitude of ±20 µm and the normal force of 600 N: (a) rough flat with DLC A in contact with the (b) uncoated cylinder.

2.3.1. Mild wear area

- **Mild wear area on DLC coating surface**

Figure IV.7 shows the mild wear area on the DLC coating surface, i.e. DLC A on rough flat, which is in contact with an uncoated cylinder. Before testing, the DLC coating had a constant thickness on the rough surface due to its great conformal property (Figure II.7). After testing, scratches can be observed on the coating surface, starting on the asperities, i.e., the coating thickness in the valley is larger than that on the asperities (Figure IV.7d), which means that the DLC material can be worn off, perhaps as a consequence of adhesion at a molecular scale or of the interaction with the counterbody and the external environment during sliding.

It is clear from Figure IV.7c that some cracks were generated in the DLC coating, which reveals that the local contact pressure exceeded the stress limit of the sample (the combination of the coating and the substrate). During the test, cracks developed into pits where the coating was detached. But, the most part of the contact area was still protected by the DLC coating until the completion of the test.

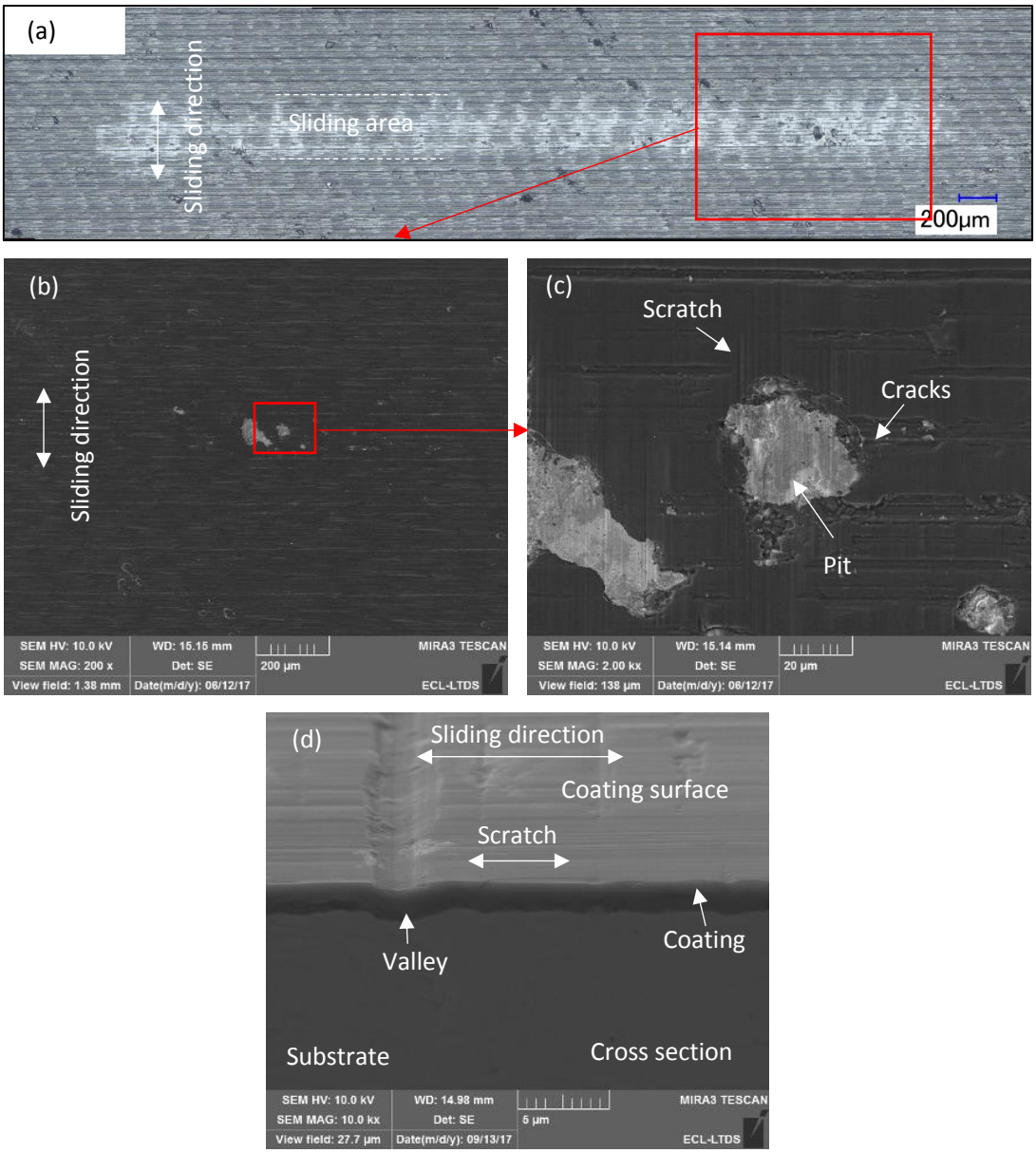

Figure IV.7. Mild wear area on the rough flat with DLC A (in contact with an uncoated cylinder): (a), (b), and (c) flat under ±20 µm and 250 N; (d) cross section of flat under ±20 µm and 600 N.

- **Mild wear area on uncoated Ti–6Al–4V surface**

Figure IV.8 shows the mild wear area on the uncoated rough flat surface, which is in contact with a cylinder surface coated with DLC A. Scratch can be observed on the Ti–6Al–4V surface (Figure IV.8c). After that, a tribofilm has been formed on the rubbed Ti–6Al–4V surface. From the analysis of EDX, the tribofilm is constituted of titanium, aluminum, vanadium and oxygen (Figure IV.8d), suggesting that the tribofilm originated from the worn Ti–6Al–4V material with severe oxidization due to the repeated sliding in air. The details of the formation of tribofilm will be presented in Chapter VI.

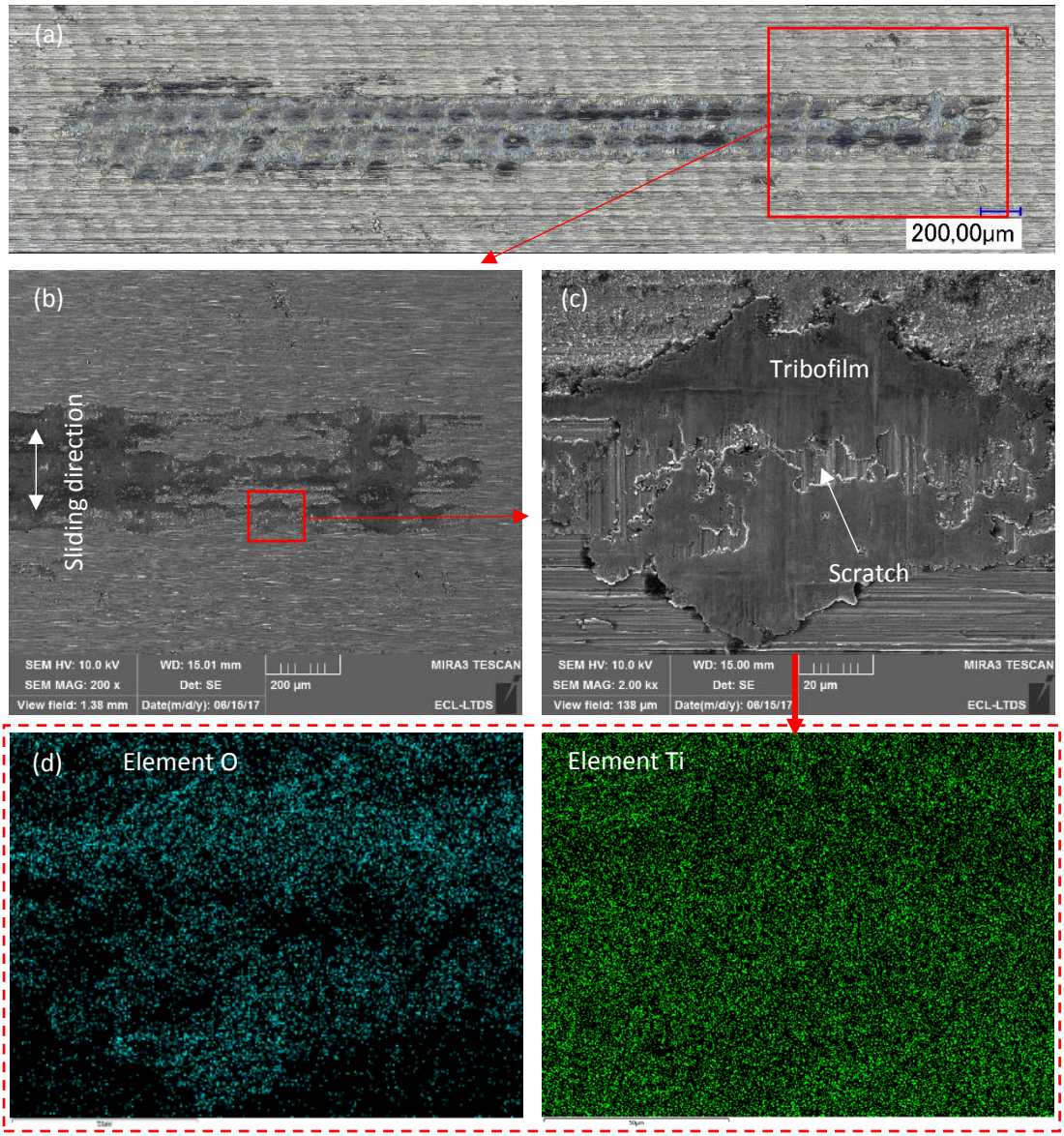

Figure IV.8. Mild wear area on the uncoated flat surface (in contact with a cylinder coated with DLC A) under the displacement amplitude of ±20 µm and the normal force of 250 N: (a) global view of the contact area; (b), (c) zoom of the contact area; (d) EDX observation of figure (c).

2.3.2. Severe wear area

- **Severe wear area on DLC coating surface**

Figure IV.9 shows a representative severe wear area on the DLC coating surface, i.e., rough flat coated with DLC A, which is in contact with an uncoated cylinder. It is clear that the coating was entirely removed at the end of the test. Therefore, the substrate of Ti–6Al–4V was in direct contact with the Ti–6Al–4V from the countersurface. From the analysis of EDX, the severe wear area was oxidized because the Ti–6Al–4V slid against the Ti–6Al–4V in the air in this area.

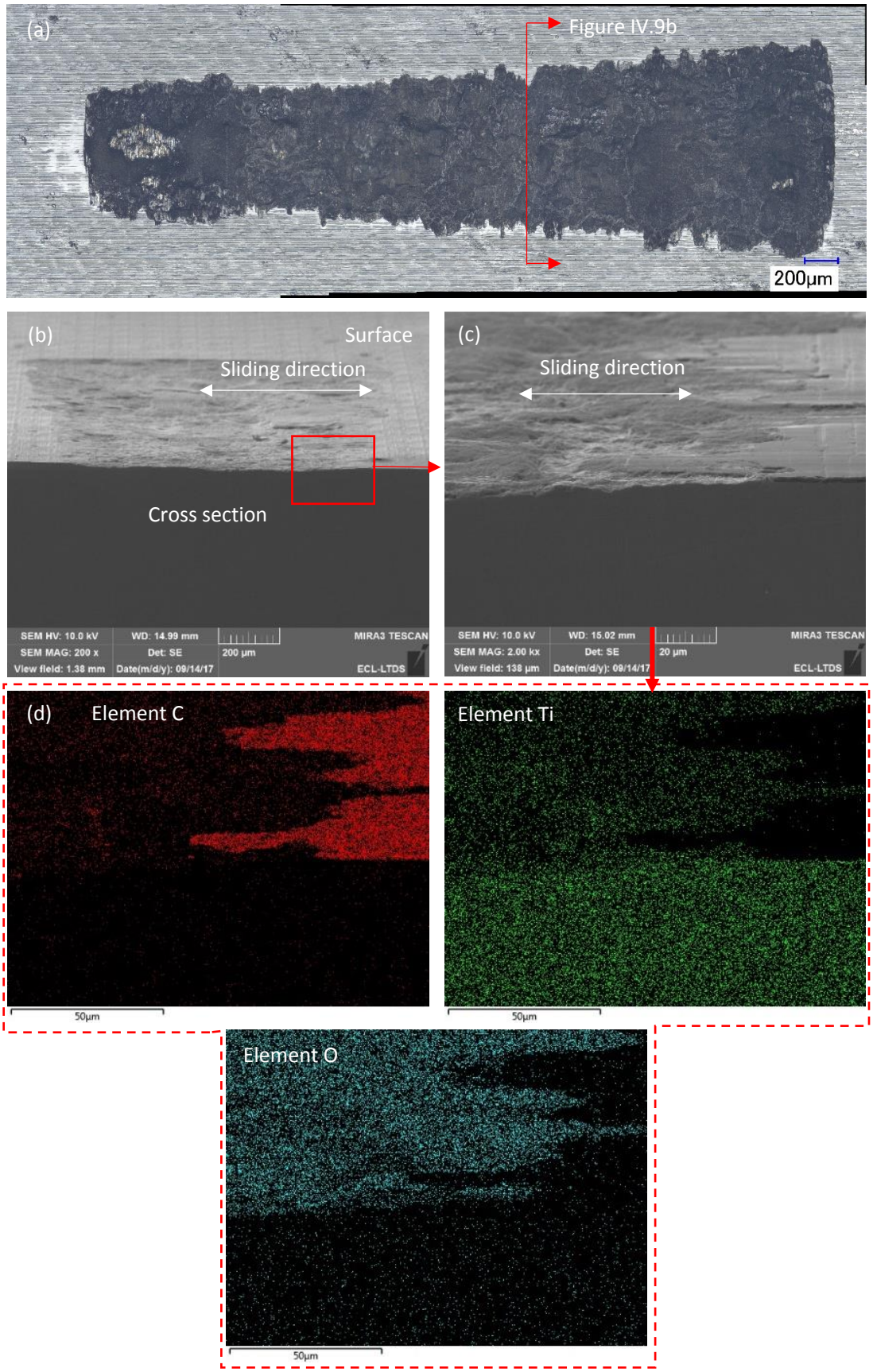

Figure IV.9. Severe wear area on the rough flat coated with DLC A (in contact with an uncoated cylinder) under the displacement amplitude of ±40 µm and the normal force of 600 N: (a) global view of the contact area; (b) cross section; (c) zoom on the right edge of the contact; (d) EDX of figure (c).

- **Severe wear area on uncoated Ti–6Al–4V surface**

Figure IV.10 shows a representative severe wear area on the Ti–6Al–4V flat surface, which is in contact with the severe wear area on a coated cylinder. The rubbed surface is damaged severely, and it is oxidized.

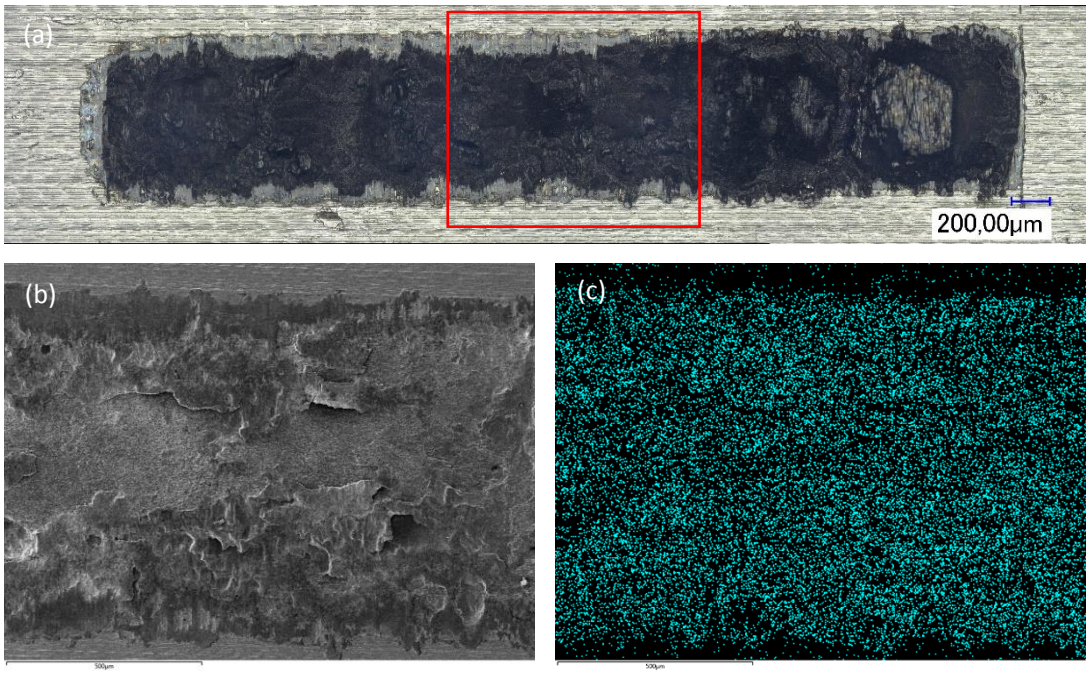

Figure IV.10. Severe wear area on the Ti–6Al–4V surface (in contact with a cylinder coated with DLC A) under the displacement amplitude of ±40 µm and the normal force of 600 N: (a) global view of the contact area; (b) SEM of the contact; (c) EDX of figure (b).

In addition, in the severe wear area, the coating is removed and the Ti–6Al–4V substrate of flat is in direct contact with the Ti–6Al–4V substrate of cylinder. This contact is similar to the test without coating. Therefore, similar damage phenomena were observed. Namely, TTS, plastic deformation, and cracks were observed in the rubbed Ti–6Al–4V surface.

2.3.3. Wear scars on flat samples

Figure IV.11, Figure IV.12, and Figure IV.13 show the wear scars from tests with the displacement amplitudes of ±20 µm, ±40 µm, and ±70 µm, respectively. Tests were performed under different normal forces and different contact conditions (different DLC coatings, different surface roughness, and different coating positions).

The damage of the wear scar is closely related to the load condition (the displacement amplitude and the normal force). When the applied normal force is lower than the threshold or the transition, the DLC coating is not removed (±20 µm, 250 N, Figure IV.11a) or only partly removed (±20 µm, 600 N, Figure IV.11a). Accordingly, the wear scar is composed of a mild wear area or both mild and severe wear areas. Moreover, with the increase in the normal force and displacement, the damage of coating becomes more severe. When the applied normal force is higher than the threshold or the transition, the coating has been almost

entirely removed (±20 µm, 1 000 N, Figure IV.11a); the wear scar is mainly composed of the severe wear area. In the transition area, the coating has been partly removed (±20 µm, 700 N, Figure IV.11a); the wear scar is composed of both the mild and the severe wear areas.

Furthermore, under the same load condition, the damage of the wear scar may be different, depending on the DLC coating types, the surface roughness, and the coating positions, which will be discussed in Section 3.

In addition, the damage of coating tends to start from one endpoint of the contact because it is difficult to create an absolutely parallel contact between the cylinder and the flat samples when setting them up, and the contact pressure of the endpoint is higher than that in other areas.

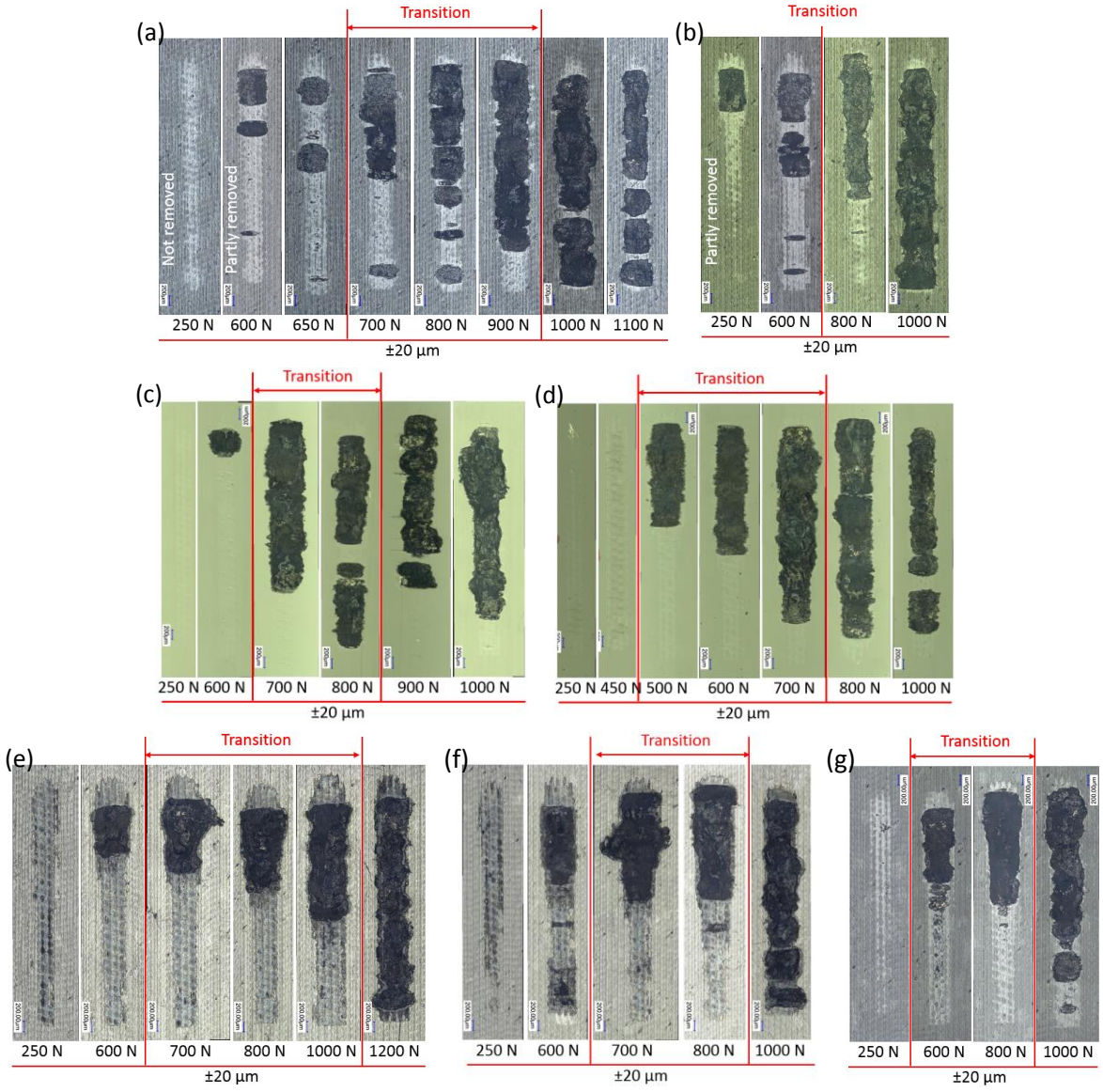

Figure IV.11. Wear scars on flats under the displacement amplitude of ±20 µm:
(a) rough flat with DLC A / uncoated cylinder; (b) rough flat with DLC B / uncoated cylinder;
(c) smooth flat with DLC A / uncoated cylinder; (d) smooth flat with DLC B / uncoated cylinder;
(e) uncoated rough flat / cylinder with DLC A; (f) uncoated rough flat / cylinder with DLC B;
(g) rough flat with DLC A / cylinder with DLC A.

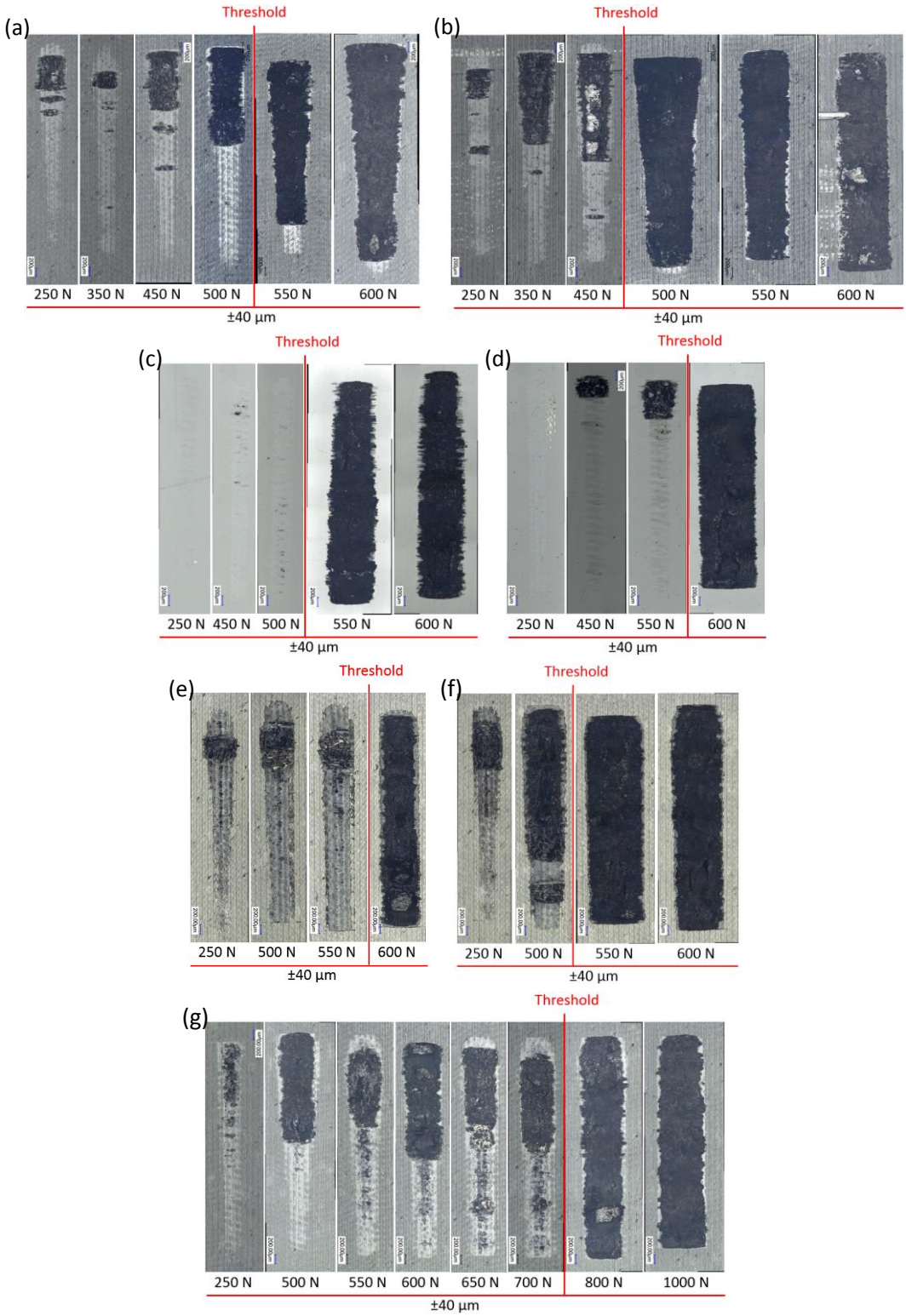

Figure IV.12. Wear scars on flats under the displacement amplitude of ±40 µm:
(a) rough flat with DLC A / uncoated cylinder; (b) rough flat with DLC B / uncoated cylinder;
(c) smooth flat with DLC A / uncoated cylinder; (d) smooth flat with DLC B / uncoated cylinder;
(e) uncoated rough flat / cylinder with DLC A; (f) uncoated rough flat / cylinder with DLC B;
(g) rough flat with DLC A / cylinder with DLC A.

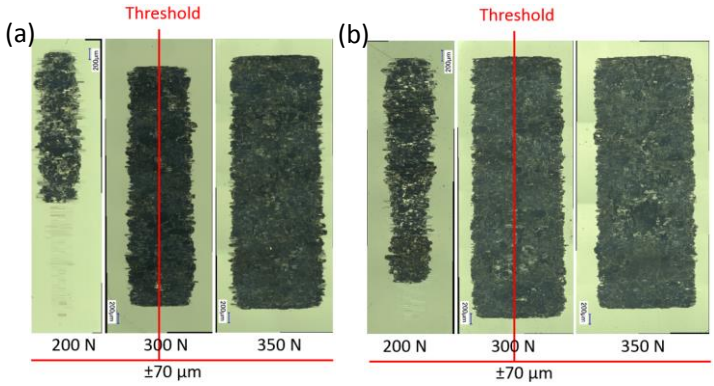

Figure IV.13. Wear scars on flats under the displacement amplitude of ±70 µm:
(a) smooth flat with DLC A / uncoated cylinder; (b) smooth flat with DLC B / uncoated cylinder.

2.4. Coating response wear maps

Coating response wear maps (as shown in Figure IV.14) were drawn in the axes (normal force and displacement amplitude) according to the comprehensive analysis of Q_{max}/P, the wear volume, and the wear scars under different load conditions. The maps can be divided into three areas:

(1) the coating working area: under small displacement and low normal force conditions, where the applied normal force is lower than the threshold or the transition area;

(2) the coating failure area: under large displacement and high normal force conditions, where the applied normal force is greater than the threshold or the transition area;

(3) the transition area: which only exists under the small displacement amplitude of ±20 µm, between coating working and failure areas.

In the coating working area, the coating is not or only partly removed. The substrate is well protected by the DLC coating. Q_{max}/P is low and the wear volume is small. In the coating failure area, the coating has almost been entirely removed, Q_{max}/P is high, and the wear volume is similar to that obtained from the tests without coatings. In the transition area, the coating is partly removed and Q_{max}/P receives an intermediate value.

The coating wear maps are different, depending on different contact conditions (i.e., different DLC coating types, different surface roughness, and different coating positions), which will be discussed in Section 3.

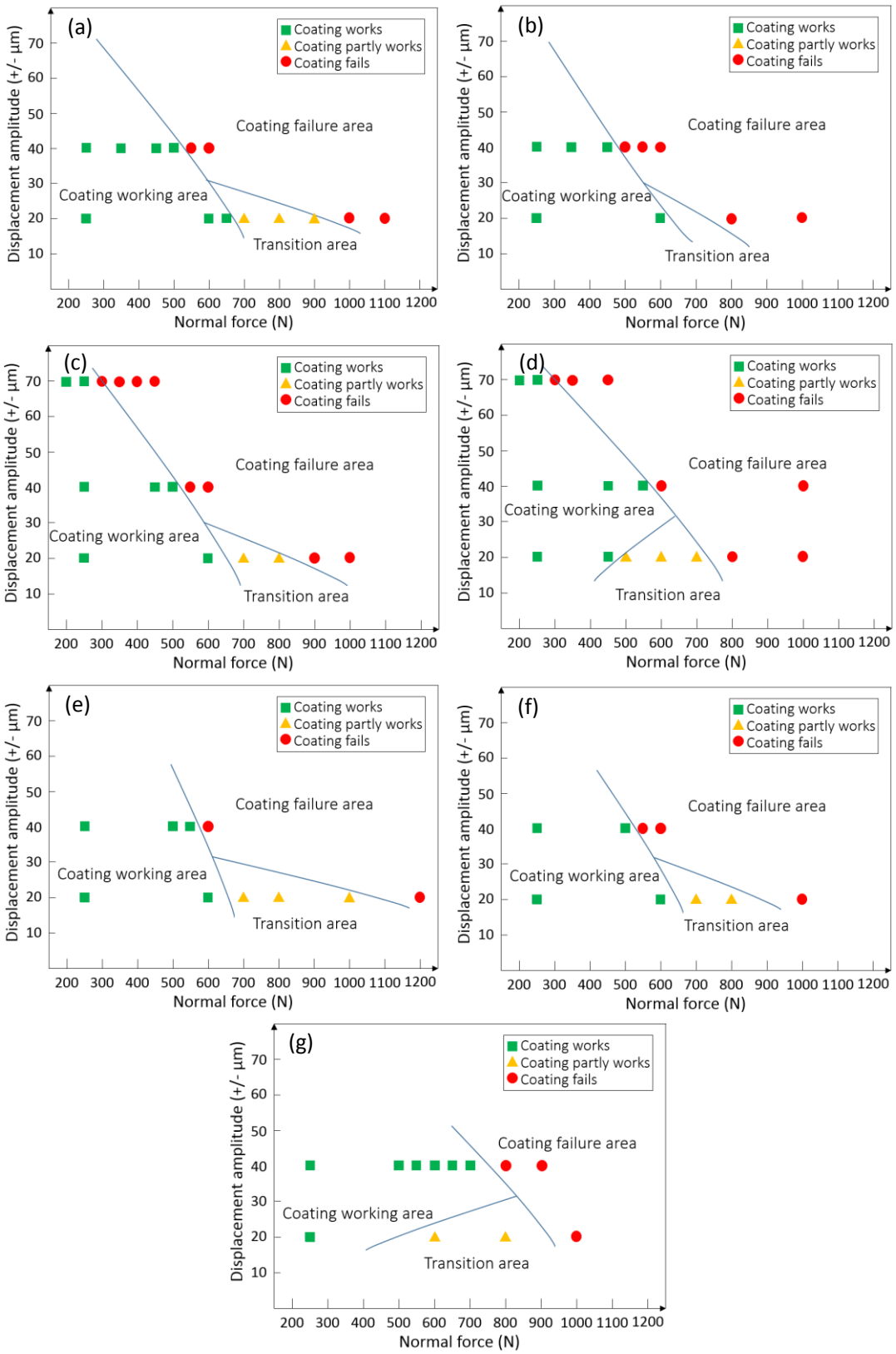

Figure IV.14. Coating response wear maps under various contact conditions:
(a) rough flat with DLC A / uncoated cylinder; (b) rough flat with DLC B / uncoated cylinder;
(c) smooth flat with DLC A / uncoated cylinder; (d) smooth flat with DLC B / uncoated cylinder;
(e) uncoated rough flat / cylinder with DLC A; (f) uncoated rough flat / cylinder with DLC B;
(g) rough flat with DLC A / cylinder with DLC A.

2.5. RCFM

Compared with the RCFM without DLC coating (Figure III.4), the presence of DLC coating renders the running conditions more complex because of the possible wear of the coating. Figure IV.15 shows the RCFM for tests with a rough flat coated with DLC A in contact with an uncoated cylinder. The RCFM can be divided into four areas:

(a) the coating working area—within the GSR,

(b) the coating failure area—within the GSR,

(c) the coating failure area—within the MSR,

(d) the transition area—within the GSR.

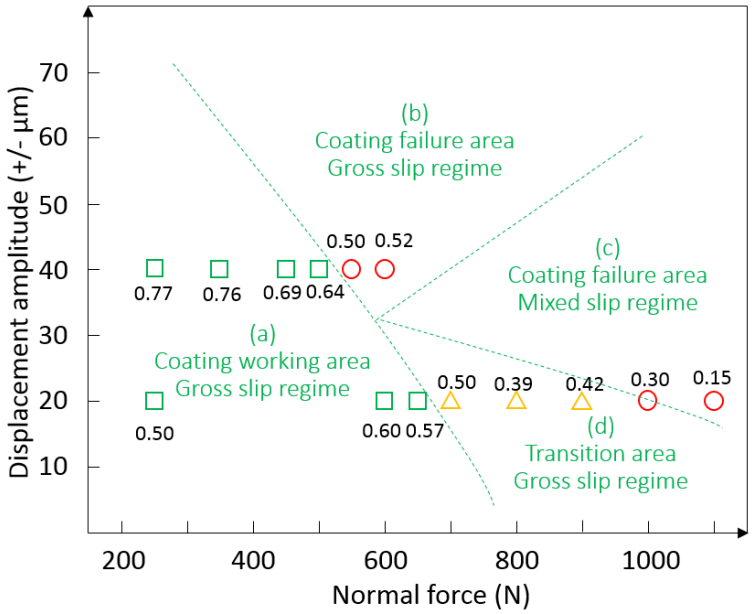

Figure IV.15. RCFM for tests with a rough flat coated with DLC A in contact with an uncoated cylinder

- **(a) coating working area—within the GSR**

In the coating working area (as shown in Figure IV.14a), the DLC coating works well during the entire test. The Ti–6Al–4V of the cylinder is mainly in contact with the DLC coating on the flat sample (Ti–6Al–4V / DLC contact). The friction coefficient (Q_{max}/P) remains at a low value. The low tangential stress and the low friction result in high values of energy ratio A. the fretting is in the GSR during the whole test.

Figure IV.16 shows the evolution of friction (Q_{max}/P), the evolution of energy ratio A, and the fretting log of a representative test with the displacement amplitude of ±20 µm and the normal force of 250 N in the area (a) coating working area–within the GSR. The friction coefficient (Q_{max}/P) is lower than 0.2 during the stable period (Figure IV.16a). The energy ratio A is high (around 0.5, Figure IV.16b). The fretting test exhibits a typical log of the GSR (Figure IV.16c).

Therefore, in the coating working area, the fretting test is always in the GSR (Figure IV.15).

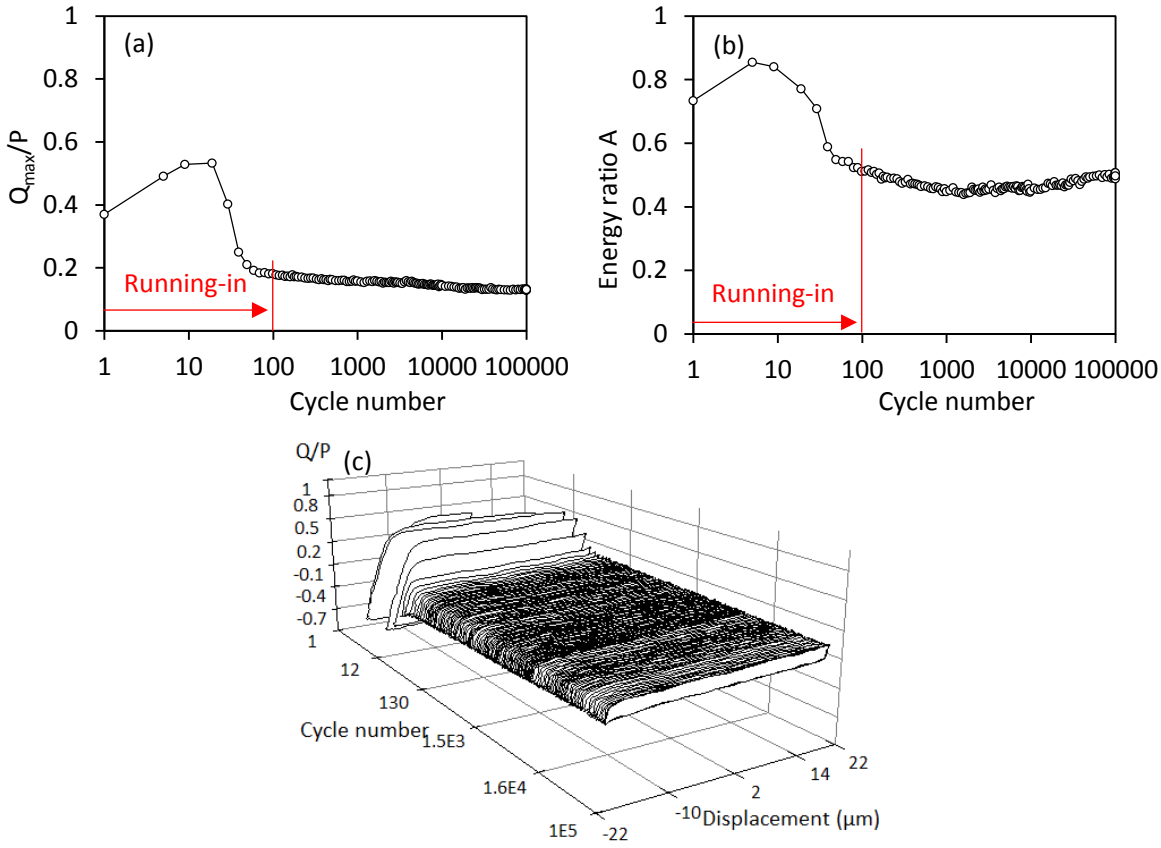

Figure IV.16. Coating working area—within the GSR, representative test under ±20 µm and 250 N: (a) evolution of Q_{max}/P; (b) evolution of energy ratio A; (c) fretting log.

- **(b) coating failure area—within the GSR**

In the coating failure area (as shown in Figure IV.14a) with a large displacement (where the fretting is in GSR for Ti–6Al–4V / Ti–6Al–4V contact, as shown in Figure III.4), the coating fails and has been removed at the beginning of the test. The Ti–6Al–4V of the cylinder is in contact directly with the substrate of the Ti–6Al–4V of the flat sample (Ti–6Al–4V / Ti–6Al–4V contact). The friction (Q_{max}/P) is high. Furthermore, the fretting test on the Ti–6Al–4V / Ti–6Al–4V contact without coating is in the GSR under the load conditions, as presented in Figure III.4. Therefore, for the test with DLC coating, the fretting still remains in the GSR after the coating is removed.

Figure IV.17 shows the evolution of friction (Q_{max}/P), the evolution of energy ratio A, and the fretting loop of a representative test with the displacement amplitude of ±40 µm and the normal force of 600 N in the area (b) coating failure area—within the GSR. The friction (Q_{max}/P) is high (around 0.6). The energy ratio A is high (around 0.5). The fretting test exhibits a typical log of the GSR.

Therefore, in the coating failure area (i.e., the coating is almost entirely removed) with a large displacement (where the fretting is in the GSR for tests without coating), the fretting test is in the GSR.

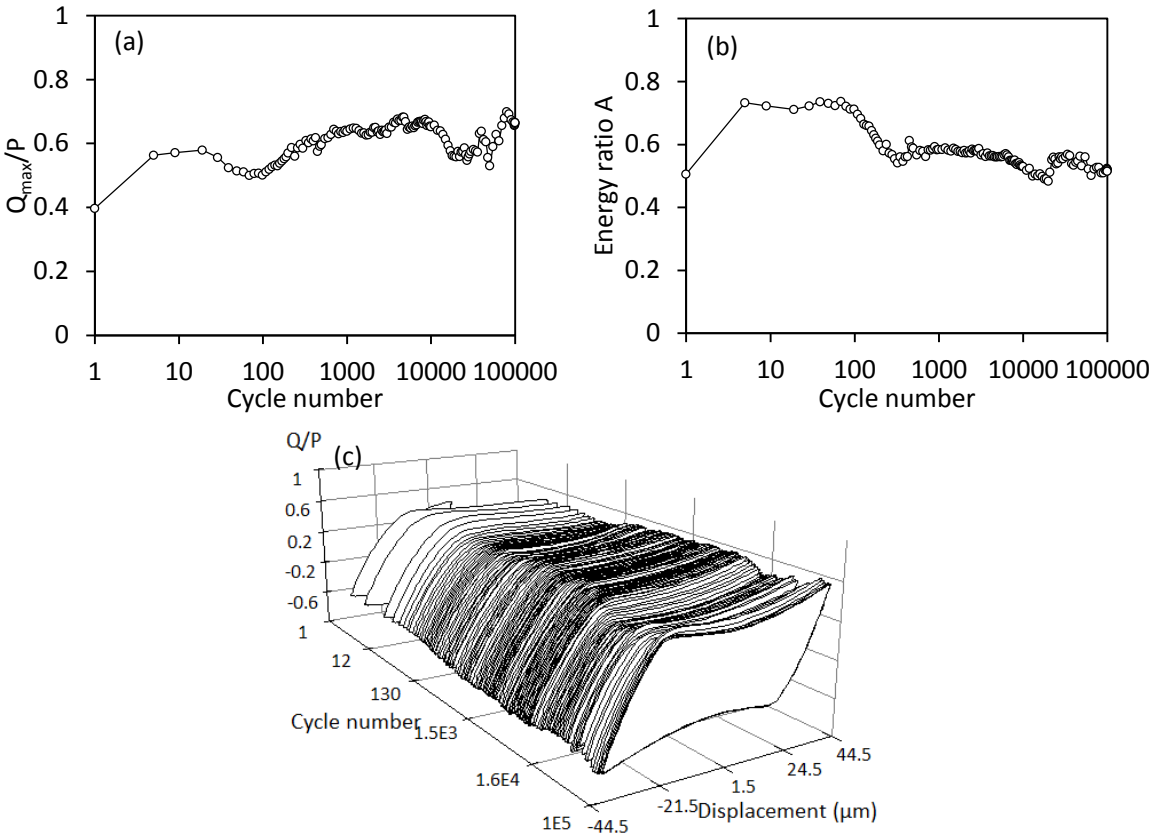

Figure IV.17. Coating failure area—within the GSR, representative test under ±40 µm and 600 N: (a) evolution of Q_{max}/P; (b) evolution of energy ratio A; (c) fretting log.

- **(c) coating failure area—within the MSR**

For tests without coatings, in the MSR, the fretting log (Figure III.2b) is composed of several gross slip loops at the beginning period of the test and, subsequently, stable partial slip loops. Therefore, regardless of the first certain cycles, the fretting is in partial slip for both the MSR and the PSR.

In the coating failure area (as shown in Figure IV.14a) with a small displacement, the entire fretting test is in the MSR (Figure IV.15).

If we consider the test under the highest normal load of 1 100 N as an example (as shown in Figure IV.18), at the beginning of the test for approximately 10 000 cycles, the friction (Q_{max}/P) is relatively low, the energy ratio A is relatively high, and the fretting is in gross slip condition because of the presence of DLC (Ti–6Al–4V / DLC contact). Furthermore, during this period, the friction shows an increase trend and the energy ratio A shows a decrease trend, because of the gradually removal of the DLC coating at the interface.

At around 10 000 cycles, the friction increases sharply to a high value (0.7–0.8) and the energy ratio A decreases sharply to a low value (0.1-0.15), which reveals that the coating totally fails. From 10 000 cycles to the end of the test, the coating is almost entirely removed. The Ti–6Al–4V of the cylinder is in contact with the Ti–6Al–4V substrate of the flat surface (Ti–

6Al–4V / Ti–6Al–4V contact). The friction is high. Energy ratio A is low. The fretting is in the partial slip condition during this period.

Therefore, the fretting is in the MSR during the entire test.

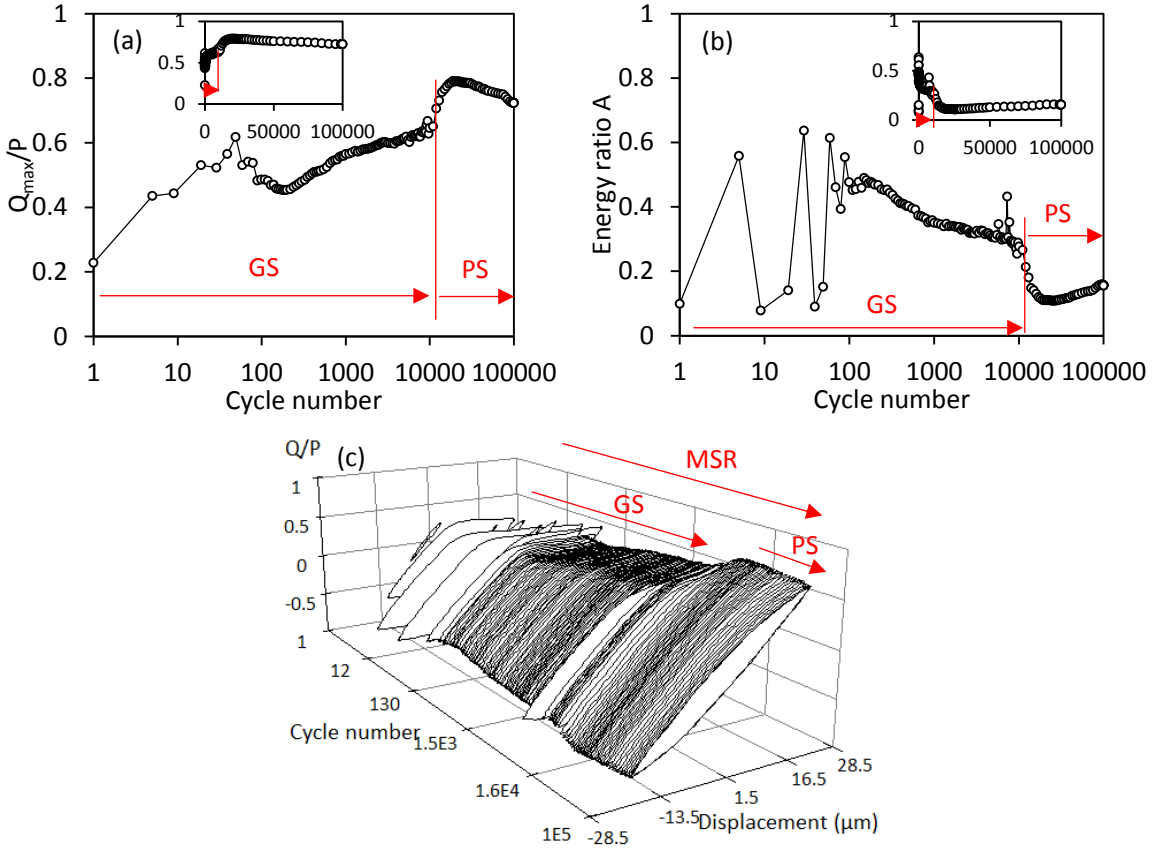

Figure IV.18. Coating failure area—within the MSR, representative test under ±20 μm and 1 100 N: (a) evolution of Q_{max}/P; (b) evolution of energy ratio A; (c) fretting log.

- **(d) transition area—within the GSR**

In the coating transition area (Figure IV.14a), the entire fretting test is in the GSR (Figure IV.15).

If we consider the test under the normal load of 800 N as an example (as shown in Figure IV.19), at the beginning of the test for approximately 20 000 cycles, the friction (Q_{max}/P) is relatively low, the energy ratio A is relatively high, and the fretting is in gross slip condition.

After that, the coating still partly works. The coating is partly removed at the end of the test. The Ti–6Al–4V of the cylinder is in contact with both the DLC coating (mild wear area, Ti–6Al–4V / DLC contact) and the substrate of the flat surface (severe wear area, Ti–6Al–4V / Ti–6Al–4V contact). The friction is in the range of 0.4–0.7. And the energy ratio is in the range of 0.3–0.5. The fretting is still in the gross slip condition until the completion of the test.

Therefore, the fretting is in the GSR during the entire test.

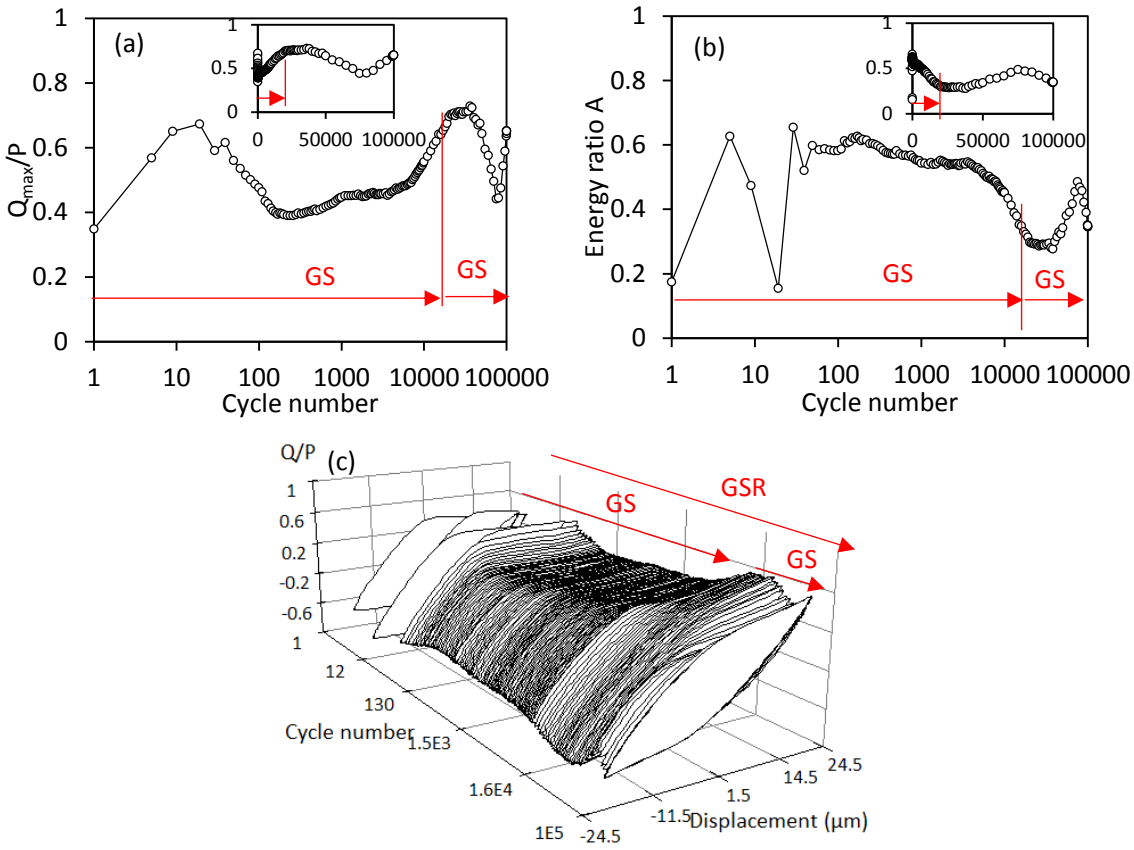

Figure IV.19. Transition area—within the GSR, representative test under ±20 μm and 800 N: (a) evolution of Q_{max}/P; (b) evolution of energy ratio A; (c) fretting log.

- **Conclusions**

RCFM for tests with DLC coating (rough flat coated with DLC A / uncoated cylinder) can be divided into four areas under the given displacement and normal force conditions: (a) the coating working area—within the GSR, (b) the coating failure area—within the GSR, (c) the coating failure area—within the MSR, and (d) the transition area—within the GSR.

2.6. Wear debris

For tests with DLC coatings, wear debris was collected, observed and analyzed. The surface damage in the severe wear area was obviously different with that in the mild wear area. Thus, the wear debris from severe wear area was compared with the wear debris from mild wear area.

- **Wear debris from the severe wear area**

Figure IV.20 shows the wear debris from the test with DLC coating under the high load condition, i.e., DLC B coated flat / uncoated cylinder contact under the displacement amplitude of ±70 μm and the normal force of 300 N. The test lies in the coating failure area, and the wear scars of the flat and cylinder samples are just composed of severe wear areas.

The debris is composed of flakes, powder and DLC particles. The flakes and powder are similar to those from tests without the coating, i.e., the flake is Ti–6Al–4V and the powder is

severely oxidized. The size of the Ti–6Al–4V flake reaches around 100 µm (Figure IV.20a), which is smaller than the size of Ti–6Al–4V flake from test without coating. The size of oxidized powder is similar to the size of oxidized powder from test without coating (in the range between tens of nanometers and two micrometers, Figure IV.20 b). The DLC particles are due to the delamination of the DLC coating. The thickness of the DLC particle is similar to the coating thickness (around 2 µm, Figure IV.20b).

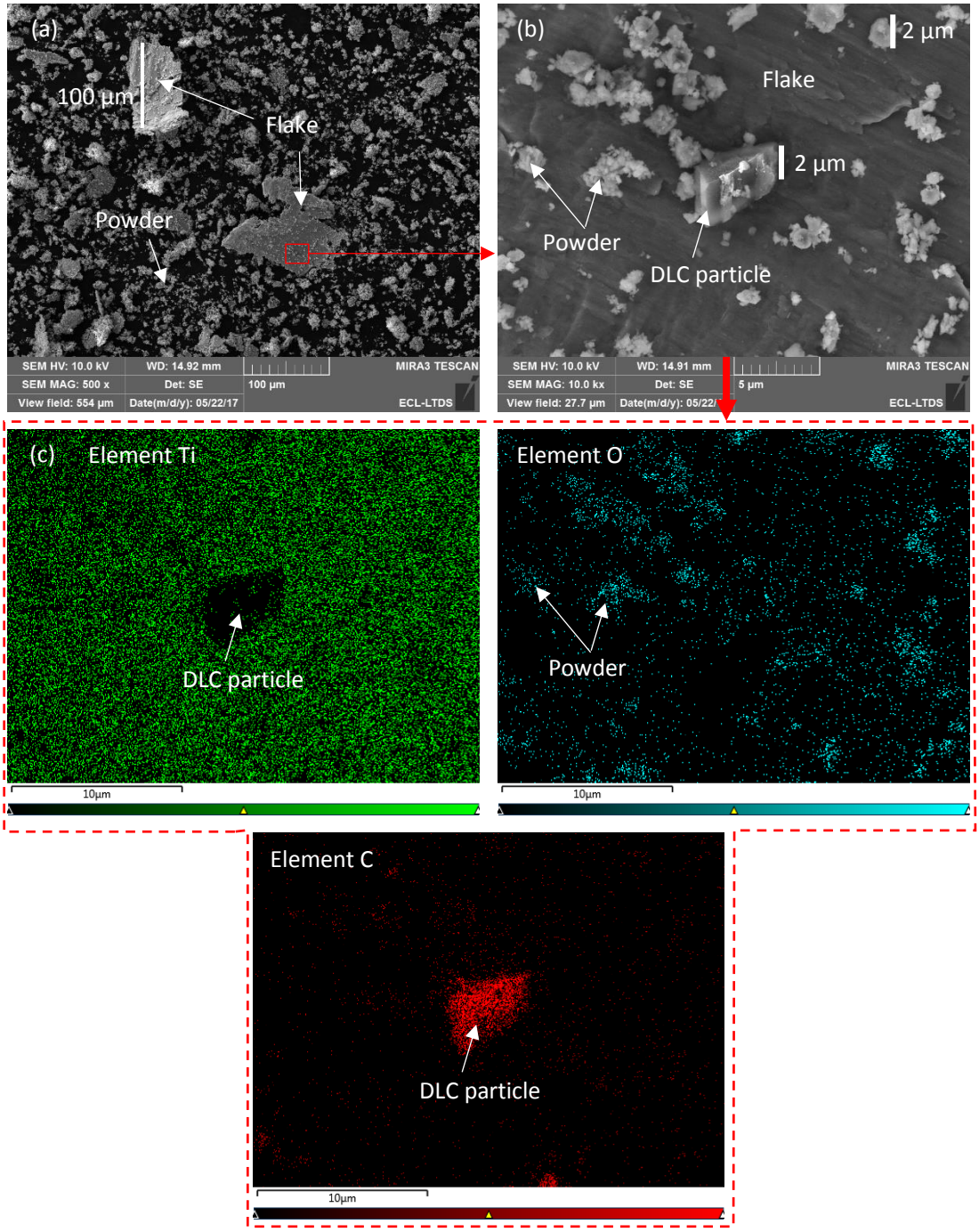

Figure IV.20. SEM and EDX observations of the wear debris from the test with coating in the coating failure area with the displacement amplitude of ±70 µm and normal force of 300 N:
(a) large scale; (b) small scale; (c) EDX of figure (b).

- **Wear debris from the mild wear area**

For the tests with the DLC coating under low load conditions, such as under the displacement amplitude of ±20 µm and the normal force of 250 N, the test is in the coating working area, and the contact surfaces are just composed of mild wear area. In the coating working area, too less debris was collected for SEM observation. It is impossible to observe the sample through the SEM before cleaning because the debris may be noxious to the SEM system. But we could get some information about the wear debris via observing the rubbed sample before cleaning using the optical microscopy (OM), as shown in Figure IV.21.

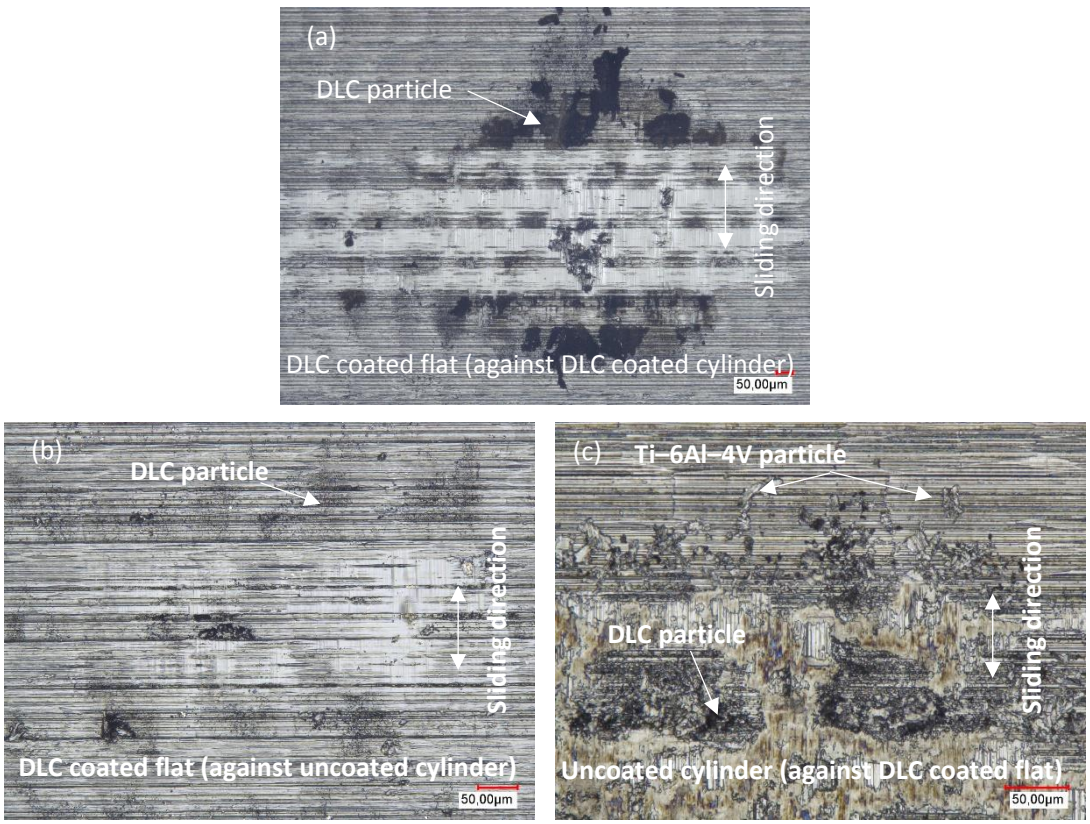

Figure IV.21. OM observation of rubbed surfaces before cleaning for tests under the low load condition with the displacement amplitude of ±20 µm and the normal force of 250 N: (a) a DLC coated flat (in contact with a DLC coated cylinder) at 100 000 cycles; (b) a DLC coated flat contact with (c) an uncoated cylinder after 100 cycles.

For the test with the DLC coated flat in contact with a DLC coated cylinder under the lowest load condition (±20 µm and 250 N), as shown in Figure IV.21a, the contact surfaces are almost totally covered by the DLC coating after 100 000 cycles. The black powder and its aggregation are DLC particles.

For the test with the DLC coated flat in contact with the uncoated cylinder under the lowest load condition, after 100 cycles, similar black powder of DLC particles are observed on the coated flat surface, as shown in Figure IV.21b. On the uncoated cylinder surface, except the black DLC particles, Ti–6Al–4V particles are observed as a consequence of abrasion, as shown in Figure IV.21c. Furthermore, a tribofilm (i.e. oxidized Ti–6Al–4V) was formed on the

uncoated cylinder surface and it would fragment during the test. Therefore, the wear debris is composed of DLC particles, Ti–6Al–4V particles and the oxidized Ti–6Al–4V particles at the end of the test under this condition.

- **Conclusions**

Wear debris from tests with coating is different from the debris from tests without coating. Without coating, wear debris was composed of Ti–6Al–4V flakes and oxidized powder. With coating, wear debris was composed of Ti–6Al–4V flakes, oxidized powder and DLC particles.

2.7 Cracks inside DLC coating

In order to improve the cohesion between the hard DLC coating and the soft Ti–6Al–4V substrate, a Si-rich interlayer was applied, as shown in Figure II.7. Under a low local contact pressure, the DLC coating material was worn off and no cracks were generated, as shown in Figure IV.7d. Under a high local contact pressure, the DLC coating including the Si-rich interlayer fractured and was removed as a whole. Under an intermediate local contact pressure, cracks could be generated between the upper layer and the Si-rich interlayer, as shown in Figure IV.22a. Then the upper layer could be delaminated, as shown in Figure IV.22b.

It can be concluded that the cohesion between the Si-rich layer and the Ti–6Al–4V substrate is stronger than the cohesion between the interlayer and the upper layer of the DLC coating.

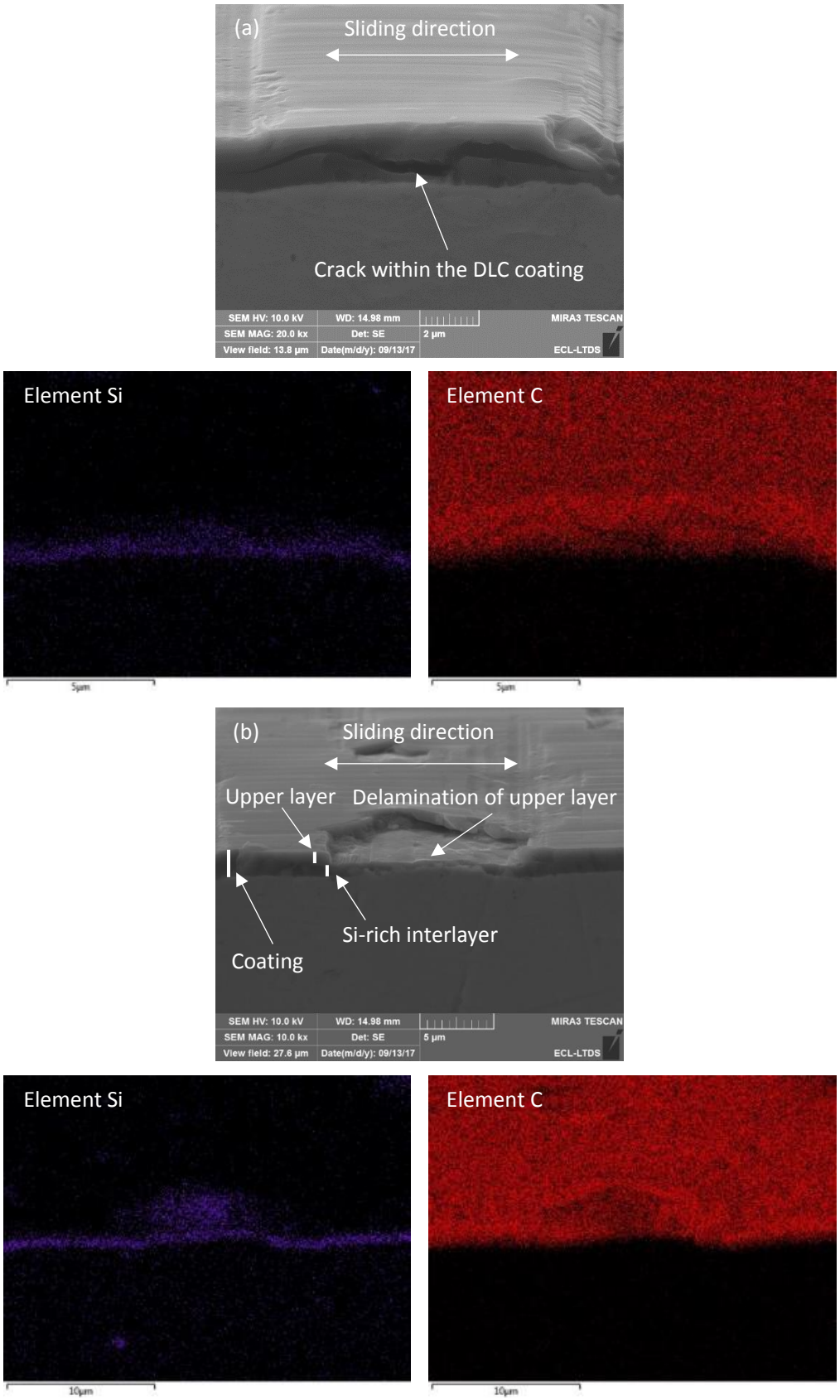

Figure IV.22. SEM and EDX observations of cross sections of DLC coated flat sample under intermediate local contact pressures: (a) the crack generated between the Si-rich layer and the upper layer; (b) the upper layer delaminates. Note that the test was conducted with a displacement amplitude of ±20 µm and the normal force of 600 N.

2.8 Conclusions

In this section, tribological performance of tests with DLC coatings was presented, including the friction, the wear volume, the surface damage, and the wear debris. The results were significantly different from the results from tests without coating. Coating response wear maps were then drawn according to the analysis of the friction, wear volume and wear scars. The maps were divided into three areas: coating working area, coating failure area, and transition area.

Obviously, the tribological performance of DLC coating was different depending on different parameters, including the DLC coating types (DLC A or DLC B), the substrate roughness (smooth surface or rough surface), and the coating positions (coating on flat, or on cylinder, or on both). The effect of parameters on fretting behavior of DLC coating will be discussed in detail in the following section.

3. Effect of parameters on fretting behavior

In this section, the effect of parameters on fretting behavior of DLC coating is discussed in detail. Specifically, the tribological properties of DLC A are compared with those of DLC B. The tribological performance of DLC coatings deposited on rough flat is compared with that on smooth flat. The fretting behaviors of tests with different coating positions (coated flat / uncoated cylinder, uncoated flat / coated cylinder, and coated flat / coated cylinder) are compared.

3.1. Comparison of different DLC coatings

Two DLC coatings, namely the DLC A and DLC B coatings, were studied in this work. Three contact configurations were used: coated rough flat / uncoated cylinder contacts, coated smooth flat / uncoated cylinder contacts, and uncoated rough flat / coated cylinder contacts. DLC A and DLC B exhibited different tribological performance in our test conditions.

- **Coated rough flat / uncoated cylinder contacts**

Figure IV.23 shows the comparison of simplified coating response wear maps for coatings DLC A and DLC B with coated rough flat / uncoated cylinder contacts.

Under the displacement amplitude of ±40 µm, the threshold of DLC A is 50 N higher than DLC B. The threshold of DLC A lies between 500 N and 550 N, while the threshold of DLC B lies between 450 N and 500 N.

Under the displacement amplitude of ±20 µm, the transition area of DLC A is higher than DLC B. The transition area of DLC A is between 650 N and 1 000 N, while, the transition area of DLC B is between 600 N and 800 N.

The coating working area of DLC A is larger than that of DLC B with coated rough flat / uncoated cylinder contacts.

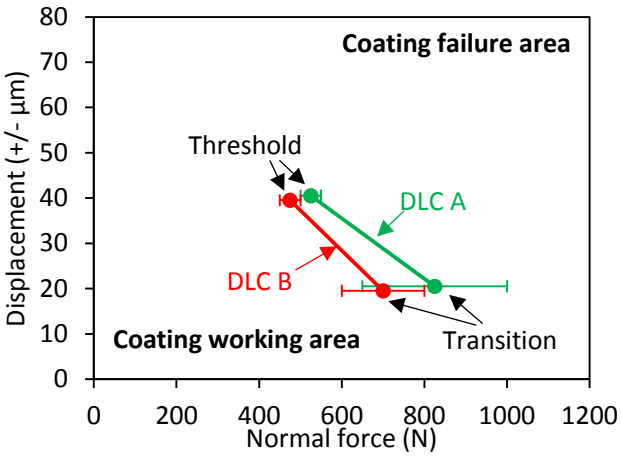

Figure IV.23. Comparison of coating response wear maps for DLC A and DLC B with coated rough flat / uncoated cylinder contacts.

In the coating working area, Q_{max}/P is low and has similar values for both the DLC A and the DLC B coatings. The wear volume is always near 0 and presents no obvious difference among different coatings. The wear scars, however, can be used to evaluate the extent of coating damage. The damage extent can be characterized by a parameter referred to as the coating removed proportion, which is defined as the ratio of the total length of the severe wear areas (L_{severe}-1 + L_{severe}-2 +…+ L_{severe}-n) over the flat–cylinder contact length (L_{total}), as shown in Figure IV.24. A higher value of the coating removed proportion means that the coating is damaged more severely.

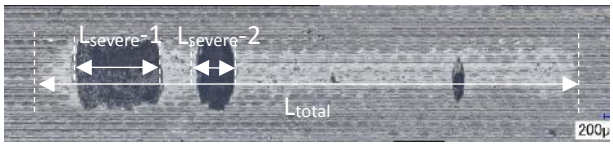

Figure IV.24. Definition of coating removed proportion.

Figure IV.25 shows the values of the coating removed proportion under the coating working area conditions. It is clear that the values for the DLC B coating are higher than those for the DLC A coating under the same load condition; this means that the damage of DLC B coating is more severe than the damage of DLC A coating.

Furthermore, the displacement amplitude and the normal force have effect on the values of coating removed proportion. Under larger displacement and higher normal force conditions, higher values are obtained; this means that the coating damage is more severe under a higher load condition.

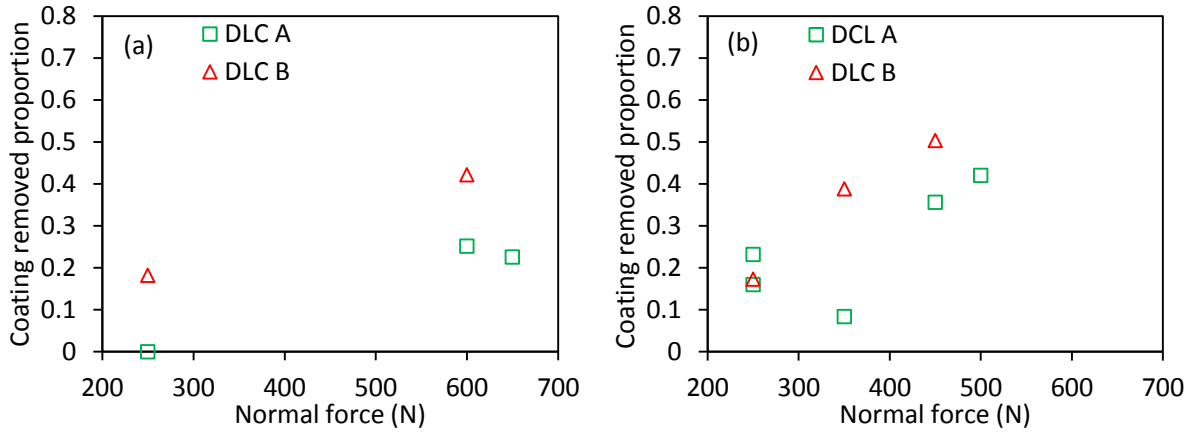

Figure IV.25. Coating removed proportion in coating working area conditions for tests with coated rough flat / uncoated cylinder contacts: (a) ±20 µm; (b) ±40 µm.

- **Coated smooth flat / uncoated cylinder contacts**

Figure IV.26 shows the comparison of simplified coating response wear maps for coatings DLC A and DLC B with coated smooth flat / uncoated cylinder contacts.

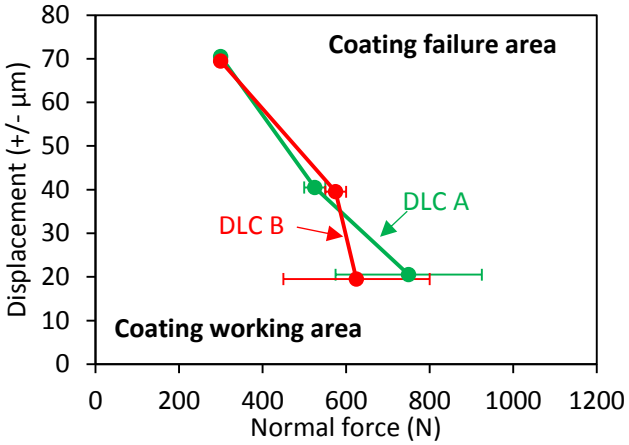

Figure IV.26. Comparison of coating response wear maps for DLC A and DLC B with coated smooth flat / uncoated cylinder contacts.

Under the large displacement amplitude of ±70 µm, DLC A and DLC B coatings exhibit the same threshold value in the normal force (namely 300 N, as shown in Figure IV.26). Figure IV.27 shows the evolution of Q_{max}/P for both DLC A and DLC B under ±70 µm conditions. When the applied normal force is lower (250 N) than the threshold, Q_{max}/P is low and remains stable during the entire test; this means that both the DLC A and DLC B coatings work until the completion of the test. When the normal force is higher (350 N) than the threshold, Q_{max}/P increases drastically at the beginning, and then remains high and stable until the end; this means that both the DLC A and DLC B coatings failed at the beginning of the test. With a value of threshold of 300 N, Q_{max}/P remains low at the beginning of the test; it then sharply increases to a very high value. The number of cycles by which Q_{max}/P has sharply increased, can be regarded as the service life of the coating. The service life of the DLC A coating is approximately

60 000 cycles, which is greater than the service life of the DLC B coating (approximately 40 000 cycles).

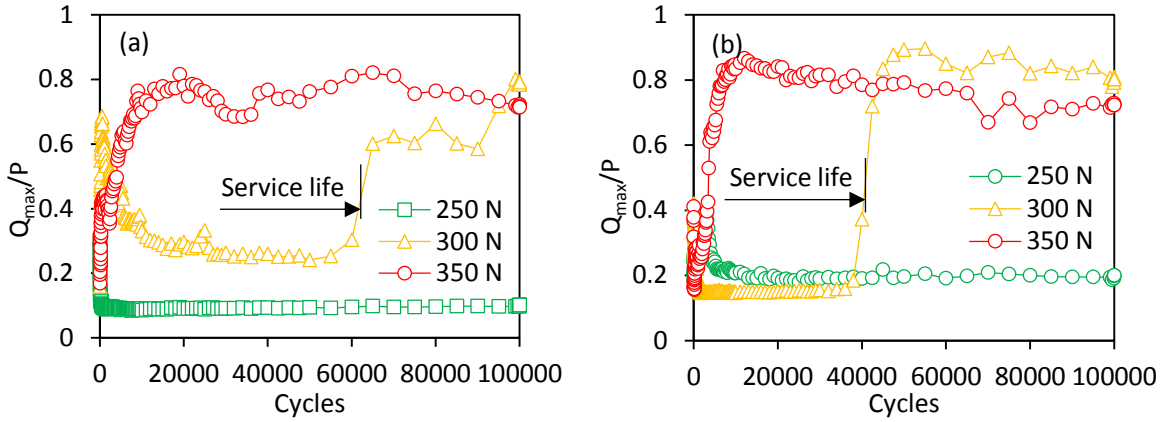

Figure IV.27. Evolution of Q_{max}/P with the number of cycles for tests on smooth flat surfaces under the ±70 µm displacement condition for various values of normal force:
(a) DLC A coating; (b) DLC B coating.

Under the displacement amplitude of ±40 µm (Figure IV.26), the threshold of DLC A is 50 N lower than DLC B. The threshold of DLC A lies between 500 N and 550 N, while the threshold of DLC B lies between 550 N and 600 N.

Under the displacement amplitude of ±20 µm, the transition area of DLC A is higher than DLC B. The transition area of DLC A is between 600 N and 900 N, while, the transition area of DLC B is between 450 N and 800 N.

Figure IV.28 shows the values of the coating removed proportion for tests with coated smooth flat under the coating working area conditions. It is clear that under the lowest conditions (normal force of 250 N), the values of the coating removed proportion are 0 for both the DLC A and the DLC B coatings. Under relatively larger displacement and higher normal force conditions, the values of the DLC B coating are higher than those of the DLC A coating; this means that the damage in the DLC B coating is more severe than that in the DLC A coating under the same load condition.

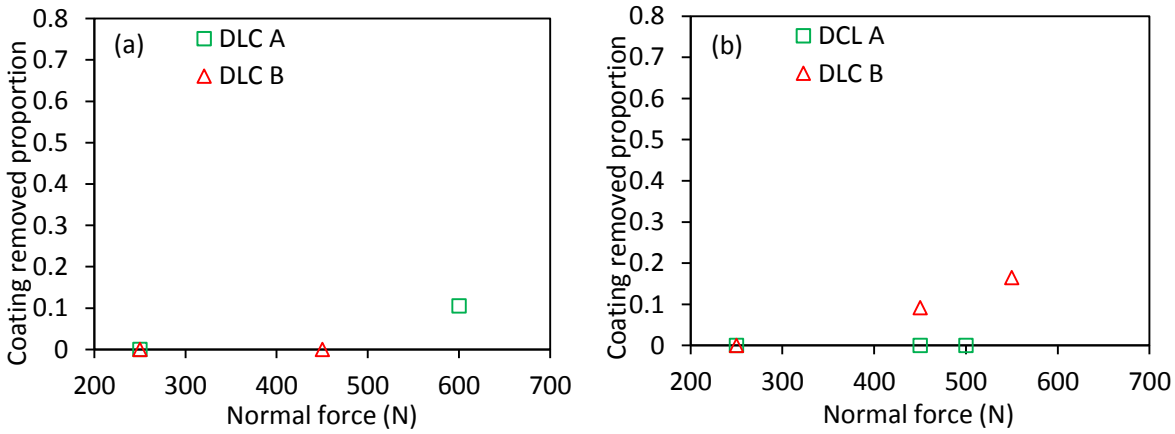

Figure IV.28. Coating removed proportion in coating working area conditions for tests with coated smooth flat / uncoated cylinder contacts: (a) ±20 µm; (b) ±40 µm.

- **Uncoated rough flat / coated cylinder contacts**

Figure IV.29 shows the comparison of simplified coating response wear maps for coatings DLC A and DLC B with uncoated rough flat / coated cylinder contacts.

Under the displacement amplitude of ±40 µm, the threshold of DLC A is 50 N higher than DLC B. The threshold of DLC A lies between 550 N and 600 N, while the threshold of DLC B lies between 500 N and 550 N.

Under the displacement amplitude of ±20 µm, the transition area of DLC A is higher than DLC B. The transition area of DLC A is between 600 N and 1 200 N, while, the transition area of DLC B is between 600 N and 1 000 N.

The coating working area of DLC A is larger than that of DLC B with uncoated rough flat / coated cylinder contacts.

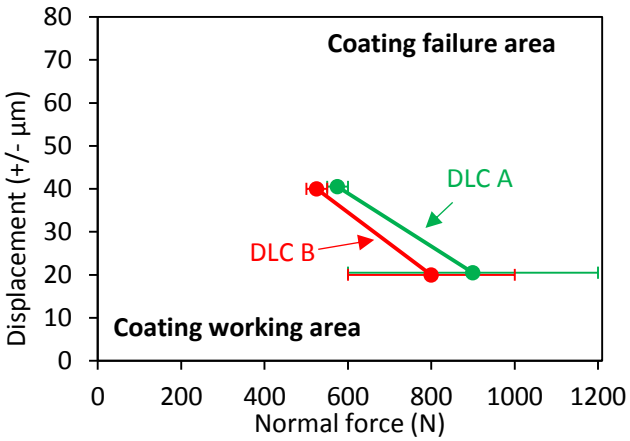

Figure IV.29. Comparison of coating response wear maps for DLC A and DLC B with uncoated rough flat / coated cylinder contacts.

Figure IV.30 shows the values of the coating removed proportion for tests with uncoated rough flat / coated cylinder contacts under the coating working area conditions. It is clear that under the lowest conditions (displacement amplitude of ±20 µm and normal force of 250 N, respectively), the values of the coating removed proportion are 0 for both the DLC A and the DLC B coatings. In other cases, the values of the DLC B coating are higher than those of the DLC A coating; this means that the damage in the DLC B coating is more severe than that in the DLC A coating under the same load condition.

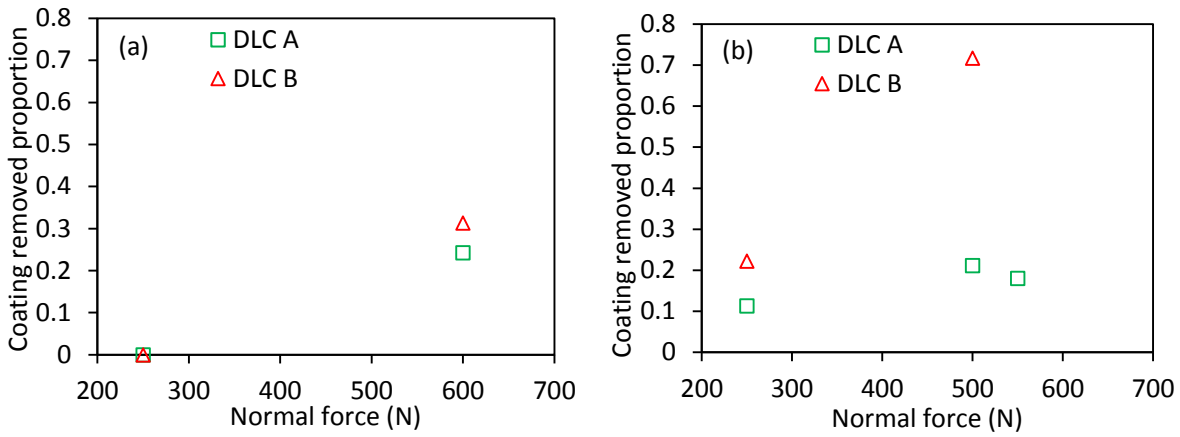

Figure IV.30. Coating removed proportion in coating working area conditions for tests with uncoated rough flat / coated cylinder contacts: (a) ±20 µm; (b) ±40 µm.

- **Conclusions**

Overall, the DLC A coating presented better tribological properties than the DLC B coating.

For coated rough flat / uncoated cylinder contacts (Figure IV.23) and for uncoated rough flat / coated cylinder contacts (Figure IV.29), coating working area of DLC A was larger than that of DLC B. For coated smooth flat / uncoated cylinder contacts (Figure IV.26), the coating working area of DLC A was similar to that of DLC B.

About the coating removed proportion, the values of DLC A were lower than those of DLC B under the same load condition in the coating working area (Figure IV.25, Figure IV.28, and Figure IV.30), which means that that the damage in the DLC A coating was milder than that in the DLC B coating.

The better tribological performance of DLC A could be attributed to its higher hardness. Specifically, when coatings function well, the fretting test was in the GSR. The hardness generally has a positive influence on the tribology properties under the gross slip condition. Therefore, the DLC A coating, which presented higher hardness, had better tribological performance than the DLC B coating.

However, in this thesis, only two types of DLC coatings (DLC A and DLC B) were compared. But, in order to get more information about the influence of mechanical properties of DLC coatings on their tribological performance, more DLC coatings with different mechanical properties should be studied.

3.2. Surface roughness

Two types of roughness on the flat surface were investigated in this thesis, namely the rough flat and smooth flat surfaces. The DLC coatings exhibited different tribological performances when deposited on different flat surfaces (rough flat and smooth flat).

- **Coating DLC A**

Figure IV.31 shows the comparison of simplified coating response wear maps for DLC A deposited on different flats (rough flat and smooth flat). Tests were conducted with a coated flat / uncoated cylinder contact.

Under the displacement condition of ±40 µm, the threshold value of normal force is the same for both the rough and the smooth flat samples (between 500 N and 550 N). Under the displacement condition of ±20 µm, the transition area for a smooth flat surface is slightly lower than the rough flat surface. Therefore, the coating working area of DLC A on a smooth flat is similar to that on a rough flat especially under the large displacement amplitude of ±40 µm.

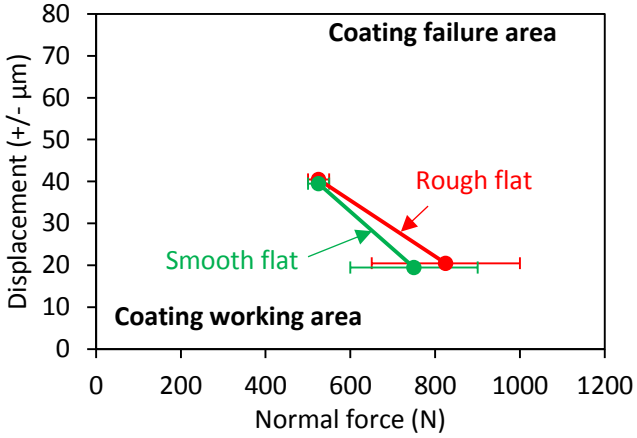

Figure IV.31. Comparison of coating response wear maps for tests with different surface roughness: flat coated with DLC A / uncoated cylinder contacts.

Figure IV.32 shows the values of coating removed proportion of DLC A for tests with different flat surface roughness under the coating working area conditions. It is clear that under the lowest conditions (displacement amplitude of ±20 µm and normal force of 250 N), the values of the coating removed proportion are 0 for both the rough and smooth flats. In other cases, the values of rough flat are higher than those of smooth flat; this means that the damage of DLC A coating is more severe when deposited on a rough flat than on a smooth flat.

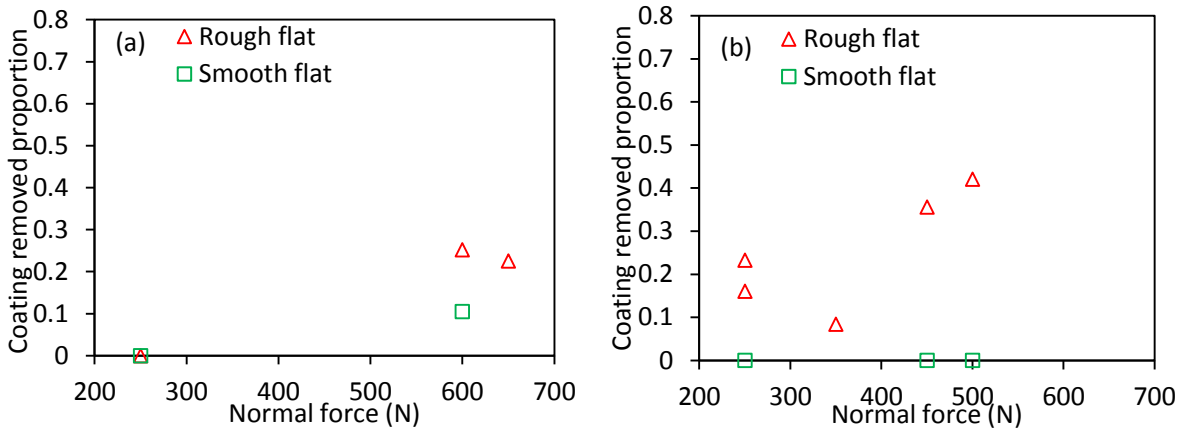

Figure IV.32. Coating removed proportion in coating working area conditions for tests with different flat surface roughness, with the contact of flat coated with DLC A / uncoated cylinder: (a) ±20 µm; (b) ±40 µm.

- **Coating DLC B**

Figure IV.33 shows the comparison of simplified coating response wear maps for DLC B deposited on different flat surface roughness. Tests were conducted with a coated flat / uncoated cylinder contact.

Under the displacement condition of ±40 µm, the threshold value of the normal force on a smooth flat is obviously higher than that on a rough flat. Under the displacement condition of ±20 µm, the transition area for a smooth flat surface is slightly lower than the rough flat surface. Therefore, the coating working area of DLC B coated on a smooth flat is larger than that on a rough flat under the large displacement amplitude of ±40 µm.

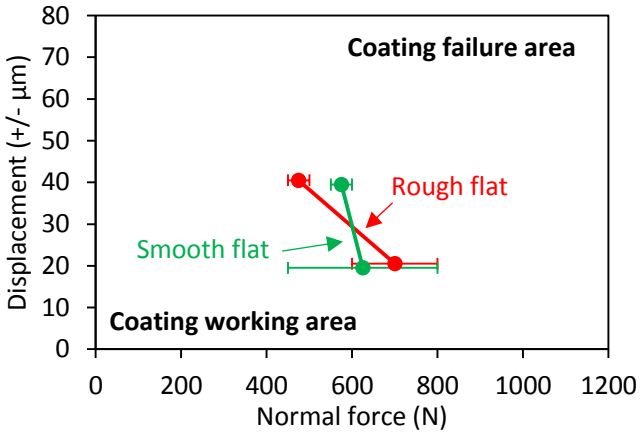

Figure IV.33. Comparison of coating response wear maps for tests with different surface roughness: flat coated with DLC B / uncoated cylinder contacts.

Figure IV.34 shows the values of the coating removed proportion of DLC B for tests with different flat surface roughness under the coating working area conditions. It is clear that the values of rough flat are obviously higher than those of the smooth flat; this means that the damage of DLC B coating is more severe when deposited on a rough flat than on a smooth flat under the same load condition.

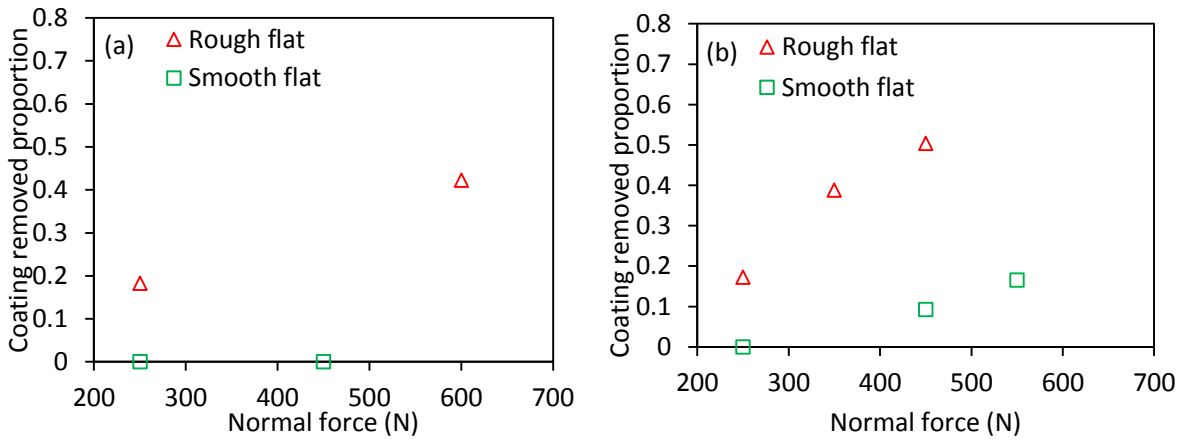

Figure IV.34. Coating removed proportion in coating working area conditions for tests with different flat surface roughness, with the contact of flat coated with DLC B / uncoated cylinder:
(a) ±20 µm; (b) ±40 µm.

- **Conclusions**

Overall, DLC coatings on a smooth surface presented better tribological performance than on a rough surface.

For DLC A, the coating working area of the coating deposited on a smooth flat surface was similar to deposited on a rough flat. For DLC B, coating working area of the coating deposited on a smooth flat was larger than deposited on a rough flat under the large displacement amplitude of ±40 µm.

About the coating removed proportion, the values of DLC coating on a smooth flat were lower than those on a rough flat under the same load condition in the coating working area (Figure IV.32 and Figure IV.34), which means that the damage of DLC coating was milder when deposited on a smooth flat than on a rough flat under the same load condition.

The better tribological performance of DLC coatings deposited on a smooth surface could be explained as following: for tests on smooth flat surfaces, the asperities from the rough cylinder were in contact with a smooth flat surface. However, for tests on rough flat surfaces, the contact between asperities from the rough flat surface and the rough cylinder surface led to higher local contact pressure. Furthermore, the DLC coating, as a type of hard coating, is sensitive to contact pressure. Therefore, DLC coatings on smooth surfaces exhibited better tribological performance than on rough surfaces.

3.3. Coating positions

Fretting tests were carried out with different coating positions: (1) coating on the flat, (2) coating on the cylinder, and (3) coating on both the flat and the cylinder. In this section, the fretting performance of coating on flat is compared with that of coating on cylinder firstly. Then, the fretting performance of coating on both flat and cylinder surfaces is compared with that of coating on one of the contact surfaces.

3.3.1. Coating on flat *vs.* coating on cylinder

- **Coating DLC A**

Figure IV.35 shows the comparison of simplified coating response wear maps for DLC A deposited on different substrate curvatures (on flat and on cylinder).

Under the displacement condition of ±40 µm, the threshold value of the normal force for coating on the cylinder (between 550 N and 600 N) is 50 N higher than that of coating on the flat (between 500 N and 550 N).

Under the displacement amplitude of ±20 µm, the transition area lies at similar range of normal forces. The transition area for tests with coating on the flat is between 650 N and 1 000 N, while, the transition area for tests with coating on the cylinder is between 600 N and 1 200 N.

The coating working area of DLC A deposited on cylinder is larger than deposited on flat under the displacement amplitude of ±40 µm.

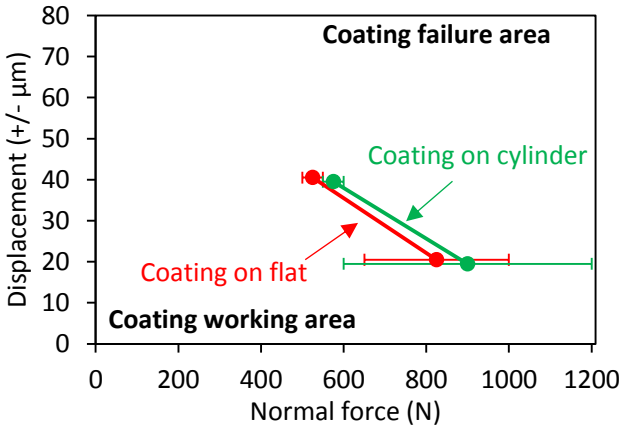

Figure IV.35. Comparison of coating response wear maps for tests with DLC A: coating on flat or coating on cylinder.

Figure IV.36 shows the values of the coating removed proportion of DLC A for tests with different substrate curvatures under the coating working area conditions. It is clear that under the displacement amplitude of ±20 µm, the values of the coating removed proportion are similar for tests on the flat or on the cylinder under the same load condition. Under the displacement amplitude of ±40 µm, the values of the coating removed proportion for tests with the coating on flat are higher than those of the coating on cylinder; this means that the damage of DLC A coating is more severe when deposited on flat surface than on cylinder surface under the same load condition.

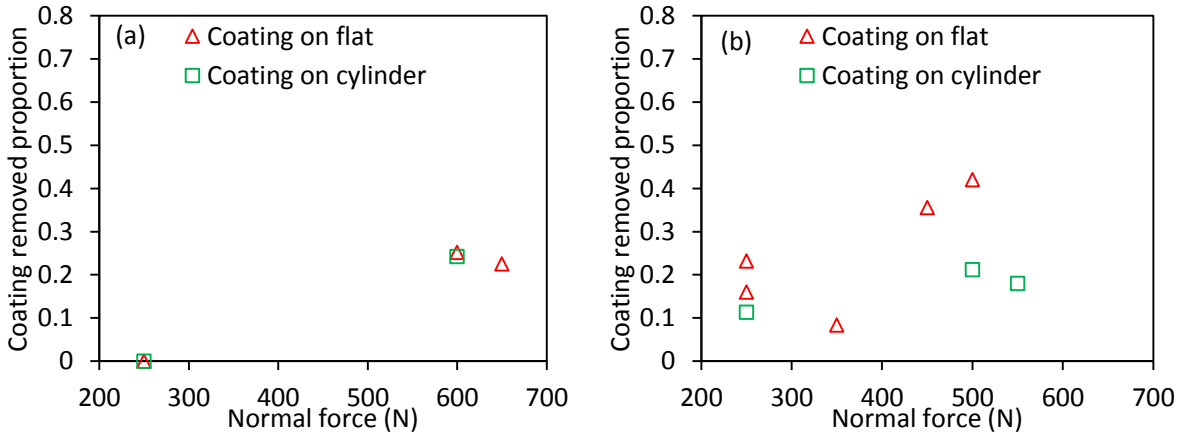

Figure IV.36.Coating removed proportion in coating working area conditions for tests with DLC A coating on the flat or on the cylinder: (a) ±20 µm; (b) ±40 µm.

- **Coating DLC B**

Figure IV.37 shows the comparison of simplified coating response wear maps for DLC B deposited on different substrate curvatures (on flat and on cylinder).

Under the displacement condition of ±40 µm, the threshold value of the normal force for coating on the cylinder (between 500 N and 550 N) is 50 N higher than that of coating on the flat (between 450 N and 500 N).

Under the displacement amplitude of ±20 µm, the transition area lies at similar range of normal forces. The transition area for tests with coating on the flat is between 600 N and 800 N, while, the transition area for tests with coating on the cylinder is between 600 N and 1 000 N.

The coating working area of DLC B deposited on cylinder is larger than deposited on flat.

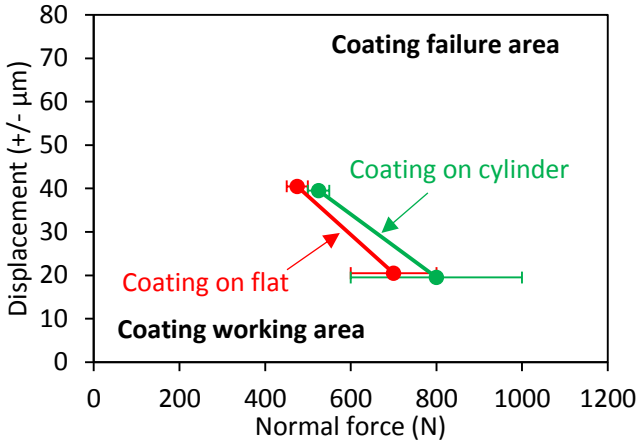

Figure IV.37. Comparison of coating response wear maps for tests with DLC B: coating on flat or coating on cylinder.

Figure IV.38 shows the values of the coating removed proportion of DLC B for tests with different substrate curvatures under the coating working area conditions. It is clear that under the displacement amplitude of ±20 µm, the values of the coating removed proportion for tests with coating on the flat are higher than those on the cylinder. Under the displacement amplitude of ±40 µm, the values of the coating removed proportion are similar for tests with coating on the flat or on the cylinder under the same load condition.

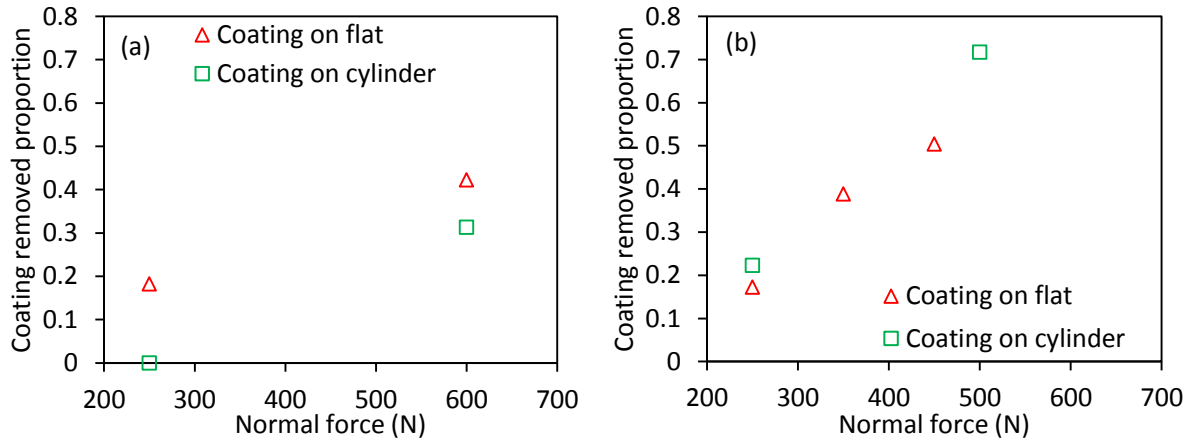

Figure IV.38.Coating removed proportion in coating working area conditions for tests with DLC B coating on the flat or on the cylinder: (a) ±20 µm; (b) ±40 µm.

- **Conclusions**

Overall, the DLC coatings deposited on the cylinder surface had slightly better tribological performance deposited on the flat surface.

For both DLC A and DLC B, the coating working area was larger when it was deposited on the cylinder than deposited on the flat (Figure IV.35 and Figure IV.37).

About the coating removed proportion, the values of coating removed proportion on the cylinder were similar to or lower than those of coating removed proportion on the flat under the same load condition in the coating working area (Figure IV.36 and Figure IV.38), which means that that the damage in coating was milder when it was deposited on the cylinder than deposited on the flat.

This is perhaps because the local pressure on the cylinder surface was static regardless of the roughness under fretting conditions (reciprocating motions). However, the local pressure on the flat surface changed periodically. The periodically change in the pressure might accelerate the failure of the hard DLC coatings.

3.3.2. Coating on one surface *vs.* coating on both surfaces

Figure IV.39 shows the simplified coating response wear map for DLC A deposited on both the flat and the cylinder. Under the displacement condition of ±40 µm, the threshold value of the normal force for coating on both contact surfaces (between 700 N and 800 N) is significantly higher than that of coating on one of the contact surfaces (around 500 N). However, under the displacement amplitude of ±20 µm, the transition area for tests with coating on both contact surfaces lies at lower normal forces than that for coating on one of the contact surfaces.

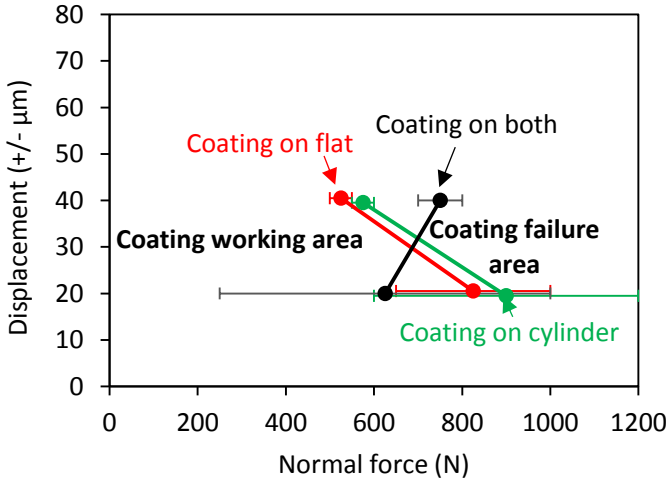

Figure IV.39. Simplified coating response wear map for tests with DLC A on both the flat and the cylinder.

Figure IV.40 shows the values of the coating removed proportion of DLC A for tests with coating on both contact surfaces. It is clear that under the displacement amplitude of ±20 µm and normal force of 250 N, the value of the coating removed proportion is 0 for the test with coating on both contact surfaces and for the test with coating on one of the contact surfaces.

Under other load conditions, the values of the coating removed proportion are much higher for tests with coating on both contact surfaces than those for tests with coating on one of the contact surfaces; this means that the damage of DLC coating is more severe when it is deposited on both contact surfaces, than deposited on one of the contact surfaces.

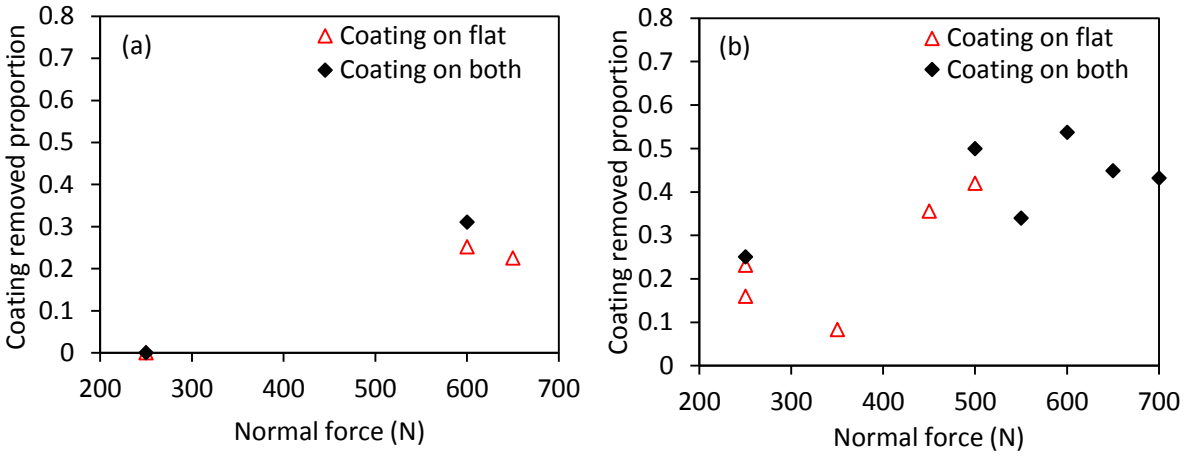

Figure IV.40. Coating removed proportion in coating working area conditions for tests with DLC A coating on both the flat and the cylinder: (a) ±20 µm; (b) ±40 µm.

It should be noted that under the displacement amplitude of ±40 µm, the threshold for test with coating on both surfaces is higher than that with coating on one of the contact surfaces (Figure IV.39). However, the damage of DLC coating is more severe when it is deposited on both contact surfaces, than deposited on one of the contact surfaces (Figure IV.40b). Furthermore, all fretting tests were performed with 100 000 cycles. With larger cycle numbers, the threshold might change, and the threshold for tests with coating on both surfaces might be lower than that with coating on one of the surfaces.

- **Conclusions**

Overall, the DLC coating deposited on both contact surfaces was not a wise solution to improve its tribological property. Even though the coating on both surfaces could bear higher normal forces under the displacement amplitude of ±40 µm, it could bear lower forces under the displacement amplitude of ±20 µm. Furthermore, under the low load conditions (i.e. in the coating working area), the DLC coating was damaged more severely when it was in contact with itself than in contact with the soft Ti–6Al–4V alloy.

4. Proposition of coating failure process

Based on the observation of wear scars and the analysis of friction and wear results, a hypothesis on the coating failure process was proposed. The failure process of DLC coatings can be divided into seven steps (Figure IV.41).

1. The wear of the DLC material (material loss of the DLC coating) decreases the coating thickness,
2. Small cracks become generated when the contact stress is above the stress limit,

3. Two or more cracks joining each other lead to small pieces of the DLC material flaking off,
4. The coating flake-off develops into small pits,
5. Then, the coating flake-off develops into large pits,
6. Next, the coating flake-off develops into a severe wear area,
7. Under large displacement amplitudes, such as ±40 µm or ±70 µm, the loss of material in the severe wear area is high. As the test progresses, the contact stress declines and the load moves mainly to the mild wear area. The mild wear area can bear the load and may be subjected to a high number of cycles when the normal force is low. When the normal force is high, the mild wear area cannot bear the load and the coating is almost entirely removed rapidly. Under the small displacement condition of ±20 µm, the loss of material on the severe wear area is very small; therefore, both the mild and the severe wear areas participate in carrying the load, and lead to a transition area in the coating response wear map.

Furthermore, the increase in the normal force or displacement accelerates the coating failure process.

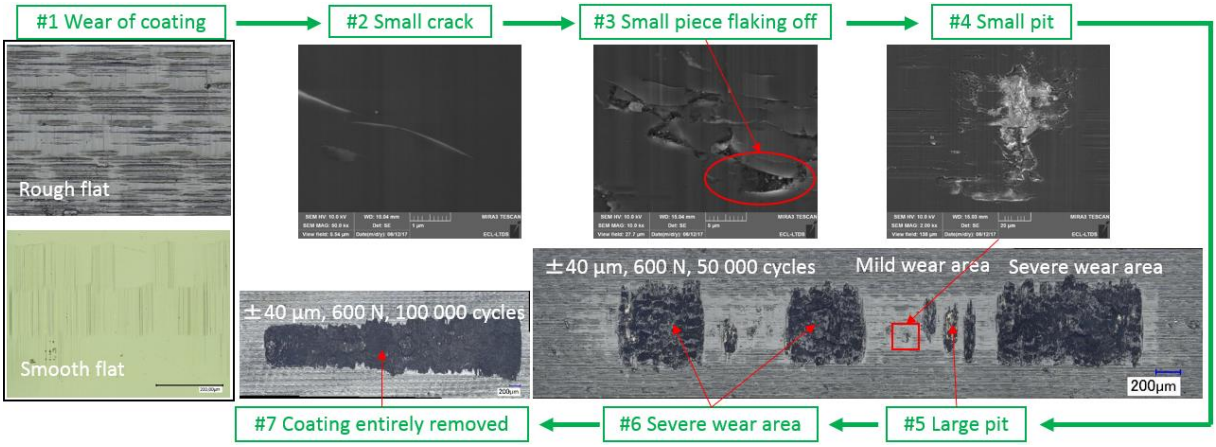

Figure IV.41. Seven steps of the coating failure process.

5. Tribological model for coating response

Based on the findings from tests with and without DLC coating (Chapter IV and Chapter III), the models shown in Figure IV.42 are proposed to explain the friction and damage response under different contact conditions.

1. For tests without the DLC coating, the contact of “Ti–6Al–4V-on-Ti–6Al–4V” led to the high friction. TTS and cracks were generated on the rubbed surfaces. The wear debris was composed of Ti–6Al–4V flakes and oxidized powder. The Ti–6Al–4V flakes were due to cracks and abrasive wear of the substrate. The oxidized powder was the result of the adhesive wear of the oxidized surface, of the fragmentation of the TTS, and of the third body particles which had undergone repeated sliding reactions,

2. For tests with the DLC coating, in the severe wear area, the DLC coating was removed. The contact situation was similar to “Ti–6Al–4V-on-Ti–6Al–4V”. The friction was high. TTS and cracks were also generated on the rubbed surfaces. DLC particles were embedded on the contact surfaces. The debris was composed of DLC particles in addition to Ti–6Al–4V flakes and the oxidized powder,
3. For tests with the DLC coating on one contact surface, in the mild wear area, the coating material was slightly worn off and cracks were generated within the coating. But the most part of the substrate was still covered by the coating. A tribofilm was formed on the rubbed Ti–6Al–4V surface. The contact situation was “tribofilm-on-DLC coating”. The friction was low. The tribofilm was constituted of oxidized worn-off Ti–6Al–4V. The wear debris was composed of Ti–6Al–4V particles, oxidized particles and DLC particles. The Ti–6Al–4V particles were due to abrasive wear of the Ti–6Al–4V surface during the running-in period. The oxidized particles were from the fragment of the tribofilm. The DLC particles were from the fracture of the DLC coating,
4. For tests with the DLC coating on both contact surfaces, in the mild wear area, the DLC material was slightly worn off and cracks were generated within the coating. The contact situation was “DLC coating-on-DLC coating”. The friction was low. The wear debris was composed of DLC particles.

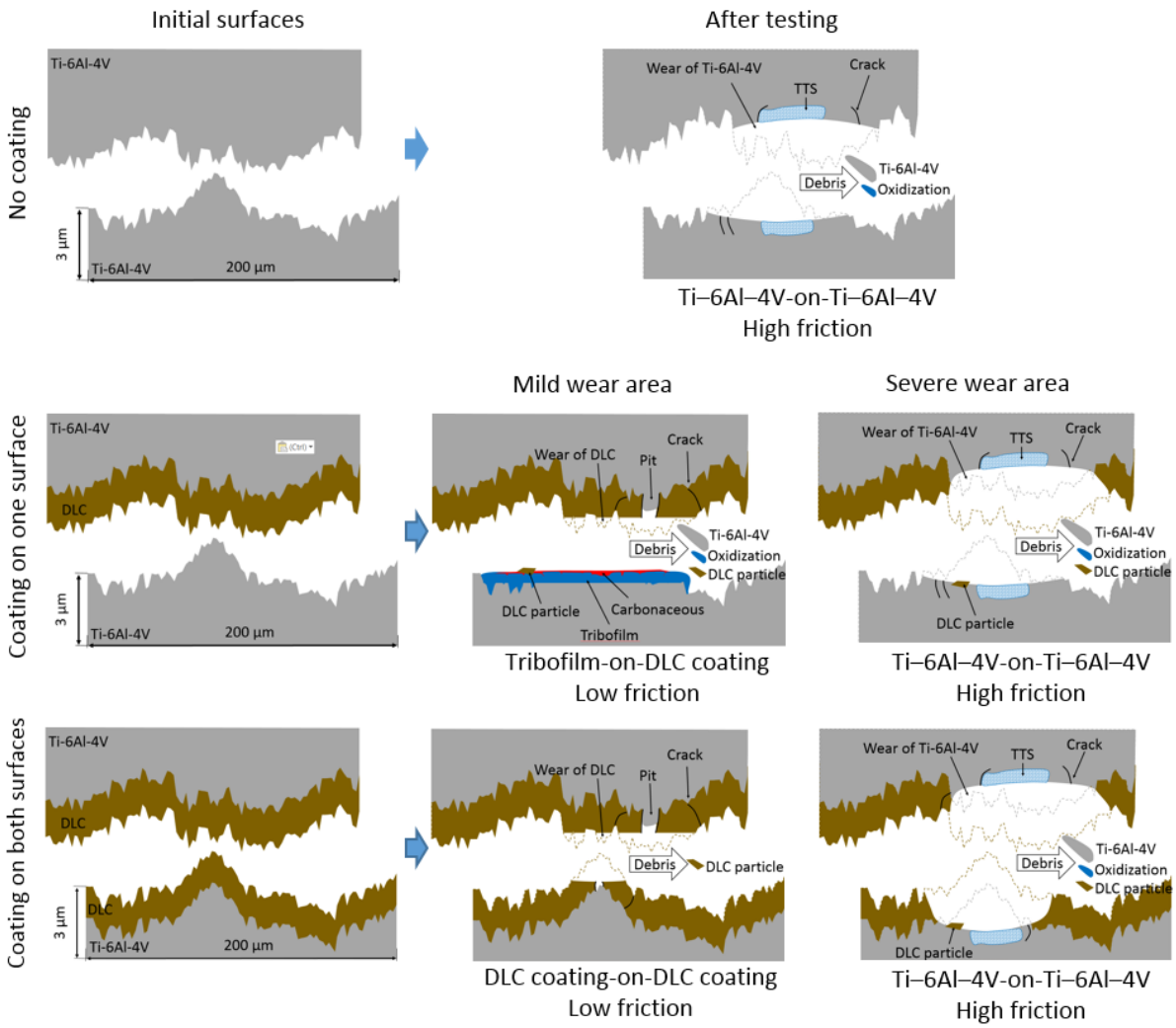

Figure IV.42. Models of friction and damage response under different contact conditions after testing.

6. Conclusions

In this chapter, the fretting behavior of DLC coatings was explored under laboratory air condition. Furthermore, the effects of different parameters (i.e., two types of DLC coatings, two types of surface roughness, and three different coating positions) on fretting behavior of DLC coatings were investigated.

Coating response wear maps were drawn according to the comprehensive analysis of friction, wear volumes, and wear scars. Coating response wear maps could be divided into three areas:

- coating working area (low load conditions),
- coating failure area (high load conditions),
- transition area (only existed under the small displacement amplitude of ±20 µm, between the coating working area and the coating failure area).

In the coating working area, the coating was not or partly removed. The friction was low. The wear volume was small. For the test with coating on both contact surfaces, the wear debris was composed of DLC particles. For the test with coating on one of the contact surfaces,

a tribofilm was formed on the uncoated Ti–6Al–4V surface, and the wear debris was composed of Ti–6Al–4V flakes, oxidized powder and DLC particles. In the coating failure area, the coating was almost entirely removed. Then the Ti–6Al–4V was in direct contact with Ti–6Al–4V. The friction was high. The wear volumes were similar to tests without coating. The wear debris was composed of Ti–6Al–4V flakes, oxidized powder and DLC particles. In the transition area, the coating was partly removed, and the friction had an intermediate value.

The harder and stiffer coating DLC A had better tribological properties than DLC B. The coating working area of DLC A was generally larger than that of DLC B. The damage of DLC A was milder than the damage of DLC B under the same load condition in the coating working area

DLC coatings deposited on a smooth flat surface presented better tribological performance than deposited on a rough flat surface. The coating working area of the coating deposited on a smooth flat was similar to or larger than deposited on a rough flat under the large displacement amplitude of ±40 μm. The damage of coating was milder when it was deposited on a smooth flat than on a rough flat.

DLC coating deposited on the cylinder exhibited better tribological performance than deposited on the flat. The coating working area was larger when it was deposited on the cylinder than deposited on the flat. The damage in coating was milder when it was deposited on the cylinder than deposited on the flat.

The DLC coating was generally damaged more severely when sliding against itself than against the soft Ti–6Al–4V alloy in the coating working area.

According to the results from fretting tests with DLC coatings, DLC coatings can be used as protective coatings into Ti–6Al–4V / Ti–6Al–4V interface for neck adapter–femoral stem contact. The Ti–6Al–4V substrate can be well protected by DLC coatings under relatively low load conditions (i.e., in the coating working area), with low friction and small wear volume.

DLC coatings generally showed high biocompatibility in previous works [156, 157]. This thesis focuses on the tribological properties of DLC coatings. The biocompatibility of the present DLC coatings should be verified before putting them into practice.

This chapter focused on the fretting performance of DLC coatings under the laboratory air condition. However, synovial fluid is present in the hip joint. The performance under the serum condition will be investigated in the next chapter. The fretting behaviors of DLC coating under laboratory air and serum conditions will be compared to explore the effect of synovial fluid.

CHAPTER V

EFFECT OF SERUM ON FRETTING BEHAVIOR OF Ti–6Al–4V AND DLC COATING

CHAPTER V: EFFECT OF SERUM ON FRETTING BEHAVIOR OF Ti–6Al–4V AND DLC COATING

CHAPTER V: EFFECT OF SERUM ON FRETTING BEHAVIOR OF Ti–6Al–4V AND DLC COATING

This chapter investigates the influence of serum on the fretting behavior of Ti–6Al–4V with a Ti–6Al–4V / Ti–6Al–4V contact and on the tribological performance of the coating DLC A with a coating / Ti–6Al–4V contact. The coating response wear map is drawn according to the friction, wear volume and wear scars under the serum condition.

1. Introduction

Synovial fluid is present in the hip joint. The local solution could accelerate the corrosion process of the metal-on-metal contacts [63]. Once the corrosion process is coupled with fretting at the contact surfaces, known as the fretting-corrosion, it might produce very large scale destructive damage mode at the interface [61]. Therefore, the fretting behavior of Ti–6Al–4V alloy should be investigated. Furthermore, the influence of serum on the fretting behavior of DLC coating has not yet be completely understood.

In this chapter, the influences of serum on the fretting behavior of Ti–6Al–4V with a Ti–6Al–4V / Ti–6Al–4V contact and on the tribological performance of the coating DLC A with a coating / Ti–6Al–4V contact are investigated. The serum, which was composed of half new born calf serum and half distilled water, was supplied into the Ti–6Al–4V / Ti–6Al–4V contact and into the DLC coating / Ti–6Al–4V contact at a rate of two drops per second. The surface roughness of flat samples was smooth. The DLC coating was DLC A. Tests were conducted under various values of displacement amplitude (±20, ±40, and ±70 μm) and normal force (200–1 200 N). The number of cycles for each test was 100 000 cycles. Friction coefficient and wear volume were measured. Wear scars and cross sections of flat samples were observed.

The RCFM for Ti–6Al–4V / Ti–6Al–4V contact and the coating response wear map for DLC coating / Ti–6Al–4V contact are constructed.

2. Effect of serum on fretting behavior of Ti–6Al–4V / Ti–6Al–4V contact

In this section, the tribological behavior of Ti–6Al–4V / Ti–6Al–4V contact under serum condition is presented. The RCFM, the friction coefficient, the wear volume, the wear scars, TTSs and cracks formed on the rubbed surfaces are detailed. These results are compared with the results from tests under laboratory air condition to investigate the effect of serum.

2.1. RCFM

For the fretting test with Ti–6Al–4V / Ti–6Al–4V contact under the serum condition with the large displacement amplitude of ±70 µm and the low normal force of 250 N, the fretting log, the representative fretting loops, and the evolution of the energy ratio A are shown in Figure V.1. From this figure, it is clear that, at the beginning of the test (19 cycles), the fretting loop has a quadrangle shape. The corresponding energy ratio A is high (around 0.89, shown in Figure V.1c). With test going, the fretting loops have a quadrangle shape but with a tip (Figure V.1a), thus the energy ratio A has a slight decrease (around 0.64 at 199 cycles and around 0.56 at 99 999 cycles). According to the fretting log, the fretting test remains in the gross slip condition during the test, thus the test is in the GSR.

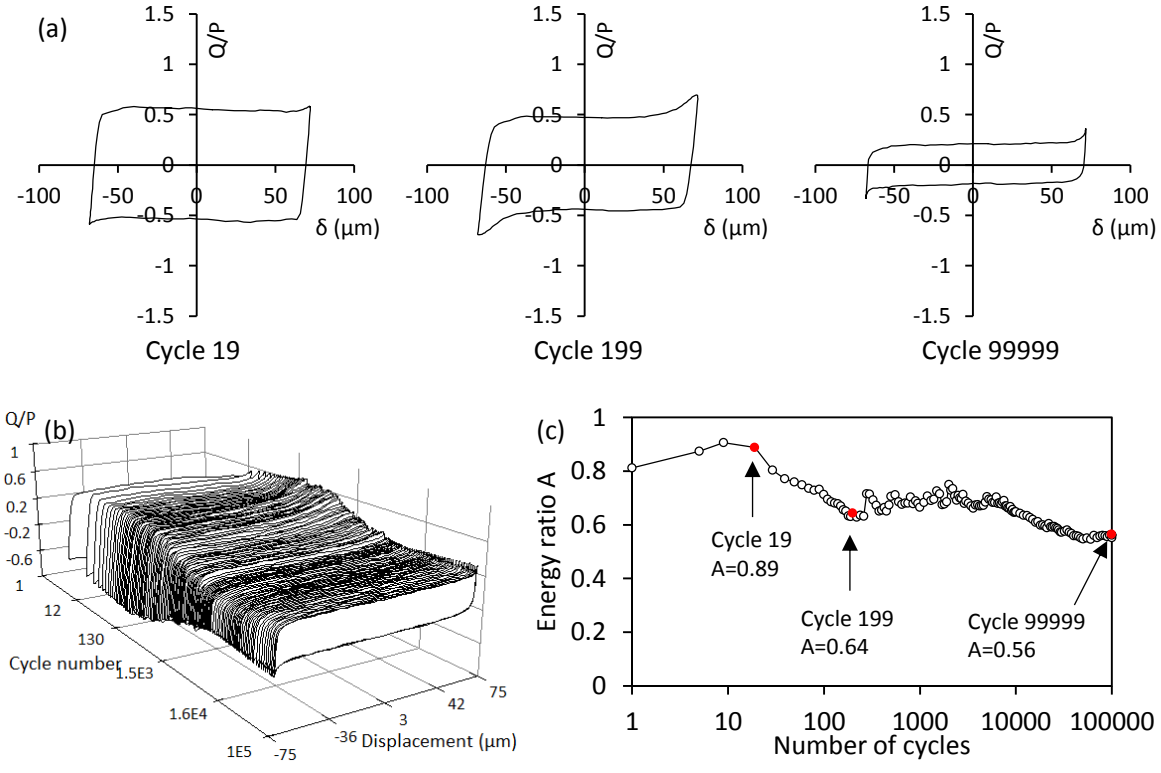

Figure V.1. Fretting test with Ti–6Al–4V / Ti–6Al–4V contact under the serum condition under the large displacement amplitude of ±70 µm and the low normal force of 250 N: (a) representative fretting loops; (b) fretting log; and (c) evolution of energy ratio A.

With the small displacement amplitude of ±20 µm and the high normal force of 1 000 N, at the beginning of the test (19 cycles), the fretting loop has an elliptic shape (Figure V.2a). The corresponding energy ratio A is low (around 0.10, as shown in Figure V.2c). The fretting cycle is characteristic of partial slip condition. Between 549 and 5 999 cycles, some quadrangle cycles occur. For example, at 549 cycles, the energy ratio A is high (around 0.67). The fretting cycle is under the gross slip condition. After that, the fretting loop changes to elliptic and remains stable with a low energy ratio A until the end of the test (around 0.30 at 99 999 cycles). This fretting cycles indicate the partial slip condition. According to the fretting log (Figure V.2b), the fretting test is under the MSR.

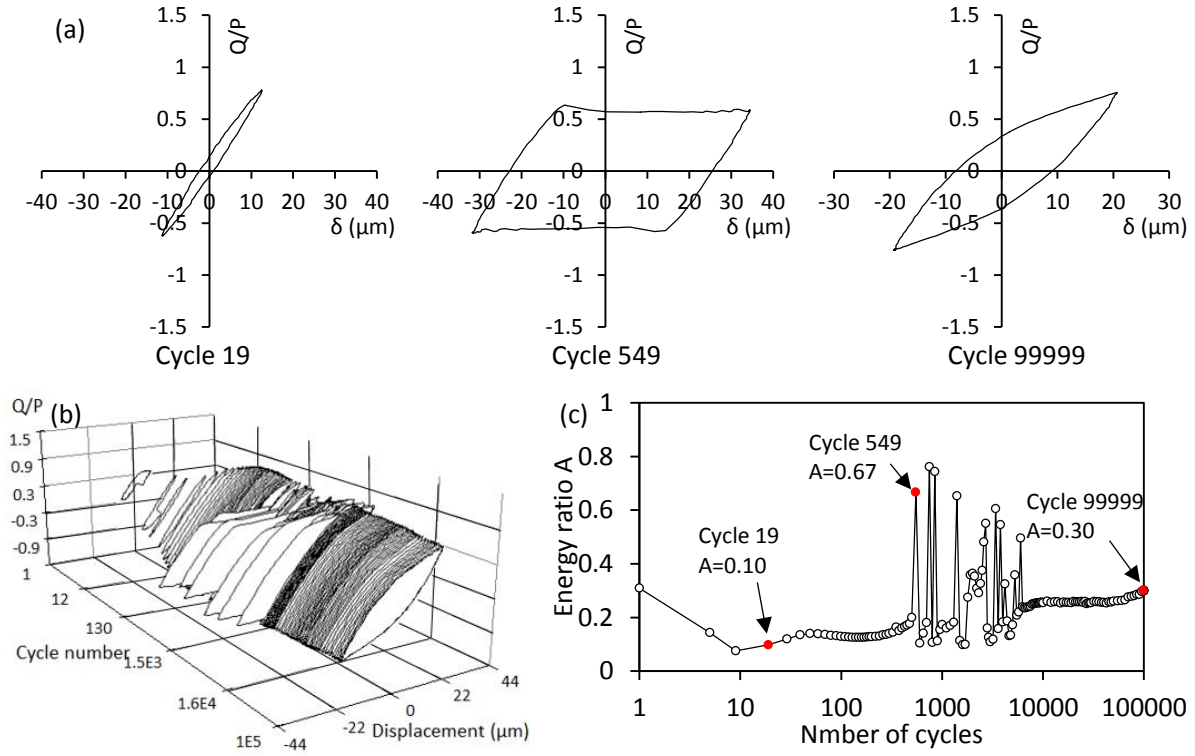

Figure V.2. Fretting test with Ti–6Al–4V / Ti–6Al–4V contact under the serum condition under the small displacement amplitude of ±20 µm and the high normal force of 1 000 N: (a) representative fretting loops; (b) fretting log; and (c) evolution of energy ratio A.

RCFM was drawn according to fretting tests with different values of displacement amplitude and normal force. The RCFM for the tests with smooth Ti–6Al–4V flat / Ti–6Al–4V cylinder under the serum condition is shown in Figure V.3. As may be observed, the RCFM is divided into GSR and MSR under the given displacement and normal force conditions. Comparing with the RCFM under laboratory air condition (Figure III.5), the presence of serum liquid has no obvious influence on neither the RCFM nor the position of the transition between the GSR and the MSR.

In most cases in the GSR (except the test under the displacement amplitude of ±70 µm and the normal force of 250 N), the values of energy ratio A under the serum condition are slightly higher than those under the laboratory air condition. For instance, under the

displacement amplitude and normal force conditions of ±40 µm and 600 N, energy ratio A is approximately 0.64 under the laboratory air condition; whereas, it is approximately 0.69 under the serum condition. However, in the MSR, energy ratio A exhibits no significant increase under the serum condition compared to that under the laboratory air condition.

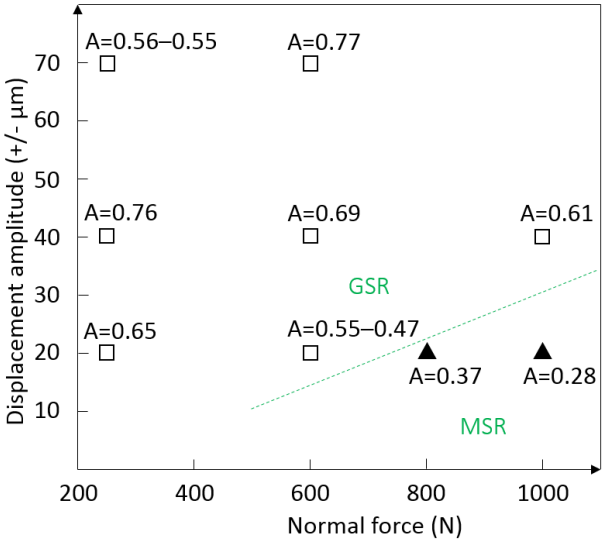

Figure V.3. RCFM for the tests with smooth Ti–6Al–4V flat / Ti–6Al–4V cylinder under the serum condition. The A values represent the average values of energy ratio during the entire test.

2.2. Friction coefficient

Figure V.4 and Figure V.5 show the evolution of Q_{max}/P for the tests with smooth Ti–6Al–4V flat / Ti–6Al–4V cylinder contact under the displacement amplitudes of ±20 µm and ±40 µm, respectively, with various values of normal force. As may be observed, Q_{max}/P increases rapidly at the beginning of the test (for approximately 100 cycles, the running-in period), and then reaches a relatively steady state until the end of the test. In the relatively stable period, the Q_{max}/P has a slight decrease trend with the test ongoing. Furthermore, for the tests with the displacement amplitude of ±20 µm and normal forces of 800 N and 1 000 N (in the MSR), there is a fluctuation period prior to reaching a steady state.

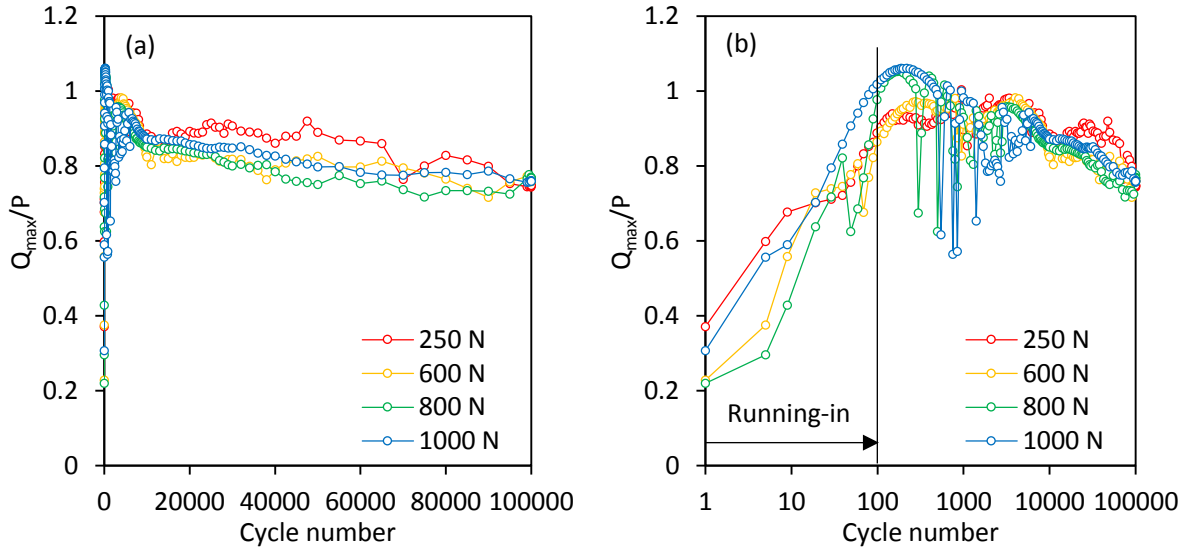

Figure V.4. Evolution of Q_{max}/P as a function of the number of cycles for tests with a smooth Ti–6Al–4V flat / Ti–6Al–4V cylinder contact under the displacement amplitude of ±20 µm: (a) linear cycle number scale; (b) logarithmic cycle number scale.

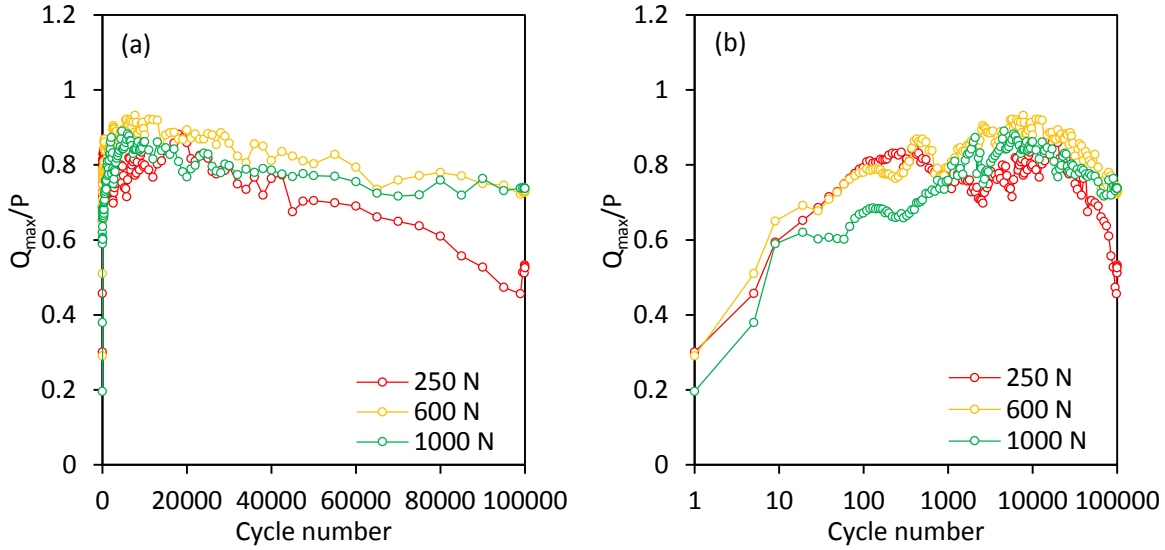

Figure V.5. Evolution of Q_{max}/P as a function of the number of cycles for tests with a smooth Ti–6Al–4V flat / Ti–6Al–4V cylinder contact under the displacement amplitude of ±40 µm: (a) linear number cycle scale; (b) logarithmic cycle number scale.

Figure V.6 shows the evolution of Q_{max}/P for the tests under the displacement amplitude of ±70 µm with various values of normal force. As may be observed, Q_{max}/P increases rapidly at the beginning of the test (for approximately 100 cycles), and then it decreases significantly to a low value of around 0.3, then it remains stable until the end of the test. With a lower normal force, the test reaches to the low friction period faster. The Q_{max}/P reaches to the low friction period at around 10 000 cycles under the normal force of 250 N, and at around 25 000 cycles under the normal force of 600 N.

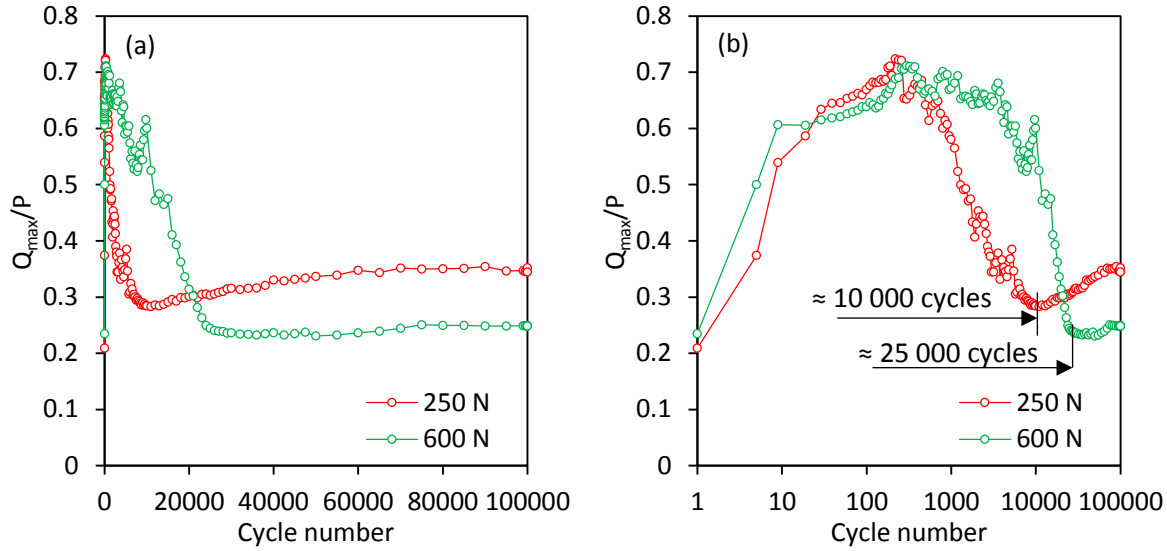

Figure V.6. The evolution of Q_{max}/P as a function of the number of cycles for tests with a smooth Ti–6Al–4V flat / Ti–6Al–4V cylinder contact under the displacement amplitude of ±70 µm: (a) linear scale; (b) logarithmic scale.

The average values of Q_{max}/P from 50 000 cycles until the completion of the test (i.e., during stable friction) are shown in Figure V.7. For tests under the laboratory air condition (Figure V.7 and Figure III.8b), the average values of Q_{max}/P are high and in the range between 0.8 and 1.2. Under serum condition, the average values of Q_{max}/P are slightly lower (around or lower than 0.8) under the displacement condition of ±20 µm and ±40 µm (Figure V.7a and Figure V.7b). Under the large displacement condition of ±70 µm, the decrease in average values of Q_{max}/P is significant (Figure V.7c). For instance, under the displacement amplitude of ±70 µm and the normal force of 600 N, the average value of Q_{max}/P reaches approximately 0.25, which may be seen as a lubricating effect of the serum, enhanced by the increase in displacement amplitude and/or sliding speed (as the fretting test was conducted with a fixed frequency of 5 Hz, the increase in displacement amplitude led also to an increase in average sliding speed).

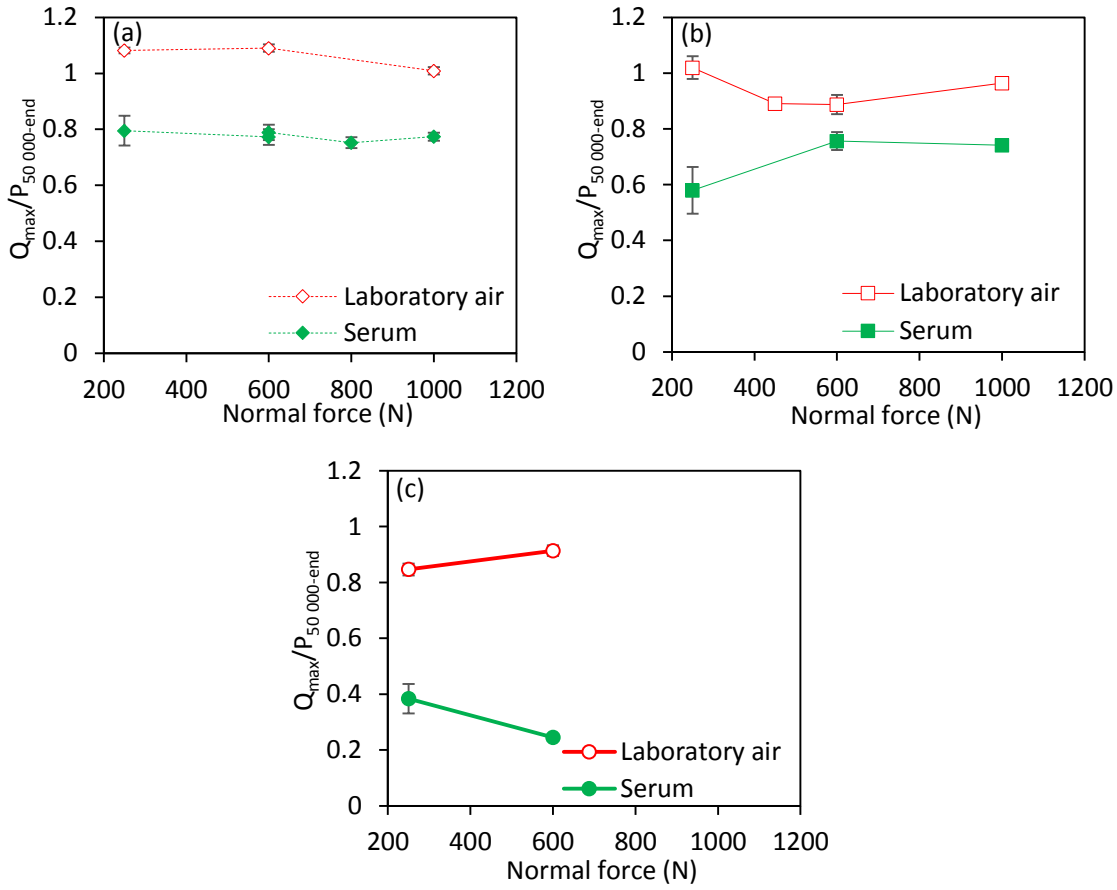

Figure V.7. Average values of Q_{max}/P from 50 000 cycles until the completion of the test with the smooth Ti–6Al–4V flat / Ti–6Al–4V cylinder contact under laboratory air and serum conditions: (a) ±20 µm; (b) ±40 µm; (c) ±70 µm

2.3. Wear volume

The presence of serum has a great influence on the total wear volume.

For tests under laboratory air condition (Figure V.8 and Figure III.9b), the wear volume increases drastically with the increase in the displacement amplitude. Under the small displacement amplitude of ±20 µm, the wear volumes are very low. Under the displacement amplitude of ±40 µm, the wear volume shows no obvious change as the normal force increases. Under the large displacement amplitude of ±70 µm, the wear volume grows significantly with the increase in the normal force.

For tests under serum condition (as shown in Figure V.8), the wear volumes are also very low under the small displacement amplitude of ±20 µm. Under the displacement amplitude of ±40 µm, the wear volumes are significantly larger than those under the laboratory air condition. However, under the large displacement amplitude of ±70 µm, the wear volumes are significantly smaller than those under the laboratory air condition. Meanwhile, under the serum condition, the wear volumes under the displacement amplitude of ±70 µm are much smaller than those under the displacement amplitude of ±40 µm. Furthermore, the wear

volume grows significantly as the normal force increases under the displacement amplitudes of ±40 µm and ±70 µm under the serum condition.

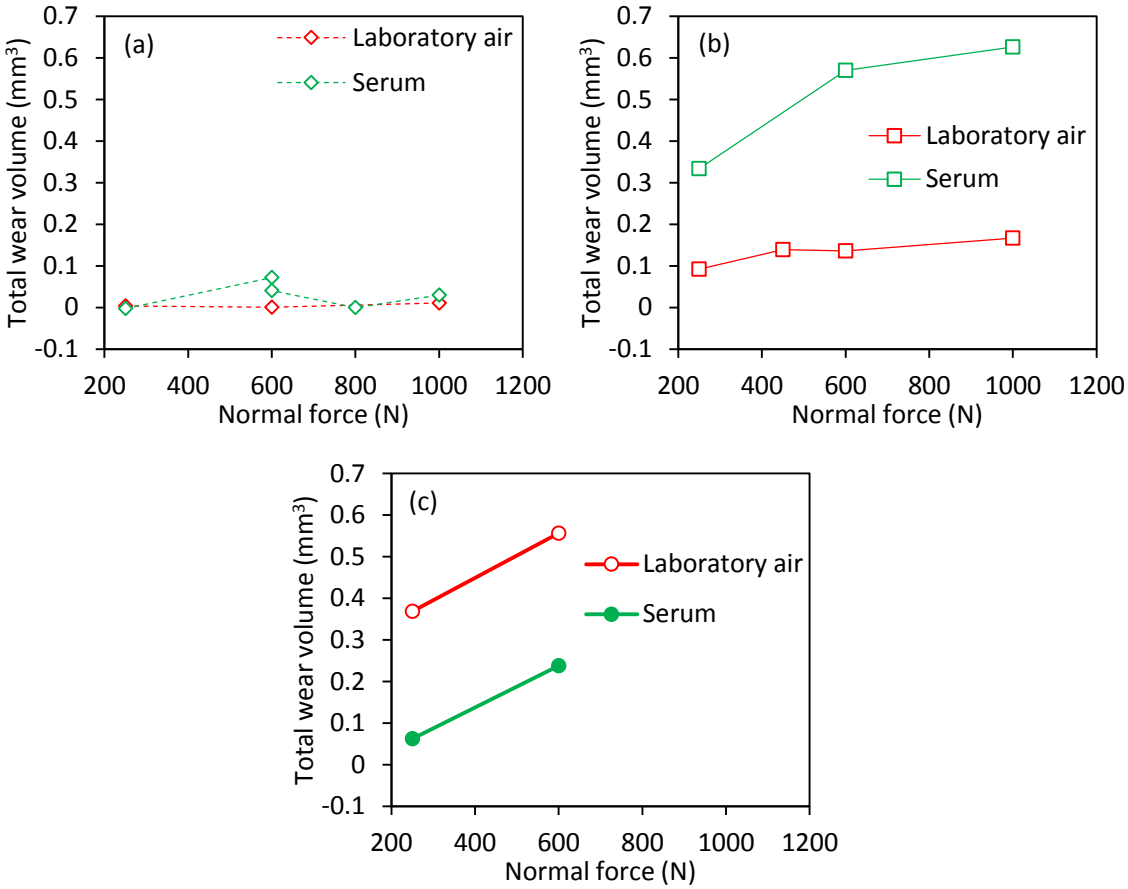

Figure V.8. Total wear volume for tests with the smooth Ti–6Al–4V flat / Ti–6Al–4V cylinder contact under laboratory air and serum conditions: (a) ±20 µm; (b) ±40 µm; (c) ±70 µm

2.4. Wear scars

The presence of serum liquid has a great influence on the wear scars.

For tests under laboratory air condition (Figure III.10), the presence of important transfers with oxygen is detected in addition to titanium, aluminum, and vanadium, indicating that adhesive wear is predominant.

For fretting tests under serum condition, wear scars of Ti–6Al–4V / Ti–6Al–4V contact surfaces under the displacement amplitudes of ±20 µm and ±40 µm are different from the wear scars under the displacement amplitude of ±70 µm.

Figure V.9 shows a representative wear scar of the Ti–6Al–4V flat surface under the serum condition with a displacement amplitude of ±20 µm and a normal force of 800 N. From the SEM images (Figure V.9), cracks are also observed on the wear scar. Cracks can propagate, mainly driven by the repeated loading, and then lead to pieces of material flaking off from the surface. Some flakes might be adhered outside of the contact.

EDX analysis was performed on the flat surface. Furthermore, nine spots were detected via EDX at different areas on the flat surface. Outside the wear scar (squares □), the content

of oxygen is negligible (near 0), and the content of carbon is very low (below 2 wt%). Inside the wear scar (triangles Δ), in addition to titanium, aluminum, and vanadium, oxygen and elements from the serum (such as carbon, chlorine, sodium, potassium, etc.) were detected. The content of oxygen reaches around 37 wt%, which suggests that the rubbed Ti–6Al–4V surface is oxidized. The presence of elements from serum (content of carbon reaches 5 wt%) suggests that the rubbed Ti–6Al–4V surfaces probably were corroded by the serum liquid during sliding, and the elements from serum participated in the formation of the oxidized layer. The corrosive process of Ti alloy by serum is supported by literature [224, 225]. Titanium alloy is able to release ions into electrolytes. On the wear scar, the rubbed titanium alloy surface is oxidized; outside the contact, a thin oxide film is also formed spontaneously. However, oxides (such as titanium oxide and vanadium oxide) can interact with the calcium, phosphate and chloride ions and dissolve in the solution, and this dissolution is further enhanced by the presence of Cl^- ions [224]. Furthermore, proteins can bind to metal ions and transport them away from the interface, encouraging further dissolution [225]. Higher contents of elements from serum were detected inside the wear scar than outside, suggesting that the sliding and wear probably enhanced the corrosive process on the rubbed surface.

In addition, outside of the wear scar, some material is adherent on the surface (labeled as “adhered material”). From the EDX analysis (circles ○), the content of oxygen is around 23 wt%. The contents of elements from serum are high (content of carbon reaches around 22 wt%), which suggests that the adhered material might be the deposition of serum proteins mixed with wear products.

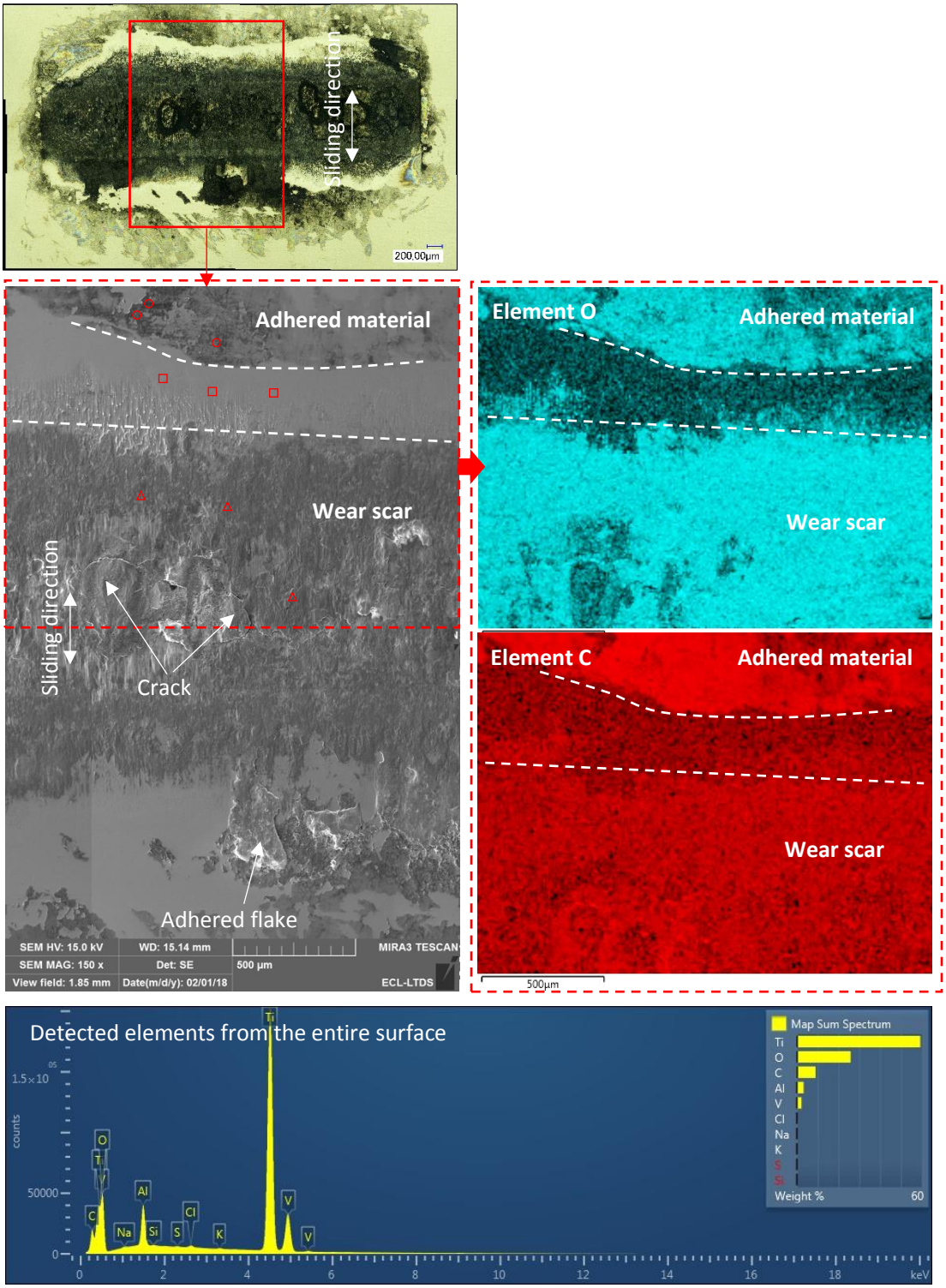

Figure V.9. SEM and EDX observations of the wear scar on the smooth flat surface after a test under the serum condition with a displacement amplitude of ±20 µm and a normal force of 800 N. The sample was ultrasonically cleaned in acetone for 30 minutes before the SEM and EDX observation.

Figure V.10 shows the wear scar of the Ti–6Al–4V flat surface under the serum condition with the large displacement amplitude of ±70 µm and a normal force of 250 N. It is clear that under the large displacement amplitude of ±70 µm, a large amount of grooves were observed on the wear scars; this suggests that the abrasive wear occurs on the contact surfaces.

Furthermore, in the middle area of the contact (where the contact pressure is higher), some adhesion spots were observed. And the quantity of oxygen is obviously higher at the adhesive spot than in the abrasive area.

From SEM image in small scale, wear particles are embedded on the contact surfaces, which serve as the abrasive particles. However, the formation process of the abrasive particles (whether it is related to the presence of serum and the displacement amplitude) is uncertain. Apparently, abrasive wear only occurs in serum condition with the large displacement amplitude. This is probably because the serum enters the interface and reduces the occurrence of metal-metal contact. Under a larger displacement amplitude, the serum enters the interface more easily. Furthermore, the increase in displacement amplitude leads to the increase in sliding speed, as the fretting test was conducted with a fixed frequency of 5 Hz. A large sliding speed associated with more serum at the interface probably enhanced the abrasive wear by the wear particles.

In addition, titanium, aluminum, vanadium, and oxygen, as well as elements from serum (such as carbon, chlorine, sodium, potassium, etc.,) were detected via EDX on the wear scar, suggesting that the rubbed surfaces were oxidized and corroded in the serum.

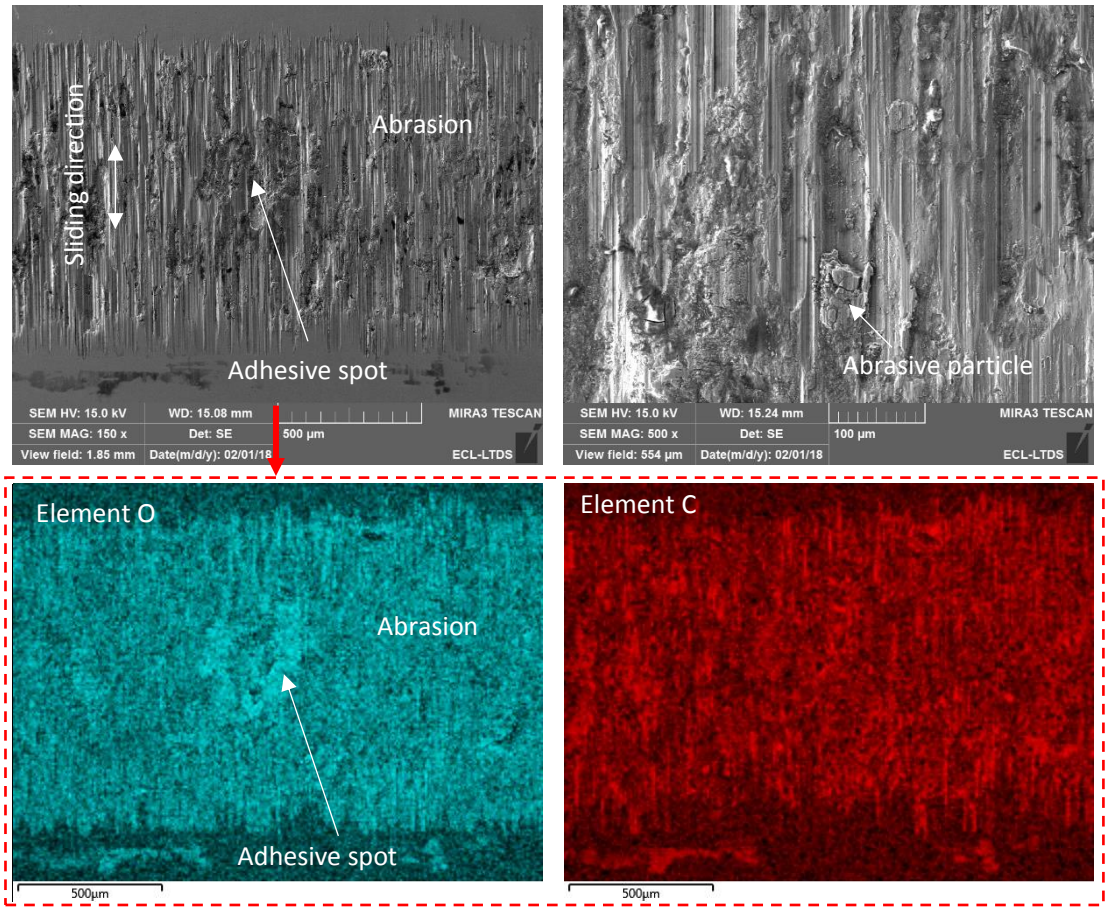

Figure V.10. SEM and EDX observations of the wear scar on the smooth flat surface after a test under the serum condition with a displacement amplitude of ±70 µm and a normal force of 250 N.

Figure V.11 shows the wear scar of the Ti–6Al–4V flat surface under the serum condition with the displacement amplitude of ±70 µm and a higher normal force of 600 N. It is clear that under a higher normal force, an adhesive wear area is developed in the middle of the contact (where the contact pressure is more important). From the analysis of EDX, the oxygen content on the adhesive wear area is higher than that on the abrasive wear area, which means that the adhesive area is oxidized more severely than the abrasive area.

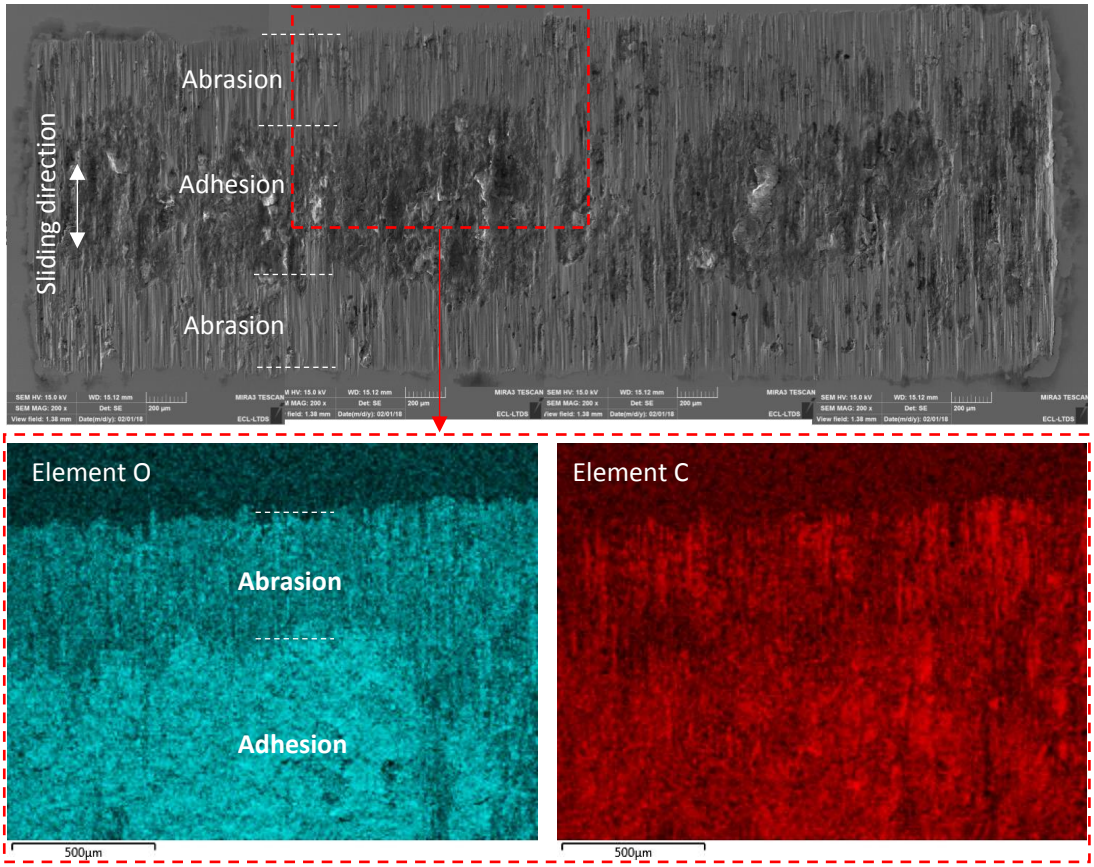

Figure V.11. SEM and EDX observations of the wear scar on the smooth flat surface after a test under the serum condition with a displacement amplitude of ±70 µm and a normal force of 600 N.

2.5. TTS

The presence of serum has a great influence on the formation of TTS. Figure V.12 shows the results of TTS observation on cross sections of flats under laboratory air condition and under serum condition. Under the laboratory air condition (Figure V.12a), TTS is widely observed on the rubbed Ti–6Al–4V surface (Figure III.11) and subsurface (Figure III.13a) under every given displacement and normal force condition. Under the serum condition (Figure V.12b), TTS is only observed under the highest normal force of 1 000 N. Furthermore, the formed TTS is only on the subsurface (as shown in Figure V.13).

Much less TTS is formed on the worn Ti–6Al–4V surface under the serum condition. This is probably because the presence of serum leads to a decrease in temperature and also a decrease in shear stress (because of the decrease in friction coefficient) at the contact area.

The heat and the shear stress generated by friction are important factors to the formation of TTS.

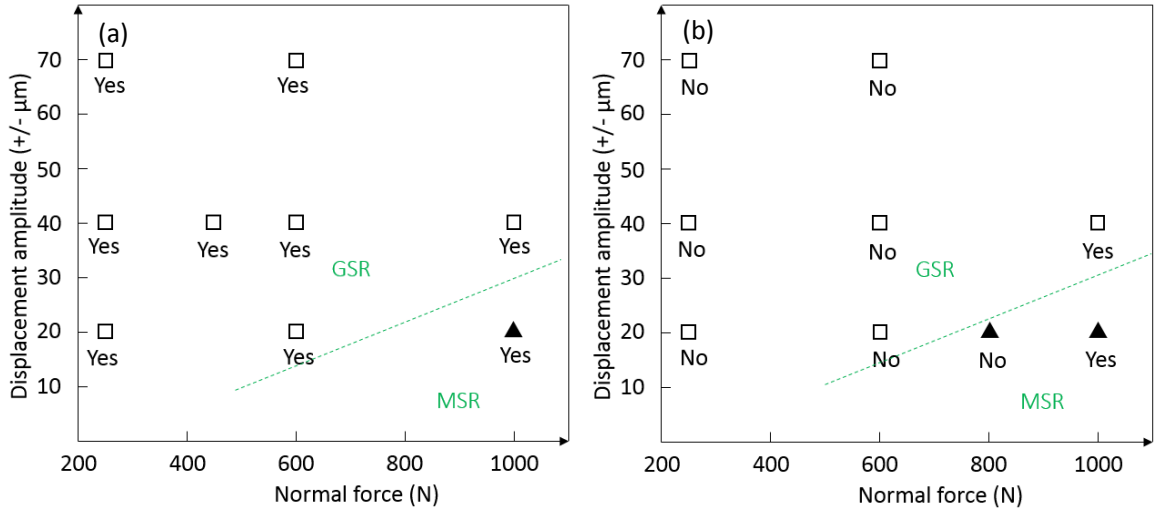

Figure V.12. Presence of TTS on the cross section of flat samples: (a) under laboratory air condition; (b) under serum condition. “Yes” represents that TTS was observed. “No” represents that no TTS was observed. The white square □ represents that the fretting test was under the GSR.
The black triangle Δ represents that the fretting test was under the MSR.

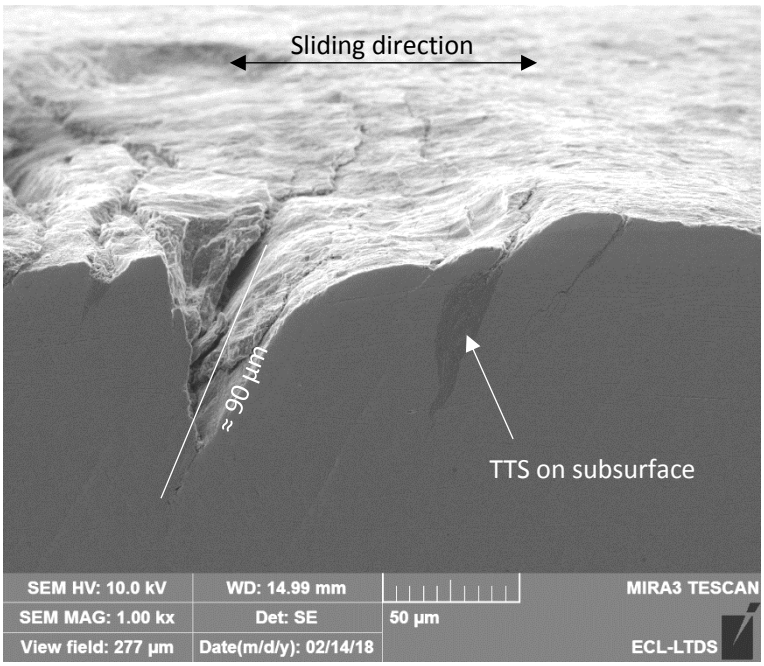

Figure V.13. SEM observation of TTS formed on the subsurface of rubbed Ti–6Al–4V flat.
The displacement amplitude is ±20 µm and the normal force is 1 000 N.

2.6. Cracks

The presence of serum has an influence on the cracks. Figure V.14 shows the values of maximal crack length observed on cross sections of flat samples under the laboratory air and under the serum conditions.

Under large displacement and low normal force conditions (±40 and ±70 µm; 250–600 N), the crack length is in the range of 1–15 µm under the laboratory condition. Under the serum condition, no visible cracks were observed.

Under the highest normal force conditions (1 000 N), the values of the maximal crack length are 23 µm (under the displacement amplitude of ±20 µm) and 14 µm (under the displacement amplitude of ±40 µm), respectively, under the laboratory air condition. Under the serum condition, the cracks are significantly longer (90 µm and 37 µm, respectively). This is probably because under high force condition, the serum liquid can enter the crack and enhances the development of crack.

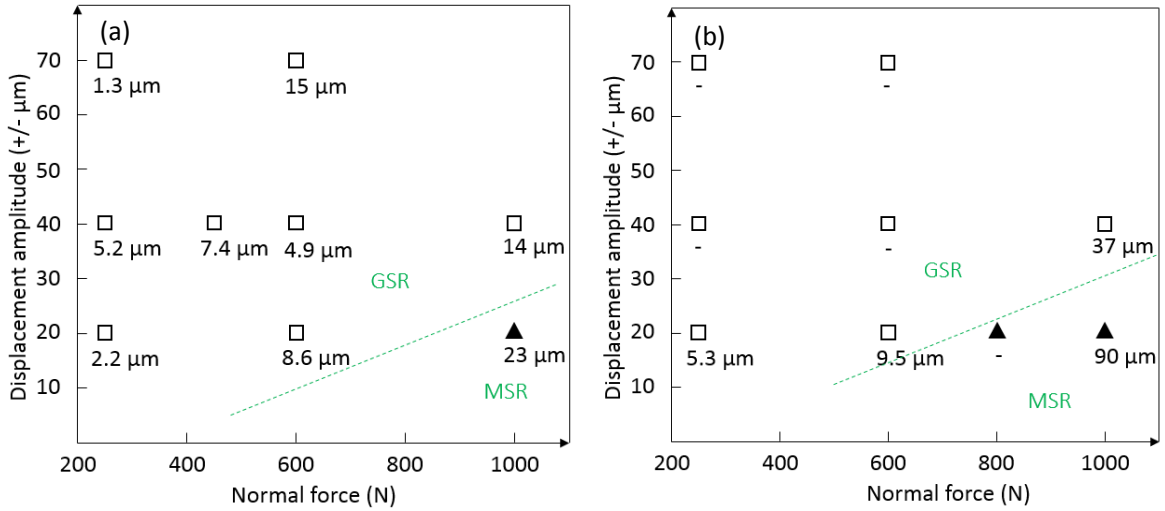

Figure V.14. Values of maximal crack length on cross sections of flat samples: (a) under laboratory air condition; (b) under serum condition (observed via SEM). The hyphen - means that no obvious cracks were observed. The white square □ represents that the fretting test was under the GSR. The black triangle Δ represents that the fretting test was under the MSR.

2.7. Analysis of effect of serum liquid on fretting behavior of Ti–6Al–4V / Ti–6Al–4V contact

The serum has a significant influence on the fretting behavior of Ti–6Al–4V / Ti–6Al–4V contact and the influence is different under different displacement conditions. Figure V.15 shows a schematic diagram that summarizes the effect of serum.

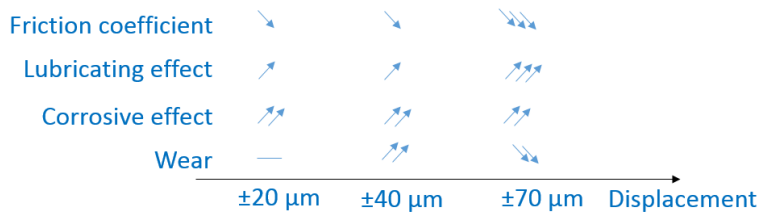

Figure V.15. Effect of serum (compared to test in laboratory air condition).

Under the smallest displacement amplitude of ±20 µm, the presence of the serum leads to a slight decrease in the average values of Q_{max}/P from the range of 1.0–1.1 to approximately 0.8. It is clear, from the EDX analysis of the wear scars under the serum conditions, that the

worn Ti–6Al–4V surfaces might be corroded due to the presence of serum during the fretting process. The wear volumes are always close to 0 under both the serum and the laboratory air conditions.

Under the displacement amplitude of ±40 µm, the presence of the serum leads to a slight decrease in the friction coefficient, from the range of approximately 0.9–1.0 to the range of approximately 0.6–0.8. Similarly to wear scars under the displacement amplitude of ±20 µm, the worn Ti–6Al–4V surfaces might be corroded. However, under the displacement amplitude of ±40 µm, the serum results in a significant increase in the total wear volume. The large wear volume might be attributed to the fretting corrosion processes. The corroded layer is easily removed by the fretting processes (i.e., mechanical processes). At the same time, the serum accelerates the corrosion of the worn surface. Therefore, the fretting corrosion processes lead to large wear volumes under the displacement amplitude of ±40 µm.

Under the largest displacement amplitude of ±70 µm, the presence of the serum leads to a significant decrease in the friction coefficient, from the range of approximately 0.85–0.9 to the range of approximately 0.25–0.35. The low friction coefficient suggests that the serum liquid has a lubricating effect under the large displacement amplitude of ±70 µm, because it is easy for the liquid to enter the interface under the large displacement condition, reducing the occurrence of metal-metal contact. Therefore, the presence of serum results in a significant decrease in the total wear volume. And the wear scars show obvious grooves indicating that the abrasive wear is predominant under the large displacement amplitude of ±70 µm with the presence of serum.

3. Effect of serum on fretting behavior of Ti–6Al–4V / DLC coating contact

In this section, the tribological performance of DLC coating under serum condition is presented, including the friction coefficient, the wear volume and the wear scars. Then the coating response map is constructed. These results are compared with the results from tests under laboratory air condition, in order to investigate the effect of serum.

3.1. Friction coefficient

- **Evolution of Q_{max}/P**

Figure V.16 shows the evolution of Q_{max}/P for tests with a smooth flat coated with DLC A in contact with an uncoated rough cylinder under the serum condition.

Under low normal force conditions (250–800 N with ±20 µm; 250–1 000 N with ±40 µm; 250–600 N with ±70 µm), Q_{max}/P decreases to low values in the range of 0.1–0.15 during the running-in period; then, it remains stable until the completion of the test. Sometimes, a peak of friction occurs (such as at around 30 000 cycles with the displacement amplitude of ±40 µm and normal force of 1 000 N). This is because the removal of coating leads to a Ti–Al–4V

substrate / Ti–6Al–4V counterbody contact (severe wear area), which might result in a high friction. With the test ongoing, the wear of the material at severe wear area leads to the contact pressure moving to the mild wear area (i.e., DLC coating / Ti–6Al–4V contact area). The friction decreases back to a low value.

Under the high normal force condition (±20 µm with 1 000 N), after a certain number of cycles (around 5 000 cycles), Q_{max}/P increases rapidly to high values; then, it remains high until the completion of the test. Under the displacement amplitude of ±40 µm with the normal force of 1 200 N, the friction is low for around 80 000 cycles and then increases to high values. Under the displacement amplitude of ±70 µm and the normal force of 1 000 N, the friction is low for around 50 000 cycles and then increases to high values.

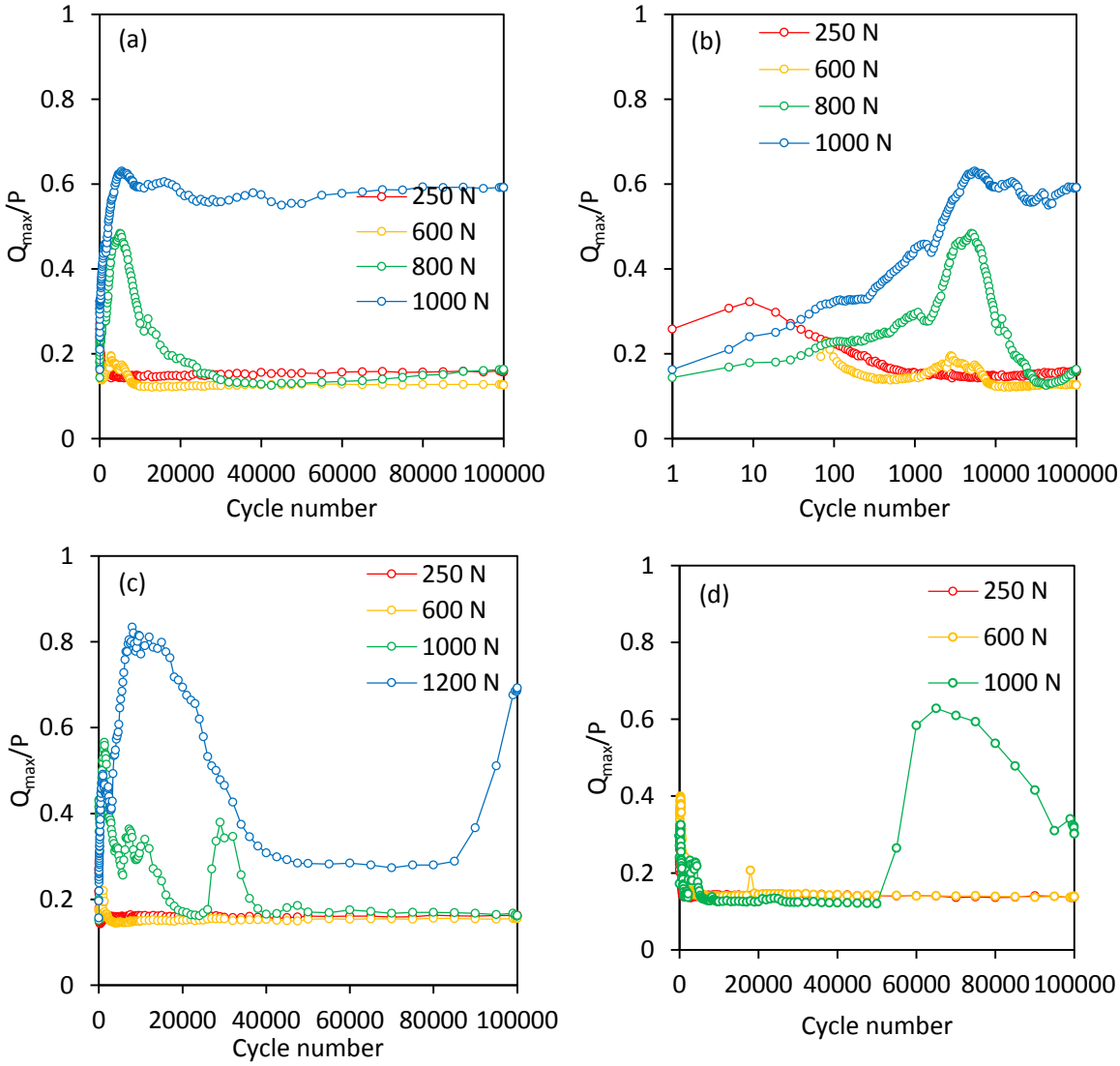

Figure V.16. Evolution of Q_{max}/P as a function of the number of cycles for tests with a smooth flat coated with DLC A / uncoated rough cylinder contact under serum condition with different displacement amplitudes: (a) ±20 µm, linear cycle number scale; (b) ±20 µm, logarithmic cycle number scale; (c) ±40 µm; (d) ±70 µm.

- **Average values of Q_{max}/P**

Figure V.17 shows the average values of Q_{max}/P during friction stable period under laboratory air condition and under serum condition.

It is clear that, with the increase in normal force, a threshold can be defined. When the applied normal force is lower than the threshold, the value of Q_{max}/P is low (around or lower than 0.2). And the values of Q_{max}/P for tests under laboratory air condition or under serum condition show no significant difference. When the applied normal force is higher than the threshold, the value of Q_{max}/P is high. And the values of Q_{max}/P under serum condition are generally lower than those under laboratory air condition. For instance, under the displacement amplitude ±20 µm and normal force of 1 000 N, the Q_{max}/P is around 0.74 under laboratory air condition; whereas, it is around 0.59 under serum condition.

The presence of serum has a significant effect on the load conditions where the threshold is observed (i.e., the position of threshold). For tests under serum condition, the thresholds extend towards higher normal forces comparing with those under the laboratory air conditions. Specifically, the presence of serum leads to an increase in the normal force where the threshold occurs from 600–700 N to 800–1 000 N under the displacement amplitude of ±20 µm, from 500–550 N to 1 000–1 200 N under the displacement amplitude of ±40 µm, and from 300 N to 600–1 000 N under the displacement amplitude of ±70 µm.

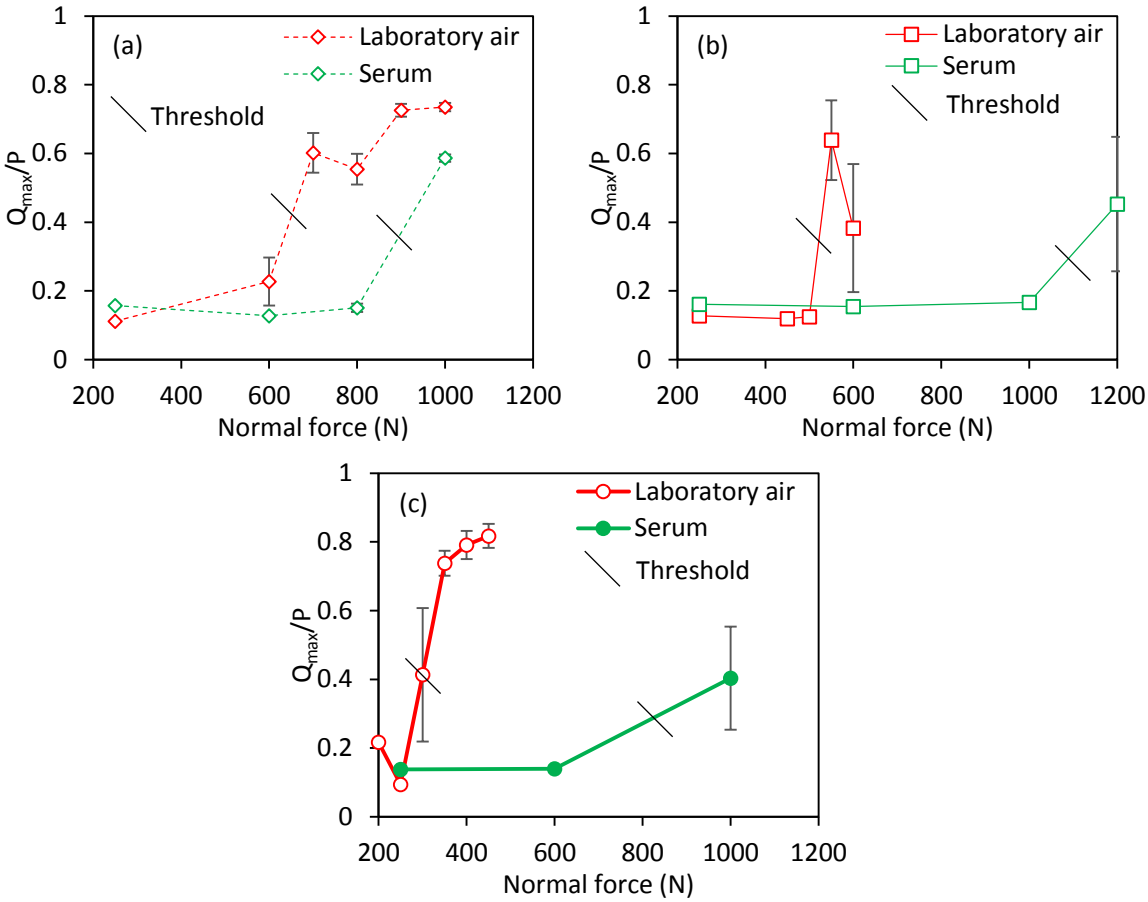

Figure V.17. Average values of Q_{max}/P for tests with a smooth flat coated with DLC A / uncoated cylinder contact under laboratory air and serum conditions: (a) ±20 µm; (b) ±40 µm; (c) ±70 µm. For tests under serum condition and for tests under laboratory air condition with the displacement amplitude of ±20 µm and ±40 µm, Q_{max}/P is the average value from 50 000 cycles to then end of the test. For tests under laboratory air condition with the displacement amplitude of ±70 µm, Q_{max}/P is the average value from 10 000 cycles to then end of the test.

3.2. Wear volume

Figure V.18 shows the total wear volumes for tests with and without DLC coating under serum condition.

For tests with coating, when the applied normal force is lower than the threshold, the wear volume is very weak, not measurable.

When the value of the applied normal force is higher than the threshold, the wear volume is close to 0 under the small displacement amplitude of ±20 µm (with 1 000 N). Under the displacement amplitude of ±40 µm (with 1 200 N), the wear volume is higher (0.17 mm^3). But, it is much smaller than the wear volume from the test without coating. This is because the coating works until around 80 000 cycles. Under the displacement amplitude of ±70 µm (with 1 000 N), the wear volume for the test with coating reaches the highest value (0.64 mm^3). The coating works until 50 000 cycles under this condition.

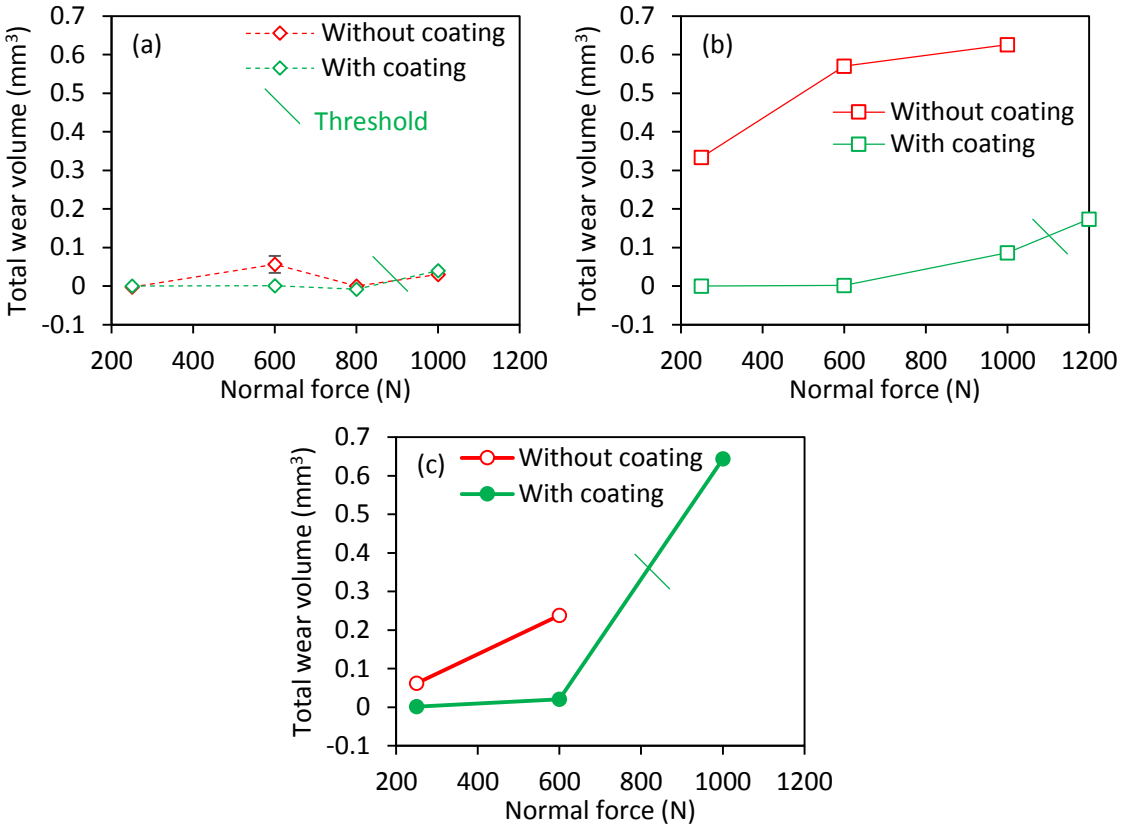

Figure V.18. Total wear volumes for tests with and without coating under serum condition: (a) ±20 µm; (b) ±40 µm; (c) ±70 µm.

Figure V.19 shows the total wear volumes for tests with DLC coating under laboratory air condition and under serum condition. It is clear that, when the applied normal force is lower than the threshold, the wear volume is always small, and the presence of serum has no significant influence. The threshold occurs at higher normal forces under the serum condition than under the laboratory air condition.

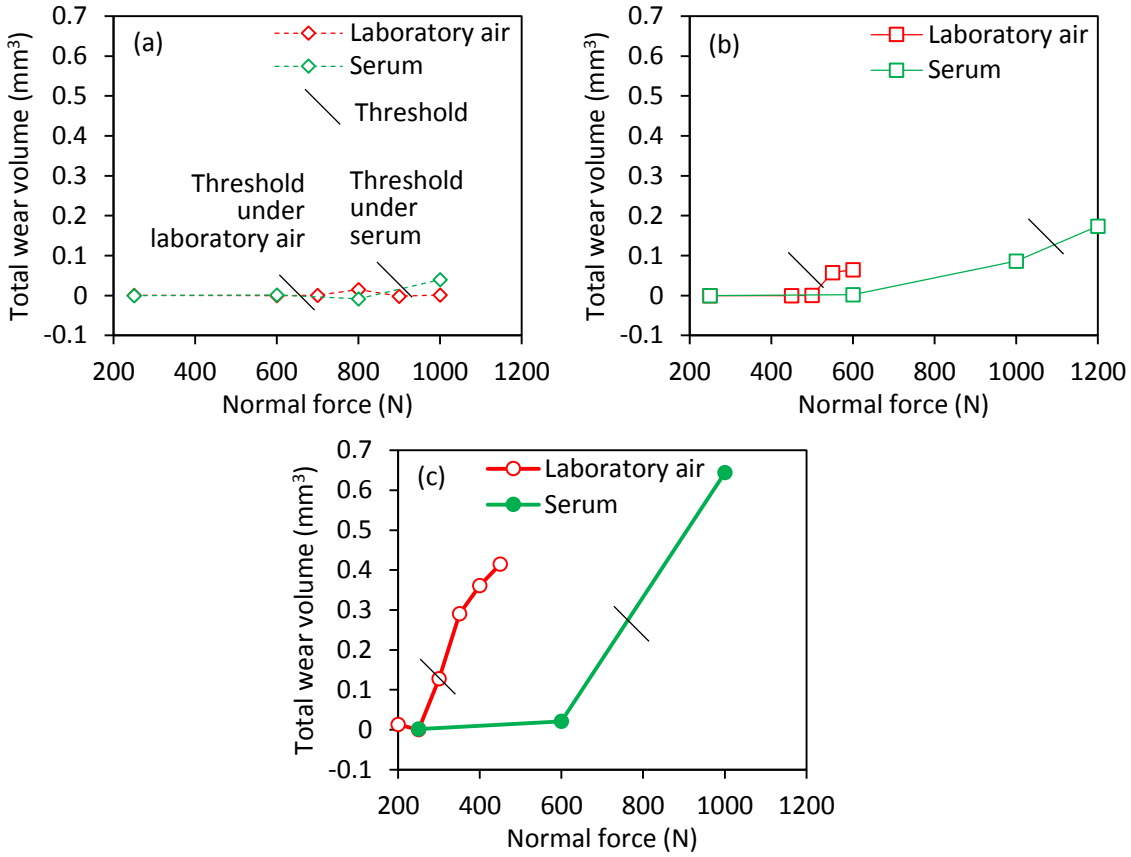

Figure V.19. Total wear volume for tests with a smooth flat coated with DLC A / uncoated cylinder contact under laboratory air and serum conditions: (a) ±20 µm; (b) ±40 µm; (c) ±70 µm.

3.3. Wear scars

Figure V.20 shows wear scars of smooth flat coated with DLC A (in contact with uncoated cylinder) under the serum condition. With the increase in the normal force, the damage of coating becomes more severe. When the value of applied normal force is lower than the threshold, the DLC coating is not removed (±20 µm and 250 N) or is only partly removed (±20 µm and 600 N). Accordingly, the wear scar is composed of a mild wear area or of both mild and severe wear areas. When the value of applied normal force is higher than the threshold, the coating has been partly removed under the low displacement condition of ±20 µm (±20 µm and 1 000 N), while, the coating has been entirely removed under the displacement conditions of ±40 µm and ±70 µm (±40 µm and 1 200 N).

In the mild wear area (i.e., on the rubbed DLC surface), EDX analysis was performed. Except carbon, no obvious chlorine, sodium and potassium elements were detected. This suggests that there is no strong interaction between DLC coating and serum, under these experimental conditions.

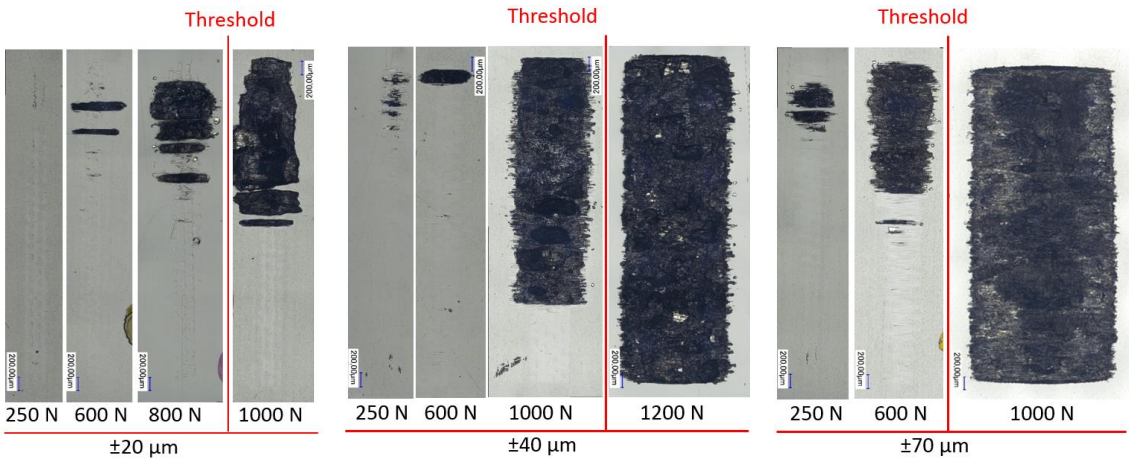

Figure V.20. Wear scars of smooth flats coated with DLC A (in contact with uncoated cylinder) under the serum condition.

In the severe wear area (i.e., on the rubbed Ti–6Al–4V surface), EDX analysis was also performed. Figure V.21 shows the EDX results on the flat after the test under the condition of ±70 µm and 1 000 N. Except elements (Ti, Al, and V) from the substrate and elements (C and Si) from coating, O, Na and Cl are detected. The presence of O reveals oxidization of the rubbed Ti–6Al–4V surface. And the presence of elements from serum (Na and Cl) suggests that the rubbed Ti–6Al–4V surface might be corroded in serum condition.

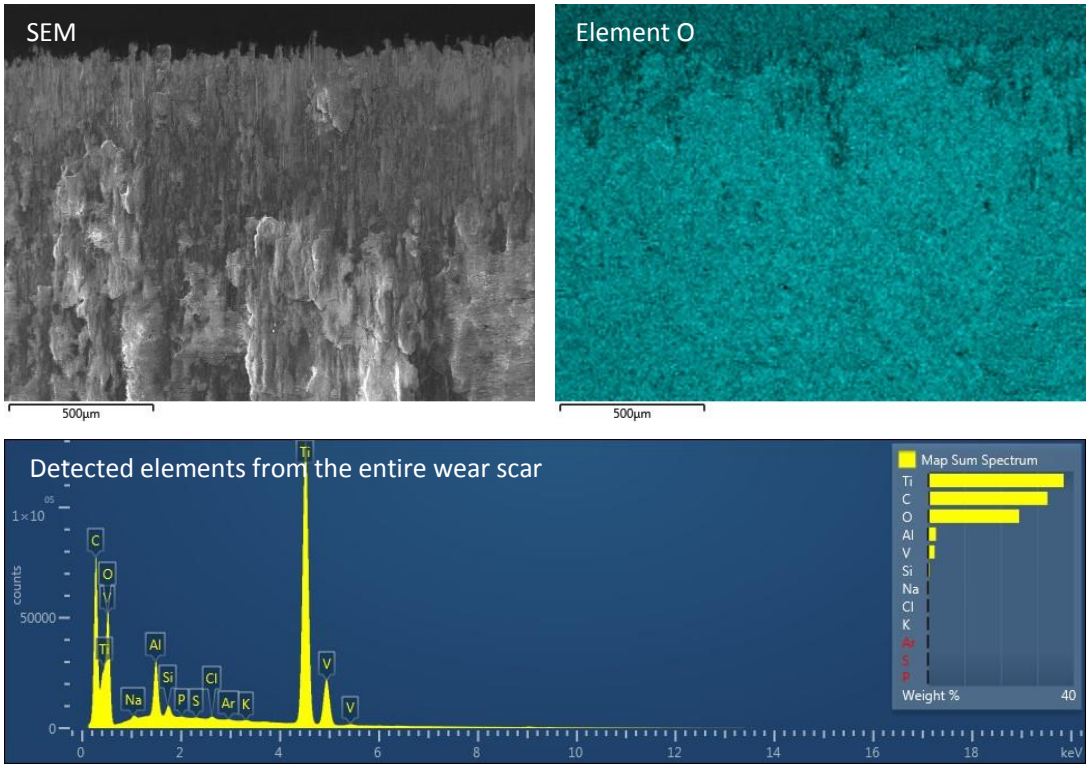

Figure V.21. SEM and EDX observations of the wear scar on coated flat after test under serum condition with the displacement amplitude of ±70 µm and the normal force of 1 000 N.

3.4. Coating response wear map

Figure V.22 shows the coating response wear map for smooth flats coated with DLC A (in contact with uncoated cylinder) under the serum condition. The map can be divided into two areas: (1) the coating working area, under the low normal force conditions, where the value of the applied normal force is lower than the threshold; (2) the coating failure area, under the high normal force conditions, where the value of the applied normal force is higher than the threshold. In the coating working area, the coating is not or is only partly removed; the values of Q_{max}/P are low and the wear volumes are small. The substrate is well protected by the DLC coating. In the coating failure area, the coating has been partly or almost entirely removed, Q_{max}/P is high, and the wear volume is small under the small displacement condition of ±20 µm, and it is large under the displacement conditions of ±40 µm and ±70 µm.

The solid curve represents the border between coating working area and coating failure area under serum condition. The dotted curve represents the border under laboratory air condition. Under laboratory air condition, the threshold lies at lower normal forces under larger displacement condition. With the serum, the coating working area extends to higher forces, which means that the presence of serum has a positive influence on the coating performance. Furthermore, the threshold lies at the highest normal force under the displacement amplitude of ±40 µm.

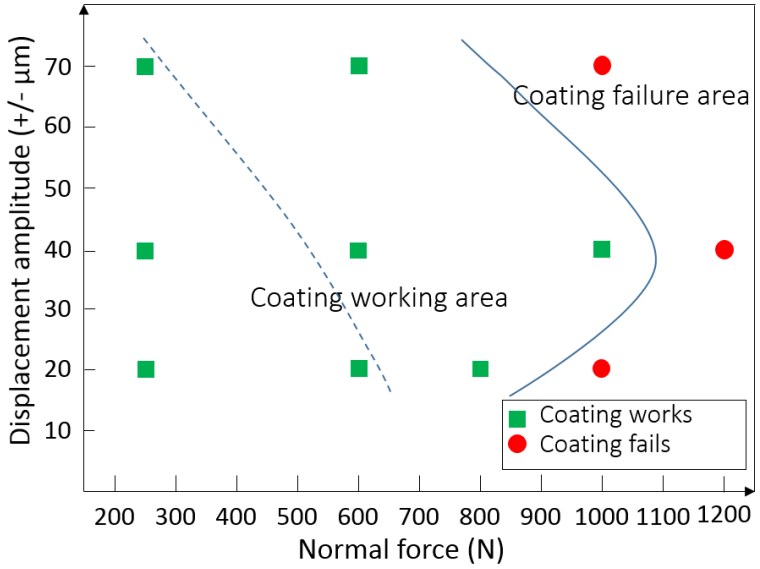

Figure V.22. Coating response wear map for smooth flats coated with DLC A (in contact with uncoated cylinder) under the serum liquid condition. Solid curve represents the border between coating working area and coating failure area under serum condition. Dotted curve represents the border under laboratory air condition.

3.5. Analysis of effect of serum liquid on fretting behavior of Ti–6Al–4V / DLC coating contact

The presence of serum has a significant effect on the tribological performance of the DLC coating. It is clear from the coating response wear map (Figure V.22) that the coating working area extends towards higher normal forces under serum condition, whatever the value of displacement amplitude.

From the point of view of analysis of threshold in normal force, for tests under serum condition, the thresholds extend towards higher normal forces comparing with those under laboratory air conditions (Figure V.17). Furthermore, the extension in the normal forces is more significant under a larger displacement amplitude. For instance, under the small displacement amplitude of ±20 µm, the threshold is between 600 N and 700 N under the laboratory air condition (the middle value, 650 N, is regarded as the value of the normal force where the threshold occurs), whereas, the threshold is between 800 N and 1 000 N under the serum condition (the middle value is 900 N). Thus, the increase in the threshold induced by the presence of serum is 250 N. The increase rate in the threshold is defined as the ratio of the increase in the normal force (250 N) over the normal force where the threshold occurs under the laboratory air condition (650 N). Therefore, the presence of serum induces an increase rate in the threshold of 38% (i.e., 250 N/650 N) under the small displacement amplitude of ±20 µm. Under the displacement amplitude of ±40 µm, the increase rate is 110%. Under the large displacement amplitude of ±70 µm, the increase rate is 191%.

The evolution of the increase rate in the threshold as a function of the displacement amplitude is shown in Figure V.23. It is clear that the increase rate in the threshold induced by the presence of serum presents a remarkable increase trend with the increase in the displacement amplitude. This means that the presence of serum has a positive effect of coating performance, and the positive effect is more significant under larger displacement amplitude.

A hypothetical explanation is proposed. No corrosion is observed on the rubbed DLC surface under serum condition, which means that the serum shows no visible chemical negative effect on the DLC coating. Under laboratory air condition, DLC coating is in contact with the solid counterbody. Under serum condition, during sliding, the serum enters the interface and separates the contact in some extend. It might change the dry friction state (regardless of the absorbed layer at the interface in air) into the mixed friction state (dry and lubricated), which might result in a positive effect on the performance of DLC coating. The friction coefficient between Ti–6Al–4V and DLC coating (i.e., in the coating working area) shows similar low values (around or below 0.2) under laboratory air and serum conditions.

With larger displacement amplitude, the serum might enter more easily the interface. Thus, the positive effect of serum is more significant. Furthermore, the increase in

displacement amplitude leads to the increase in sliding speed, as the fretting test was conducted with a fixed frequency of 5 Hz. A higher sliding speed may enhance the presence of serum between the two solid surfaces.

In addition, from Figure V.22, under laboratory air condition, the threshold lies at a lower normal force under a larger displacement amplitude. With the serum, the positive influence on the DLC coating performance is more significant under a larger displacement amplitude. Thus, the threshold lies at the highest normal force under the displacement amplitude of ±40 µm.

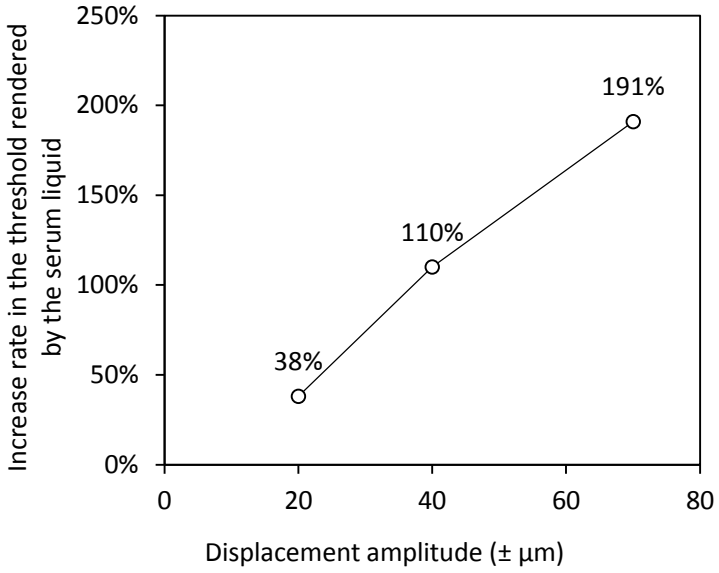

Figure V.23. Evolution of the increase rate in the threshold induced by the presence of serum as a function of the displacement amplitude.

4. Conclusions

In this chapter, the influence of serum on the fretting behavior of Ti–6Al–4V and DLC coating was investigated.

For the fretting tests of Ti–6Al–4V / Ti–6Al–4V, the presence of the serum had different effect on the fretting behavior, depending on the displacement amplitude:

- Under the displacement amplitude of ±40 µm, the friction coefficients were slightly lower (0.6–0.8); however, the total wear volumes were significantly larger comparing with those under the laboratory air conditions,
- Under the displacement amplitude of ±70 µm, the friction coefficients were significantly lower (0.25–0.35) and the total wear volumes were significantly smaller comparing with those under the laboratory air conditions.

For fretting tests of DLC coating / Ti–6Al–4V, there is no obvious chemical interaction between the rubbed DLC surface and the serum.

The coating response wear map could be divided into two areas: the coating working area (low normal force conditions) and the coating failure area (high normal force conditions).

The presence of serum had a positive influence on the tribological performance of the DLC coating. Furthermore, the positive influence was more significant under a larger displacement amplitude condition. The increase rates in the threshold induced by the presence of serum were 38%, 110%, and 191% under the displacement amplitudes of ±20 μm, ±40 μm, and ±70 μm, respectively.

Synovial fluid is present in the hip joint. According to the results in this chapter, the presence of serum had no visible negative influence on the investigated DLC coating. Therefore, the DLC coating can be applied into Ti–6Al–4V / Ti–6Al–4V interface for neck adapter–femoral stem contact with the presence of synovial fluid.

CHAPTER VI

UNDERSTANDING LOW FRICTION OF DLC COATING UNDER LOW LOAD CONDITION

CHAPTER VI: UNDERSTANDING LOW FRICTION OF DLC COATING UNDER LOW LOAD CONDITION

CHAPTER VI: UNDERSTANDING LOW FRICTION OF DLC COATING UNDER LOW LOAD CONDITION

This chapter investigates the origin of low friction for the DLC coating / Ti–6Al–4V contact under low load conditions in dry condition. In addition, the effect of surface roughness is investigated. Different analytical techniques for surfaces are put together in order to propose a tribological model for the evolution of DLC coating / Ti–6Al–4V contact.

1. Introduction

From Chapter IV, the DLC coating / Ti–6Al–4V contact presented low friction in the coating working area (i.e., under low load conditions). Figure VI.1 shows the evolution of the friction coefficient (Q_{max}/P) between DLC coated flats and an uncoated Ti–6Al–4V cylinder. The friction coefficient is relatively high at the beginning of the test, then it decreases to low values (below 0.2) in the running-in period for around 100 cycles, and then remains relatively stable until the end of the test.

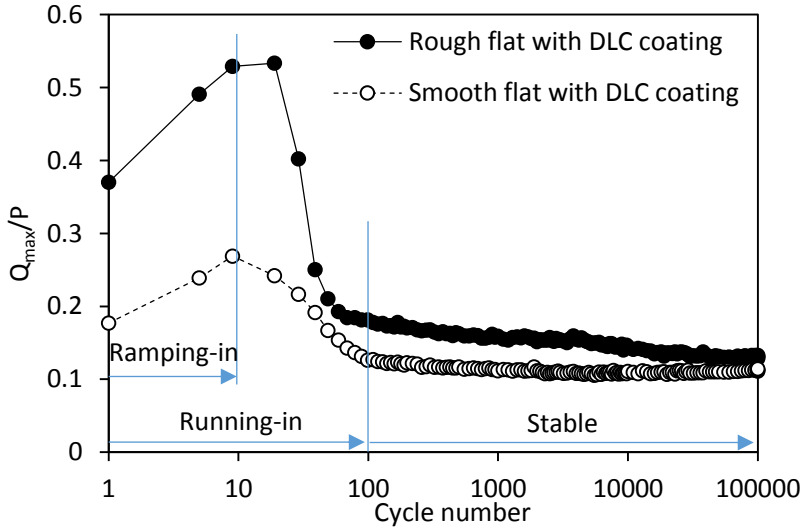

Figure VI.1. Evolution of Q_{max}/P as a function of the number of cycles for rough and smooth flats coated with DLC A in contact with an uncoated Ti–6Al–4V cylinder under the laboratory air condition with the displacement amplitude of ±20 µm and the normal force of 250 N.

In this chapter, the origin of the low friction is investigated. Tests were conducted with a DLC A coated flat / uncoated cylinder contact, with the small displacement amplitude of ±20 µm and the low normal force of 250 N, under the laboratory air condition (temperature: 18–23 °C, humidity: 30–50%).

After the test, different analytical techniques were used to analyze the rubbed surfaces. Raman spectroscopic measurements were conducted on the rubbed and unrubbed DLC coating surfaces and on the rubbed Ti–Al–4V surface to investigate the structural characterization of carbon. Nano-indentation tests were performed using the CSM method on the rubbed and unrubbed Ti–6Al–4V surfaces. Micro-pillars were manufactured and compressed on the rubbed and unrubbed Ti–6Al–4V surfaces. Nano-indentation tests and compression of micro-pillar were conducted to measure the mechanical properties of rubbed Ti–6Al–4V surface.

At last, a tribological model for the evolution of DLC coating / Ti–6Al–4V contact is proposed.

2. Friction coefficient under different contact conditions

It is clear from Figure VI.1 that the friction coefficient for the DLC coating / Ti–6Al–4V contact decreases from high values to low values during the first around 100 cycles (i.e. the running-in period). The evolution of friction coefficient may be due to modification of DLC coating surface and/or Ti–6Al–4V surface and/or generation of debris, due to friction. To clarify which part of the contact surfaces (the rubbed DLC coating surface, the rubbed Ti–6Al–4V countersurface, or both) led to the low friction, three different series of tests were conducted (Figure VI.2).

In series 1, after the running-in period (100 cycles), the test was stopped and restarted again for another 100 cycles. After that, the test was stopped again. The contact was opened and put into contact again. Then, the test was restarted again. Thus, the rubbed DLC coating surface and the rubbed Ti–6Al–4V surface were in contact.

In series 2, after the running-in period (100 cycles), the flat and cylinder contact was opened. And then the cylinder was rotated to present a new Ti–6Al–4V surface for the contact with the already-rubbed DLC coating surface. Then, the test was restarted again.

In series 3, after the running-in period (100 cycles), the contact was opened, and the flat was moved to a new position to present a new DLC coating surface for the contact with the already-rubbed Ti–6Al–4V surface. Then, the test was restarted again.

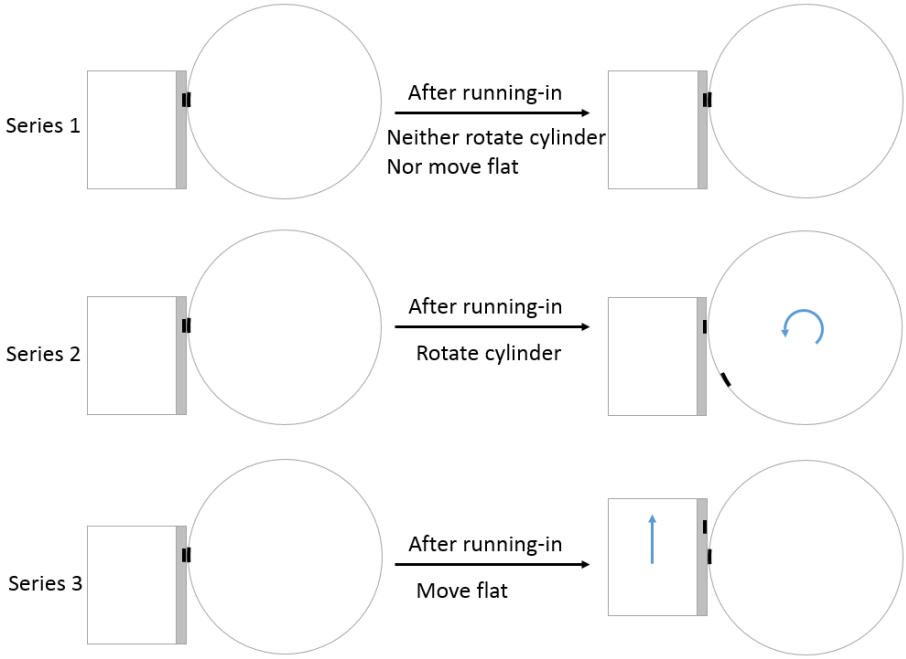

Figure VI.2. Schematic diagram for three series of tests.

2.1. Rubbed DLC coating surface / rubbed Ti–6Al–4V surface contact

In series 1, after the running-in period (100 cycles), the test was stopped and restarted for another 100 cycles (as shown by the black dotted curve from cycles 101 to 200 in Figure VI.3).

A continuous low friction coefficient was obtained except for the first 10 cycles (between cycles 101 and 110), because of the ramping-in period.

At cycle 201, the contact of the flat and cylinder was opened and then put again into contact. The normal force was applied, and the test was continued for another 100 cycles. This process was repeated two times every 100 cycles.

As shown by the black dotted curves from cycles 201 to 400 in Figure VI.3, putting into contact the already-rubbed Ti–6Al–4V surface (cylinder) with the already-rubbed DLC coating (flat) resulted in a new small running-in period because of the change in the pressure distribution when reloaded. Compared to the running-in period from cycles 0 to 100, the new small running-in period had a much lower maximal friction coefficient. Specifically, the maximal friction coefficient during the test from cycles 201 to 300 was 0.3 with the rough flat. It was lower (0.18) with the smooth flat. In addition, the maximal friction coefficient during the test from cycles 301 to 400 was lower than that from cycles 201 to 300, which may be due to modification of surfaces, because of wear.

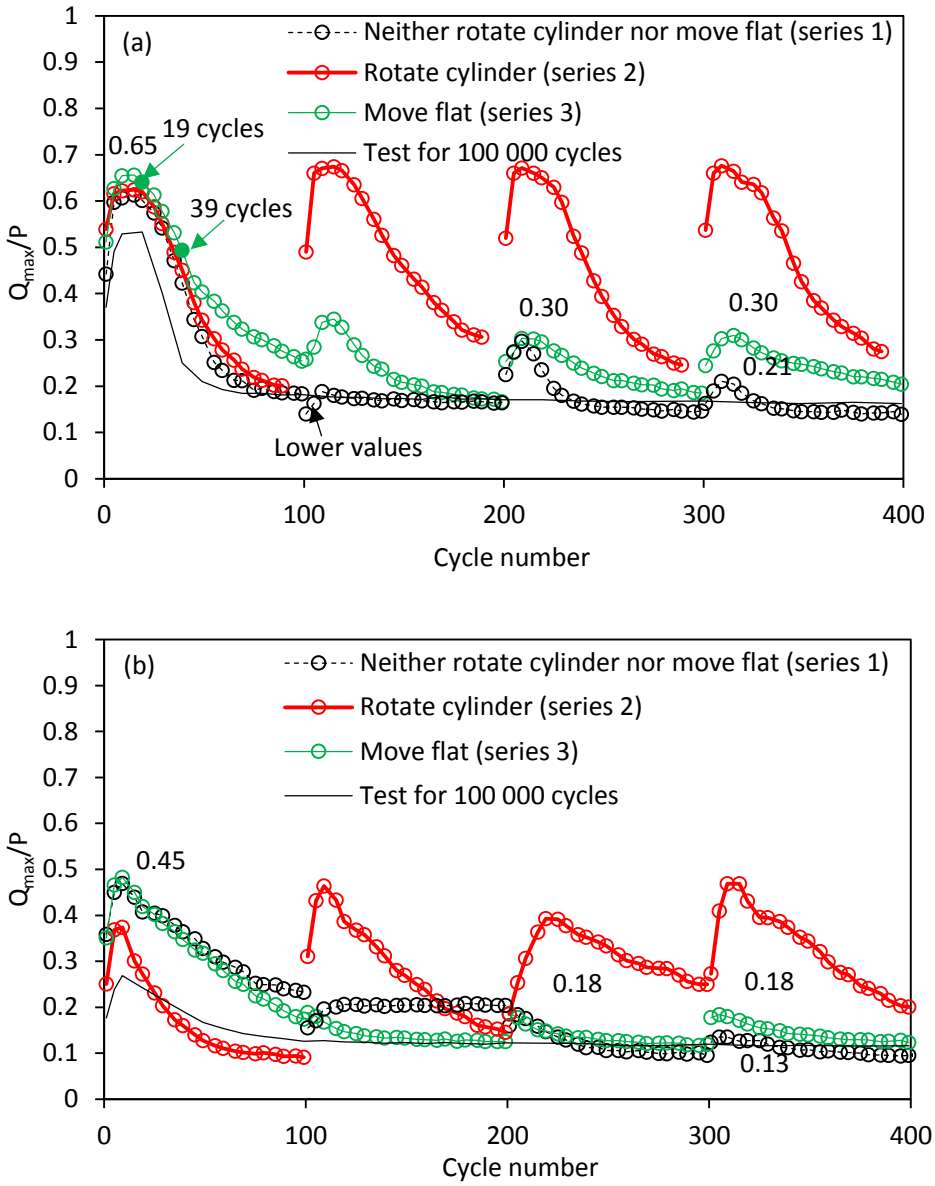

Figure VI.3. Evolutions of Q_{max}/P under different contact conditions for DLC A coated flat / uncoated Ti–6Al–4V cylinder contact under the laboratory air condition with the displacement amplitude of ±20 µm and the normal force of 250 N: (a) rough flat; (b) smooth flat.

2.2. Rubbed DLC coating surface / new Ti–6Al–4V surface contact

In series 2, after the running-in period (100 cycles), the flat and cylinder contact was opened. And then, the cylinder was rotated to present a new Ti–6Al–4V surface for the contact with the already-rubbed DLC coating surface. The normal force was applied again, and the test was continued for another 100 cycles. This process was repeated three times.

As shown by the red solid curves in Figure VI.3, putting into contact a new Ti–6Al–4V surface (cylinder) with the already-rubbed DLC coating (flat) led to a new running-in period. Furthermore, the new running-in period was almost identical to the one from the test with the new Ti–6Al–4V surface in contact with the new DLC coating. In other words, as soon as a

new surface of Ti–6Al–4V came into contact, a 100-cycles running-in period was necessary to cause a decrease in the friction coefficient. Moreover, the maximal friction coefficient was approximately 0.65 during each 100 cycles for tests with the rough flat (Figure VI.3a). For tests with the smooth flat, the maximal friction coefficient was lower (approximately 0.45, as shown in Figure VI.3b), as expected.

2.3. New DLC coating surface / rubbed Ti–6Al–4V surface contact

In series 3, after the running-in period (100 cycles), the contact was opened, and the flat was moved to a new position to present a new DLC coating surface for the contact with the already-rubbed Ti–6Al–4V surface. The normal force was applied again, and the test was continued for another 100 cycles. This process was repeated three times.

As shown by the green fine curves in Figure VI.3, putting into contact a new DLC coating surface (flat) with the already-rubbed Ti–6Al–4V surface (cylinder) led to a new small running-in period, which was similar to the small running-in period of the test in series 1 from cycles 201 to 300 (i.e., the already-rubbed Ti–6Al–4V surface in contact with the already-rubbed DLC coating). Furthermore, in series 3, the maximal friction coefficient during each small running-in period showed no obvious decrease.

2.4. Conclusions on running-in

The relationship between the friction and the contact condition is shown in Table VI.1. It can be concluded that the friction is closely dependent on the Ti–6Al–4V surface state. Specifically, a new Ti–6Al–4V surface always leads to high friction, and a rubbed Ti–6Al–4V surface always leads to low friction. The DLC coating surface state has no influence on the low friction.

Table VI.1. Relationship between the friction and the contact condition.

	DLC coating surface	Ti–6Al–4V countersurface	Friction during running-in
New test	New	New	High
Series 1	Rubbed	Rubbed	Low
Series 2	Rubbed	New	High
Series 3	New	Rubbed	Low

3. Evolution of wear scars

From section 2, it is known that the Ti–6Al–4V surface after the running-in period is the key factor for low friction. To better understand the tribological behavior between the DLC coating and Ti–6Al–4V, the evolution of the contact surfaces (both Ti–6Al–4V and DLC coating) was explored. Tests were carried out on the rough coated flat with different numbers of cycles: 0 (maintaining the surfaces in contact for 10 s, then opening the contact), 1, 20, 40, 100 (just after the running-in period), and 100 000 cycles. On the smooth coated flat, tests were carried

out with 0, 1, 100, and 100 000 cycles. Wear scars of Ti–6Al–4V and DLC coating were inspected with digital microscope, interferometer, SEM and EDX. The influence of roughness was explored.

3.1. Contact only (0 fretting cycle)

The DLC coating (flat) and Ti–6Al–4V (cylinder) surfaces were put into contact with the applied normal force of 250 N for 10 s, and then the contact was opened.

- **Rough flat / rough cylinder**

The Ti–6Al–4V surface is shown in Figure VI.4, and the rough DLC coating surface is shown in Figure VI.5. It is clear from Figure VI.4 that some Ti–6Al–4V was removed, and scratches were observed on the cylinder surface. On the DLC coating surface, some material was adhered (Figure VI.5). Furthermore, from the analysis of EDX, this adhered material was composed of titanium, aluminum, and vanadium, thus suggesting that Ti–6Al–4V was transferred from the cylinder surface to the DLC coating surface. No obvious oxygen was detected in the transferred Ti–6Al–4V.

There are two possibilities leading to the transfer: (1) adhesion between the DLC coating and Ti–6Al–4V; and (2) abrasion of rough hard DLC surface on the soft Ti–6Al–4V alloy. For abrasion process, relative motion between the contact surfaces is required. The relative motion might be derived from the elastic and plastic deformation of samples under the application of the normal force, and/or from the roughness of the samples.

In addition, no obvious carbon element was transferred from the DLC coating to the Ti–6Al–4V surface.

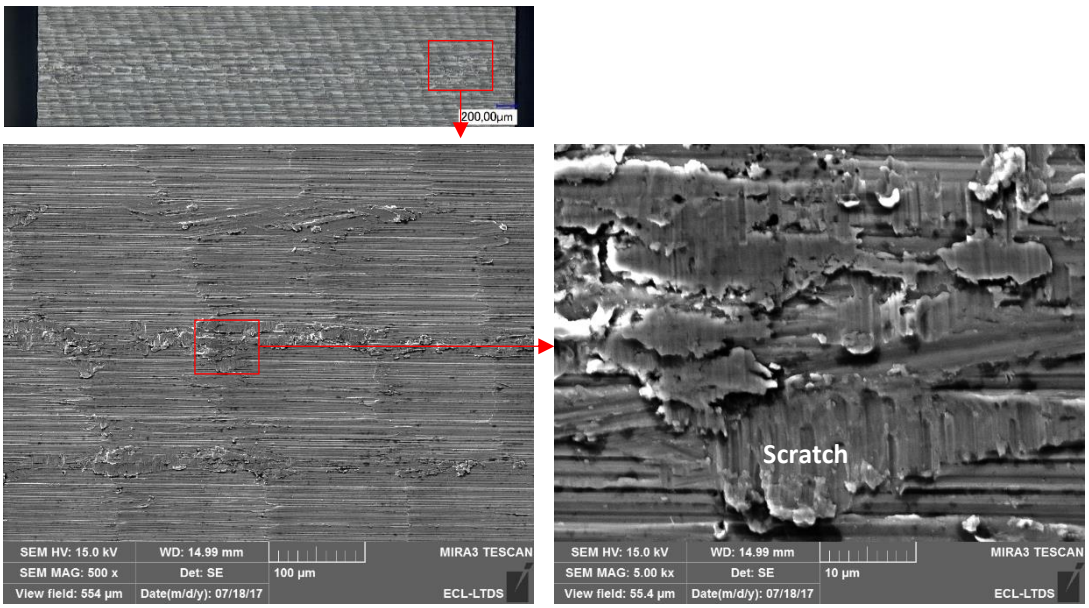

Figure VI.4. Ti–6Al–4V surface (in contact with rough DLC coated flat) at cycle number 0.

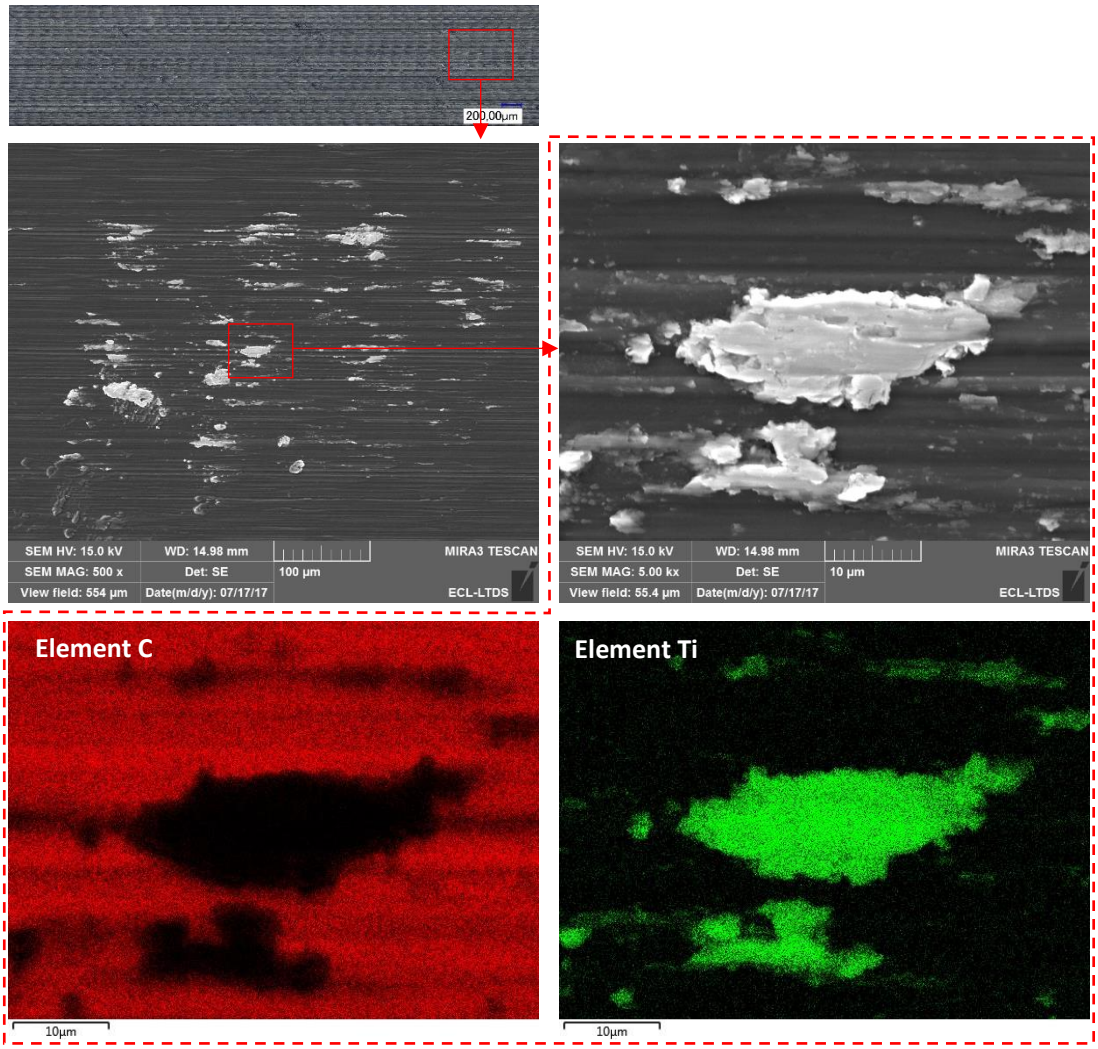

Figure VI.5. Rough DLC coating surface (in contact with Ti–6Al–4V surface) at cycle number 0.

- **Smooth flat / rough cylinder**

For the test with the smooth flat, the Ti–6Al–4V surface is shown in Figure VI.6, and the smooth DLC coating surface is shown in Figure VI.7. It is clear from the SEM of the cylinder surface that less Ti–6Al–4V was removed (Figure VI.6), and the damage on the cylinder surface was milder when it was in contact with the smooth flat than when in contact with the rough flat (Figure VI.4). Accordingly, less Ti–6Al–4V was adhered to the smooth DLC surface (Figure VI.7). Furthermore, from the interferometer image on the smooth DLC surface, indentation points were observed on the flat with the maximal depth of 0.4 µm, which means that the local contact pressure between the asperity of the rough cylinder and the smooth DLC coating was larger than the elastic limit of the flat. Similarly, the local contact pressure between the rough cylinder and the rough flat was also larger than the elastic limit of the flat, but the change of the profile was unmeasurable on the rough surface.

Because of the smoothness of the smooth DLC coating surface, the abrasion process could be negligible. Therefore, the Ti–6Al–4V transfer from cylinder to the smooth flat was mainly derived from the adhesion. This is the reason why less Ti–6Al–4V was transferred to

the smooth DLC surface than to the rough DLC surface. It can also be concluded that the adhesion did occur between the DLC surface and the Ti–6Al–4V surface before the friction starts.

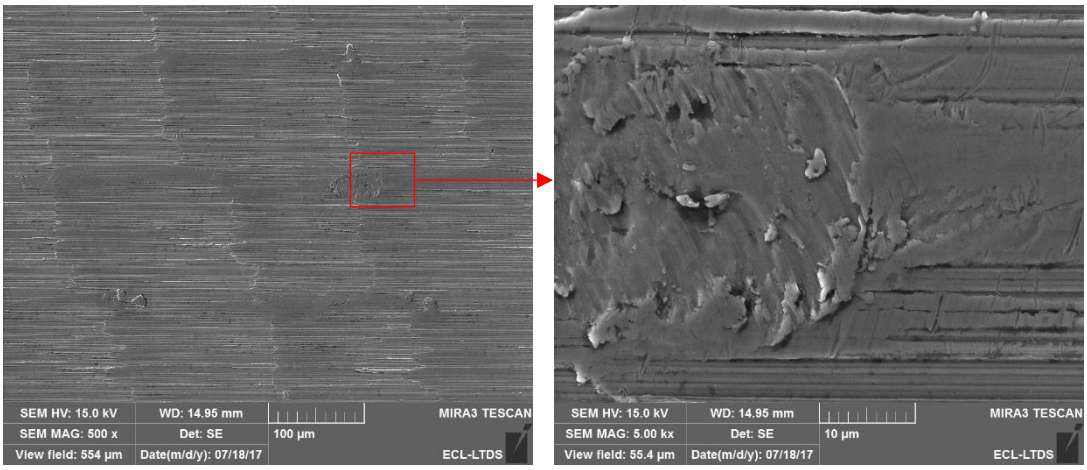

Figure VI.6. Ti–6Al–4V surface (in contact with smooth DLC coated flat) at cycle number 0.

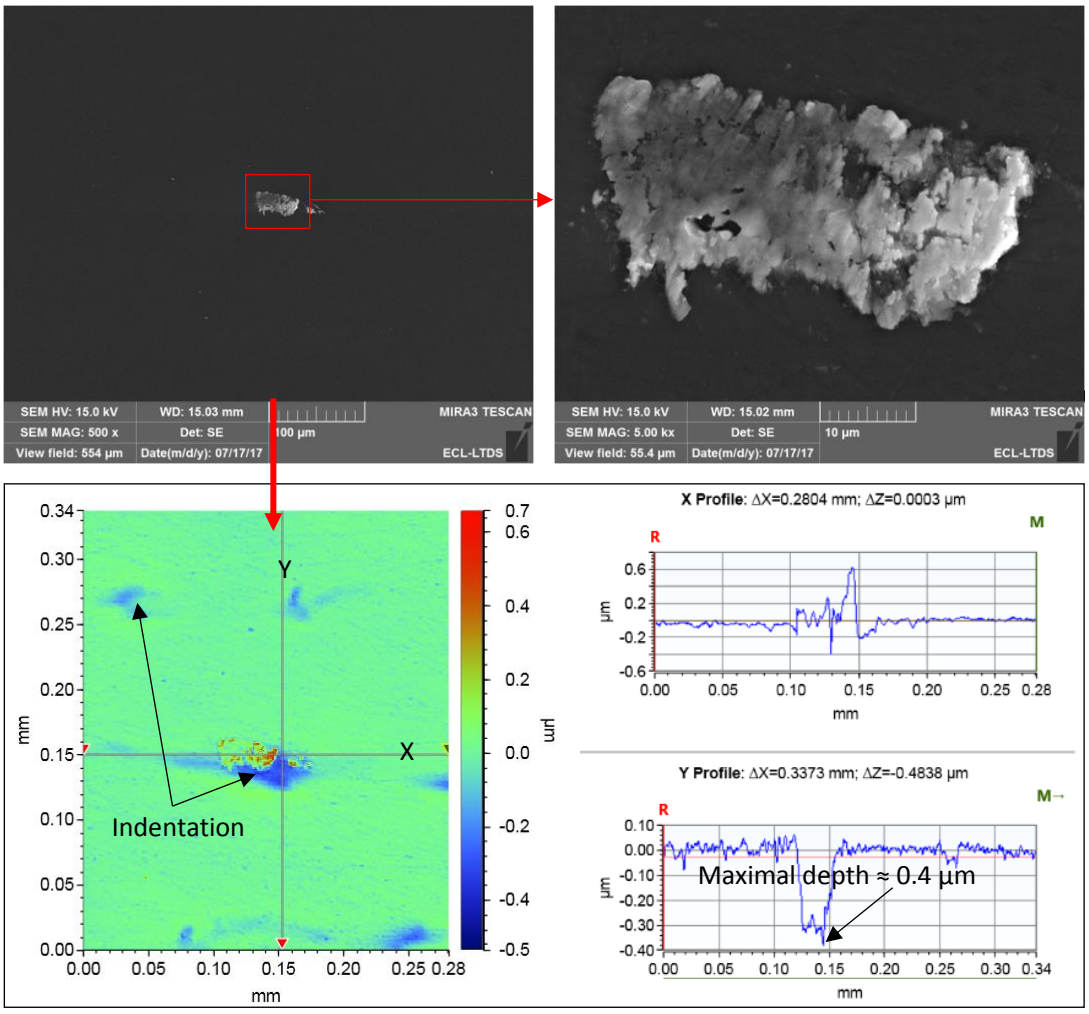

Figure VI.7. Smooth DLC coating surface (in contact with Ti–6Al–4V surface) at cycle number 0.

3.2. After 1 cycle

- **Rough flat / rough cylinder**

Figure VI.8 shows the Ti–6Al–4V surface and the rough DLC coating surface after 1 cycle. Compared to the test before sliding (i.e., the cycle number is 0, Figure VI.4 and Figure VI.5), the damage on the cylinder surface was more severe with obvious scratches parallel to the fretting direction. And much more Ti–6Al–4V was transferred to the rough DLC surface (Figure 6.7b), this is because the sliding motion significantly enhanced the abrasion process between the rough DLC surface and Ti–6Al–4V surface.

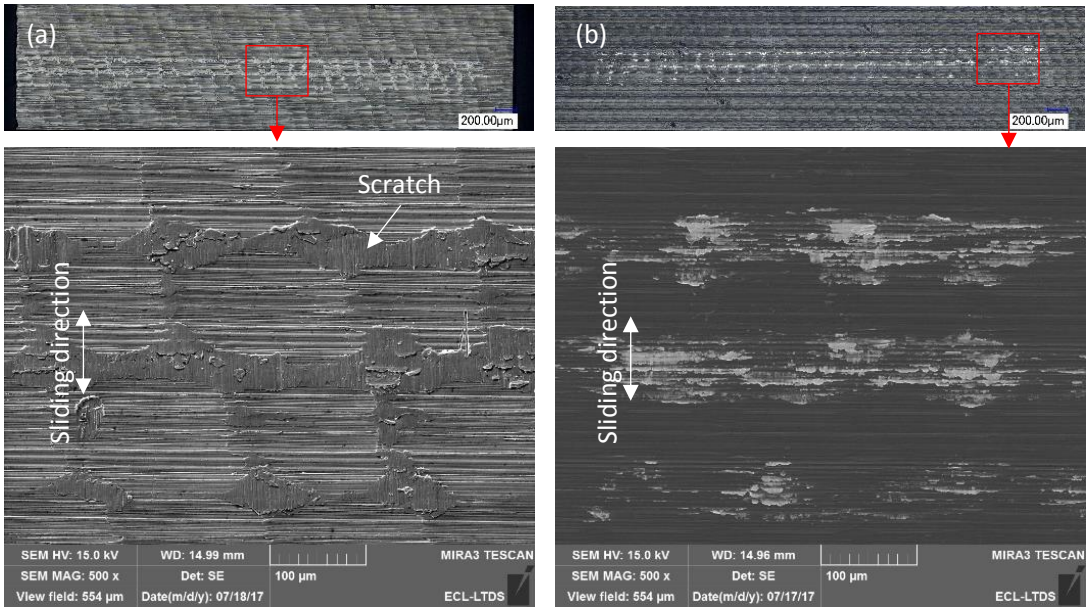

Figure VI.8. (a) Ti–6Al–4V surface in contact with (b) rough DLC coating surface after 1 cycle.

- **Smooth flat / rough cylinder**

Figure VI.9 shows the Ti–6Al–4V surface and the smooth DLC coating surface after 1 cycle. Compared to the test before sliding (i.e., the cycle number is 0, Figure VI.6 and Figure VI.7), the damage on the cylinder surface was slightly more severe, with scratches on the Ti–6Al–4V surface (Figure VI.9a), and slightly more Ti–6Al–4V material was adhered to the DLC surface (Figure VI.9b). This is because the sliding motion slightly enhanced the adhesion process between the smooth DLC surface and Ti–6Al–4V surface.

Compared to the test on the rough DLC coating surface with the same cycle number of 1 (Figure VI.8), the damage on the Ti–6Al–4V surface was much milder, and much less Ti–6Al–4V was adhered to the smooth DLC surface.

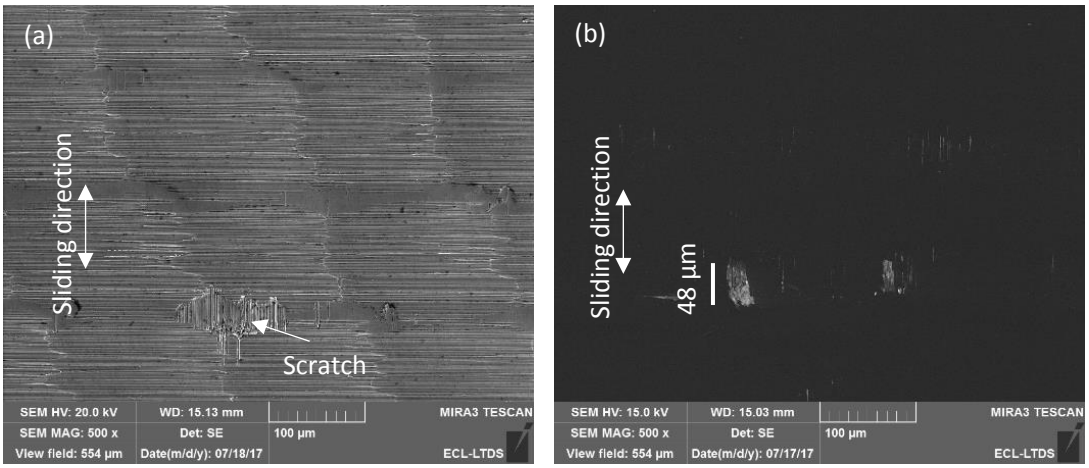

Figure VI.9. (a) Ti–6Al–4V surface in contact with (b) smooth DLC coating surface after 1 cycle.

At the beginning of the test, Ti–6Al–4V was worn off from the cylinder as a consequence of adhesion (when in contact with a smooth DLC coating surface) or both adhesion and abrasion (when in contact with a rough DLC coating surface). Energy was needed to break the metallic bonds in the Ti–6Al–4V side. The dissipated energy during each cycle was an integral of displacement and friction force. Therefore, the friction was high at the beginning of the test (Figure VI.1).

In addition, more Ti–6Al–4V was worn off when sliding against a rough DLC coating surface than against a smooth DLC coating surface. Therefore, the friction is higher on a rough DLC coating surface than on a smooth DLC coating surface.

3.3. After 20 cycles (in running-in)

- **Rough flat / rough cylinder**

Figure VI.10 shows the Ti–6Al–4V surface after 20 cycles (i.e. in the running-in period, when the friction coefficient is high). It is clear that, the Ti–6Al–4V was worn off, resulting in scratches on the cylinder surface. Meanwhile, some worn-off material was pressed in the contact, forming a tribofilm on the rubbed Ti–6Al–4V surface. From the EDX analysis, the tribofilm was composed of titanium, aluminum, vanadium, and a quantity of oxygen, suggesting that the tribofilm was worn-off Ti–6Al–4V alloy with severe oxidation due to the repeated sliding in air. Furthermore, cracks were generated perpendicularly to the sliding direction because of the repeated sliding and the stress variation (Figure VI.10c and Figure VI.10d). In addition, DLC particles were observed at some spots on the tribofilm surface (Figure VI.10f and Figure VI.10g).

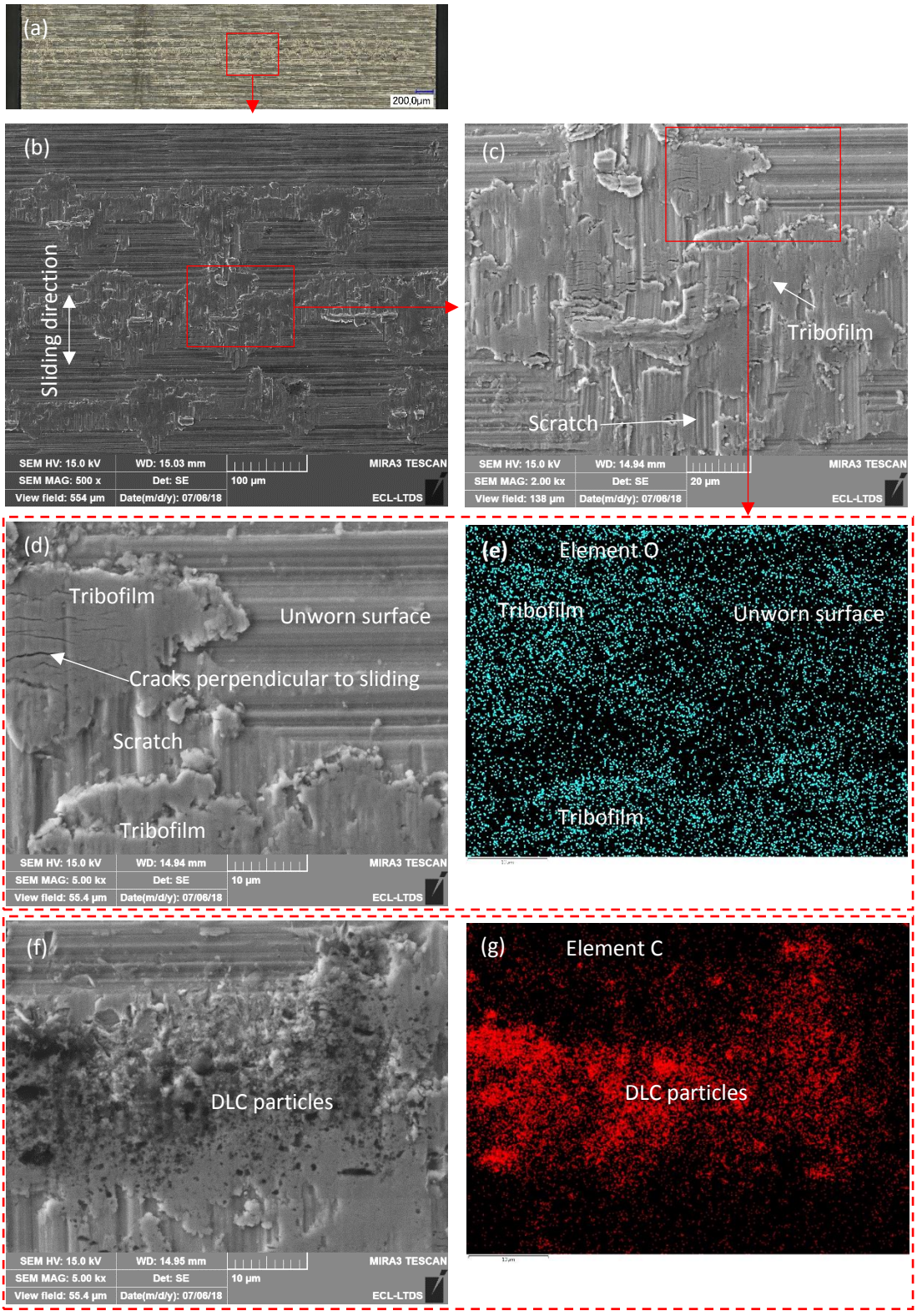

Figure VI.10. Ti–6Al–4V surface (in contact with rough DLC coated flat) after 20 cycles.

Figure VI.11 shows the rough DLC coating surface after 20 cycles. Compared to the flat surface after 1 cycle (Figure VI.8b), much less Ti–6Al–4V was adhered to the DLC surface (Figure VI.11b). From the analysis of EDX (Figure VI.11e), the adhered material was composed of titanium, aluminium and vanadium. No visible oxygen is detected. This suggests that the adhered material was derived from the Ti–6Al–4V transfer (probably at the beginning of the

test), not from the tribofilm material formed on rubbed Ti–6Al–4V surface during the test. The adhered material was worn off with the test ongoing.

It is clear from the observation of SEM and EDX (Figure V.11c) that, a small part of coating was detached. That is why DLC particles were observed on the countersurface (Figure VI.10f and Figure VI.10g).

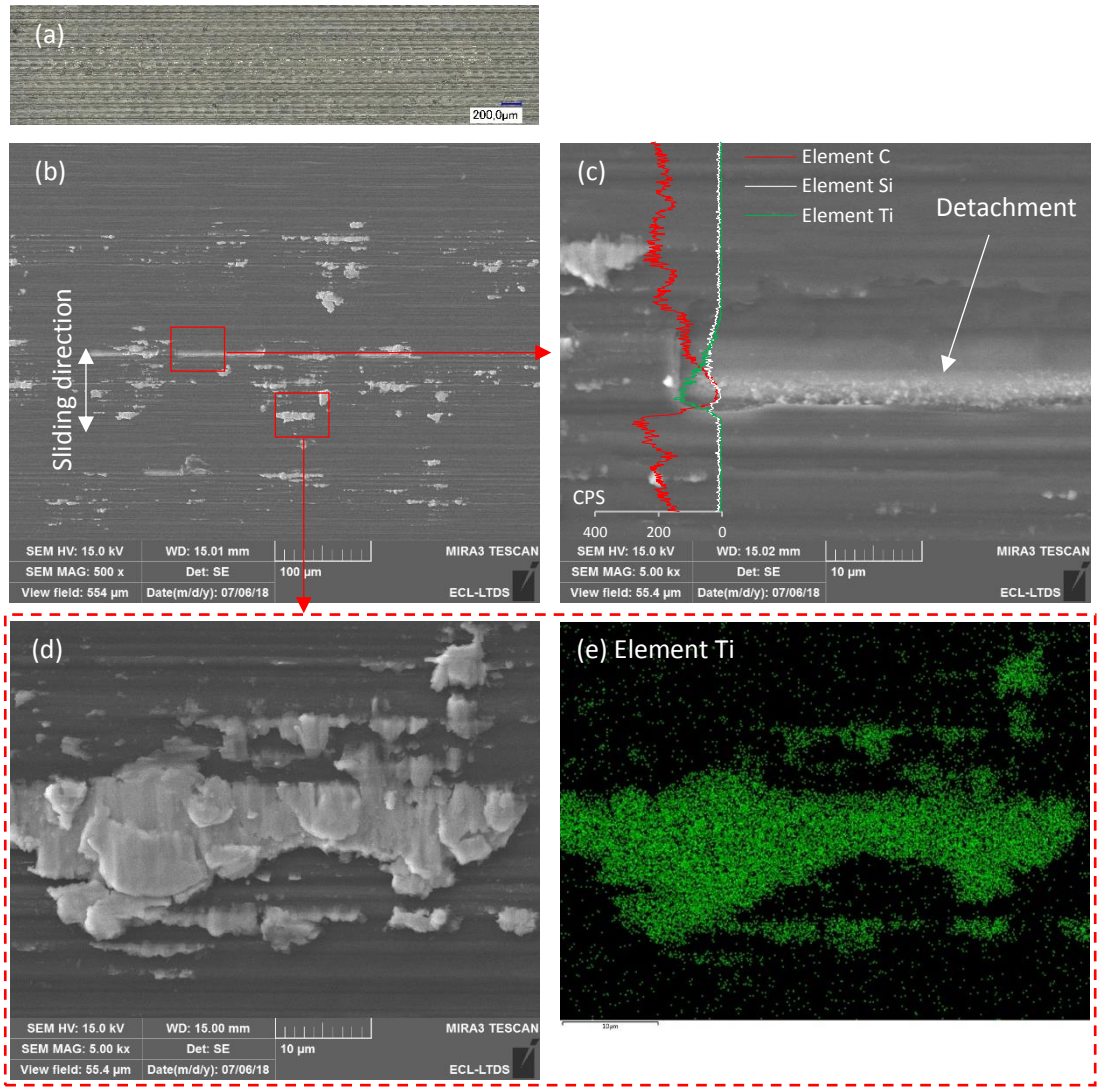

Figure VI.11. Rough DLC coating surface (in contact with Ti–6Al–4V surface) after 20 cycles.

3.4. After 40 cycles (in running-in)

- **Rough flat / rough cylinder**

Figure VI.12 shows the Ti–6Al–4V surface after 40 cycles (when the friction coefficient is at an intermediate value of around 0.49 (Figure VI.3), before reaching the steady-state). Figure VI.13 shows the DLC coating surface after 40 cycles. With the test ongoing from 20 cycles to 40 cycles, more tribofilm material was formed on the rubbed Ti–6Al–4V. And the rubbed area was almost totally covered by tribofilm (Figure VI.12). Less adhered Ti–6Al–4V was observed on the DLC surface (Figure VI.13). Besides, coating detachment was also observed on the flat (Figure VI.13c) and DLC particles were also observed on the cylinder surface (Figure VI.12e).

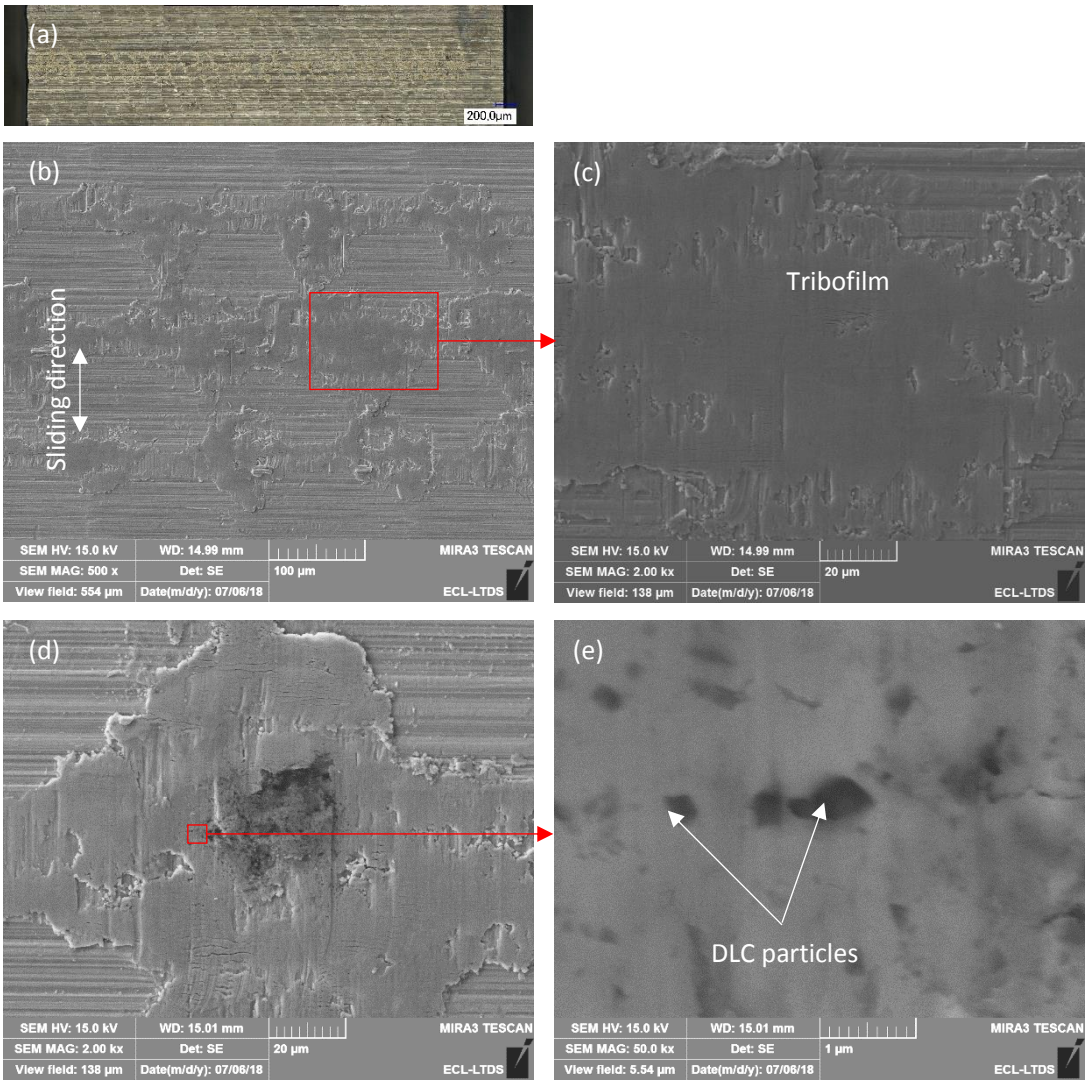

Figure VI.12.Ti–6Al–4V surface (in contact with rough DLC coated flat) after 40 cycles.

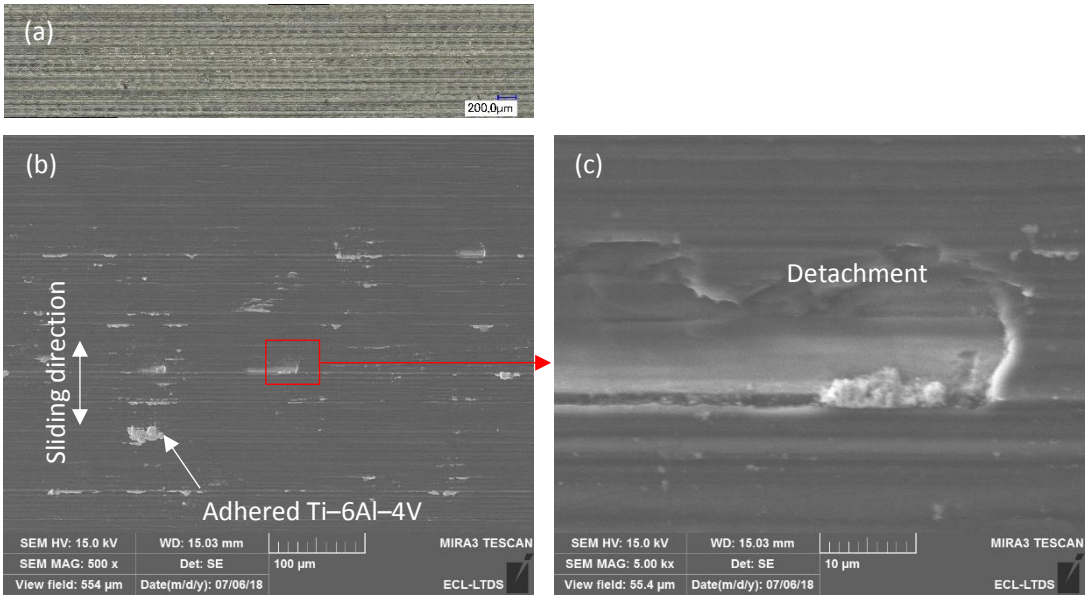

Figure VI.13. Rough DLC coating surface (in contact with rough DLC coated flat) after 40 cycles.

3.5. After 100 cycles (just after running-in)

- **Rough flat / rough cylinder**

Figure VI.14 shows the Ti–6Al–4V surface after 100 cycles (just after the running-in period). With the test ongoing from 40 cycles (in the running-in period) to 100 cycles (just after the running-in), the friction coefficient decreased from around 0.49 to around 0.2 (Figure VI.3). More Ti–6Al–4V surface went into contact due to wear. More tribofilm material formed on the Ti–6Al–4V surface (Figure VI.14b). Cracks were also observed on tribofilm (Figure VI.14c). Oxygen was also detected on the tribofilm material (not presented). DLC particles were also observed on the tribofilm surface (Figure VI.14e). In addition, EDX observation seems to indicate the presence of a “thin carbonaceous film” on the tribofilm surface.

Furthermore, cracks inside the tribofilm perpendicular to the sliding direction revealed that the tribofilm was difficult to remove by the DLC surface. The adhesive force between the DLC coating and tribofilm was lower than the cohesive forces in the cylinder side (i.e., cohesive forces inside the tribofilm and inside the Ti–6Al–4V alloy and the bonding force between the tribofilm and Ti–6Al–4V alloy). The dissipated energy at the interface was low, and the friction coefficient was low.

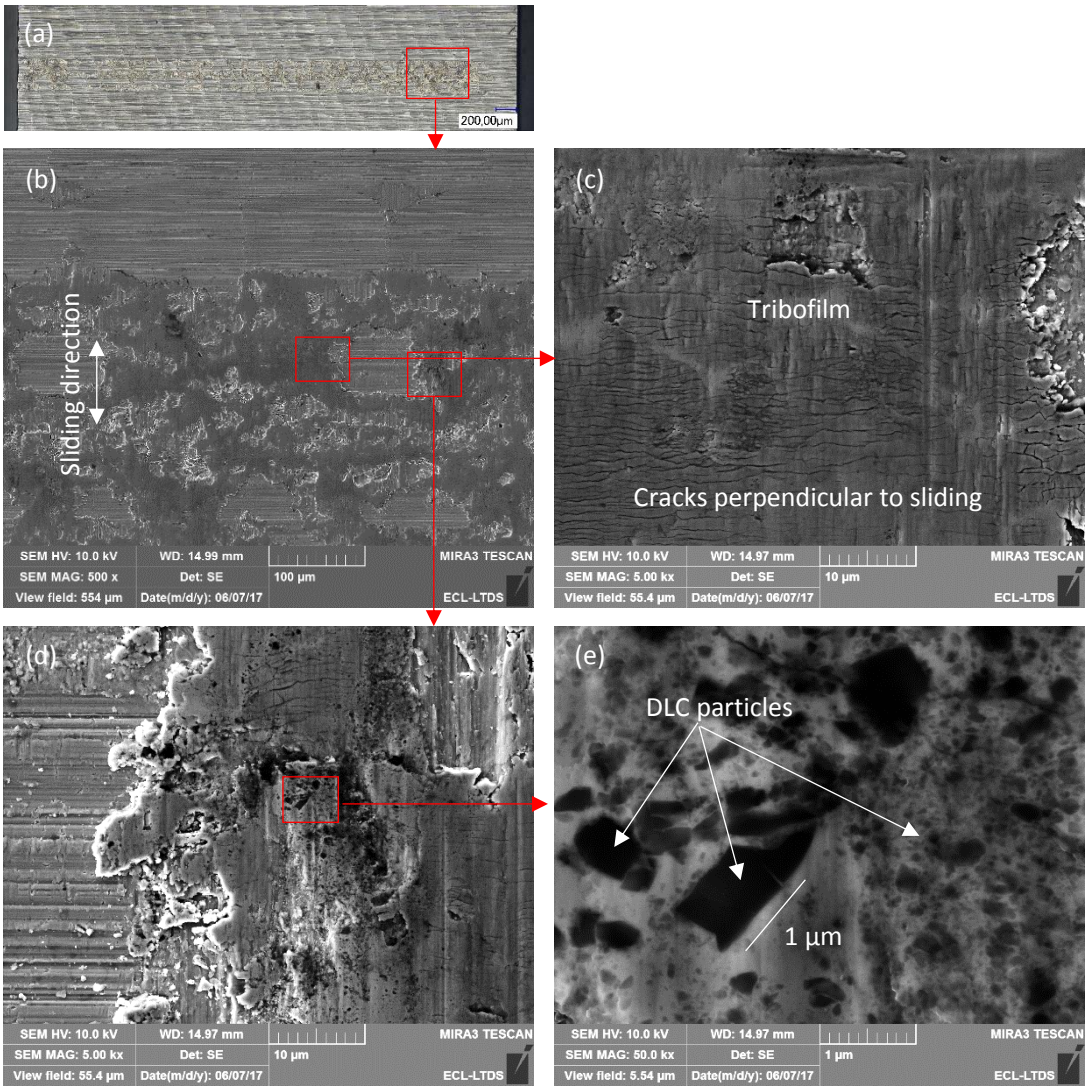

Figure VI.14. Ti–6Al–4V surface (in contact with rough DLC coating surface) after 100 cycles.

Figure VI.15 shows the rough DLC coating surface after 100 cycles (just after the running-in period). With the test ongoing from 40 cycles to 100 cycles, less adhered Ti–6Al–4V was observed on the DLC surface, because the original adhered Ti–6Al–4V on the DLC surface was gradually removed under repeated sliding. The formed tribofilm separated the DLC coating and Ti–6Al–4V surfaces from direct contact, obstructing the Ti–6Al–4V transfer from the cylinder to the DLC surface.

Furthermore, scratches were observed on the DLC surface (Figure VI.15c), indicating that the DLC material could be worn off. Moreover, the DLC coating on the rough flat was fractured. Cracks were generated (Figure VI.15d). Some pieces of coating were flaked off (Figure VI.15e) and transferred to the countersurface (Figure V.14e) and/or ejected as debris. The size of the flaking-off shown in Figure VI.15e reached around 1 µm. The maximum size of the DLC particles on the countersurface (Figure VI.14e) also reached around 1 µm. Under repeated sliding, some DLC flakes were crushed into smaller particles (Figure VI.14e).

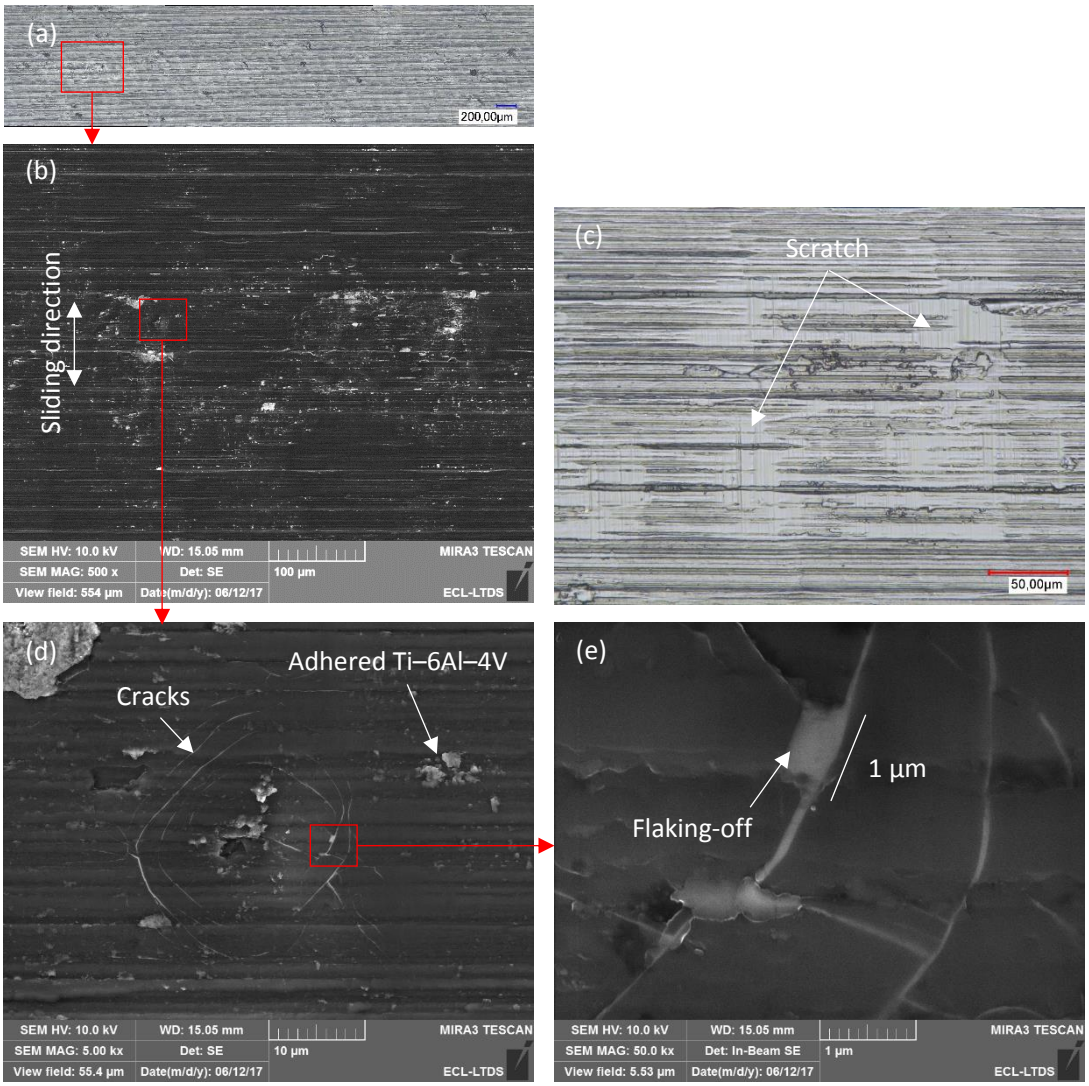

Figure VI.15. Rough DLC coating surface (in contact with Ti–6Al–4V surface) after 100 cycles.

- **Smooth flat / rough cylinder**

Figure VI.16 shows the Ti–6Al–4V surface (in contact with the smooth flat) after 100 cycles. The tribofilm was formed on the Ti–6Al–4V surface and the tribofilm was oxidized.

Figure VI.16b shows that, on the top surface of the tribofilm, there was a “thin carbonaceous film”. The darker the area on the SEM image is, the higher content of carbon is detected by EDX. In addition, there was no cracks formed on the tribofilm, which is probably due to the smoothness of the countersurface (smooth DLC coating).

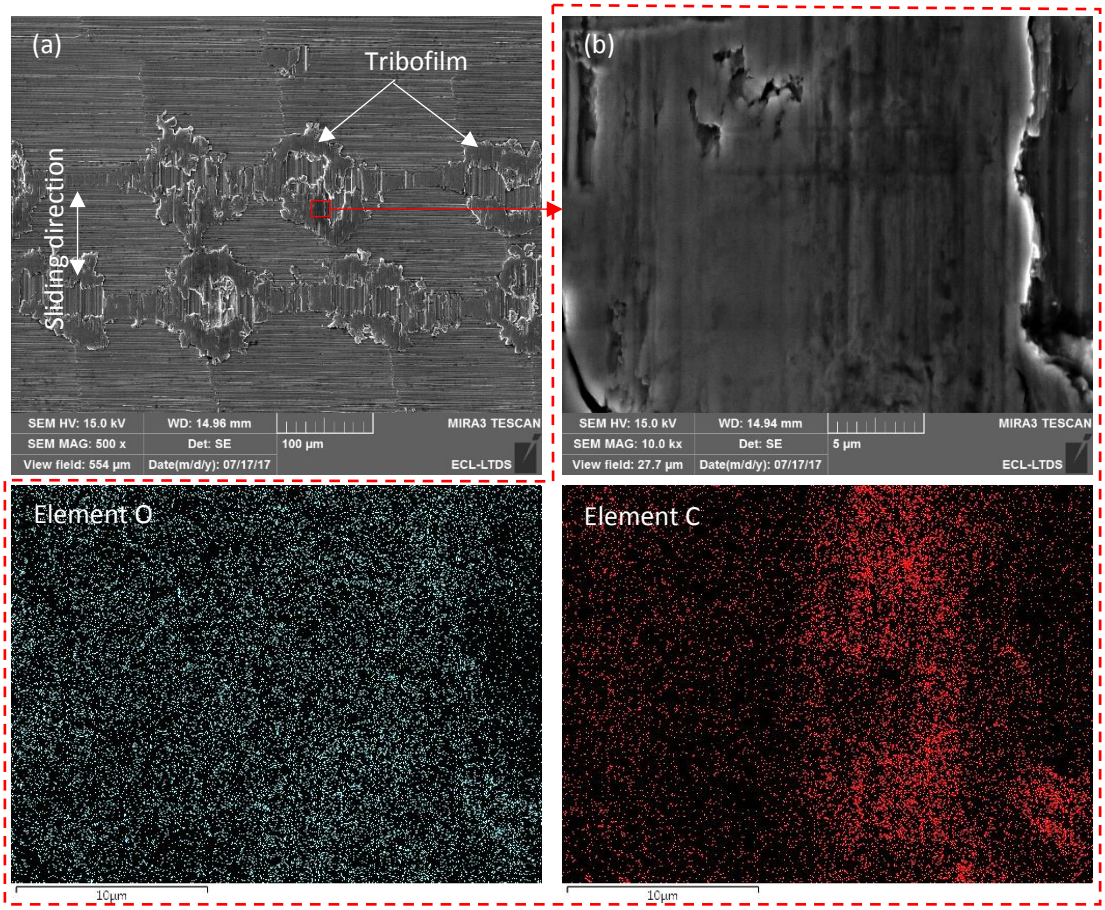

Figure VI.16. Ti–6Al–4V surface (in contact with smooth DLC coated flat) after 100 cycles: (a) large scale; (b) close-up of the tribofilm.

On the DLC coating side, the coating was not fractured, as shown in Figure VI.17. Correspondingly, no cracks were generated on the DLC coating, and no DLC particles were observed on the Ti–6Al–4V countersurface (Figure VI.16). Some Ti–6Al–4V alloy was adhered to the DLC coating surface.

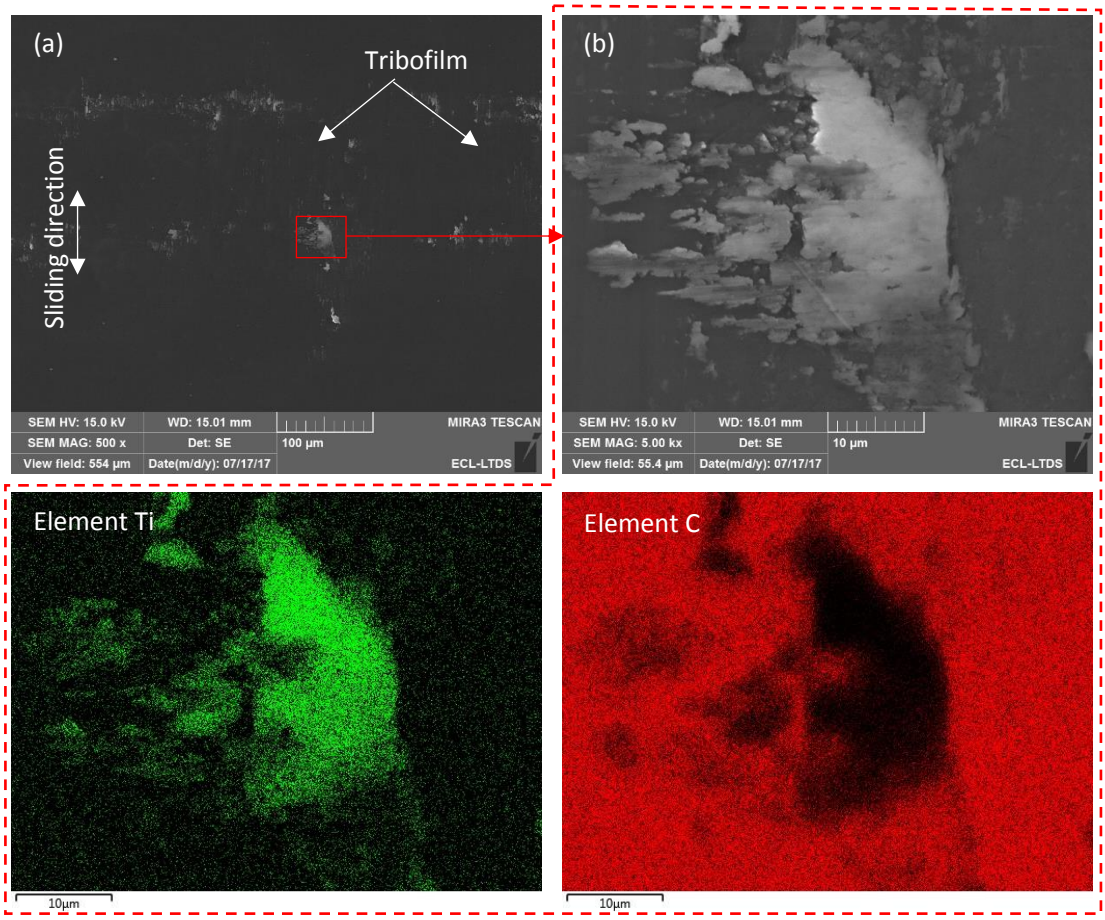

Figure VI.17. Smooth DLC coating surface (in contact with Ti–6Al–4V surface) after 100 cycles: (a) large scale; (b) close-up of the adhered Ti alloy.

3.6. After 100 000 cycles

- **Rough flat / rough cylinder**

Figure VI.18 shows the Ti–6Al–4V surface and the rough DLC coating surface after 100 000 cycles. Compared to the Ti–6Al–4V surface after 100 cycles (Figure VI.14), slightly more tribofilm material was formed on the cylinder after 100 000 cycles (Figure VI.18a). Therefore, the friction coefficient decreased slightly from around 0.2 to 0.13 between 100 and 100 000 cycles (Figure VI.1). Furthermore, the cracks on the DLC coating (Figure VI.15) were developed into pits (Figure VI.18b) where the coating was removed. Meanwhile, no adhered Ti–6Al–4V material was observed on the DLC coating surface.

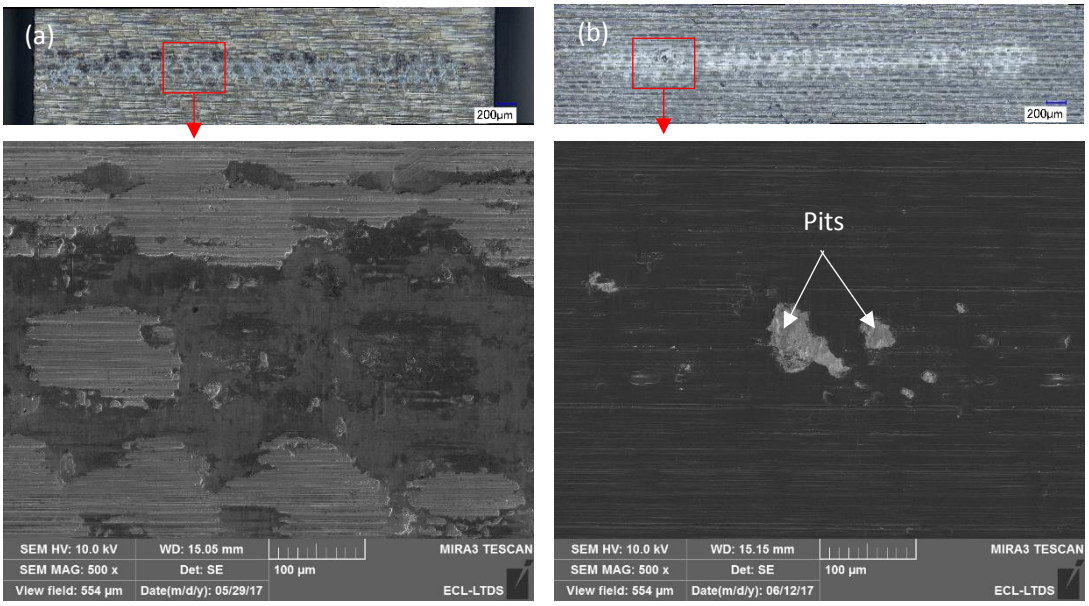

Figure VI.18. (a) Ti–6Al–4V surface in contact with (b) rough DLC coating surface after 100 000 cycles.

- **Smooth flat / rough cylinder**

Figure VI.19 shows the Ti–6Al–4V surface and the smooth DLC coating surface after 100 000 cycles. The tribofilm on the Ti–6Al–4V surface (Figure VI.19a) was similar to that of the test at 100 cycles (Figure VI. 16a); i.e., no more tribofilm material formed on the cylinder. Therefore, the friction coefficient showed no change in the stable period between 100 and 100 000 cycles (Figure VI.1). On the DLC coating surface, scratches could be observed. However, no cracks were generated; i.e., the DLC coating on the smooth flat did not break until 100 000 cycles. Note that the white points on the coating surface were the holes formed during the coating deposition process.

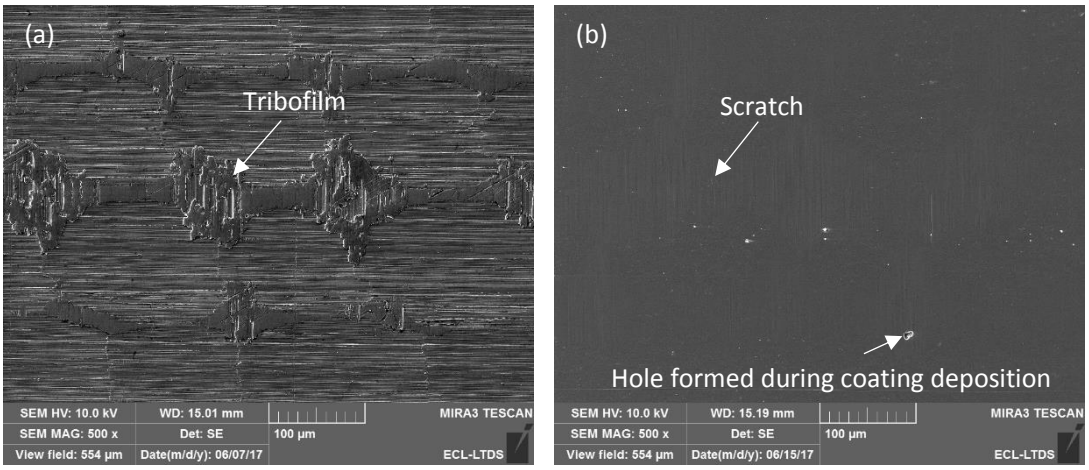

Figure VI.19. (a) Ti–6Al–4V surface in contact with (b) smooth DLC coating surface after 100 000 cycles.

3.7. Conclusions

Figure VI.20 and Figure VI.21 show the evolution of rough Ti–6Al–4V surface and rough DLC coating surface, respectively. At the beginning of the test (contact only or after 1 cycle), Ti–6Al–4V was transferred from the cylinder to the DLC surface as a consequence of adhesion

and abrasion (for rough Ti–6Al–4V / rough DLC coating contact) or as a consequence of adhesion (for rough Ti–6Al–4V / smooth DLC coating contact). The energy needed to break the metallic bonds in the Ti–6Al–4V side led to the high friction. After that, the worn-off material started to form a tribofilm on the rubbed Ti–6Al–4V surface. And more tribofilm material was accumulated with the test ongoing. A thin carbonaceous film was formed on the tribofilm surface. The tribofilm and the carbonaceous layer obstructed the Ti–6Al–4V transfer from cylinder to DLC surface. And the friction between the DLC surface and the tribofilm decreased to low values (around 0.2) after 100 cycles. After that, with the test ongoing during the low friction stage, the tribofilm showed no significant change and the friction coefficient remained low.

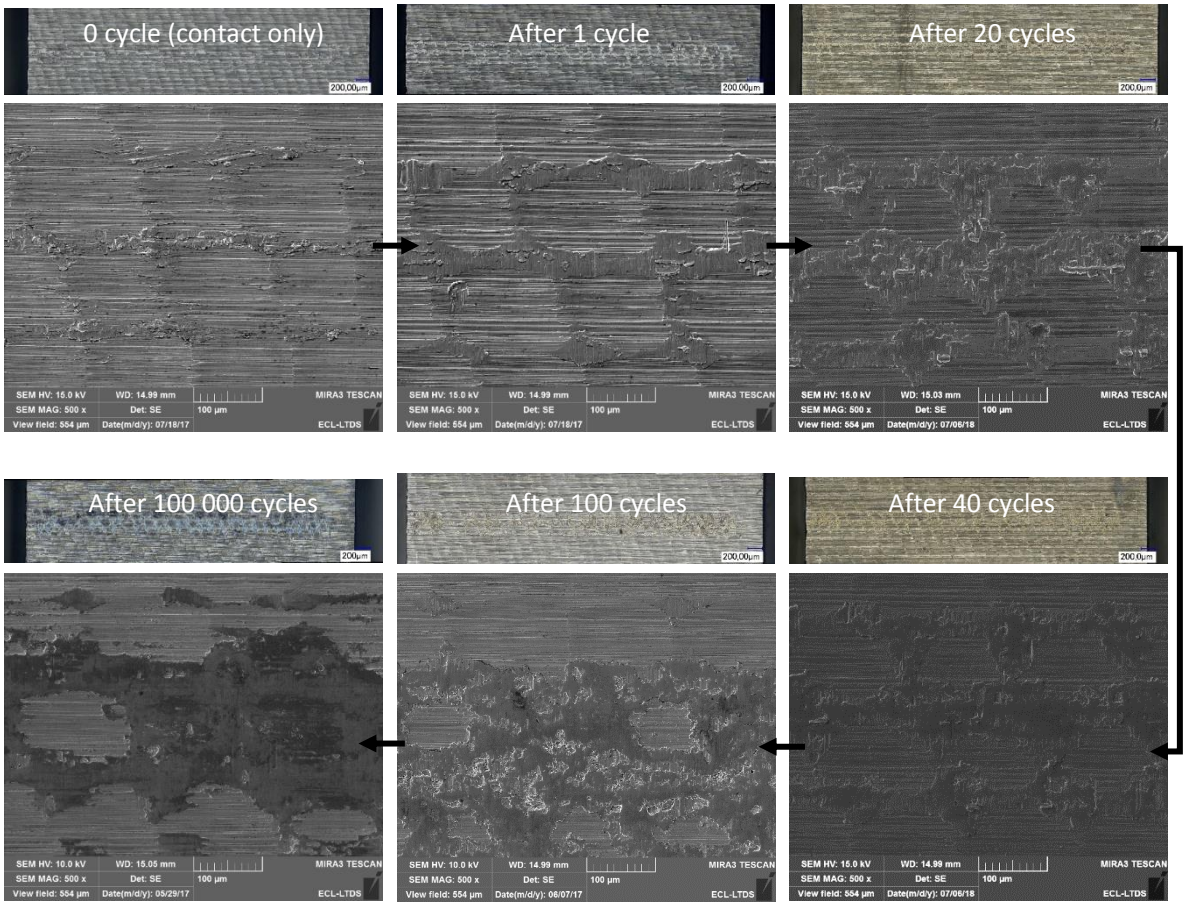

Figure VI.20. Evolution of rough Ti–6Al–4V surface (in contact with rough DLC coating surface).

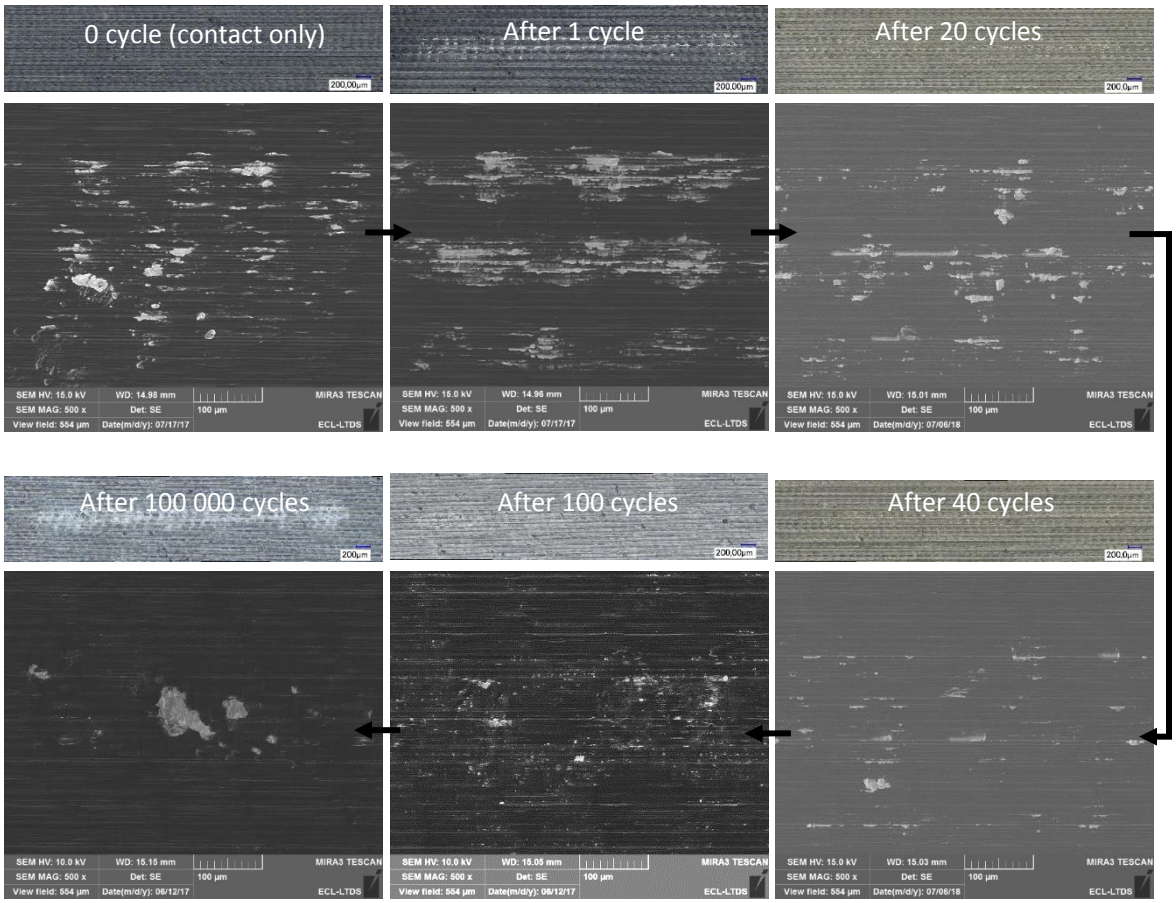

Figure VI.21. Evolution of rough DLC coating surface (in contact with rough Ti–6Al–4V surface).

4. Properties of rubbed contact surfaces

To measure the properties of rubbed Ti–6Al–4V surface (i.e., the tribofilm and the carbonaceous film), the wear scars on the uncoated Ti–6Al–4V flats (in contact with DLC coated cylinders) were analyzed. The tribofilm and carbonaceous layer were formed on the Ti–6Al–4V flat surface, which was easier for analysis than on a cylindrical surface. The friction coefficient evolution was similar for Ti–6Al–4V flat / DLC coated cylinder contact and DLC coated flat / Ti–6Al–4V cylinder.

Samples for analysis were from tests with 100 000 cycles under various values of displacement amplitude and normal force. But all of them were in the mild wear area, where the tribofilm and carbonaceous layer were formed on the rubbed Ti–6Al–4V.

4.1. Thickness of tribofilm

The cross sections of the Ti–6Al–4V flat were cut, polished, and then observed with SEM with an observation angle of 6°, as shown in Figure VI.22. In the center area of the contact, the tribofilm thickness reached approximately 0.7 µm (Figure VI.22a). The tribofilm material heaped up in the valley on the border area of the contact, leading to the maximal thickness of approximately 2 µm (Figure VI.22b).

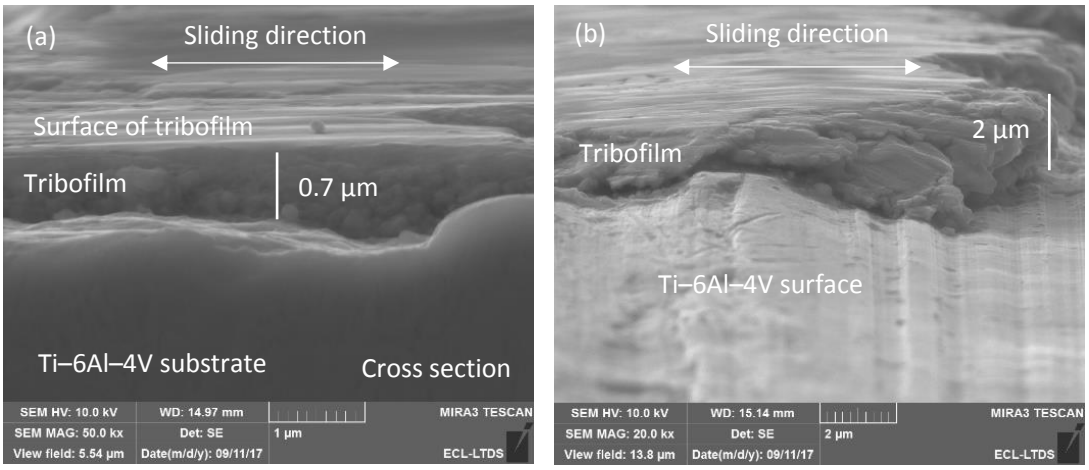

Figure VI.22.Cross sections of rubbed Ti–6Al–4V surface: (a) center area (±40 µm and 500 N) and (b) border area of the contact (±40 µm and 250 N).

4.2. Raman spectroscopy on rubbed surfaces

Raman spectroscopy consists of measuring the intensity of inelastically scattered light by a material as a function of the wavelength [226]. It is an interesting, non-destructive tool for structural characterisation of carbon [227].

Raman spectroscopic measurements were performed on the unworn DLC surface, worn DLC surface, tribofilm surface, and unworn Ti–6Al–4V surface using a Raman spectrometer (XploRA, HORIBA Scientific). The laser with wavelength of 785 nm and power of 35 mW was adopted. And all Raman spectra were recorded with a 600 lines/mm grating.

Three measurements were performed at different spots on each surface, and they showed very similar spectra. Figure VI.23 shows the Raman spectra on the unworn DLC, worn DLC, tribofilm, and Ti–6Al–4V surfaces.

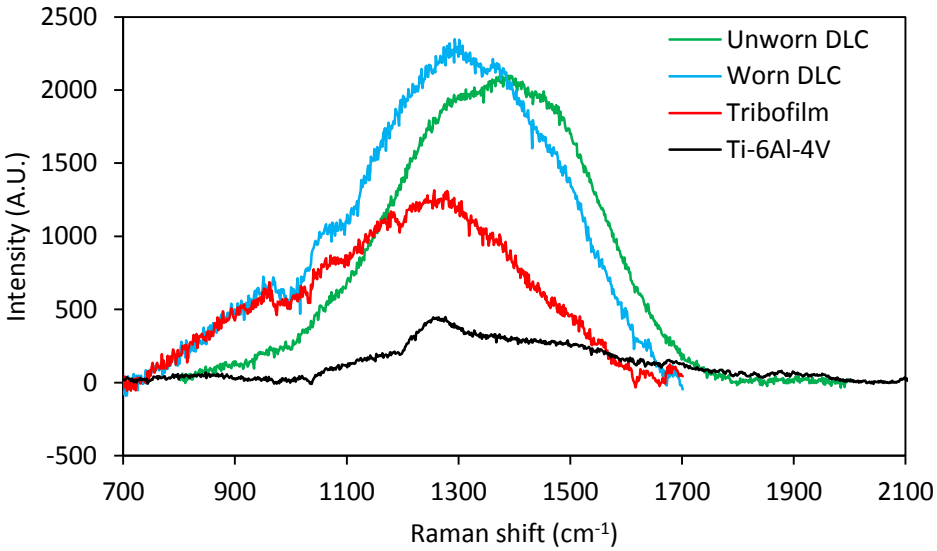

Figure VI.23. Raman spectra acquired on the unworn and worn regions of DLC coated flat, on tribofilm formed on the worn Ti–6Al–4V flat, and on the unworn Ti–6Al–4V flat. All measurements were performed in the mild wear area.

According to pervious works, the Raman spectra of DLC mainly consist of G and D peaks [227]. The G peak is due to the bond stretching of all pairs of sp^2 atoms in both rings and chains. The D_1 and D_2 peaks are due to the breathing modes of sp^2 ring-like atoms. The Gaussian fit was used in this study to fit the Raman spectra in order to extract typical characteristics, such as the position and intensity of peaks.

Figure VI.24 shows Gaussian fitting of the Raman spectra on the unworn DLC surface, the worn DLC surface, and the tribofilm surface. A careful analysis of the position of G peak and the ratio of intensity of D and G peaks ($I(D_1+D_2)/I(G)$) may provide information about the structural changes occurring on the DLC surface under sliding. The fitting results are shown in Table VI.2.

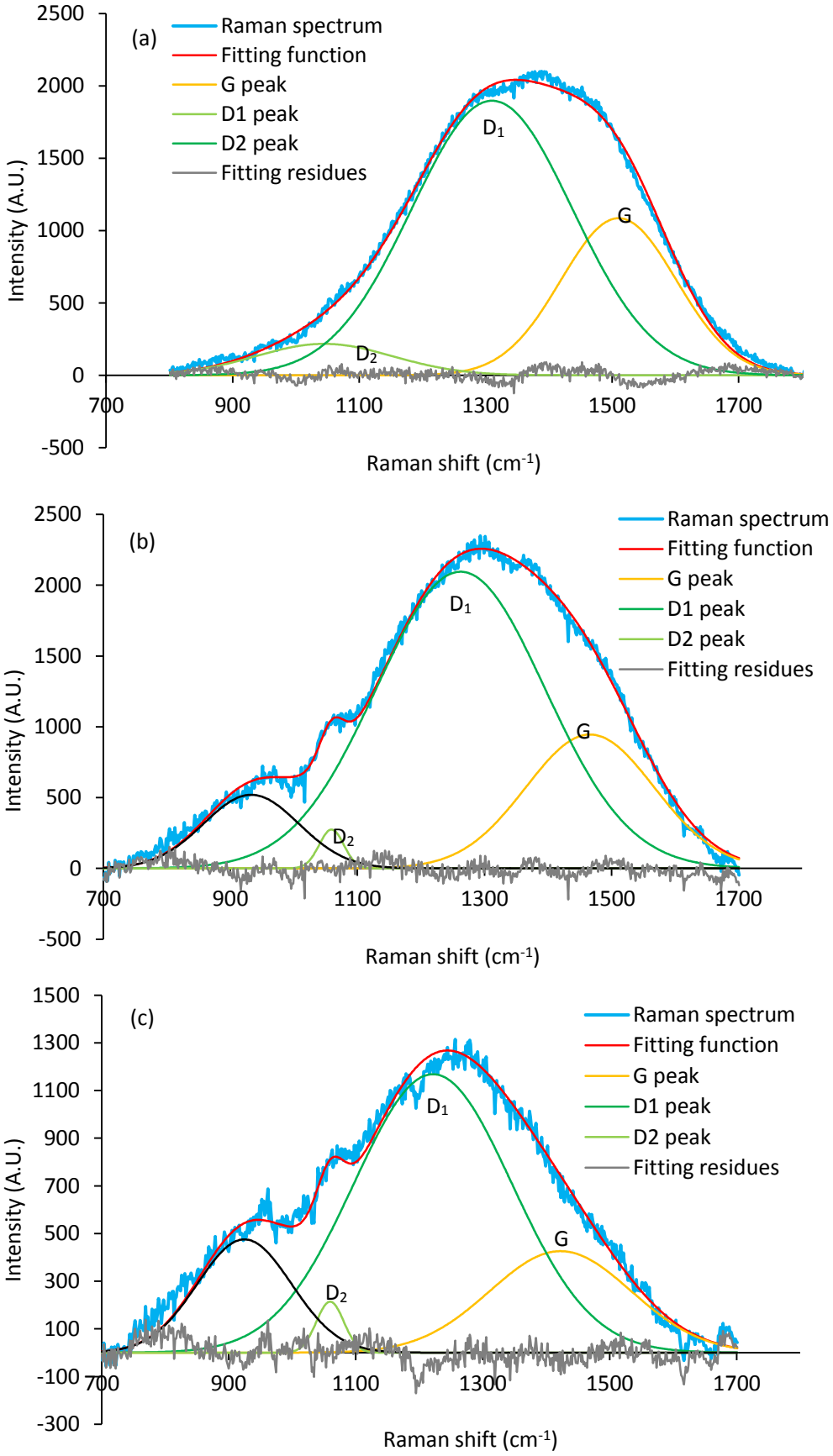

Figure VI.24. Gaussian fitting of a Raman spectrum acquired (a) on the unworn DLC surface, (b) on the worn DLC surface, and (c) on the tribofilm surface.

Table VI.2. Gaussian fitting results from Raman spectra on unworn DLC, worn DLC and tribofilm.

		Unworn DLC	Worn DLC	Tribofilm
G peak	Position	1499 ± 13	1462 ± 16	1426 ± 10
	Intensity	1014 ± 77	1084 ± 301	382 ± 46
D_1 peak	Position	1307 ± 6	1258 ± 16	1221 ± 1
	Intensity	1823 ± 122	2323 ± 414	1085 ± 90
D_2 peak	Position	1056 ± 11	1057 ± 2	1061 ± 2
	Intensity	242 ± 31	309 ± 24	185 ± 26
$I(D_1+D_2)/I(G)$		2.04 ± 0.08	2.55 ± 0.67	3.33 ± 0.13

The unworn DLC surface (outside the contact area) exhibits a typical spectrum for hydrogenated amorphous carbon coating (a-C:H) with dominant peaks (G and D_1) and a wide shoulder caused by a small D_2 peak at low wavenumbers [228]. The G and D_1 peaks lie at around 1 500 cm^{-1} and 1 300 cm^{-1}, respectively. The ratio of intensity of D and G peaks ($I(D_1+D_2)/I(G)$) is around 2.04.

The spectrum of the worn DLC surface (inside wear track) exhibits clear differences compared to the unworn DLC surface (outside wear track), as shown in Figure VI.23. The G peak shifts towards lower wavenumbers, which means a higher level of order in the carbon amorphous network [226]. The $I(D_1+D_2)/I(G)$ increases (to around 2.55), suggesting an increase in the size of the sp^2 ring-like carbon clusters [226, 227]. In addition, a peak is detected at around 930 cm^{-1}, which may probably be due to some oxidization processes. The difference Raman spectra inside and outside the wear track on the DLC surface reveals that a structural transformation occurred on the DLC surface during sliding.

The Raman spectrum acquired on the tribofilm (formed on Ti–6Al–4V surface) is similar to that on the worn DLC surface, such as the similar positions of peaks, and high values of $I(D_1+D_2)/I(G)$, but with a lower photoluminescence background intensity (Figure VI.23). This means that the transformed material on the worn DLC surface was transferred to the countersurface (i.e., to the tribofilm surface). This corresponds to the “carbonaceous film” observed via SEM and EDX on the tribofilm surface (Figure VI.16b).

It can be concluded that structural transformation occurred on the rubbed DLC surface during sliding. And the transformed carbonaceous material was transferred to counterbody. And we believe that the transformed carbonaceous material still remained on the rubbed DLC surface. Therefore, the rubbed Ti–6Al–4V / rubbed DLC contact was “Ti–6Al–4V + tribofilm + carbonaceous film” / “carbonaceous film + DLC coating” contact.

Further exploration needs to be performed to investigate the nature of the transformed carbonaceous film.

4.3. Nano-indentation on tribofilm

Nano-indentation tests were conducted with CSM method to measure the hardness and elastic modulus of the tribofilm and the Ti–6Al–4V substrate (Figure VI.25). The tribofilm was formed on a rough uncoated flat, which was in contact with a DLC coated cylinder, under the displacement amplitude of ±70 µm and the normal force of 200 N. The measurement was repeated nine times at different positions. The maximal indentation load was 100 mN.

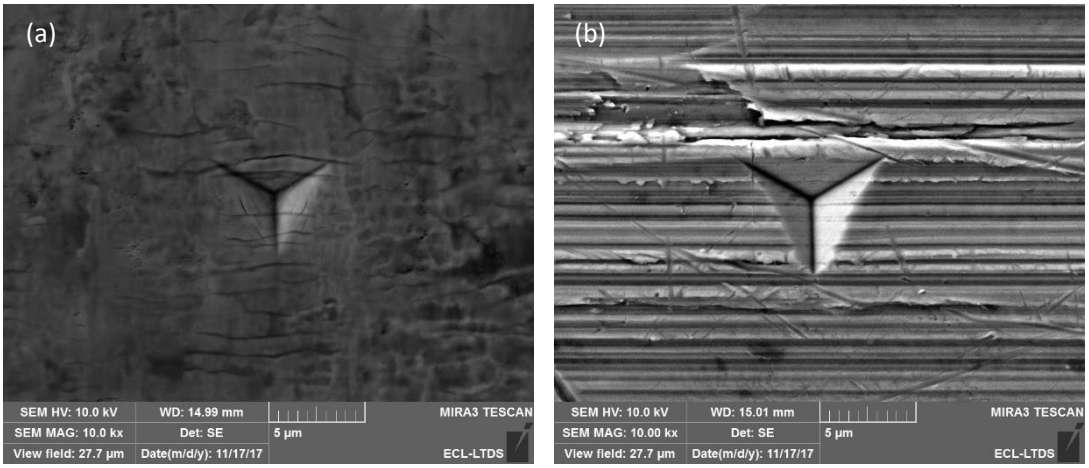

Figure VI.25. SEM observation of nano-indent: (a) on tribofilm (±70 µm and 200 N); (b) on rough Ti–6Al–4V flat.

The nano-hardness and elastic modulus of the tribofilm and the Ti–6Al–4V substrate are shown in Figure VI.26. For the Ti–6Al–4V substrate, the hardness was 3.9 ± 1.5 GPa, and the elastic modulus was 130 ± 30 GPa. For the tribofilm, the hardness was higher than that of the substrate. With increasing the penetration depth, there was a plateau between 60 and 120 nm, with an average value of 10 ± 0.1 GPa, which was approximately 2.6 times higher than the hardness of the substrate. After that, the hardness decreased due to the substrate effect. Concerning the elastic modulus, the average value between 60 and 120 nm was 170 ± 3 GPa, which was 1.3 times higher than the elastic modulus of the substrate.

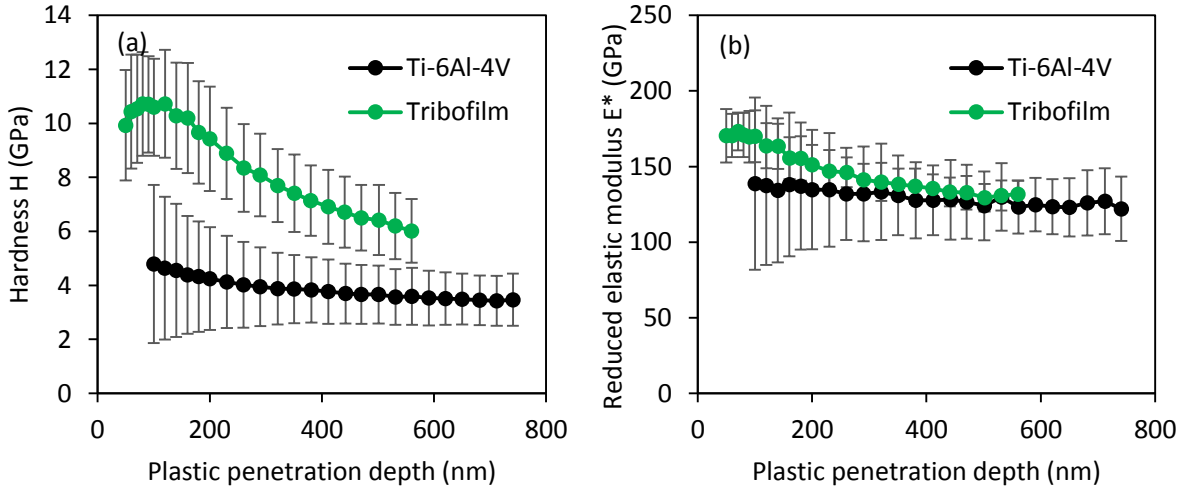

Figure VI.26. (a) Nano-hardness and (b) elastic modulus of tribofilm and of Ti–6Al–4V substrate.

It should be noted that the work-hardening of the substrate surface might have contributed to the high hardness measured on the tribofilm. From the etched cross section (Figure VI.27), the microstructure of the substrate beneath the tribofilm showed no obvious difference with that outside the contact, which suggests that the contribution of work-hardening on the substrate surface was negligible.

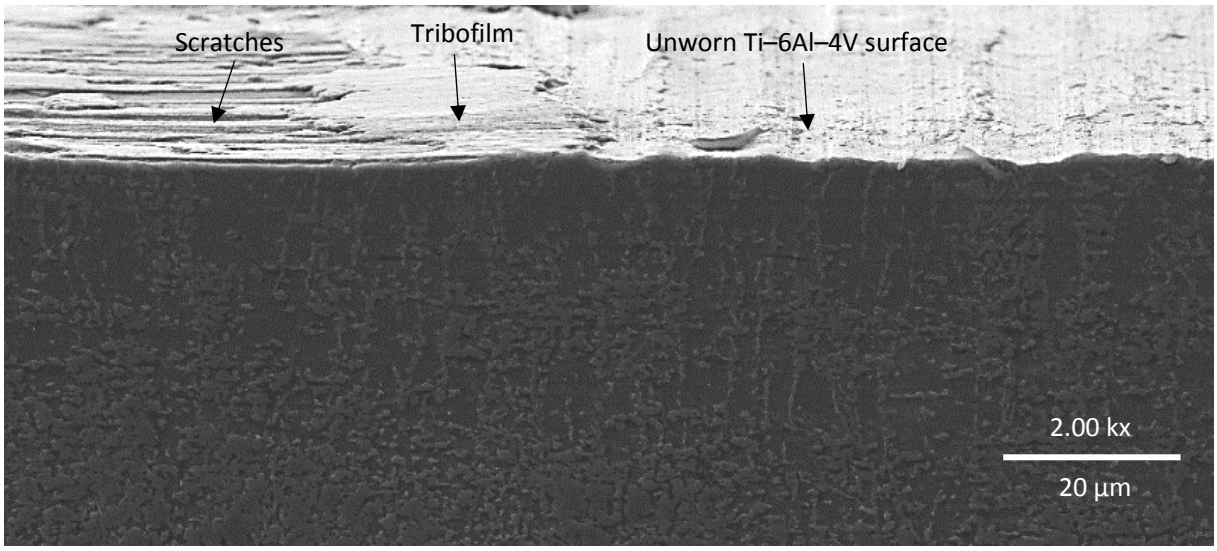

Figure VI.27. SEM observation of etched cross section beneath and outside the contact area.

4.4. Compression of micro pillar of tribofilm

Micro-pillars were milled on the tribofilm and on the Ti–6Al–4V surfaces. The tribofilm was formed on a rough uncoated flat, which was in contact with a DLC coated cylinder, under the displacement amplitude of ±20 µm and the normal force of 250 N. The manufacture process was mentioned in Section 5.6, in Chapter II. On the tribofilm surface, small pillars were milled with the diameter of around 1.3 µm and the height of around 2.0 µm. Small pillars were also milled on the Ti–6Al–4V surface. Furthermore, large pillars were also machined on the Ti–6Al–4V surface with the diameter of around 4.0 µm and the height of around 7.0 µm. In total, six small pillars were milled on the tribofilm surface. Three large pillars and three small pillars were milled on the Ti–6Al–4V surface.

Micro-pillars were compressed by a diamond flat punch (diameter 10 µm). The force–displacement (F–δ) curves were obtained after the correction of sample, punch, and frame compliance for pillar compression (the correction processes are shown in Appendix C). F is the compression force on the pillar top surface. Displacement δ is the reduction of the height of the pillar. Figure VI.28 shows representative force-displacement curves.

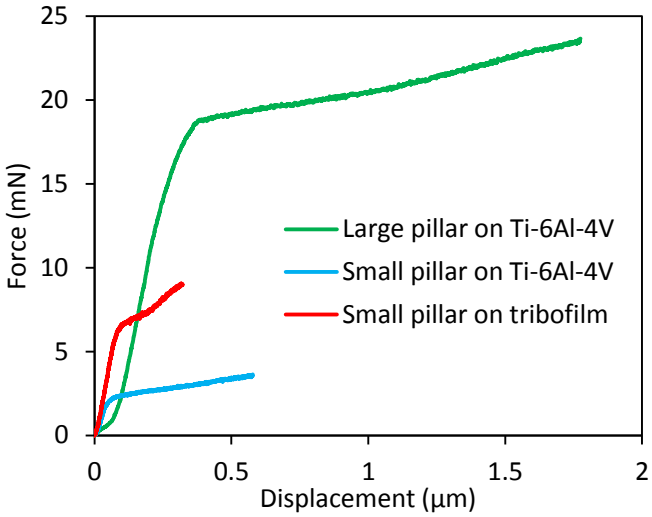

Figure VI.28. Representative force-displacement curves.

To compare the mechanical properties between the tribofilm and the Ti–6Al–4V substrate, the influence of pillar size should be removed. Thus, the stress–strain (σ–ε) curves were obtained based on the force–displacement curves. The strain (ε) was calculated according to the formula $\varepsilon=\delta/L$, where L is the initial height of the pillar before compression. The stress (σ) was calculated according to the formula $\sigma=F/(\pi a^2)$, where a is the radius of the pillar top surface before compression (the radius of the pillar was presumed to be constant during compression for data analysis). Figure VI.29 shows the stress–strain curves of all the pillars.

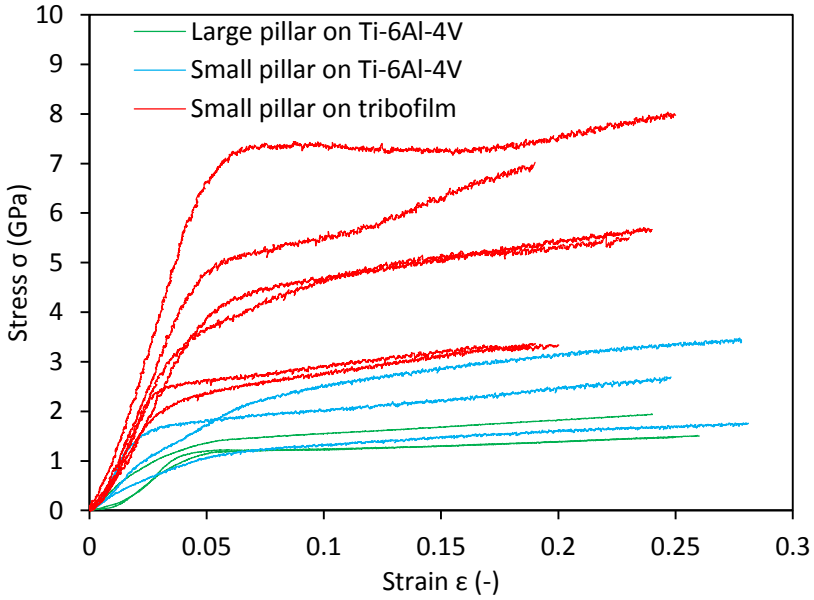

Figure VI.29. Stress–stain curves for 12 micro-pillars.

- **Large pillar on Ti–6Al–4V**

Figure VI.30 shows a stress–strain curve for a representative large Ti–Al–4V pillar. The corresponding SEM images are shown in Figure VI.31.

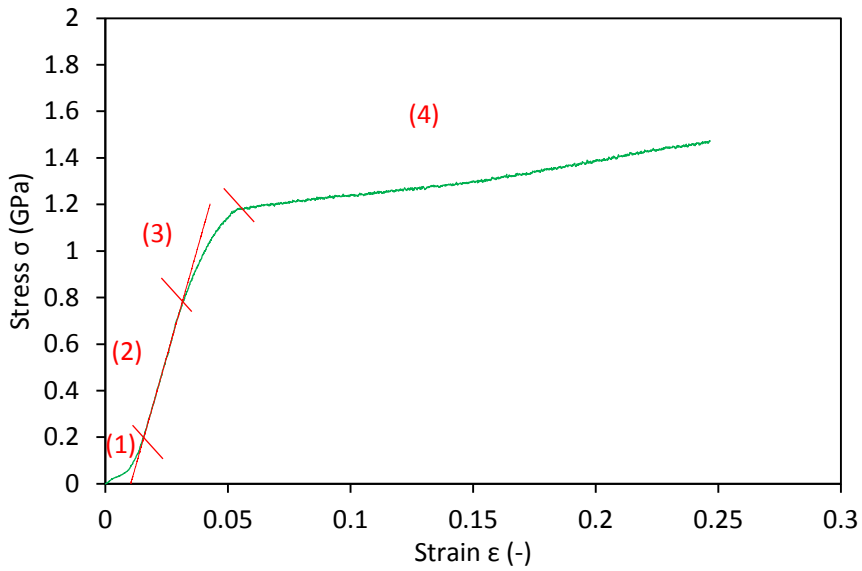

Figure VI.30. Representative stress–strain curve for a large pillar on Ti–6Al–4V.

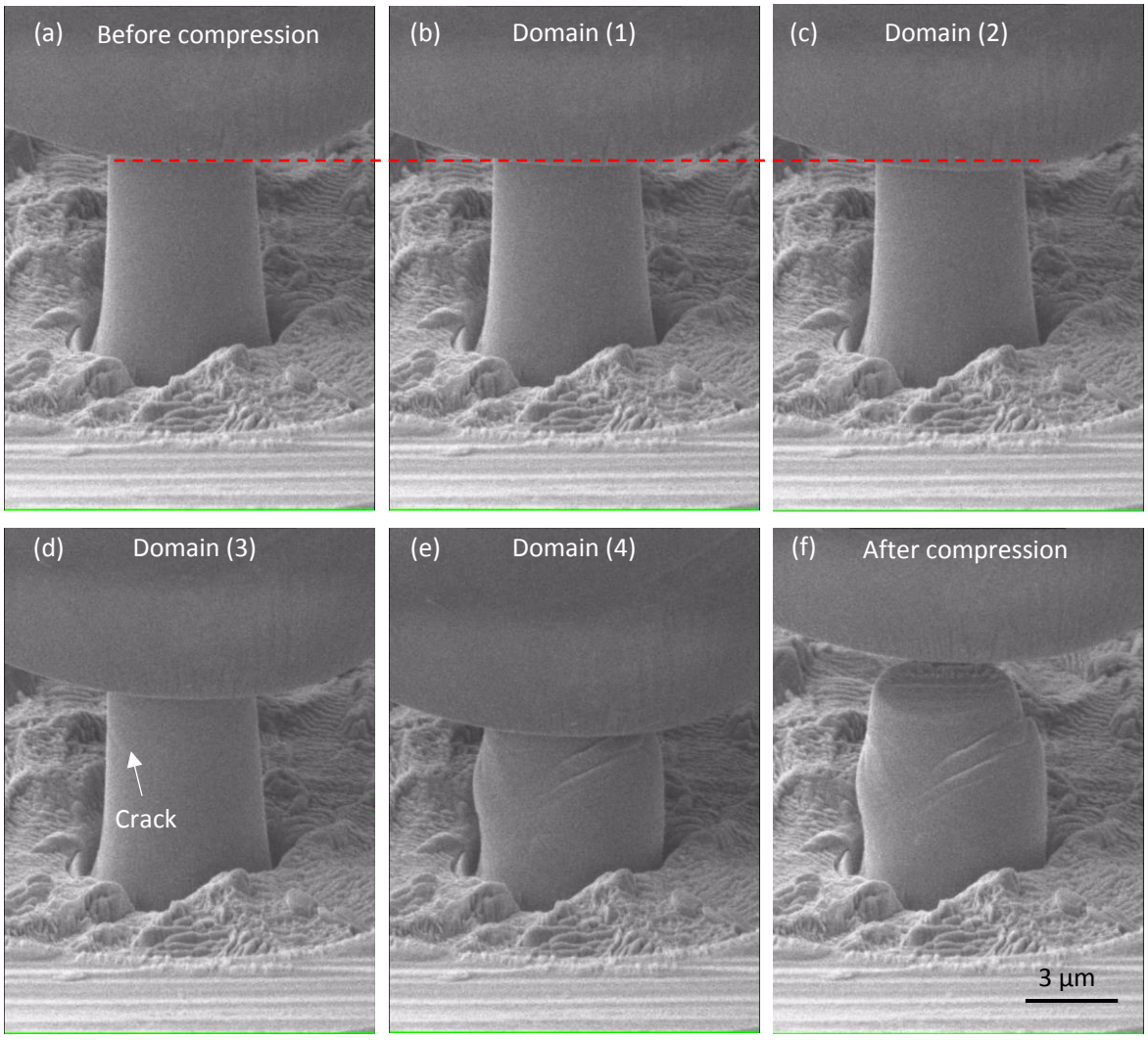

Figure VI.31. SEM observation of compression of a large pillar on Ti–6Al–4V: (a) before compression; (b) in domain (1); (c) in domain (2); (d) in domain (3); (e) in domain (4); and (f) after compression.

According to the stress–strain curve, the micro-compression undergoes four domains (Figure VI.30). In domain (1), the asperities of the rough Ti–6Al–4V surface firstly come into contact with the punch. The contact is asperities-on-punch contact. The asperities have low stiffness, leading to a small slope of stress to strain (i.e. $\Delta\sigma/\Delta\varepsilon$ ratio). With compression force increasing, the asperities are pressed and the real contact area increases, thus the $\Delta\sigma/\Delta\varepsilon$ ratio increases gradually. In domain (2), the stress–strain curve is linear-like, which suggests that the pillar mainly undergoes elastic deformation during this period. In domain (3), cracks start to generate and propagate (as shown in Figure VI.31d), leading to a decrease in the $\Delta\sigma/\Delta\varepsilon$ ratio. Furthermore, plastic deformation might occur during this period, which also makes contribution to the decline in the $\Delta\sigma/\Delta\varepsilon$ ratio. In domain (4), significant slippage at the crack interface occurs, resulting in much lower $\Delta\sigma/\Delta\varepsilon$ ratios. At the same time, severe plastic deformation occurs and the pillar becomes barrel-like.

- **Small pillar on Ti–6Al–4V**

Figure VI.32 shows stress–strain curves for small pillars on Ti–6Al–4V. The corresponding SEM images are shown in Figure VI.33.

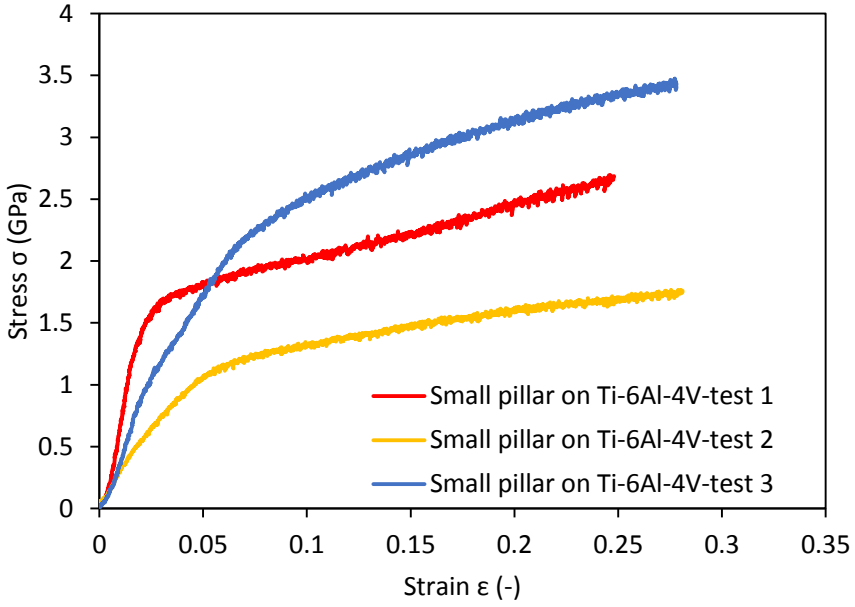

Figure VI.32. Stress–strain curves for small pillars on Ti–6Al–4V.

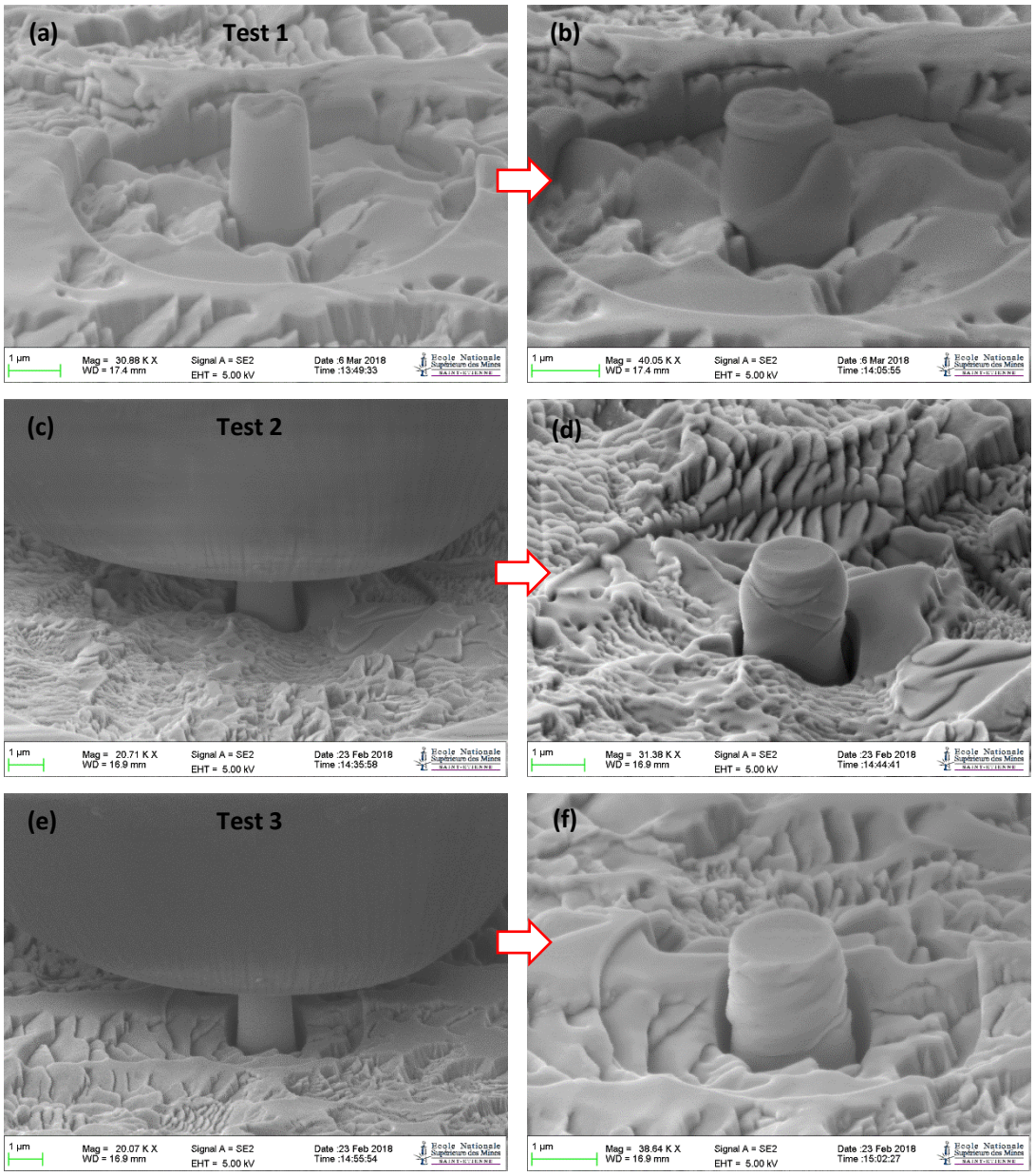

Figure VI.33. SEM observation of small pillars on Ti–6Al–4V before and after compression: (a, b) test 1; (c, d) test 2; (e, f) test 3.

It is clear that, for small pillars on Ti–6Al–4V surface, the domain (1) of stress–strain curves are significantly shorter comparing with that for large Ti–6Al–4V pillars, because the effect of original surface roughness (i.e., the asperities) is weaker on the small pillar. Besides, these three curves show obvious difference to each other (including different $\Delta\sigma/\Delta\varepsilon$ ratios in domain (2), and different stress values in domain (4)). This is probably because the small pillar is in a single or a few Ti–6Al–4V alloy grains and the mechanical properties might be anisotropic in a single grain.

In addition, cracks, slippage, and plastic deformation were also observed on the compressed pillars (Figure VI.33).

- **Small pillar on tribofilm**

Figure VI.34 shows the stress–strain curves for small pillars on tribofilm. Figure VI.35 shows SEM images of two representative compression tests.

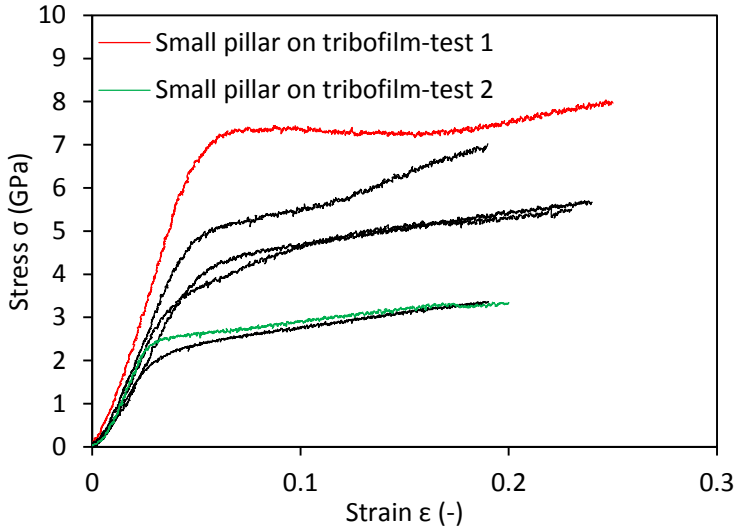

Figure VI.34. Stress–strain curves for six small pillars on tribofilm.

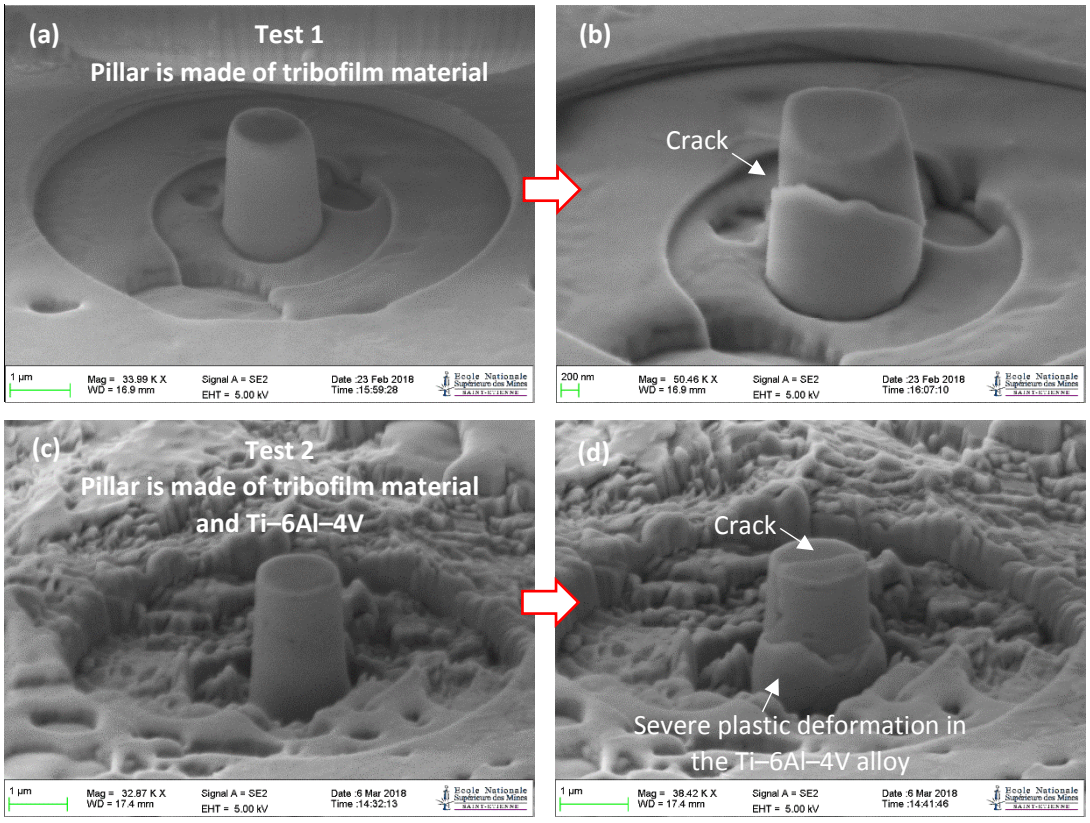

Figure VI.35. SEM observation of small pillars on tribofilm before and after compression: (a, b) test 1, pillar is made of tribofilm material; (c, d) test 2, pillar is made of tribofilm in the upper part and Ti–6Al–4V alloy in the bottom part.

It should be noted that the thickness of the tribofilm is in the range of around 0.7–2.0 µm. Therefore, in test 1, the pillar which is milled on the tribofilm with large local thickness, only consists of the tribofilm material. The stress–strain curve represents the mechanical

properties of the tribofilm material. The stress has the highest values in the domain (4) (as shown in Figure VI.34). After compression, obvious crack is generated but the plastic deformation is weak (From Figure VI.35a).

In test 2, the pillar which is milled on the tribofilm with small local thickness, consists of the tribofilm material in the upper part and the Ti–6Al–4V alloy in the bottom part. The stress–strain curve represents the combined consequence of the upper tribofilm material and the bottom Ti–6Al–4V alloy. The stress has relatively lower values (but still higher than pure Ti–6Al–4V pillars, as shown in Figure VI.29). After compression, in the upper part (i.e., the tribofilm part), obvious crack is generated but the plastic deformation is weak (Figure VI.35d). In the bottom part (i.e., the Ti–6Al–4V part), severe plastic deformation occurs.

- **Elastic modulus of micro-pillar compression**

Compression modulus (E_s) is defined as the slope of stress to strain ($\Delta\sigma/\Delta\varepsilon$) in the domain (2) (i.e., in the elastic deformation period). Figure VI.36 shows all the values of compression modulus for micro-pillars on Ti–Al–4V and tribofilm.

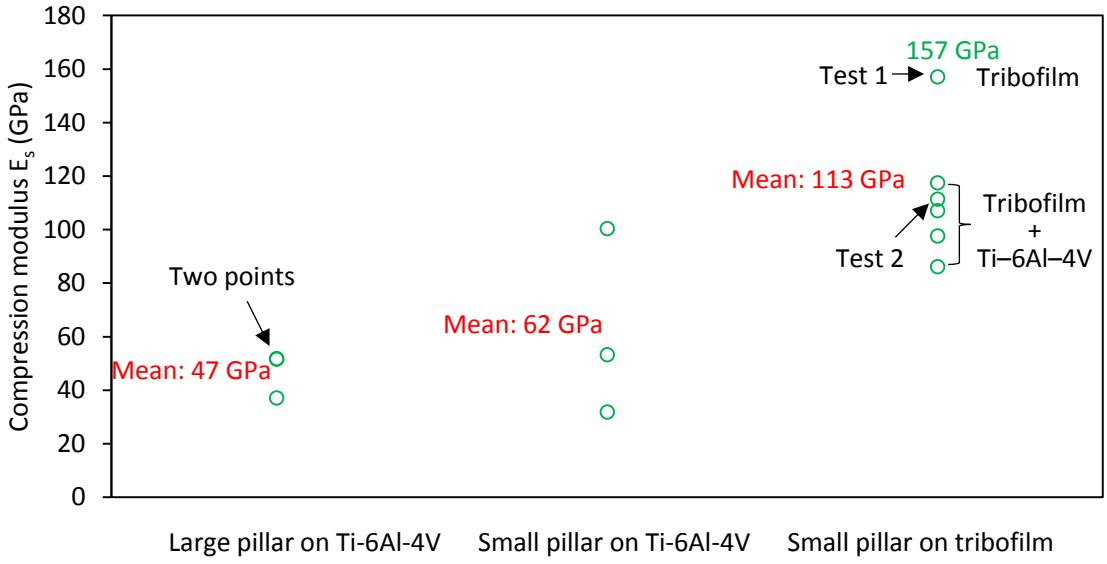

Figure VI.36. Elastic modulus of micro-pillar compression.

It is clear from Figure VI.36 that, for large Ti–6Al–4V pillars, the compression modulus is around 47 GPa. For small Ti–6Al–4V pillars, the compression modulus is similar (around 62 GPa with a large deviation). For small pillars on the tribofilm, the compression modulus is around two times larger (around 113 GPa). Furthermore, the pillar which only consists of tribofilm material exhibits the highest compression modulus (157 GPa from test 1). The pillars which consist of tribofilm material in the top part and Ti–6Al–4V alloy in the bottom part exhibit relatively lower compression modulus (the lower points) than the pure tribofilm pillar.

It can be concluded that in the micro-pillar compression test, the elastic modulus of tribofilm is significantly larger than Ti–6Al–4V substrate.

- **Yield strength of micro-pillar compression**

The yield strength ($\sigma_{0.2}$) was calculated for all stress–strain curves. The calculation processes are shown in Figure VI.37. The effect of asperities contact in domain (1) was removed. The values of yield stress ($\sigma_{0.2}$) for all the pillars are shown in Figure VI.38.

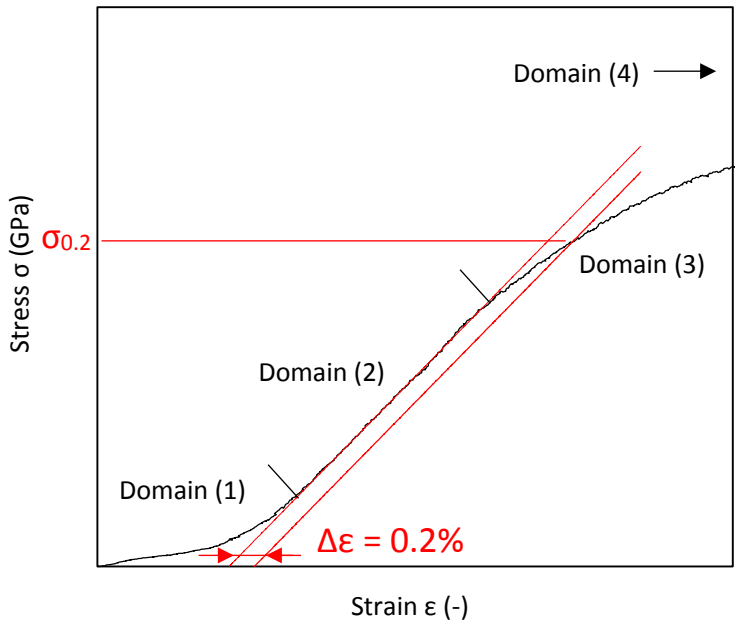

Figure VI.37. Calculation process of yield strength ($\sigma_{0.2}$).

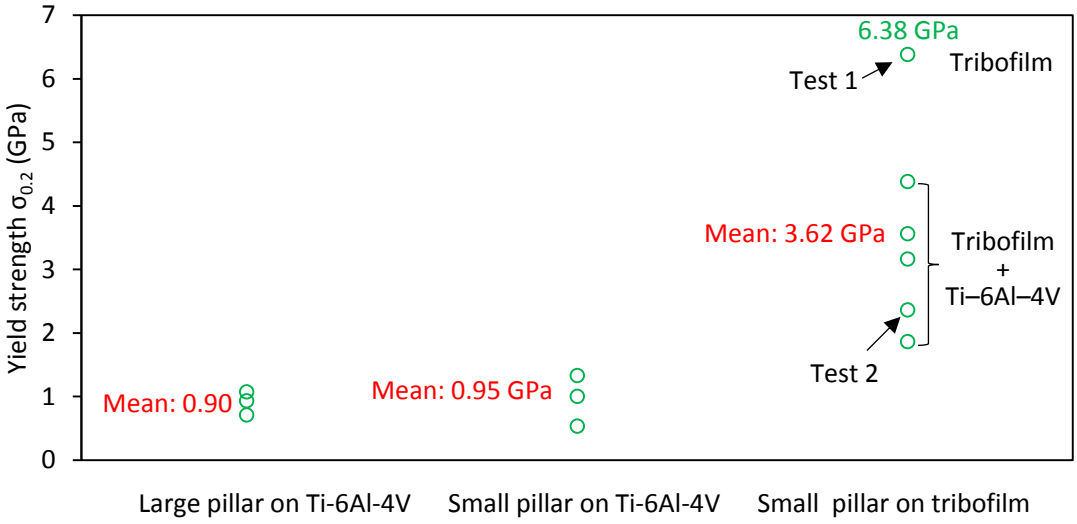

Figure VI.38. Yield strength ($\sigma_{0.2}$) of micro-pillar compression.

It is clear from Figure VI.38 that, for large Ti–6Al–4V pillars, the yield strength is around 0.90 GPa. For small Ti–6Al–4V pillars, the yield strength ($\sigma_{0.2}$) is very similar (around 0.95 GPa). For small pillars on the tribofilm, the yield strength is around four times larger (around 3.62 GPa). Furthermore, the pillar which only consists of tribofilm material exhibits the highest yield strength (6.38 GPa from test 1). The pillars which consist of tribofilm material in the top

part and Ti–6Al–4V alloy in the bottom part exhibit relatively lower yield strength (the lower points) than the pure tribofilm pillar but higher than the Ti–6Al–4V pillars.

It can be concluded that, in the micro-pillar compression test, the yield strength ($\sigma_{0.2}$) of tribofilm is significantly larger than Ti–6Al–4V substrate.

In addition, the yield strength ($\sigma_{0.2}$) and the compression modulus have a positive relationship, as shown in Figure VI.39.

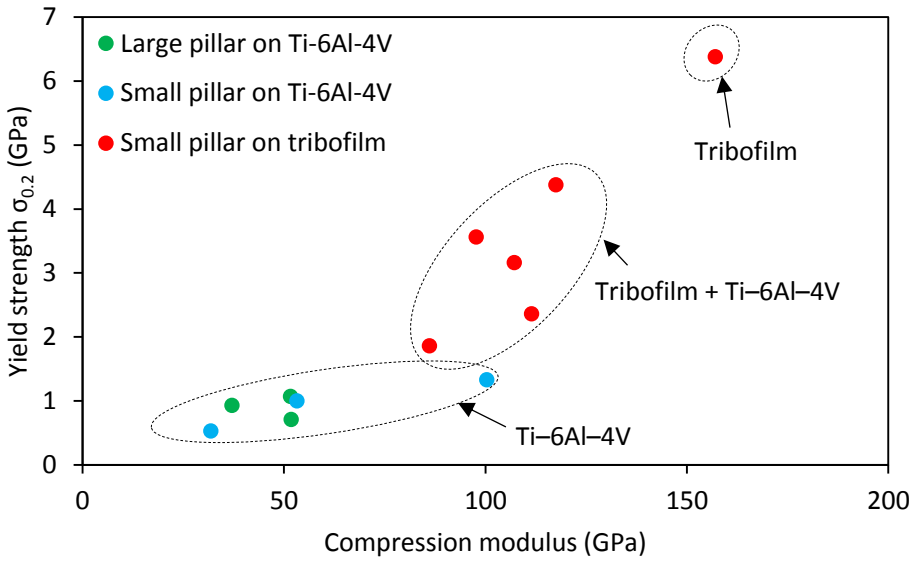

Figure VI.39. Relationship between yield strength ($\sigma_{0.2}$) and compression modulus.

4.5. Conclusions

For tests between DLC coating and Ti–6Al–4V under low load conditions, a tribofilm was formed on the Ti–6Al–4V rubbed surface in the mild wear area, with a thickness of around 0.7–2 µm. A structural transformation occurred on the rubbed DLC surface. The transformed carbonaceous material was transferred to tribofilm surface.

The mechanical properties measured by nano-indentation and compression of micro-pillars on the tribofilm and on the Ti–6Al–4V substrate are shown in Table VI.3. The tribofilm exhibits higher hardness, higher elastic modulus, and higher yield strength than Ti–6Al–4V. The hardness (H) of tribofilm (10 GPa) is 2.6 times higher than that of the Ti–6Al–4V substrate (3.9 GPa). The elastic modulus (E^*) measured by nano-indentation on the tribofilm (170 GPa) is 1.3 times larger than that on the Ti–6Al–4V substrate (130 GPa). The compression modulus (E_s) of micro-pillar of tribofilm (157 GPa) is around 3 times larger than that of micro-pillar of Ti–6Al–4V (47–62 GPa). The yield strength ($\sigma_{0.2}$) of micro-pillar of tribofilm (6.38 GPa) is around 7 times larger than that of micro-pillar of Ti–6Al–4V (0.90–0.95 GPa).

Table VI.3.Mechanical properties of the tribofilm and the unworn Ti–6Al–4V.

Mechanical properties	Ti–6Al–4V	Tribofilm	Tribofilm/Ti–6Al–4V ratio
Hardness H from nano-indentation (GPa)	3.9 ± 1.5	10 ± 0.1	2.6
Elastic modulus E^* from nano-indentation (GPa)	130 ± 30	170 ± 3	1.3
Elastic modulus E_s from micro-compression (GPa)	47–62	157	2.5–3.3
Yield strength ($\sigma_{0.2}$) from micro-compression (GPa)	0.90–0.95	6.38	6.7–7.1

It should be noted that the values of elastic modulus (E^*) measured by nano-indentation are higher than the values of elastic modulus (E_s) measured by compression of micro-pillars. This is probably due to the difference in measurement methods. The nano-indentation was performed on the surface. The bulk material around the nano-indent made contribution to the results. Whereas, the material around the pillar was removed and the obtained values were only derived from the pillar. Meanwhile, it can be seen that during nano-indentation measurement, the substrate effect is significant, whereas, during compression on pillar, the substrate effect is much weaker. That is why the difference on the elastic modulus between tribofilm and Ti–6Al–4V is smaller (1.3 times) from nano-indentation measurement, whereas it is larger (around 3 times) from compression of pillars.

5. Tribological model for tribofilm formation

Based on the results of the friction coefficient and analysis of wear scars of the DLC coating and the counterbody, a tribological model is proposed to explain the evolution of surfaces in the DLC coating / Ti–6Al–4V contact in fretting, as shown in Figure VI.40. The evolution of friction can be divided into three periods: high-friction period, decreasing-friction period, and low-friction period.

- **High-friction period**

At the beginning of the test, Ti–6Al–4V was transferred from the cylinder to the smooth DLC coating surface as a consequence of adhesion and to the rough DLC surface as a consequence of adhesion and abrasion. The important energy needed to break the metallic bonds in the Ti–6Al–4V led to a high friction coefficient.

In addition, the sliding enhanced the abrasion effect of the hard rough DLC surface on the soft Ti–6Al–4V alloy. Therefore, more Ti–6Al–4V was worn off and a higher friction coefficient was obtained when the cylinder sliding against the rough DLC coating surface than against the smooth DLC surface.

- **Decreasing-friction period**

The worn-off Ti–6Al–4V was pressed repeatedly at the interface and was oxidized as a consequence of running the test in air. With the test ongoing, the oxidized worn-off Ti–6Al–4V material formed a tribofilm on the rubbed Ti–6Al–4V surface. The tribofilm had higher hardness, higher elastic modulus, and higher yield strength than the Ti–6Al–4V substrate. Meanwhile, a structural transformation occurred on the rubbed DLC surface. And the

transformed carbonaceous material was transferred to the counterbody, forming a carbonaceous layer on the tribofilm surface.

- **Low-friction period**

A functional tribofilm was achieved after the running-in period, and a thin carbonaceous film presented on the tribofilm surface and on the rubbed DLC surface. The material transfer from the Ti–6Al–4V side to the DLC coating surface was obstructed. The adhesive force between the DLC coating and the tribofilm was low. Thus the friction coefficient was low.

In addition, the DLC coating on the rough flat broke, and DLC particles adhered to the tribofilm during the running-in period. When the test was run for a long time (100 000 cycles), the cracks of the DLC coating on the rough flat developed into pits. However, the DLC coating on the smooth flat did not break.

Besides, wear debris were generated (Figure IV.21c and Figure IV.21d). The abrasion of rough DLC coating on the Ti–6Al–4V surface led to the ejection of Ti–6Al–4V flakes. Under reciprocating sliding, the initial adhered Ti–6Al–4V on the DLC coating surfaces was worn off and was ejected from the contact. Meanwhile, the flaking-off of the tribofilm might lead to wear debris of oxidized titanium alloy particles. The broken DLC coating resulted in the generation of wear debris made of DLC particles.

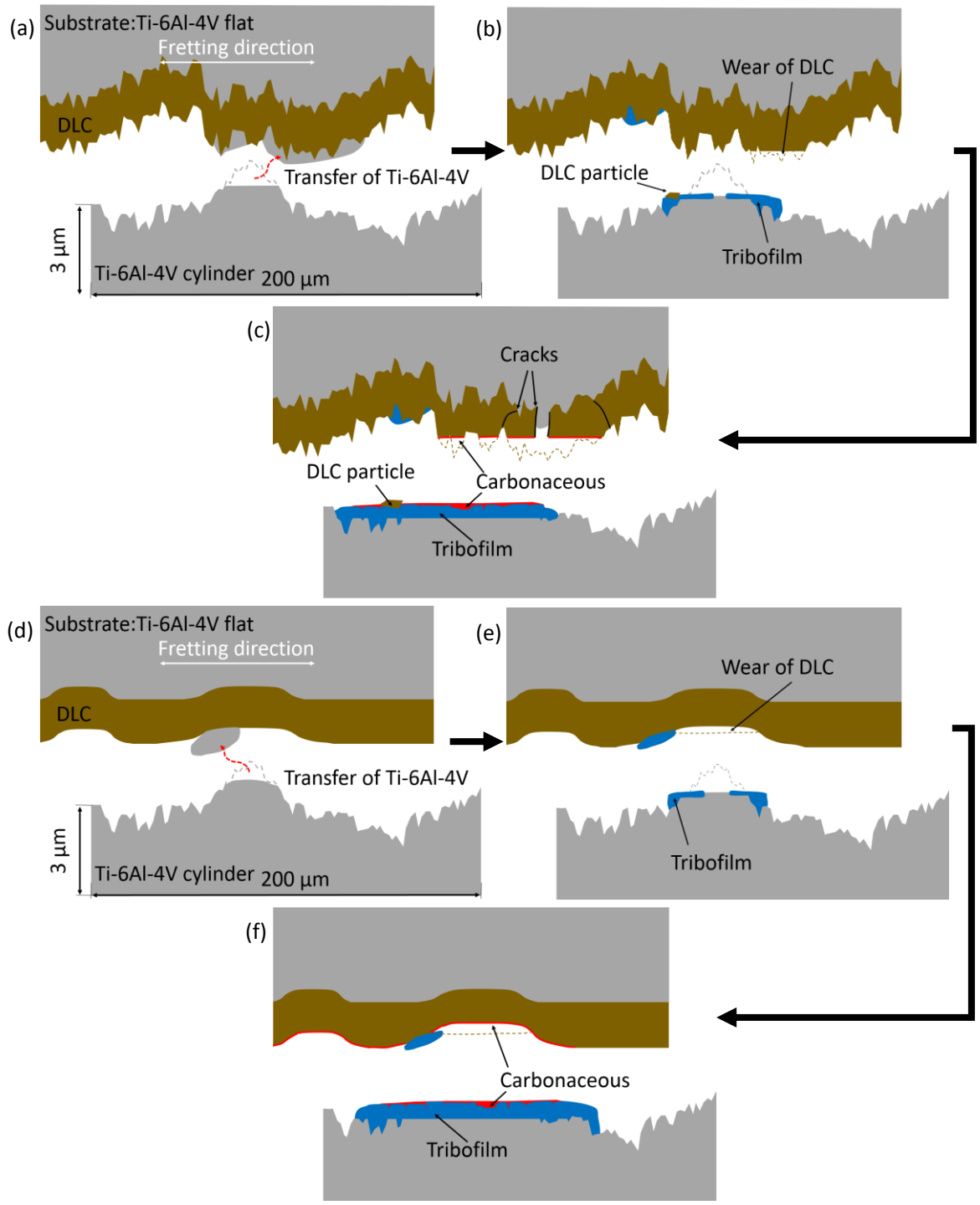

Figure VI.40. Schematic model for evolution of contact surfaces: (a) high-friction period, (b) decreasing-friction period, and (c) low-friction period for tests with rough flat; (d) high-friction period, (e) decreasing-friction period, and (f) low-friction period for tests with smooth flat.

6. Analysis of origin of low friction

For the test with the DLC coating / Ti–6Al–4V contact, after running-in period (i.e. in the low friction stage), a tribofilm, which is oxidized worn-off Ti–6Al–4V, is formed on the rubbed Ti–6Al–4V surface. The tribofilm has higher hardness, higher elastic modulus, and higher yield strength than the Ti–6Al–4V substrate. On the rubbed DLC surface, a carbonaceous film is

formed. The carbonaceous layer has different structure with the DLC coating. And, the carbonaceous material is transferred to the countersurface. The contact situation is “DLC coating + carbonaceous film” on “carbonaceous film + tribofilm + Ti–6Al–4V”.

In addition, the evolution of friction coefficient from test with the DLC coated rough flat / DLC coated rough cylinder contact under the displacement amplitude of ±20 µm and normal force of 250 N is shown in Figure VI.41 (green curve). The friction coefficient remains low during the entire test. At the beginning of the test, the contact situation is “DLC coating surface” on “DLC coating surface”. The friction coefficient is around 0.20. After that, the friction coefficient shows a slight increase to around 0.26. The increase of friction is probably because of the break of DLC particles on the rough surface. With the test ongoing, the DLC surfaces become smooth, and a carbonaceous layer formed on the rubbed DLC surface. The contact situation is “DLC coating + carbonaceous layer” on “carbonaceous layer + DLC coating”. The friction is around 0.17.

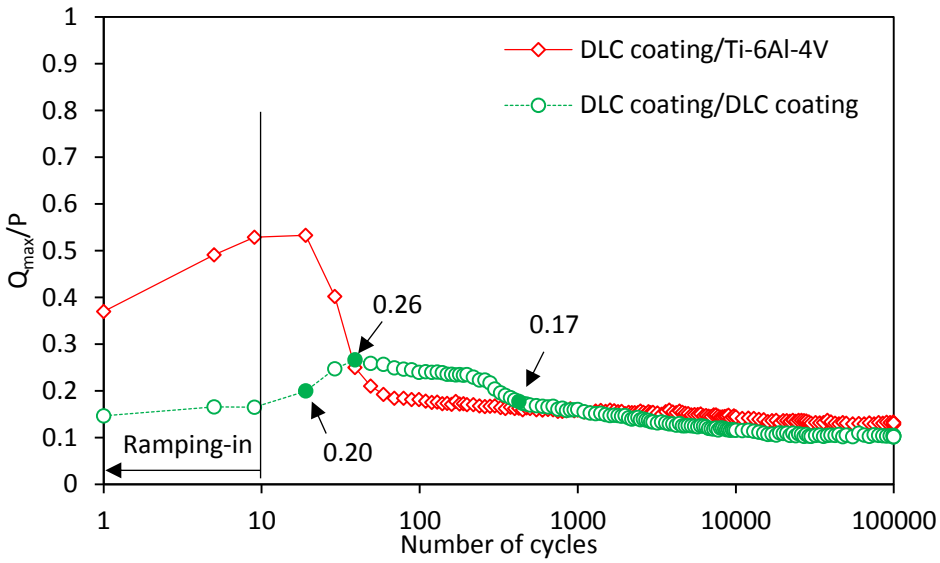

Figure VI.41. Evolution of the friction coefficient for DLC coating / DLC coating contact and for DLC coating / Ti–6Al–4V contact under the displacement amplitude of ±20 µm and normal force of 250 N.

The relationship between the friction and the contact situations is shown in Table VI.4. It is clear that the friction coefficient for DLC coating is dependent on the properties of the countersurface. However, the DLC surface state, new DLC or rubbed DLC (i.e., DLC + carbonaceous layer), has no obvious influence on the friction.

When the countersurface is Ti–6Al–4V (#1 and #3), the friction is high. This is because the soft Ti–6Al–4V is easy to be transferred to the new DLC surface (#1) and to the rubbed DLC surface (i.e., DLC + carbonaceous surface) (#3), as a consequence of adhesion and abrasion.

When the countersurface is rubbed Ti–6Al–4V (i.e., carbonaceous layer + tribofilm) (#2 and #4), the friction is always low. Comparing the low friction of “DLC / carbonaceous + tribofilm” contact (#4) with the high friction of “DLC + carbonaceous / Ti–6Al–4V” contact (#3), it seems that the presence of the tribofilm is the key factor to the low friction. The presence

of carbonaceous layer on the rubbed DLC surface cannot stop the Ti–6Al–4V transfer and thus cannot lead to low friction (#3). The low friction between the DLC coating and the tribofilm is probably because of the high hardness and high elasticity of the tribofilm material.

When the countersurface is another DLC coating, which has high hardness and high elasticity (#5 and #6), the friction is always low. The presence of carbonaceous layer between two DLC coating surfaces seems to have no obvious influence on the friction.

Table VI.4. Relationship between the friction and the contact situations.

No.	Flat / cylinder	DLC coating surface	Countersurface	Friction
#1	New DLC / new Ti–6Al–4V	DLC	Ti–6Al–4V	High
#2	Rubbed DLC / rubbed Ti–Al–4V	DLC + carbonaceous	Tribofilm + carbonaceous	Low
#3	Rubbed DLC / new Ti–6Al–4V	DLC + carbonaceous	Ti–6Al–4V	High
#4	New DLC / rubbed Ti–6Al–4V	DLC	Tribofilm + carbonaceous	Low
#5	New DLC / new DLC	DLC	DLC	Low
#6	Rubbed DLC / rubbed DLC	DLC + carbonaceous	DLC + carbonaceous	Low

7. Conclusions

In this chapter, the origin of low friction between the DLC coating and Ti–6Al–4V under low load conditions in the coating working area was investigated.

The friction coefficient decreased from approximately 0.5 to a lower value (below 0.2) during the running-in period, corresponding approximately to the first 100 cycles; then, it remained low and stable until the end of the test.

After the running-in period, a new Ti–6Al–4V surface in contact with the already-rubbed DLC coating led to a new running-in period (i.e., high friction). However, a new DLC coating surface in contact with the already-rubbed Ti–6Al–4V surface resulted in a low friction coefficient. Therefore, the rubbed Ti–6Al–4V surface after the running-in period was the key factor to the low friction.

At the beginning of the test, the Ti–6Al–4V surface was in direct contact with the DLC coating surface. Ti–6Al–4V was transferred to the DLC surface as a consequence of adhesion (and abrasion), leading to high friction.

During the running-in period, a tribofilm with a thickness of approximately 0.7–2 μm, composed of worn-off Ti–6Al–4V with severe oxidization, gradually formed on the rubbed Ti–6Al–4V surface. The hardness, elastic modulus, yield strength of the tribofilm were higher than those of the Ti–6Al–4V substrate. A thin carbonaceous layer was formed on the rubbed DLC surface, and it was transferred to the countersurface (i.e., tribofilm surface). The structure of the carbonaceous layer is different from the DLC coating. The tribofilm and carbonaceous material separated the Ti–6Al–4V and the DLC coating from direct contact and led to the low friction after the running-in period.

In addition, the rougher DLC coating surface led to a higher friction coefficient and more severe damage to the Ti–6Al–4V surface. The DLC coating on the rough flat broke before 100 cycles; however, on the smooth flat, it did not break until 100 000 cycles.

A tribological model for tribofilm formation and an analysis of origin of low friction were proposed, based on comprehensive observations of friction evolution and wear scars with different analytical tools.

GENERAL CONCLUSIONS AND PERSPECTIVES

General conclusions

The contact between the neck adapter and femoral stem in modular hip joints is subject to fretting during walking. Ti–6Al–4V alloy is one of the widely used materials for femoral stems and neck adapters. However, Ti–6Al–4V / Ti–6Al–4V contacts present high friction and severe adhesive wear under fretting conditions. DLC coatings have been widely used in many applications to decrease friction and wear between two metallic parts in contact. Thus, they could be used for neck adapter / femoral stem contact. The objectives of this thesis are to investigate the influence of DLC coatings on the fretting behavior of Ti–6Al–4V alloy for neck adapter and femoral stem applications.

Literature studies were performed including the development of DLC coatings and different parameters influencing tribological behavior of contacts. According to the literature studies, one shortcoming of DLC coatings for tribological applications is the poor cohesion due to the mismatch of mechanical properties (hardness and elastic modulus) between the coating and the substrate. Thus, one of the objectives of this thesis is to explore the influence of mechanical property of DLC coating on its fretting performance. Furthermore, according to the literature studies, the initial surface roughness and the coating position have influence on the tribological performance of contacts. Thus, another two objectives of this thesis are to investigate the influence of surface roughness and coating position on the fretting behavior of Ti–6Al–4V and DLC coatings. In addition, synovial fluid is present in the hip joint. The local solution might have corrosion effect on metals and might influence the tribological performance of DLC coatings. Thus, one of the objectives of this thesis is to investigate the influence of synovial fluid on the fretting behavior of Ti–6Al–4V and DLC coating.

At first, the fretting behavior of Ti–6Al–4V / Ti–6Al–4V contact was studied under laboratory air condition. In order to investigate the influence of initial surface roughness on fretting behavior of Ti–6Al–4V / Ti–6Al–4V contact, two types of flat samples with different roughness (smooth flat with the roughness S_a of around 20 nm; and rough flat with the roughness S_a of around 400 nm) were used for fretting tests. Those tests were carried out with different values of displacement amplitude (±20, ±40, ±70 µm) and normal force (250–1 000 N). The results served as baselines for the study of the effect of DLC coatings. Summarized results are shown in Figure Concl.1.

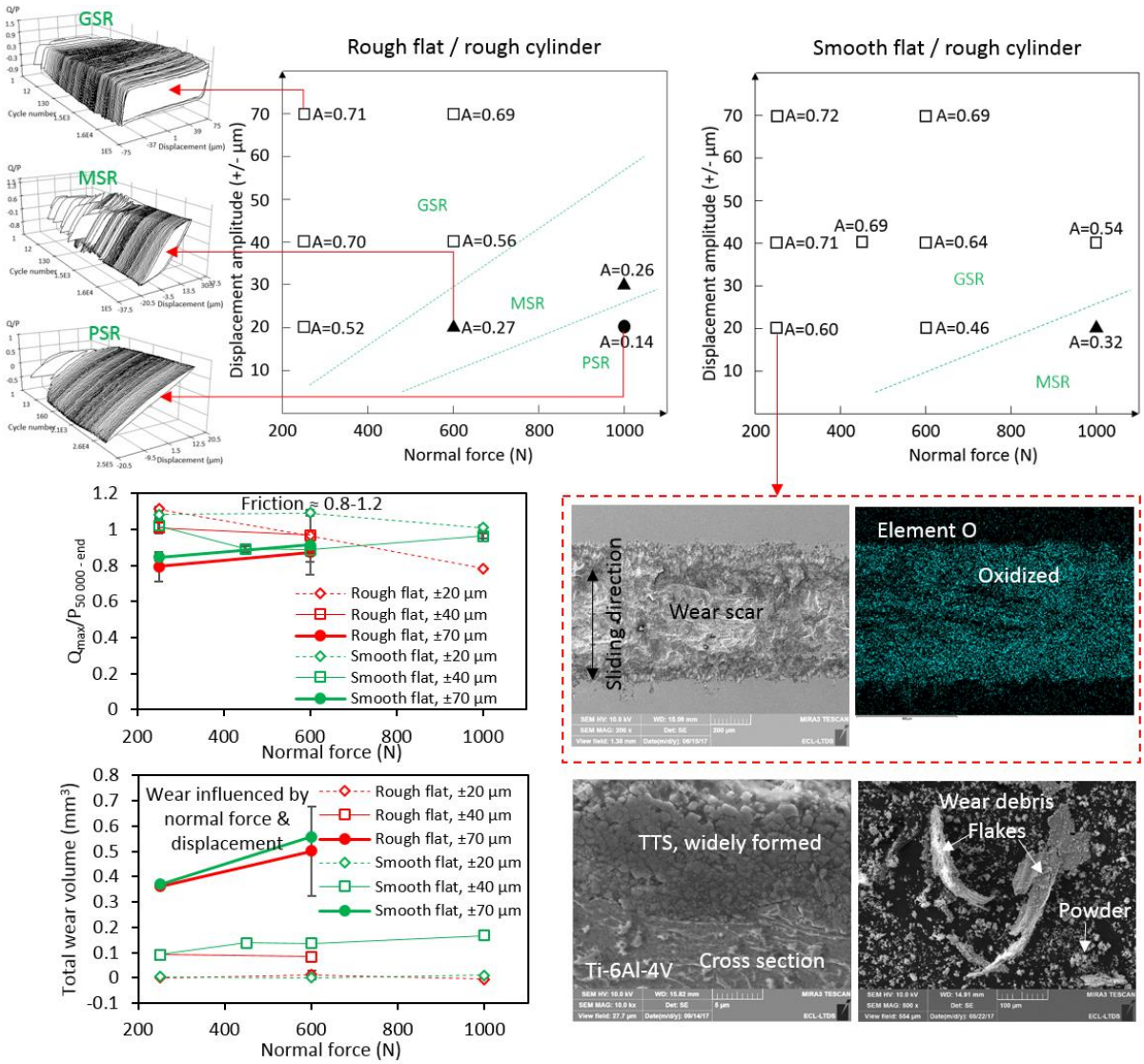

Figure Concl.1. Influence of roughness on fretting behavior of Ti–6Al–4V / Ti–6Al–4V contact.

- The RCFMs were constructed for fretting tests with Ti–6Al–4V / Ti–6Al–4V contacts. The RCFM for tests on a rough flat was divided into the GSR, the MSR, and the PSR. On a smooth flat surface, the GSR and the MSR extended towards higher normal force and lower displacement, and the PSR vanished under the given displacement and normal force conditions.
- The friction coefficient increased during the running-in period (for around 100 cycles) and then remained steady until the end of the test. The stable friction coefficients were in the range of 0.8–1.2.
- The wear volumes were very low in the MSR and the PSR. Under the GSR, the wear volume increased significantly with the increase in the displacement. With the increase in the normal force, the wear volume showed an increase under the displacement amplitude of ±70 µm, and showed no obvious change under the displacement amplitude of ±40 µm.
- On the wear scars, adhesive wear was dominant. And the wear scar was oxidized. TTS was widely observed on cross sections. And the TTS was oxidized. Cracks were widely observed,

and longer cracks were observed in the MSR and the PSR. The wear debris consisted of Ti–6Al–4V flakes and oxidized powder.

- The initial surface roughness had no visible influence on the friction coefficient, the wear volume, the wear scars, and the TTS.

In order to understand the effect of DLC coatings on the fretting behavior of Ti–6Al–4V alloy, Ti–6Al–4V samples were coated with a DLC coating via PACVD. In order to explore the influence of mechanical properties of DLC coatings on their fretting performances, two DLC coatings (DLC A with higher hardness of around 29 GPa and higher elastic modulus of around 236 GPa; and DLC B with lower hardness of around 18 GPa and lower elastic modulus of around 148 GPa) were used for fretting tests. In order to investigate the influence of surface roughness on the fretting performance of DLC coatings, two types of flat samples with different roughness (smooth flat with the roughness S_a of around 20 nm; and rough flat with the roughness S_a of around 400 nm) were coated with a DLC coating (DLC A or DLC B). In order to investigate the influence of coating position on the fretting behavior of DLC coating, three coating position configurations (coating on the flat, on the cylinder, and on both the flat and the cylinder) were adopted for testing. Fretting tests were carried out under laboratory air condition with different values of displacement amplitude (±20, ±40, ±70 μm) and normal force (200–1 200 N).

- Coating response wear maps were constructed according to the comprehensive analysis of friction, wear volumes, and wear scars. Coating response wear maps could be divided into three areas: coating working area (low load conditions), coating failure area (high load conditions), and transition area (only existing under the low displacement amplitude of ±20 μm, between the coating working area and the coating failure area), as shown in Figure Conclu.2.
- In the coating working area, the coating was not or partly removed. The friction was low. The wear volume was small. In the coating failure area, the coating was almost entirely removed. Then, the Ti–6Al–4V was in direct contact with Ti–6Al–4V. The friction was high. In the transition area, the coating was partly removed, and the friction had an intermediate value.
- The harder and stiffer coating DLC A had better tribological properties than DLC B.
- DLC coatings deposited on a smooth flat surface presented better tribological performance than deposited on a rough flat surface.
- DLC coating deposited on the cylinder exhibited better tribological performance than deposited on the flat. The DLC coating was generally damaged more severely when sliding against itself than against the soft Ti–6Al–4V alloy in the coating working area.

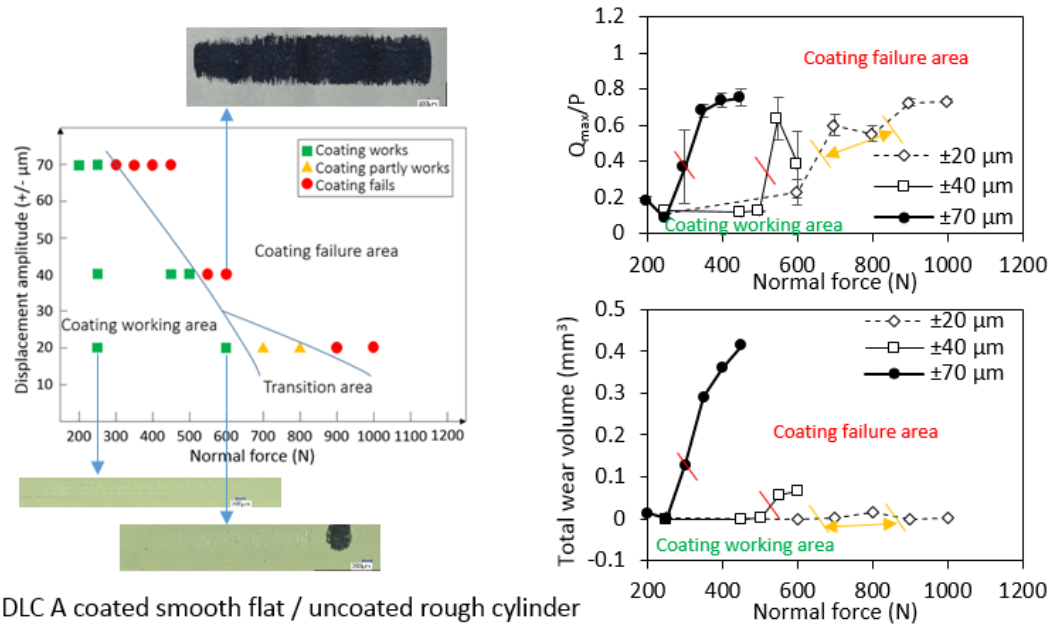

Figure Concl.2. Coating response wear map for DLC A coated on smooth flat (in contact with uncoated rough cylinder).

In order to investigate the influence of synovial fluid on the fretting behavior of Ti–6Al–4V and DLC coating, serum (half new born calf serum and half distilled water) was applied into the Ti–6Al–4V / Ti–6Al–4V contact (i.e. uncoated smooth flat / uncoated rough cylinder) and into DLC coating / Ti–6Al–4V contact (i.e. DLC A coated smooth flat / uncoated rough cylinder) at a rate of 2 drops per second during testing. Fretting tests were carried out with different values of displacement amplitude (±20, ±40, ±70 µm) and normal force (250–1 000 N for Ti–6Al–4V / Ti–6Al–4V contact; 250–1 200 N for DLC coating / Ti–6Al–4V contact).

- For the fretting tests of Ti–6Al–4V / Ti–6Al–4V, the presence of the serum had different effect on the fretting behavior, depending on the displacement amplitude (as shown in Figure Concl.3): under the displacement amplitude of ±40 µm, the friction coefficients were slightly lower (0.6–0.8); however, the total wear volumes were significantly larger comparing with those under the laboratory air conditions. Under the displacement amplitude of ±70 µm, the friction coefficients were significantly lower (0.25–0.35) and the total wear volumes were significantly smaller comparing with those under the laboratory air conditions.
- For fretting tests of DLC coating / Ti–6Al–4V, the rubbed DLC surface was not chemically damaged by the serum.
- The presence of serum had a positive influence on the tribological performance of the DLC coating. The coating working area extended towards higher normal forces (as shown in Figure Concl.4). Furthermore, the positive influence was more significant under a larger displacement amplitude. The increase rates in the threshold induced by the presence of

serum were 38%, 110%, and 191% under the displacement amplitudes of ±20 µm, ±40 µm, and ±70 µm, respectively.

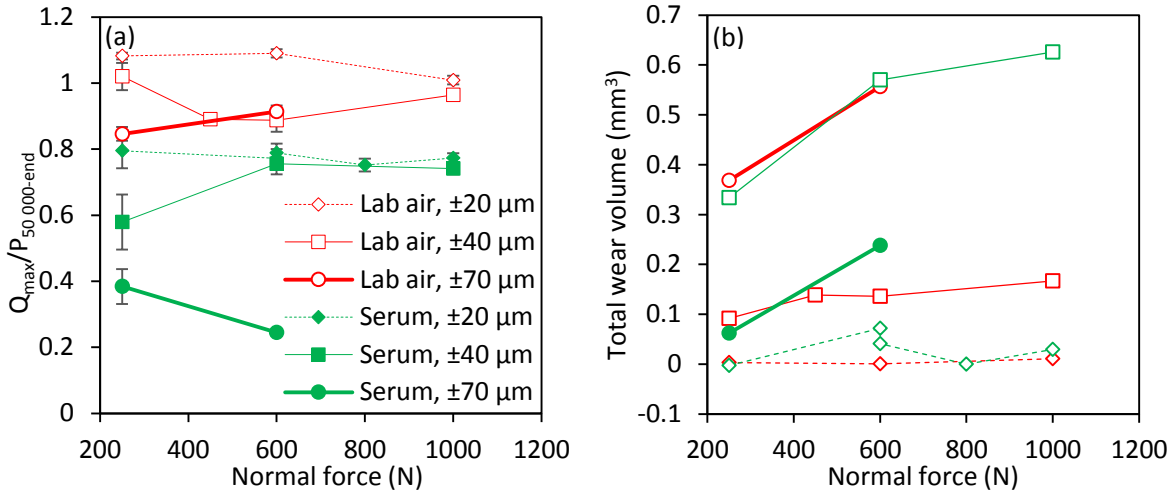

Figure Concl.3. Effect of serum on friction and wear of Ti–6Al–4V / Ti–6Al–4V contact: (a) Q/P; (b) total wear volume.

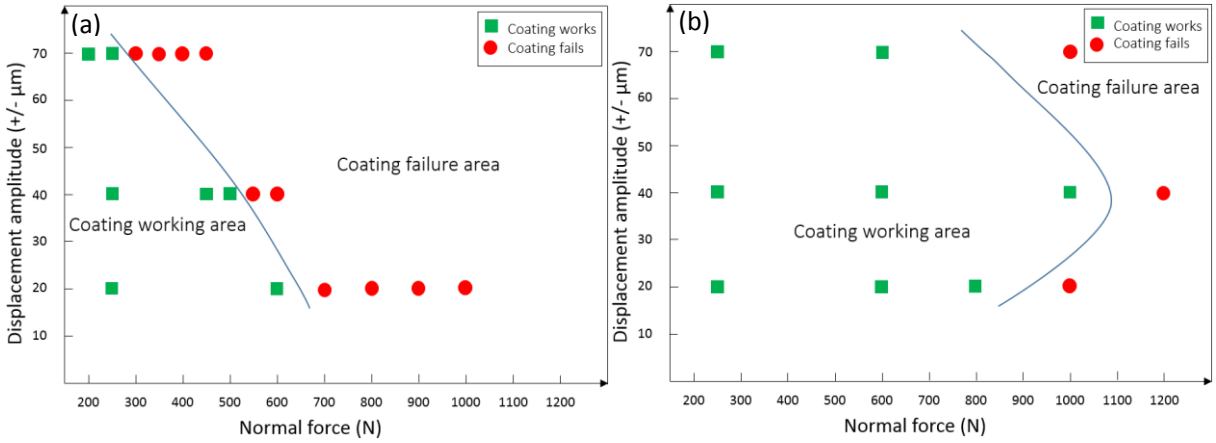

Figure Concl.4. Coating wear maps for DLC A coated on smooth flat in contact with uncoated rough cylinder (a) under laboratory air condition and (b) under serum condition.

According to the tests with DLC coatings, the friction was low in the coating working area (i.e. under low load conditions). Thus, the origin of low friction for the DLC coating / Ti–6Al–4V contacts (DLC A coated rough flat / uncoated rough cylinder; and DLC A coated smooth flat / uncoated rough cylinder) was investigated under the laboratory air condition with the displacement amplitude of ±20 µm and normal force of 250 N. Tests were carried out with different numbers of cycles: 0 (contact only), 1, 20, 40, 100, 100 000 cycles. Summarized results are shown in Figure Concl.5.

- For fretting tests of DLC coating / Ti–6Al–4V under low load condition, the friction coefficient decreased from high values (around 0.5) to low values (below 0.2) during the running-in period for around 100 cycles; then, it remained low and stable until the end of the test.

- At the beginning of the test, the Ti–6Al–4V surface was in direct contact with the DLC coating surface. Ti–6Al–4V was transferred to the DLC surface as a consequence of adhesion (and abrasion), leading to high friction.
- During the running-in period, a tribofilm with a thickness of approximately 0.7–2 µm, composed of worn-off Ti–6Al–4V with severe oxidization, gradually formed on the damaged Ti–6Al–4V surface. The hardness, elastic modulus, yield strength of the tribofilm were higher than those of the Ti–6Al–4V substrate. A thin carbonaceous layer was formed on the rubbed DLC surface, and it was transferred to the countersurface (i.e., tribofilm surface). The structure of the carbonaceous layer was different from the DLC coating. The tribofilm and carbonaceous material separated the Ti–6Al–4V and the DLC coating from direct contact and led to the low friction after the running-in period.
- Comparing with the smooth DLC coating surface, the rougher DLC coating surface led to a higher friction coefficient and more severe damage to the coating / Ti–6Al–4V contact. The DLC coating on the rough flat broke before 100 cycles; however, on the smooth flat, it did not break until the end of the test (100 000 cycles).

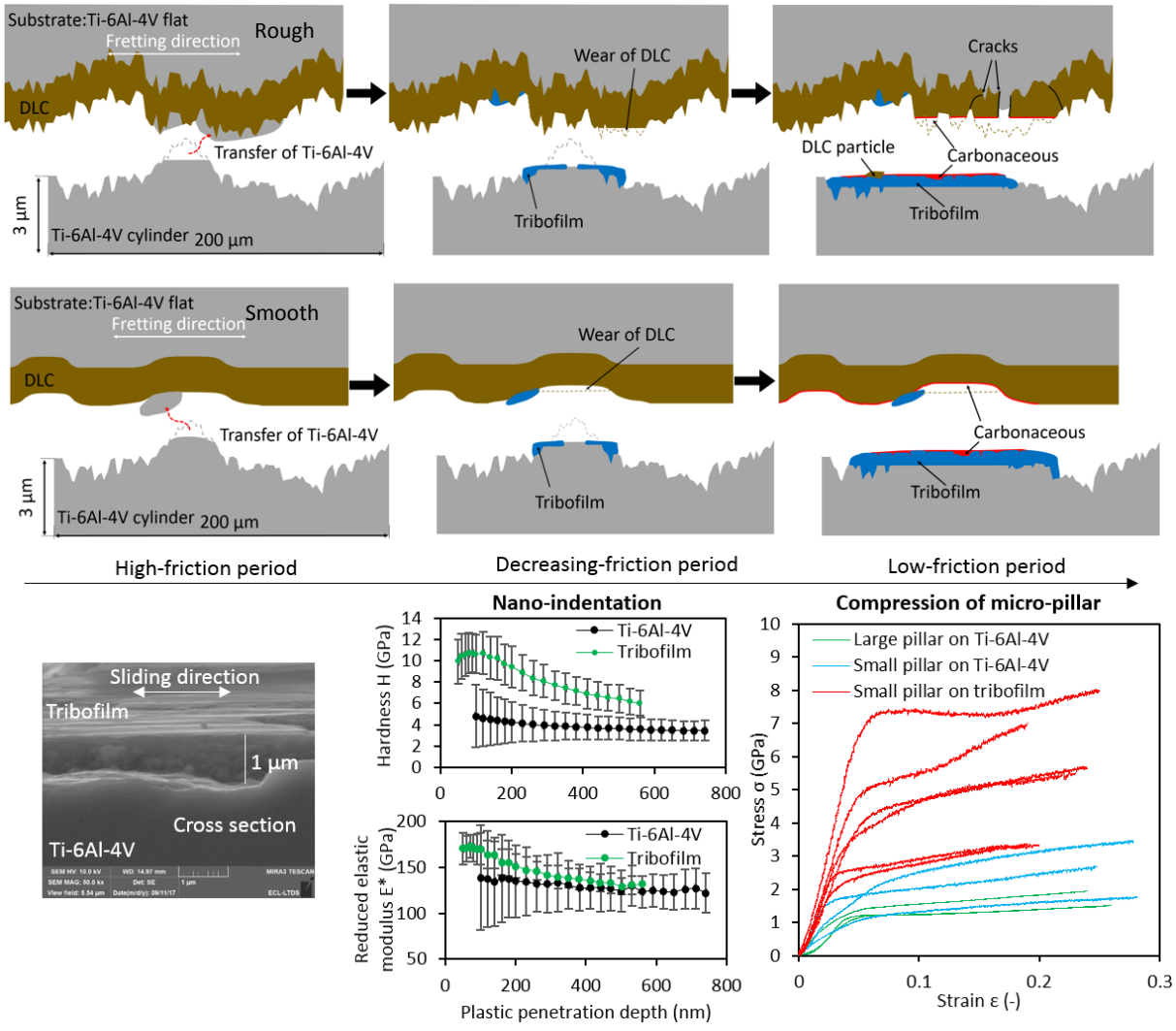

Figure Concl.5. Evolution of DLC coating / Ti–6Al–4V contact under low load, and properties of tribofilm.

The fretting behaviors of DLC coatings as well as the Ti–6Al–4V substrate were investigated for neck adapter and femoral stem applications. In brief, DLC coatings can be used as protective coatings into Ti–6Al–4V / Ti–6Al–4V interface for neck adapter–femoral stem contact. The Ti–6Al–4V substrate can be well protected by DLC coatings under relatively low load conditions (i.e., in the coating working area), with low friction coefficient and small wear volume. DLC A has better tribological properties than DLC B. To have better fretting performance, the DLC coating should be deposited on a smooth substrate surface rather than on a rough surface. Furthermore, the presence of serum has positive influences on the fretting performance of the DLC coating.

Perspectives

In this thesis, the tribological behaviors of DLC coatings and Ti–6Al–4V substrate were investigated under a wide range of conditions, including different normal forces, three values of displacement amplitude, two types of DLC coating, two types of surface roughness, three deposition positions, and different environments. However, there are still several interesting aspects that could be further explored.

- The corrosion process of Ti–6Al–4V / Ti–6Al–4V contact under serum condition could be further investigated in details.
- The nature of carbonaceous film formed on the tribofilm surface could be further explored.
- The biocompatibility of the DLC coatings (studied in this thesis) and their wear debris should be investigated before putting them into practice.
- Tests on real parts, with DLC coated neck adapter surface, following standards for stem, should be performed and analyzed.

REFERENCES

[1] B.M. Wroblewski, P.D. Siney, P.A. Fleming, Charnley low-friction arthroplasty, J. Bone Joint Surg. (Br.) 89-B (2007) 1015–1018.

[2] R. Pivec, A.J. Johnson, S.C. Mears, M.A. Mont, Hip arthroplasty, The Lancet 380 (2012) 1768–1777.

[3] T.M. Grupp, T. Weik, W. Bloemer, H.-P. Knaebel, Modular titanium alloy neck adapter failures in hip replacement - failure mode analysis and influence of implant material, BMC Musculoskelet. Disord. 2010 11:3. http://www.biomedcentral.com/1471-2474/11/3

[4] S.Y. Jauch, G. Huber, H. Haschke, K. Sellenschloh, M.M. Morlock, Design parameters and the material coupling are decisive for the micromotion magnitude at the stem–neck interface of bi-modular hip implants, Med. Eng. Phys. 36 (2014) 300–307.

[5] L. Kunčická, R. Kocich, T.C. Lowe, Advances in metals and alloys for joint replacement, Prog. Mater. Sci. 88 (2017) 232–280.

[6] G. Dearnaley, J.H. Arps, Biomedical applications of diamond-like carbon (DLC) coatings: A review, Surf. Coat. Technol.200 (2005) 2518–2524.

[7] S. Salih, A. Hamer, Hip and knee replacement, Surg. Oxf. 31 (2013) 482–487.

[8] J.M. Murnaghan, A.J. Hamer, Hip and knee replacement, Surg. Oxf., 28 (2010) 508–513.

[9] A. King, J.R.A. Phillips, Total hip and knee replacement surgery, Surg. Oxf. 34 (2016) 468–474.

[10] J. Charnley, Surgery of the Hip-joint, Br. Med. J. 5176 (1960) 821–826.

[11] B.M. Wroblewski, Professor Sir John Charnley (1911–1982), Rheumatology 41 (2002) 824–825.

[12] http://www.jointsurgery.in/hip-replacement/types-of-hip-replacement/

[13] I.D. Learmonth, C. Young, C. Rorabeck, The operation of the century: total hip replacement, The Lancet 370 (2007) 1508–1519.

[14] W.T. Gofton, E.M. Illical, R.J. Feibel, P.R. Kim, P.E. Beaulé, A Single-Center Experience With a Titanium Modular Neck Total Hip Arthroplasty, J. Arthroplasty 32 (2017) 2450–2456.

[15] S.K. Fokter, A. Moličnik, R. Kavalar, P. Pelicon, R. Rudolf, N. Gubeljak, Why do some titanium-alloy total hip arthroplasty modular necks fail?, J. Mech. Behav. Biomed. Mater. 69 (2017) 107–114.

[16] Q. Chen, G.A. Thouas, Metallic implant biomaterials, Mater. Sci. Eng. R Rep. 87 (2015) 1–57.

[17] J. Walczak, F. Shahgaldi, F. Heatley, In vivo corrosion of 316L stainless-steel hip implants: morphology and elemental compositions of corrosion products, Biomaterials 19 (1998) 229–237.

[18] https://www.thebalance.com/type-316-and-316l-stainless-steel-2340262

[19] M. Semlitsch, Properties of Wrought CoNiCrMo Alloy Protasul-10, a Highly Corrosion and Fatigue Resistant Implant Material for Joint Endoprostheses, Eng. Med.9 (1980) 201–207.

[20] http://www.aircraftmaterials.com/data/titanium/ti6al4v.html

[21] U.I. Thomann, P.J. Uggowitzer, Wear–corrosion behavior of biocompatible austenitic stainless steels, Wear 239 (2000) 48–58.

[22] S.H. Teoh, Fatigue of biomaterials: a review, International Journal of Fatigue 22 (2000) 825–837.

[23] N.S. Manam, W.S.W. Harun, D.N.A. Shri, S.A.C. Ghani, T. Kurniawan, M.H. Ismail, M.H.I. Ibrahime, Study of corrosion in biocompatible metals for implants: A review, J. Alloys Compd. 701 (2017) 698–715.

[24] Y. Liao, E. Hoffman, M. Wimmer, A. Fischer, J. Jacobs, L. Marks, CoCrMo Metal-on-Metal Hip Replacements, Phys. Chem. Chem. Phys. 15 (2013) 1–26.

[25] A. Yamamoto, R. Honma, M. Sumita, Cytotoxicity evaluation of 43 metal salts using murine fibroblasts and osteoblastic cells, J. Biomed. Mater. Res. 39 (1998) 331–340.

[26] X. Mao, A.A. Wong, R.W. Crawford, Cobalt toxicity - an emerging clinical problem in patients with metal-on-metal hip prostheses?, Med. J. Aust. 194 (2011) 649–651.

[27] F. Bartolomeu, M. Sampaio, O. Carvalho, E. Pinto, N. Alves, J.R. Gomes, F.S. Silva, G. Miranda, Tribological behavior of Ti6Al4V cellular structures produced by Selective Laser Melting, J. Mech. Behav. Biomed. Mater. 69 (2017) 128–134.

[28] M. Buciumeanu, A. Araujo, O. Carvalho, G. Miranda, J.C.M. Souza, F.S. Silva, B. Henriques, Study of the tribocorrosion behaviour of Ti6Al4V–HA biocomposites, Tribol. Int. 107 (2017) 77–84.

[29] A.F. Yetim, F. Yildiz, Y. Vangolu, A. Alsaran, A. Celik, Several plasma diffusion processes for improving wear properties of Ti6Al4V alloy, Wear 267 (2009) 2179–2185.

[30] Z.X. Zhang, H. Dong, T. Bell, B.S. Xu, The effect of deep-case oxygen hardening on the tribological behaviour of a–C:H DLC coatings on Ti6Al4V alloy, J. Alloys Compd. 464 (2008) 519–525.

[31] B. Regener, C. Krempaszky, E. Werner, M. Stockinger, Modelling the micromorphology of heat treated Ti6Al4V forgings by means of spatial tessellations feasible for FEM analyses of microscale residual stresses, Comput. Mater. Sci. 52 (2012) 77–81.

[32] A.M. Gallardo-Moreno, M.A. Pacha-Olivenza, L. Saldana, C. Perez-Giraldo, J.M. Bruque, N. Vilaboa, M.L. Gonzalez-Martin, In vitro biocompatibility and bacterial adhesion of physico-chemically modified Ti6Al4V surface by means of UV irradiation, Acta Biomater. 5 (2009) 181–192.

[33] R. Kumazawa, F. Watari, N. Takashi, Y. Tanimura, M. Uo, Y. Totsuka, Effects of Ti ions and particles on neutrophil function and morphology, Biomaterials 23 (2002) 3757–3764.

[34] S.V. Verstraeten, L. Aimo, P.I. Oteiza, Aluminium and lead: molecular mechanisms of brain toxicity, Arch. Toxicol. 82 (2008) 789–802.

[35] G. Bergmann, F. Graichen, A. Rohlmann, A. Bender, B. Heinlein, G.N. Duda, M.O. Heller, M.M. Morlock, Realistic loads for testing hip implants, Biomed. Mater. Eng. 20 (2010) 65–75.

[36] M. Baxmann, S.Y. Jauch, C. Schilling, W. Blömer, T.M. Grupp, M.M. Morlock, The influence of contact conditions and micromotions on the fretting behavior of modular titanium alloy taper connections, Med. Eng. Phys. 35 (2013) 676–683.

[37] S.Y. Jauch, G. Huber, E. Hoenig, M. Baxmann, T.M. Grupp, M.M. Morlock, Influence of material coupling and assembly condition on the magnitude of micromotion at the stem–neck interface of a modular hip endoprosthesis, J. Biomech. 44 (2011) 1747–1751.

[38] J.L. Gilbert, M. Mehta, B. Pinder, Fretting crevice corrosion of stainless steel stem–CoCr femoral head connections: Comparisons of materials, initial moisture, and offset length, J. Biomed. Mater. Res. B Appl. Biomater. 88B (2009) 162–173.

[39] https://en.wikipedia.org/wiki/Fretting

[40] Z.R. Zhou, K. Nakazawa, M.H. Zhu, N. Maruyama, Ph. Kapsa, L. Vincent, Progress in fretting maps, Tribol. Int. 39 (2006) 1068–1073.

[41] S. Fouvry, Ph. Kapsa, L. Vincent, Analysis of sliding behaviour for fretting loadings: determination of transition criteria, Wear 185 (1995) 35–46.

[42] S. Hannel, S. Fouvry, Ph. Kapsa, L. Vincent, The fretting sliding transition as a criterion for electrical contact performance, Wear 249 (2001) 761–770.

[43] O. Vingsbo, S. Söderberg, On fretting maps, Wear 126 (1988) 131–147.

[44] S. Fouvry, Ph. Kapsa, L. Vincent, An elastic–plastic shakedown analysis of fretting wear, Wear 247 (2001) 41–54.

[45] D. Siva Rama Krishna, Y. Sun, Effect of thermal oxidation conditions on tribological behaviour of titanium films on 316L stainless steel, Surf. Coat. Technol. 198 (2005) 447–453.

[46] D. Siva Rama Krishna, Y. Sun, Thermally oxidised rutile-TiO2 coating on stainless steel for tribological properties and corrosion resistance enhancement, Appl. Surf. Sci. 252 (2005) 1107–1116.

[47] L. Duisabeau, P. Combrade, B. Forest, Environmental effect on fretting of metallic materials for orthopaedic implants, Wear 256 (2004) 805–816.

[48] A. Chiba, K. Kumagai, N. Nomura, S. Miyakawa, Pin-on-disk wear behavior in a like-on-like configuration in a biological environment of high carbon cast and low carbon forged Co–29Cr–6Mo alloys, Acta Mater. 55 (2007) 1309–1318.

[49] A. Çelik, Ö. Bayrak, A. Alsaran, İ. Kaymaz, A.F. Yetim, Effects of plasma nitriding on mechanical and tribological properties of CoCrMo alloy, Surf. Coat. Technol. 202 (2008) 2433–2438.

[50] V. Fridrici, S. Fouvry, Ph. Kapsa, Effect of shot peening on the fretting wear of Ti–6Al–4V, Wear 250 (2001) 642–649.

[51] V. Fridrici, S. Fouvry, Ph. Kapsa, Fretting wear behavior of a Cu–Ni–In plasma coating, Surf. Coat. Technol. 163–164 (2003) 429–434.

[52] Y. Itoh, A. Itoh, H. Azuma, T. Hioki, Improving the tribological properties of Ti–6Al–4V alloy by nitrogen-ion implantation, Surf. Coat. Technol. 111 (1999) 172–176.

[53] C. Tassin, F. Laroudie, M. Pons, L. Lelait, Improvement of the wear resistance of 316L stainless steel by laser surface alloying, Surf. Coat. Technol. 80 (1996) 207–210.

[54] http://asm.matweb.com/search/SpecificMaterial.asp?bassnum=MQ316Q

[55] M. Talha, C.K. Behera, O.P. Sinha, A review on nickel-free nitrogen containing austenitic stainless steels for biomedical applications, Mater. Sci. Eng. C 33 (2013) 3563–3575.

[56] A.J. Saldívar-García, H.F. López, Microstructural effects on the wear resistance of wrought and as-cast Co-Cr-Mo-C implant alloys, J. Biomed. Mater. Res. A 74A (2005) 269–274.

[57] A. Fischer, S. Weiß, M.A. Wimmer, The tribological difference between biomedical steels and CoCrMo-alloys, J. Mech. Behav. Biomed. Mater. 9 (2012) 50–62.

[58] H. Güleryüz H. Çimenoğlu, Effect of thermal oxidation on corrosion and corrosion–wear behaviour of a Ti–6Al–4V alloy, Biomaterials 25 (2004) 3325–3333.

[59] P.A. Dearnley, K.L. Dahm, H. Çimenoğlu, The corrosion–wear behaviour of thermally oxidised CP-Ti and Ti–6Al–4V, Wear 256 (2004) 469–479.

[60] N.J. Hallab, 6.607–Fretting Corrosion of Orthopedic Implants, Comprehensive Biomaterials 6 (2011) 89–96.

[61] D. Royhman, M. Patel, J.J. Jacobs, M.A. Wimmer, N.J. Hallab, M.T. Mathew, In vitro simulation of fretting-corrosion in hip implant modular junctions: The influence of pH, Med. Eng. Phys. 52 (2018) 1–9.

[62] D. Royhman, M. Patel, M.J. Runa, M. A. Wimmer, J.J. Jacobs, N.J. Hallab, M.T. Mathew, Fretting-corrosion behavior in hip implant modular junctions: The influence of friction energy and pH variation, J. Mech. Behav. Biomed. Mater. 62 (2016) 570–587.

[63] V. Swaminathan J.L. Gilbert, Fretting corrosion of CoCrMo and Ti6Al4V interfaces, Biomaterials 33 (2012) 5487–5503.

[64] R. Pivec, R.M. Meneghini, W.J. Hozack, G.H. Westrich, M.A. Mont, Modular Taper Junction Corrosion and Failure: How to Approach a Recalled Total Hip Arthroplasty Implant, J. Arthroplasty 29 (2014) 1–6.

[65] https://openi.nlm.nih.gov/detailedresult.php?img=PMC2824687_1471-2474-11-3-5&req=4

[66] https://www.limacorporate.com/medical/130/h-max.html?country=72

[67] P. Wodecki, D. Sabbah, G. Kermarrec, I. Semaan, New type of hip arthroplasty failure related to modular femoral components: Breakage at the neck-stem junction, Orthop. Traumatol. Surg. Res. 99 (2013) 741–744.

[68] D.B. Luo, Selection of coatings for tribological applications (PhD thesis), Ecully, Ecole centrale de Lyon, 2009.

[69] D.B. Luo, V. Fridrici, Ph. Kapsa, Evaluating and predicting durability of bonded solid lubricant coatings under fretting conditions, Tribol. Int. 44 (2011) 1577–1582.

[70] D. B. Luo, V. Fridrici, Ph. Kapsa, Selecting solid lubricant coatings under fretting conditions, Wear 268 (2010) 816–827.

[71] D. B. Luo, V. Fridrici, Ph. Kapsa, Relationships between the fretting wear behavior and the ball cratering resistance of solid lubricant coatings, Surf. Coat. Technol. 204 (2010) 1259–1269.

[72] K. Holmberg, A concept for friction mechanisms of coated surfaces, Surf. Coat. Technol. 56 (1992) 1–10.

[73] D.B. Luo, V. Fridrici, Ph. Kapsa, A systematic approach for the selection of tribological coatings, Wear 271 (2011) 2132–2143.

[74] J. Zhang, A.A. Polycarpou, J. Economy, An Improved Tribological Polymer-Coating System for Metal Surfaces, Tribol. Lett. 38 (2010) 355–365.

[75] J. Yang, On the use of statistical analysis for tribological evaluation of a solid lubricant (PhD thesis), Ecully, Ecole Centrale de Lyon, 2013.

[76] J.-Y. Lee, D.-S. Lim, Tribological behavior of PTFE film with nanodiamond, Surf. Coat. Technol. 188–189 (2004) 534–538.

[77] W.-R. Chang, An elastic-plastic contact model for a rough surface with an ion-plated soft metallic coating, Wear 212 (1997) 229–237.

[78] M.A. Sherbiney, J. Halling, Friction and wear of ion-plated soft metallic films, Wear 45 (1977) 211–220.

[79] C. Donnet, J.M. Martin, Th. Le Mogne, M. Belin, Super-low friction of MoS2 coatings in various environments, Tribol. Int. 29 (1996) 123–128.

[80] http://webcache.googleusercontent.com/search?q=cache:http://industrialcoatingsworld.com/low-friction-coatings/mos2-low-friction-coatings&gws_rd=cr&dcr=0&ei=EHvLWsfiJsTikgWqtJWgAQ

[81] https://www.quora.com/What-is-the-molecular-structure-of-graphite .html

[82] K.P. Furlan, J.D.B. de Mello, A.N. Klein, Self-lubricating composites containing MoS_2: A review, Tribol. Int. 120 (2018) 280–298.

[83] R. Hauert, J. Patscheider, From Alloying to Nanocomposites—Improved Performance of Hard Coatings, Adv. Eng. Mater. 2 (2000) 247–259.

[84] A. Chauhan, R. Vaish, Hard coating material selection using multi-criteria decision making, Mater. Des. 44 (2013) 240–245.

[85] E. Santecchia, A.M.S. Hamouda, F. Musharavati, E. Zalnezhad, M. Cabibbo, S. Spigarelli, Wear resistance investigation of titanium nitride-based coatings, Ceram. Int. 41 (2015) 10349–10379.

[86] S. Zhang, W. Zhu, TiN coating of tool steels: a review, J. Mater. Process. Technol. 39 (1993) 165–177.

[87] Y. Tanno, A. Azushima, Effect of counter materials on coefficients of friction of TiN coatings with preferred grain orientations, Wear 266 (2009) 1178–1184.

[88] A. Azushima, Y. Tanno, H. Iwata, K. Aoki, Coefficients of friction of TiN coatings with preferred grain orientations under dry condition, Wear 265 (2008) 1017–1022.

[89] K. Xiao, W. Xue, Zh.L. Li, J.R. Wang, X.M. Li, Ch.F. Dong, J.Sh. Wu, X.G. Li, D. Wei, Effect of sintering temperature on the microstructure and performance of a ceramic coating obtained by the slurry method, Ceram. Int. 44 (2018) 11180–11186.

[90] K.A. Habib, J.J. Saura, C. Ferrer, M.S. Damra, E. Giménez, L. Cabedo, Comparison of flame sprayed Al_2O_3/TiO_2 coatings: Their microstructure, mechanical properties and tribology behavior, Surf. Coat. Technol. 201 (2006) 1436–1443.

[91] D.I. Pantelis, P. Psyllaki, N. Alexopoulos, Tribological behaviour of plasma-sprayed Al_2O_3 coatings under severe wear conditions, Wear 237 (2000) 197–204.

[92] H. Leiste, U. Dambacher, S. Ulrich, H. Holleck, Microstructure and properties of multilayer coatings with covalent bonded hard materials, Surf. Coat. Technol. 116–119 (1999) 313–320.

[93] A.S. Argon, V. Gupta, H.S. Landis, J.A. Cornie, Intrinsic toughness of interfaces between SiC coatings and substrates of Si or C fibre, J. Mater. Sci. 24 (1989) 1207–1218.

[94] I.P. Hayward, Friction and wear properties of diamonds and diamond coatings, Surf. Coat. Technol. 49 (1991) 554–559.

[95] I.P. Hayward, I.L. Singer, L.E. Seitzman, Effect of roughness on the friction of diamond on CVD diamond coatings, Wear 157 (1992) 215–227.

[96] Z. Feng, Y. Tzeng, J.E. Field, Friction of diamond on diamond in ultra-high vacuum and low-pressure environments, J. Phys. Appl. Phys. 25 (1992) 1418–1424.

[97] J. Robertson, Diamond-like amorphous carbon, Mater. Sci. Eng. R Rep. 37 (2002) 129–281.

[98] H.Q. Wan, Y.L. Jia, Y.P. Ye, H.Y. Xu, H.X. Cui, L. Chen,H.D. Zhou, J.M. Chen, Tribological behavior of polyimide/epoxy resin-polytetrafluoroethylene bonded solid lubricant coatings filled with in situ-synthesized silver nanoparticles, Prog. Org. Coat. 106 (2017) 111–118.

[99] J. Xu, Z.R. Zhou, C.H. Zhang, M.H. Zhu, J.B. Luo, An investigation of fretting wear behaviors of bonded solid lubricant coatings, J. Mater. Process. Technol. 182 (2007) 146–151.

[100] M.H. Zhu, Z.R. Zhou, An investigation of molybdenum disulfide bonded solid lubricant coatings in fretting conditions, Surf. Coat. Technol. 141 (2001) 240–245.

[101] D.G. Armour, Ion beam deposition, Nucl. Instrum. Methods Phys. Res. Sect. B Beam Interact. Mater. At. 89 (994) 325–331.

[102] https://en.wikipedia.org/wiki/Ion_beam_deposition

[103] J.L. Vossen, Thin Film Processes, Elsevier (2012).

[104] D.M. Mattox, Handbook of Physical Vapor Deposition (PVD) Processing (2nd Edition), William Andrew (2010).

[105] W.D. Westwood, Physical Vapor Deposition, Microelectronic Materials and Processes (1989) 133–201.

[106] J.-H. Park, T.S. Sudarshan, Chemical Vapor Deposition, ASM International (2001).

[107] K.F. Jensen, Chemical Vapor Deposition, Advances in Chemistry 221 (1989) 199–263.

[108] J.-O. Carlsson, P.M. Martin, Chapter 7 - Chemical Vapor Deposition, Handbook of Deposition Technologies for Films and Coatings (3rd Edition), Boston: William Andrew Publishing (2010) 314–363.

[109] N. Ye, J.-Y. Wang, R.I. Boughton, M.-C. Hong, Chapter 20 - Functional Crystals, Modern Inorganic Synthetic Chemistry (Second Edition) (2017) 575-611.

[110] K. Bewilogua, D. Hofmann, History of diamond-like carbon films — From first experiments to worldwide applications, Surf. Coat. Technol. 242 (2014) 214–225.

[111] J. Robertson, Requirements of ultrathin carbon coatings for magnetic storage technology, Tribol. Int. 36 (2003) 405–415.

[112] A.C. Ferrari, Diamond-like carbon for magnetic storage disks, Surf. Coat. Technol. 180–181 (2004) 190–206.

[113] G.W. Malaczynski, A.H. Hamdi, A.A. Elmoursi, X. Qiu, Diamond-like carbon coating for aluminum 390 alloy — automotive applications, Surf. Coat. Technol. 93 (1997) 280–286.

[114] M. Kano, Diamond-Like Carbon Coating Applied to Automotive Engine Components, Tribol. Online 9 (2014) 135–142.

[115] C.A. Love, R.B. Cook, T.J. Harvey, P.A. Dearnley, R.J.K. Wood, Diamond like carbon coatings for potential application in biological implants—a review, Tribol. Int. 63 (2013) 141–150.

[116] D. Choudhury, J. Lackner, R.A. Fleming, J. Goss, J. Chen, M. Zou, Diamond-like carbon coatings with zirconium-containing interlayers for orthopedic implants, J. Mech. Behav. Biomed. Mater. 68 (2017) 51–61.

[117] L. Swiatek, A. Olejnik, J. Grabarczyk, A. Jedrzejczak, A. Sobczyk-Guzenda, M. Kaminska, W. Jakubowski, W. Szymanski, D. Bociaga, Multi-doped diamond like-carbon coatings (DLC-Si/Ag) for biomedical applications fabricated using the modified chemical vapour deposition method, Diam. Relat. Mater. 67 (2016) 54–62.

[118] R. Hauert, An overview on the tribological behavior of diamond-like carbon in technical and medical applications, Tribol. Int. 37 (2004) 991–1003.

[119] S. Bhowmick, A.T. Alpas, Minimum quantity lubrication drilling of aluminium–silicon alloys in water using diamond-like carbon coated drills, Int. J. Mach. Tools Manuf. 48 (2008) 1429–1443.

[120] S. Bhowmick, A.T. Alpas, The performance of hydrogenated and non-hydrogenated diamond-like carbon tool coatings during the dry drilling of 319 Al, Int. J. Mach. Tools Manuf. 48 (2008) 802–814.

[121] Q. Wei, J. Narayan, Superhard diamondlike carbon: preparation, theory, and properties, Int. Mater. Rev. 45 (2000) 133–164.

[122] J. Robertson, Mechanical properties and structure of diamond-like carbon, Diam. Relat. Mater. 1 (1992) 397–406.

[123] J. Robertson, Properties of diamond-like carbon, Surf. Coat. Technol. 50 (1992) 185–203.

[124] J. Robertson, Electronic structure of diamond-like carbon, Diam. Relat. Mater. 6 (1997) 212–218.

[125] J. Fontaine, Towards the use of diamond-like carbon solid lubricant coatings in vacuum and space environments, Proc. Inst. Mech. Eng. Part J-J. Eng. Tribol. 222 (2008) 1015–1029.

[126] J. Robertson, Structural models of a–C and a–C:H, Diam. Relat. Mater. 4 (1995) 297–301.

[127] J. Robertson, E.P. O'Reilly, Electronic and atomic structure of amorphous carbon, Phys. Rev. B 35 (1987) 2946–2957.

[128] E.P. O'Reilly, J. Robertson, D. Beeman, Electronic structure of amorphous carbon, J. Non-Cryst. Solids 77–78 (1985) 83–86.

[129] J. Robertson, Electronic processes in hydrogenated amorphous carbon, J. Non-Cryst. Solids 198–200 (1996) 615–618.

[130] W. Jacob, W. Möller, On the structure of thin hydrocarbon films, Appl. Phys. Lett. 63 (1993) 1771–1773.

[131] A. Grill, Diamond-like carbon: state of the art, Diam. Relat. Mater. 8 (1999) 428–434.

[132] C. Casiraghi, J. Robertson, A.C. Ferrari, Diamond-like carbon for data and beer storage, Mater. Today 10 (2007) 44–53.

[133] Y. Lifshitz, S.R. Kasi, J.W. Rabalais, Subplantation model for film growth from hyperthermal species: Application to diamond, Phys. Rev. Lett. 62 (1989) 1290–1293.

[134] Y. Lifshitz, S.R. Kasi, J.W. Rabalais, W. Eckstein, Subplantation model for film growth from hyperthermal species, Phys. Rev. B 41 (1990) 10468–10480.

[135] J. Robertson, Deposition mechanisms for promoting sp^3 bonding in diamond-like carbon, Diam. Relat. Mater. 2 (1993) 984–989.

[136] J. Robertson, The deposition mechanism of diamond-like a–C and a–C: H, Diam. Relat. Mater. 3 (1994) 361–368.

[137] W. Möller, Modeling of the sp^3/sp^2 ratio in ion beam and plasma-deposited carbon films, Appl. Phys. Lett. 59 (1991) 2391–2393.

[138] W. Möller, Plasma and surface modeling of the deposition of hydrogenated carbon films from low-pressure methane plasmas, Appl. Phys. A 56 (1993) 527–546.

[139] C.A. Davis, A simple model for the formation of compressive stress in thin films by ion bombardment, Thin Solid Films 226 (1993) 30–34.

[140] P.J. Fallon, V. S. Veerasamy, C.A. Davis, J. Robertson, G.A.J. Amaratunga, W.I. Milne, J. Koskinen, Properties of filtered-ion-beam-deposited diamondlike carbon as a function of ion energy, Phys. Rev. B 48 (1993) 4777–4782.

[141] A. von Keudell, W. Jacob, Interaction of hydrogen plasmas with hydrocarbon films, investigated by infrared spectroscopy using an optical cavity substrate, J. Vac. Sci. Technol. Vac. Surf. Films 15 (1997) 402–407.

[142] S. Waidmann, M. Knupfer, J. Fink, B. Kleinsorge, J. Robertson, Electronic structure studies of undoped and nitrogen-doped tetrahedral amorphous carbon using high-resolution electron energy-loss spectroscopy, J. Appl. Phys. 89 (2001) 3783–3792.

[143] M. Chhowalla, J. Robertson, C.W. Chen, S.R.P. Silva, C.A. Davis, G.A.J. Amaratunga, W.I. Milne, Influence of ion energy and substrate temperature on the optical and electronic properties of tetrahedral amorphous carbon (ta–C) films, J. Appl. Phys. 81 (1997) 139–145.

[144] Sh. Xu, D. Flynn, B.K. Tay, S. Prawer, K.W. Nugent, S.R.P. Silva, Y. Lifshitz, W.I. Milne, Mechanical properties and Raman spectra of tetrahedral amorphous carbon films with high sp^3 fraction deposited using a filtered cathodic arc, Philos. Mag. B 76 (1997) 351–361.

[145] B. Schultrich, H.-J. Scheibe, D. Drescher, H. Ziegele, Deposition of superhard amorphous carbon films by pulsed vacuum arc deposition, Surf. Coat. Technol. 98 (1998) 1097–1101.

[146] M. Weiler, S. Sattel, T. Giessen, K. Jung, H. Ehrhardt, V.S. Veerasamy, J. Robertson, Preparation and properties of highly tetrahedral hydrogenated amorphous carbon, Phys. Rev. B 53 (1996) 1594–1608.

[147] S. Sattel, J. Robertson, H. Ehrhardt, Effects of deposition temperature on the properties of hydrogenated tetrahedral amorphous carbon, J. Appl. Phys. 82 (1997) 4566–4576.

[148] P. Koidl, C. Wild, B. Dischler, J. Wagner, M. Ramsteiner, Plasma Deposition, Properties and Structure of Amorphous Hydrogenated Carbon Films, Mater. Sci. Forum. 52–53 (1990) 41–70.

[149] M.A. Tamor, W.C. Vassell, K.R. Carduner, Atomic constraint in hydrogenated "diamond-like" carbon, Appl. Phys. Lett. 58 (1991) 592–594.

[150] J.W. Zou, K. Reichelt, K. Schmidt, B. Dischler, The deposition and study of hard carbon films, J. Appl. Phys. 65 (1989) 3914–3918.

[151] A.C. Ferrari, S.E. Rodil, J. Robertson, W.I. Milne, Is stress necessary to stabilise sp^3 bonding in diamond-like carbon?, Diam. Relat. Mater. 11 (2002) 994–999.

[152] A.C. Ferrari, B. Kleinsorge, N.A. Morrison, A. Hart, V. Stolojan, J. Robertson, Stress reduction and bond stability during thermal annealing of tetrahedral amorphous carbon, J. Appl. Phys. 85 (1999) 7191–7197.

[153] A. Anttila, R. Lappalainen, V.-M. Tiainen, M. Hakovirta, Superior attachment of high-quality hydrogen-free amorphous diamond films to solid materials, Adv. Mater. 9 (1997) 1161–1164.

[154] A.A. Voevodin, S.D. Walck, J.S. Zabinski, Architecture of multilayer nanocomposite coatings with super-hard diamond-like carbon layers for wear protection at high contact loads, Wear 203–204 (1997) 516–527.

[155] G. Gotzmann, J. Beckmann, C. Wetzel, B. Scholz, U. Herrmann, J. Neunzehn, Electron-beam modification of DLC coatings for biomedical applications, Surf. Coat. Technol. 311 (2017) 248–256.

[156] L. Anne Thomson, F.C. Law, N. Rushton, J. Franks, Biocompatibility of diamond-like carbon coating, Biomaterials 12 (1991) 37–40.

[157] M. Allen, B. Myer, N. Rushton, In vitro and in vivo investigations into the biocompatibility of diamond-like carbon (DLC) coatings for orthopedic applications, J. Biomed. Mater. Res. 58 (2001) 319–328.

[158] G. Taeger, L.E. Podleska, B. Schmidt, M. Ziegler, D. Nast-Kolb, Comparison of Diamond-Like-Carbon and Alumina-Oxide articulating with Polyethylene in Total Hip Arthroplasty, Mater. Sci. Eng. Technol. 34 (2003) 1094–1100.

[159] A. Grill, Review of the tribology of diamond-like carbon, Wear 168 (1993) 143–153.

[160] A. Grill, Tribology of diamondlike carbon and related materials: an updated review, Surf. Coat. Technol. 94–95 (1997) 507–513.

[161] R. Hauert, A review of modified DLC coatings for biological applications, Diam. Relat. Mater. 12 (2003) 583–589.

[162] K. Enke, H. Dimigen, H. Hübsch, Frictional properties of diamondlike carbon layers, Appl. Phys. Lett. 36 (1980) 291–292.

[163] K.D. Koshigan, F. Mangolini, J.B. McClimon, B. Vacher, S. Bec, R.W. Carpick, J. Fontaine, Understanding the hydrogen and oxygen gas pressure dependence of the tribological properties of silicon oxide–doped hydrogenated amorphous carbon coatings, Carbon 93 (2015) 851–860.

[164] C. Donnet, A. Grill, Friction control of diamond-like carbon coatings, Surf. Coat. Technol. 94–95 (1997) 456–462.

[165] C. Donnet, J. Fontaine, A. Grill, T.L. Mogne, The role of hydrogen on the friction mechanism of diamond-like carbon films, Tribol. Lett. 9 (2001) 137–142.

[166] T. Kunze, M. Posselt, S. Gemming, G. Seifert, A.R. Konicek, R.W. Carpick, L. Pastewka, M. Moseler, Wear, Plasticity, and Rehybridization in Tetrahedral Amorphous Carbon, Tribol. Lett. 53 (2014) 119–126.

[167] A.R. Konicek, D.S. Grierson, P.U.P.A. Gilbert, W.G. Sawyer, A.V. Sumant, R.W. Carpick, Origin of Ultralow Friction and Wear in Ultrananocrystalline Diamond, Phys. Rev. Lett. 100 (2008) 235502.

[168] Y. Liu, A. Erdemir, E.I. Meletis, A study of the wear mechanism of diamond-like carbon films, Surf. Coat. Technol. 82 (1996) 48–56.

[169] J.-P. Hirvonen, R. Lappalainen, J. Koskinen, A. Anttila, T.R. Jervis, M. Trkula, Tribological characteristics of diamond-like films deposited with an arc-discharge method, J. Mater. Res. 5 (1990) 2524–2530.

[170] H. Ronkainen, J. Koskinen, J. Likonen, S. Varjus, J. Vihersalo, Characterization of wear surfaces in dry sliding of steel and alumina on hydrogenated and hydrogen-free carbon films, Diam. Relat. Mater. 3 (1994) 1329–1336.

[171] H. Ronkainen, J. Likonen, J. Koskinen, S. Varjus, Effect of tribofilm formation on the tribological performance of hydrogenated carbon coatings, Surf. Coat. Technol. 79 (1996) 87–94.

[172] H. Ronkainen, S. Varjus, J. Koskinen, K. Holmberg, Differentiating the tribological performance of hydrogenated and hydrogen-free DLC coatings, Wear 249 (2001) 260–266.

[173] A.A. Voevodin, A.W. Phelps, J.S. Zabinski, M.S. Donley, Friction induced phase transformation of pulsed laser deposited diamond-like carbon, Diam. Relat. Mater. 5 (1996) 1264–1269.

[174] B. Marchon, M.R. Khan, N. Heiman, P. Pereira, A. Lautie, Tribochemical wear on amorphous carbon thin films, IEEE Trans. Magn. 26 (1990) 2670–2675.

[175] B. Marchon, N. Heiman, M.R. Khan, Evidence for tribochemical wear on amorphous carbon thin films, IEEE Trans. Magn. 26 (1990) 168–170.

[176] C. Donnet, Recent progress on the tribology of doped diamond-like and carbon alloy coatings: a review, Surf. Coat. Technol. 100–101 (1998) 180–186.

[177] J.C. Damasceno, S.S. Camargo, F.L. Freire, R. Carius, Deposition of Si-DLC films with high hardness, low stress and high deposition rates, Surf. Coat. Technol. 133–134 (2000) 247–252.

[178] M. Ban T. Hasegawa, Internal stress reduction by incorporation of silicon in diamond-like carbon films, Surf. Coat. Technol. 162 (2003) 1–5.

[179] G.Q. Yu, B.K. Tay, Z. Sun, L.K. Pan, Properties of fluorinated amorphous diamond like carbon films by PECVD, Appl. Surf. Sci. 219 (2003) 228–237.

[180] E.H.A. Dekempeneer, J. Meneve, J. Smeets, S. Kuypers, L. Eersels, R. Jacobs, Structural, mechanical and tribological properties of plasma-assisted chemically vapour deposited hydrogenated C_xN_{1-x}:H films, Surf. Coat. Technol. 68–69 (1994) 621–625.

[181] T.-A. Yeh, C.-L. Lin, J.M. Sivertsen, J.H. Judy, Friction, wear and elasto-plastic stress analysis of rf-sputtered carbon-nitrogen protective coatings for rigid magnetic storage disks, J. Magn. Magn. Mater. 120 (1993) 314–318.

[182] H. Dimigen, C.-P. Klages, Microstructure and wear behavior of metal-containing diamond-like coatings, Surf. Coat. Technol. 49 (1991) 543–547.

[183] W. Dai, P. Ke, A. Wang, Microstructure and property evolution of Cr-DLC films with different Cr content deposited by a hybrid beam technique, Vacuum 85 (2011) 792–797.

[184] A. Amanov, T. Watabe, R. Tsuboi, S. Sasaki, Fretting wear and fracture behaviors of Cr-doped and non-doped DLC films deposited on Ti–6al–4V alloy by unbalanced magnetron sputtering, Tribol. Int. 62 (2013) 49–57.

[185] D. Bociąga, W. Jakubowski, P. Komorowski, A. Sobczyk-Guzenda, A. Jędrzejczak, D Batory, A. Olejnik, Surface characterization and biological evaluation of silver-incorporated DLC coatings fabricated by hybrid RF PACVD/MS method, Mater. Sci. Eng. C 63 (2016) 462–474.

[186] C. Benndorf, Structural and mechanical properties of niobium-containing amorphous hydrogenated carbon films (Nb–C:H), Mater. Sci. Eng. A 140 (1991) 795–801.

[187] K. Bewilogua, R. Wittorf, H. Thomsen, M. Weber, DLC based coatings prepared by reactive d.c. magnetron sputtering, Thin Solid Films 447–448 (2004) 142–147.

[188] S. Buchegger, N. Schuster, B. Stritzker, A. Wixforth, C. Westerhausen, Multilayer diamond-like amorphous carbon coatings produced by ion irradiation of polymer films, Surf. Coat. Technol. 327 (2017) 42–47.

[189] Ch. Wei, J.-Y. Yen, Effect of film thickness and interlayer on the adhesion strength of diamond like carbon films on different substrates, Diam. Relat. Mater. 16 (2007) 1325–1330.

[190] Y. Lin, Z. Zhou, K.Y. Li, Improved wear resistance at high contact stresses of hydrogen-free diamond-like carbon coatings by carbon/carbon multilayer architecture, Appl. Surf. Sci. (2017). https://doi.org/10.1016/j.apsusc.2017.11.118

[191] F. Cemin, L.T. Bim, C.M. Menezes, M.E.H. Maia da Costa, I.J.R. Baumvol, F. Alvarez, C.A. Figueroa, The influence of different silicon adhesion interlayers on the tribological behavior of DLC thin films deposited on steel by EC-PECVD, Surf. Coat. Technol. 283 (2015) 115–121.

[192] C. Rincón, G. Zambrano, A. Carvajal, P. Prieto, H. Galindo, E. Martınez, A. Lousa, J. Esteve, Tungsten carbide/diamond-like carbon multilayer coatings on steel for tribological applications, Surf. Coat. Technol. 148 (2001) 277–283.

[193] L.F. Bonetti, G. Capote, L.V. Santos, E.J. Corat, V.J. Trava-Airoldi, Adhesion studies of diamond-like carbon films deposited on Ti6Al4V substrate with a silicon interlayer, Thin Solid Films 515 (2006) 375–379.

[194] C. Wei, Y.-S. Wang, F.-C. Tai, The role of metal interlayer on thermal stress, film structure, wettability and hydrogen content for diamond like carbon films on different substrate, Diam. Relat. Mater.18 (2009) 407–412.

[195] C. Wei, C.-H. Chen, The effect of thermal and plastic mismatch on stress distribution in diamond like carbon film under different interlayer/substrate system, Diam. Relat. Mater. 17 (2008) 1534–1540.

[196] W. Zhang, A. Tanaka, B.S. Xu, Y. Koga, Study on the diamond-like carbon multilayer films for tribological application, Diam. Relat. Mater. 14 (2005) 1361–1367.

[197] S. Yang, D.G. Teer, Investigation of sputtered carbon and carbon/chromium multi-layered coatings, Surf. Coat. Technol. 131 (2000) 412–416.

[198] A.A. Voevodin, J.M. Schneider, C. Rebholz, A. Matthews, Multilayer composite ceramicmetal-DLC coatings for sliding wear applications, Tribol. Int. 29 (1996) 559–570.

[199] K.J. Kubiak, T.G. Mathia, S. Fouvry, Interface roughness effect on friction map under fretting contact conditions, Tribol. Int. 43 (2010) 1500–1507.

[200] K.J. Kubiak, T.W. Liskiewicz, T.G. Mathia, Surface morphology in engineering applications: Influence of roughness on sliding and wear in dry fretting, Tribol. Int. 44 (2011) 1427–1432.

[201] R. Elleuch, K. Elleuch, H. Ben Abdelounis, H. Zahouani, Surface roughness effect on friction behaviour of elastomeric material, Mater. Sci. Eng. A 465 (2007) 8–12.

[202] A. Aubert, J.P. Nabot, J. Ernoult, P. Renaux, Preparation and properties of MoS_x films grown by d.c. magnetron sputtering, Surf. Coat. Technol. 41 (1990) 127–134.

[203] J. Yang, V. Fridrici, M. Messaadi, Ph. Kapsa, Survival and factorial analysis of durability and friction coefficient of a solid lubricant under different working conditions, Wear 302 (2013) 998–1009.

[204] J. Yang, V. Fridrici, M. Messaadi, Ph. Kapsa, The effect of porous substrate on the tribological performance of a MoS_2 based coating in fretting by statistical analysis, Wear 330–331 (2015) 122–135.

[205] Y.-H. Li, G.-B. Rao, L.-J. Rong, Y.-Y. Li, The influence of porosity on corrosion characteristics of porous NiTi alloy in simulated body fluid, Mater. Lett. 57 (2002) 448–451.

[206] S. Affatato, M. Spinelli, M. Zavalloni, C. Mazzega-Fabbro, M. Viceconti, Tribology and total hip joint replacement: Current concepts in mechanical simulation, Med. Eng. Phys. 30 (2008) 1305–1317.

[207] P. Couvrat, M. Denis, M. Langer, S. Mitura, P. Niedzielski, J. Marciniak, The corrosion tests of amorphous carbon coatings deposited by r.f. dense plasma onto steel with different chromium contents, Diam. Relat. Mater. 4 (1995) 1251–1254.

[208] C.A.G.S. Oliveira, M.F. Stein, E. Saito, H. Zanin, L.S. Vieira, L. Raniero, V.J. Trava-Airoldi, A.O. Lobo, F.R. Marciano, Effect of gold oxide incorporation on electrochemical corrosion resistance of diamond-like carbon, Diam. Relat. Mater. 53 (2015) 40–44.

[209] C.P. Fenili, F. Silvio de Souza, G. Marin, S.M.H. Probst, C. Binder, A.N. Klein, Corrosion resistance of low-carbon steel modified by plasma nitriding and diamond-like carbon, Diam. Relat. Mater. 80 (2017) 153–161.

[210] L. Chandra, M. Allen, R. Butter, N. Rushton, A.H. Lettington, T.W. Clyne, The effect of exposure to biological fluids on the spallation resistance of diamond-like carbon coatings on metallic substrates, J. Mater. Sci. Mater. Med. 6 (1995) 581–589.

[211] L. Chandra, M. Allen, R. Butter, N. Rushton, A.H. Lettington, T.W. Clyne, The effect of biological fluids on the adhesion of diamond-like carbon films to metallic substrates, Diam. Relat. Mater. 4 (1995) 852–856.

[212] http://www.science-et-medecine.fr/hanche/tiges-femorales/a-cimenter/

[213] http://www.tshungary.hu/dok/DLC_coating_equipment.pdf

[214] J.M. Wheeler, J. Michler, Elevated temperature, nano-mechanical testing in situ in the scanning electron microscope, Rev. Sci. Instrum. 84 (2013) 045103-1–15.

[215] A. Viat, G. Guillonneau, S. Fouvry, G. Kermouche, S. Sao Joao, J. Wehrs, J. Michler, J.-F. Henne, Brittle to ductile transition of tribomaterial in relation to wear response at high temperatures, Wear 392–373 (2017) 60–68.

[216] G. Guillonneau M. Mieszala, J. Wehrs, J. Schwiedrzik, S. Grop, D. Frey, L. Philippe, J.-M. Breguet, J. Michler, J.M. Wheeler, Nanomechanical testing at high strain rates: New instrumentation for nanoindentation and microcompression, Mater. Des. 148 (2018) 39–48.

[217] R. Rabe, J.-M. Breguet, P. Schwaller, S. Stauss, F.-J. Haug, J. Patscheider, J. Michler, Observation of fracture and plastic deformation during indentation and scratching inside the scanning electron microscope, Thin Solid Films 469–470 (2004) 206–213.

[218] S. Fouvry, V. Fridrici, C. Langlade, Ph. Kapsa, L. Vincent, Palliatives in fretting: A dynamical approach, Tribol. Int. 39 (2006) 1005–1015.

[219] S. Fouvry, P. Duo, Ph. Perruchaut, A quantitative approach of Ti–6Al–4V fretting damage: friction, wear and crack nucleation, Wear 257 (2004) 916–929.

[220] Z.R. Zhou, E. Sauger, J.J. Liu, L. Vincent, Nucleation and early growth of tribologically transformed structure (TTS) induced by fretting, Wear 212 (1997) 50–58.

[221] E. Sauger, L. Ponsonnet, J.M. Martin, L. Vincent, Study of the tribologically transformed structure created during fretting tests, Tribol. Int. 33 (2000) 743–750.

[222] E. Sauger, S. Fouvry, L. Ponsonnet, Ph. Kapsa, J.M. Martin, L. Vincent, Tribologically transformed structure in fretting, Wear 245 (2000) 39–52.

[223] V. Fridrici, S. Fouvry, Ph. Kapsa, P. Perruchaut, Prediction of cracking in Ti–6Al–4V alloy under fretting-wear: use of the SWT criterion, Wear 259 (2005) 300–308.

[224] V.A. Alves, R.Q. Reis, I.C.B. Santos, D.G. Souza, T. de F. Gonçalves, M.A. Pereira-da-Silva, A. Rossi, L.A. da Silva, In situ impedance spectroscopy study of the electrochemical corrosion of Ti and Ti–6Al–4V in simulated body fluid at 25 °C and 37°C, Corrosion Science 51 (2009) 2473–2482.

[225] M.A. Khan, R.L. Williams, D.F. Williams, The corrosion behaviour of Ti–6Al–4V, Ti–6Al–7Nb and Ti–13Nb–13Zr in protein solutions, Biomaterials 20 (1999) 631–637.

[226] K.D. Koshigan, Understanding the influence of environment on the solid lubrication processes of carbon-based thin films (PhD thesis), Ecully, Ecole Centrale de Lyon, 2015.

[227] A.C. Ferrari, Determination of bonding in diamond-like carbon by Raman spectroscopy, Diam. Relat. Mater. 11 (2002) 1053–1061.

[228] F.C. Tai, S.C. Lee, J. Chen, C. Wei, S.H. Chang, Multipeak fitting analysis of Raman spectra on DLCH film, J. Raman Spectrosc. 40 (2009) 1055–1059.

[229] G. Guillonneau, G. Kermouche, S. Bec, J.-L. Loubet, Extraction of Mechanical Properties with Second Harmonic Detection for Dynamic Nanoindentation Testing, *Exp. Mech.* 52 (2012) 933–944.

[230]I.N. Sneddon, The relation between load and penetration in the axisymmetric Boussinesq problem for a punch of arbitrary profile, *Int. J. Eng. Sci.* 3 (1956) 47–57.

Journal articles based on this work

Published

(1) H.H. Ding, V. Fridrici, G. Bouvard, J. Geringer, Ph. Kapsa, Influence of calf serum on fretting behaviors of Ti–6Al–4V and diamond-like carbon coating for neck adapter–femoral stem contact, Tribology Letters (2018) 66:110. https://doi.org/10.1007/s11249-018-1069-z

(2) H.H. Ding, V. Fridrici, J. Geringer, J. Fontaine, Ph. Kapsa, Influence of diamond-like carbon coatings and roughness on fretting behaviors of Ti–6Al–4V for neck adapter–femoral stem contact, Wear 406–407 (2018) 53–67. https://doi.org/10.1016/j.wear.2018.04.001

Under review

(1) H.H. Ding, V. Fridrici, J. Geringer, J. Fontaine, Ph. Kapsa, Low-friction study between diamond-like carbon coating and Ti–6Al–4V under fretting conditions.

(2) H.H. Ding, V. Fridrici, G. Bouvard, J. Geringer, J. Fontaine, Ph. Kapsa, Influence of the diamond-like carbon coating and deposition positions on fretting behaviors of Ti–6Al–4V alloy.

(3) H.H. Ding, V. Fridrici, G. Guillonneau, S. Sao-Joao, J. Geringer, J. Fontaine, Ph. Kapsa, Investigation on mechanical properties of tribofilm formed on Ti–6Al–4V surface when sliding against a DLC coating: using nano-indentation and micro-pillar compression techniques.

APPENDIX

Appendix A. Calculation of normal force corresponding to the real contact conditions

For a cylinder / flat contact, the calculation of the contact pressure relies on the following equations AppA.1, AppA.2, and AppA.3.

$$\frac{1}{E^*} = \frac{1-\nu_1^2}{E_1} + \frac{1-\nu_2^2}{E_2} \quad \text{(AppA.1)}$$

where E^* is the reduced modulus. E_1, E_2, ν_1 and ν_2 are the Young's modulus and the Poisson ratio for the flat and cylinder, respectively.

$$a = 2\sqrt{\frac{PR}{\pi E^* L}} \quad \text{(AppA.2)}$$

where P is the normal force, R is radius of the cylinder, L is the contact width, a is the half length of the contact, as shown in Figure AppA.1.

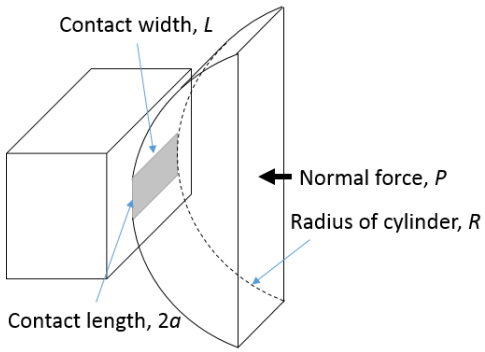

Figure AppA.1. Cylinder / flat contact area.

$$p_0 = \frac{2P}{\pi L a} \quad \text{(AppA.3)}$$

where p_0 is the maximum contact pressure.

According to equations AppA.1, AppA.2, and AppA.3, the relationship between the normal force P and the maximum contact pressure p_0 is shown in Equation AppA.4.

$$P = p_0^2 \pi R L \left(\frac{1-\nu_1^2}{E_1} + \frac{1-\nu_2^2}{E_2}\right) \quad \text{(AppA.4)}$$

In this study, the flat and cylinder are made of Ti–6Al–4V alloy. From the results of nano-indentation on Ti–6Al–4V surface, $E_1 = E_2 = 120$ GPa. $\nu_1 = \nu_2 = 0.35$. So, $E^* \approx 62.68$ GPa. $R = 10$ mm = 0.01 m; $L = 5$ mm = 0.005 m;

So:

$$P = \frac{p_0^2 \times \pi \times 0.01 \times 0.005}{67.61 \times 10^9} \quad \text{(AppA.5)}$$

For $p_0 = 280$ MPa, normal force $P \approx 180$ N. For $p_0 = 690$ MPa, normal force $P \approx 1\,100$ N. Therefore, normal forces between 200 N and 1 200 N were applied in this study.

Appendix B. Calculation of wear volume

Figure AppB.1 shows typical wear scar profiles on flat and cylinder samples measured though the 2D contact profilometer parallel to the sliding direction.

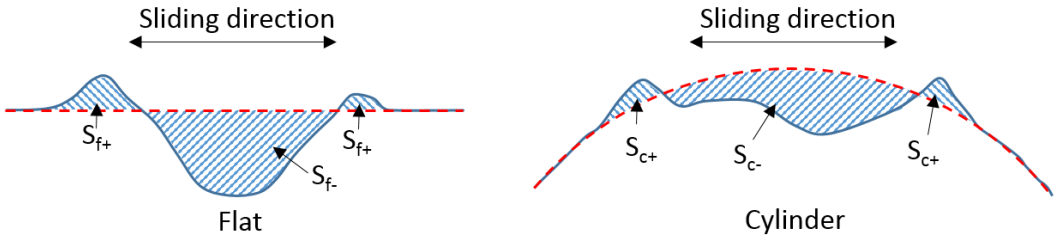

Figure AppB.1. Typical profiles of wear tracks on flat and cylinder samples.

The wear volume is calculated according to the profiles. Take the flat as an example, the area of material removal on the profile section is:

$$S_f = \sum S_{f-} - \sum S_{f+} \quad \text{(AppB.1)}$$

On each wear scar, 10 profiles were measured, and the interval between neighboring profiles was 0.5 mm. The wear volume of flat, V_f, is calculated as follow:

$$V_f = \sum_{i=1}^{10} S_f \times \frac{1}{10} \times L \quad \text{(AppB.2)}$$

where *L* is the contact width between flat and cylinder samples. In this study, *L* is around 5 mm.

The total wear volume, V_{total}, i.e. the sum of the wear volumes of the flat and the cylindrical surfaces, is shown in Equation AppB.3:

$$V_{total} = V_f + V_c \quad \text{(AppB.3)}$$

Appendix C. Correction of sample, punch, frame compliance for pillar compression

During the compression of micro-pillar, the displacement and the load are recorded as a function of the test time. Figure AppC. 1 shows typical raw data.

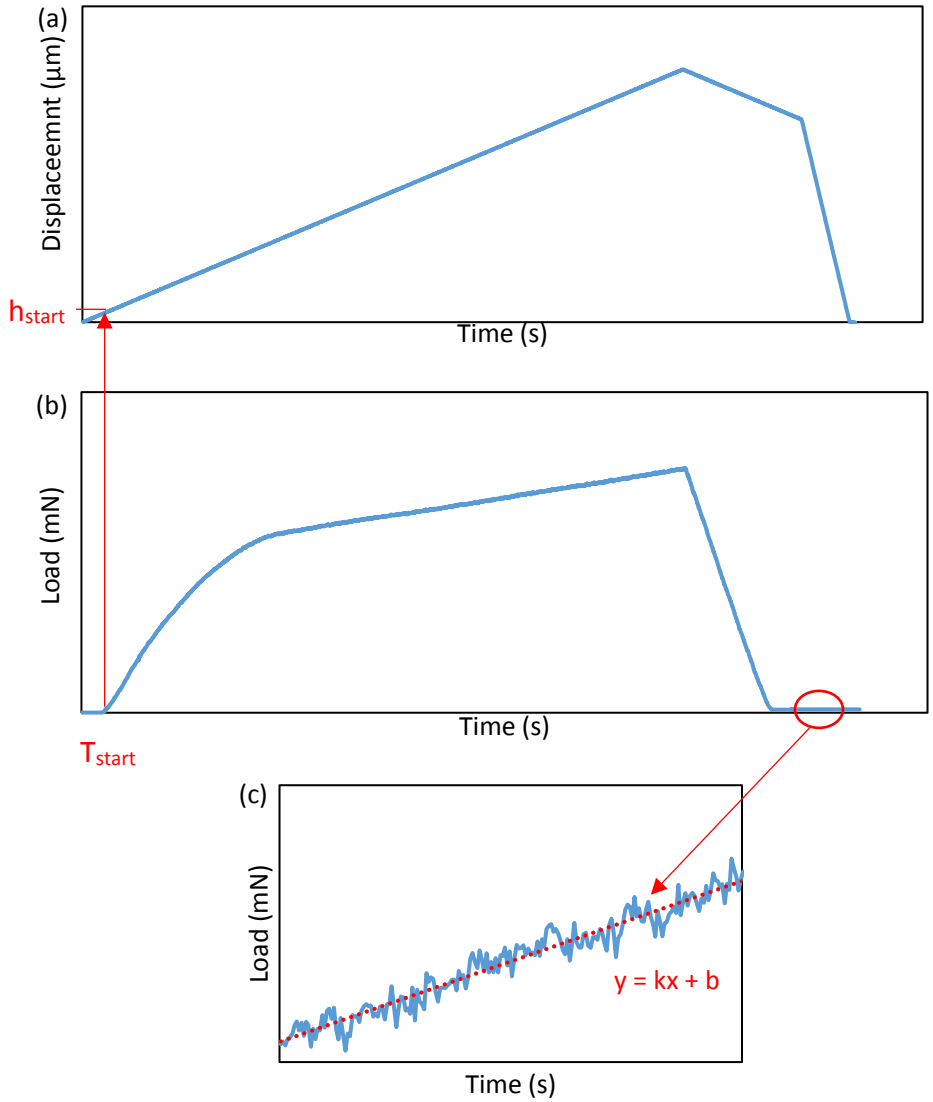

Figure AppC.1. Raw data: (a) Displacement and (b), (c) load as a function of test time.

At time T_{start} (Figure AppC.1b), the load begins to increase, which means that the contact between the punch and the pillar starts. The corresponding displacement h_{start} (Figure AppC.1a) is deduced from the measured displacement. Then we get the corrected displacement.

After the compression, the load increases slightly due to the thermal drift. The load is corrected through subtracting the fitting straight line from the load curve. Then we obtain the corrected load.

The corrected displacement consists of the displacement of pillar, displacement of the frame, displacement of the diamond punch and the displacement of the sample, as shown in Equation AppC.1.

$$h_{pillar} = h_c - h_{frame} - h_{diamond} - h_{sample} \quad \text{(AppC.1)}$$

where h_{pillar} is the displacement of pillar. h_c is the corrected displacement. $h_{diamond}$ is the displacement of the punch. h_{sample} is the displacement of the substrate of the sample.

There is a relationship between the force, the contact stiffness, and the displacement, as shown in Equation AppC.2.

$$h = \frac{P}{S} \quad \text{(AppC.2)}$$

where P is the force. S is the contact stiffness. h is the displacement.

So, the h_{pillar} can be calculated as shown in Equation AppC.3.

$$h_{pillar} = h_c - \frac{P}{S_{frame}} - \frac{P}{S_{diamond}} - \frac{P}{S_{sample}} \quad \text{(AppC.3)}$$

where P is the corrected load. S_{frame} is the contact stiffness of the frame, depending on the compression system, which is around 284 mN/μm in this study. $S_{diamond}$ is the contact stiffness of the punch. S_{sample} is the contact stiffness of the substrate. The next step is to calculate the contact stiffness $S_{diamond}$ and S_{sample}.

Based on Sneddon's relationship [229, 230], a geometry-independent relation involving the contact stiffness, contact radius and contact modulus E_c^* can be derived:

$$S = 2E_c^* a \quad \text{(AppC.4)}$$

where a is the contact radius, which can be determined from the measurement of the sizes of pillar via SEM. The contact modulus of punch, $E_{diamond}^*$, is adopted as 1 150 GPa in this thesis. The contact modulus of sample, E_{Ti}^*, is determined by the nano-indentation measurement, which is around 120 GPa.

So, the displacement of the pillar and the load are determined. The load–displacement curve can be drawn.

Appendix D. Abbreviations

a–C, hydrogen free amorphous carbon;

a–C:H, hydrogenated amorphous carbon;

a–C:H:X, modified hydrogenated amorphous carbon, where X is non-metallic element;

a–C:H:Me, metal containing hydrogenated amorphous carbon;

CSS, contact start–stop;

CVD, chemical vapor deposition;

DLC, diamond-like carbon;

EDX, energy dispersive X-ray spectroscopy;

FCC, face-centered cubic;

FTIR, Fourier transform infrared spectroscopy;

GSR, gross slip regime;

HCP, hexagonal close packed;

HV, high vacuum;

IBAD, ion beam-assisted deposition;

IBD, ion beam deposition;

MoS_2, molybdenum disulfide;

MSR, mixed slip regime;

PACVD, plasma-assisted chemical vapor deposition;

PECVD, plasma-enhanced chemical vapor deposition;

PMMA, polymethyl methacrylate;

PSR, partial slip regime;

PTFE, polytetrafluorethylene;

PVD, physical vapor deposition;

Q, tangential force;

RCFM, running condition fretting map;

RH, relative humidity;

TEM, transmission electron microscopy;

THR, total hip replacement;

UHMWPE, ultrahigh molecular weight polyethylene;

UHV, ultra-high vacuum;

δ, displacement.

dernière page de la thèse

AUTORISATION DE SOUTENANCE

Vu les dispositions de l'arrêté du 25 mai 2016,

Vu la demande des directeurs de thèse

Monsieur P. KAPSA et Monsieur V. FRIDRICI

et les rapports de

Mme C. LANGLADE
Professeur - UTBM - Laboratoire Interdisciplinaire Carnot de Bourgogne - UMR 6303 CNRS
Site de Sévenans - 90010 Belfort cedex

et de

M. J. DENAPE
Professeur - ENI Tarbes - Laboratoire Génie de Production (LGP) - Avenue d'Azereix
BP 1629 - 65016 Tarbes cedex

Monsieur DING Haohao

est autorisé à soutenir une thèse pour l'obtention du grade de **DOCTEUR**

Ecole doctorale MATERIAUX

Fait à Ecully, le 22 octobre 2018

P/Le directeur de l'E.C.L.
La directrice des Etudes

M-A. GALLAND

ECOLE CENTRALE DE LYON
Service Scolarité
ECULLY